1-2021

Ga-based III-V semiconductor photoanodes for solar fuels and novel techniques to investigate their photocorrosion.

Sahar Pishgar
University of Louisville

Ga-BASED III-V SEMICONDUCTOR PHOTOANODES FOR SOLAR FUELS AND NOVEL TECHNIQUES TO INVESTIGATE THEIR PHOTOCORROSION

By

Sahar Pishgar
B.S. , Sharif University of Technology, 2012
M.S. , University of Louisville, 2017

A Dissertation
Submitted to the Faculty of the
College of Arts and Science at the University of Louisville
in Partial Fulfillment of the Requirements
for the Degree of

Doctor of Philosophy
in Physics

Department of Physics and Astronomy
University of Louisville
Louisville, Kentucky

May 2021

Ga-BASED III-V SEMICONDUCTOR PHOTOANODES FOR SOLAR FUELS AND NOVEL TECHNIQUES TO INVESTIGATE THEIR PHOTOCORROSION

By

Sahar Pishgar
B.S. , Sharif University of Technology, 2012
M.S. , University of Louisville, 2017

A Dissertation Approved on

April 28, 2021

By the Following Dissertation Committee:

_____

Dr. Gamini Sumanasekara

_____

Dr. Joshua Spurgeon

_____

Dr. Ming Yu

_____

Dr. Serban Smadici

DEDICATION

Dedicated to my parents, who have raised me to the person I am today.

You are always in my heart.

ACKNOWLEDMENTS

First and foremost, I would like to express my deepest appreciation and thanks to my advisor, Joshua Spurgeon for his great support and guidance throughout my graduate school at UofL. I appreciate his dedication to make my experience productive despite of all research challenges we have faced. He has been very generous with his time and knowledge to help me with different steps. I loved our group meetings because he has always been prepared with well-organized thoughts and research ideas to encourage the team and keep us going. During my six years at UofL, I have seen many of my friends who have eventually become disillusioned with their advisor, but I can honestly say that I would definitely choose the same research group if I had to make the decision over again. I also wish to thank Josh for creating such an encouraging and friendly environment in the group and making my graduate school such a memorable experience.

I am also thankful to Gamini Sumanasekera, who provided a situation that I could follow my research interests in Solar Fuels lab. Gamini helped me developing my material characterization skills, specifically resistivity and Hall effect measurements. He has always been very supportive and never hesitated his time and advice.

I would like to acknowledge my Ph.D. committee members, Serban Smadici and Ming Yu for their time, valuable comments and suggestions to improve my dissertation.

My thanks also go to all theme leaders and team members in the Conn Center, specially to Mahendra Sunkara. I also would like to express my appreciation to Jacek Jasinski in Materials Characterization lab, who is a great resource for all Conn Center members. He has always patiently helped me to learn the techniques specifically X-ray Photoelectron Spectroscopy.

I have worked with many fellow graduate students and post-doctoral fellows at Conn Center, and I would especially like to thank my former and current research group members as their help has been absolutely vital to my success. I appreciate the help of Sudesh Kumari, post-doctoral fellow. She has been very supportive and taught me a lot to get started in the lab when I joined the group. I am grateful to Saumya Gulati for her assistance and true friendship. Her sense of humor made the office life much more interesting. I also wish to thank Jacob Strain who has always been willing to help with anything. His hard work and passion in research have been inspiring. I also want to thank the rest of my team members at Conn Center, Matthew Mulvehill, Sylvia Liang, Sandesh Uttarwar, Francois Nkurunziza and Ramachandra Rao, Rong Zhao, Manthila Rajapakse, Bhupendra Karki and Sonia Calero for their help and kindness.

I wish to show my appreciation to Department of Physics and Astronomy for supporting me over these years, specially Jayanthi Chakram, Chris Davis and David Brown. I would also like to acknowledge the support from School of Interdisciplinary and Graduate Studies through “doctoral dissertation completion award”.

I have been lucky to have some amazing friends who have always supported me and I would like to thank them. I am indebted to Faren and Meysam for their support and precious friendship from the very first moment that we landed in Louisville, they made me feel like home. Thanks to Sahar G for her kindness and all the funny and happy moments we had together.

Finally, special thanks to my family. I am sincerely grateful to my parents for their love and always believing in me. I'm also heartily thankful to my siblings, they have loved and aided me along the entire path. I would like to specially thank Ali, for his tremendous support and guidance through my life, who taught me to dream big and persevere.

My deepest gratitude to my love, Niknam, who has been my soulmate through all the ups and downs of this journey. He always believes in me, even when I do not. I wouldn't be able to make it through without his support. I'm grateful for his endless love that keeps me going.

ABSTRACT

Ga-BASED III-V SEMICONDUCTOR PHOTOANODES FOR SOLAR FUELS AND NOVEL TECHNIQUES TO INVESTIGATE THEIR PHOTOCORROSION

Sahar Pishgar

April 28, 2021

Solar energy is one of the most abundant renewable energy sources. However, the diurnal variation of the sun as well as seasonal and weather effects, limits the widespread global implementation of solar energy. Thus, Cost-effective energy storage is critical to overcome the intermittent nature of solar energy available on the earth. Photoelectrolysis of water to oxygen and hydrogen fuel is a promising large-scale solution to store intermittent solar energy in a dense and portable form. Photoelectrochemical (PEC) water-splitting, or artificial photosynthesis, research strives to develop a semiconductor photoelectrode with both high efficiency and long-term stability. Semiconductors of the III–V class are among the most promising materials for high efficiency solar fuels applications. However, they suffer from severe instability in acidic and alkaline electrolyte and fundamental understanding of the corrosion mechanism of III-V semiconductors is of significant importance for the solar fuels community. This dissertation is focused on study of photocorrosion of

Gallium based III-V semiconductors. A thorough review of important in-situ analytical techniques for the investigation of materials stability is given. The review explains some of the main in-situ electrochemical characterization techniques, briefly explaining the principle of operation and the necessary modifications for in-situ operation, and highlighting key relevant work in applying the method for the investigation of material stability and interfacial properties for electrocatalysts and photoelectrode materials.

Next, in this dissertation, the corrosion of n-GaP, a promising III–V material for tandem top subcells, was investigated in strongly acidic electrolyte using an in-situ UV-Vis spectroscopy technique to monitor dissolved Ga and P species as a function of applied bias and time. The changing faradaic efficiency of the electrochemical GaP oxidation reaction was calculated from this data and used to interpret the corrosion process in conjunction with SEM and XPS characterization. In addition, corrosion measurements were made with thin conformal coatings of TiO_2 as a protective barrier layer on the GaP surface. Although the protective coating slowed the rate of GaP dissolution, the TiO_2 layers produced herein contributed significant charge-transfer resistance and still showed similar trends in the corrosion faradaic efficiency vs. time as the bare n-GaP.

Further, photocorrosion of n-GaAs, one of the most well-developed and efficient III-V semiconductors was studied in strongly acidic electrolyte. Three type of Ir, OER co-catalyst, were tested to investigate their affect on photocorrosion of n-GaAs. In-situ UV-Vis spectroscopy was utilized to monitor the corrosion faradaic efficiency and the results showed decreased dissolution faradaic efficiency to a small

degree over the first 15 minutes for samples with thin layers of Ir. SEM and XPS characterization have also been used to understand the photocorrosion mechanism.

To develop high efficiency and stable water splitting systems new semiconductor materials with appropriate band gap, band edge positions, charge carrier mobility and chemical stability are demanded. Synthesis of ternary III-V alloys enable us to tune the band gap of III-V semiconductor with changing the compositions according to the requirements of PEC systems. Herein, optical and electrical properties of a novel III-V ternary alloy $GaSb_xP_{(1-x)}$, synthesized in Conn Center for Renewable Energy Research by Halide Vapor Phase Epitaxy (HVPE) is reported. The effect of Sb addition on the band gap of the semiconductor was studied utilizing diffuse reflectance spectroscopy and photoluminescence spectroscopy. Band gap of HVPE-grown $GaSb_xP_{(1-x)}$ film, with x=0.03-0.06 is decreased due to Sb incorporation to the lattice of GaP indicating that it can be a promising photoabsorber for PEC systems. In addition, incorporation of Sb to the lattice of GaP was estimated using Vegard's law and X-ray diffraction spectrum of samples. Finally, resistivity and Hall effect measurements were performed to study the electrical properties of $GaSb_xP_{(1-x)}$ films.

TABLE OF CONTENTS

LIST OF TABLES

LIST OF FIGURES

CHAPTER 1

INTRODUCTION

1.1 Solar Fuels

Global energy consumption has increased rapidly recently and is still on rise due to expanding population and economic growth of countries. As shown in Figure 1 about 80% of consumed energy is provided by fossil fuels combustion[1] which release a large amount

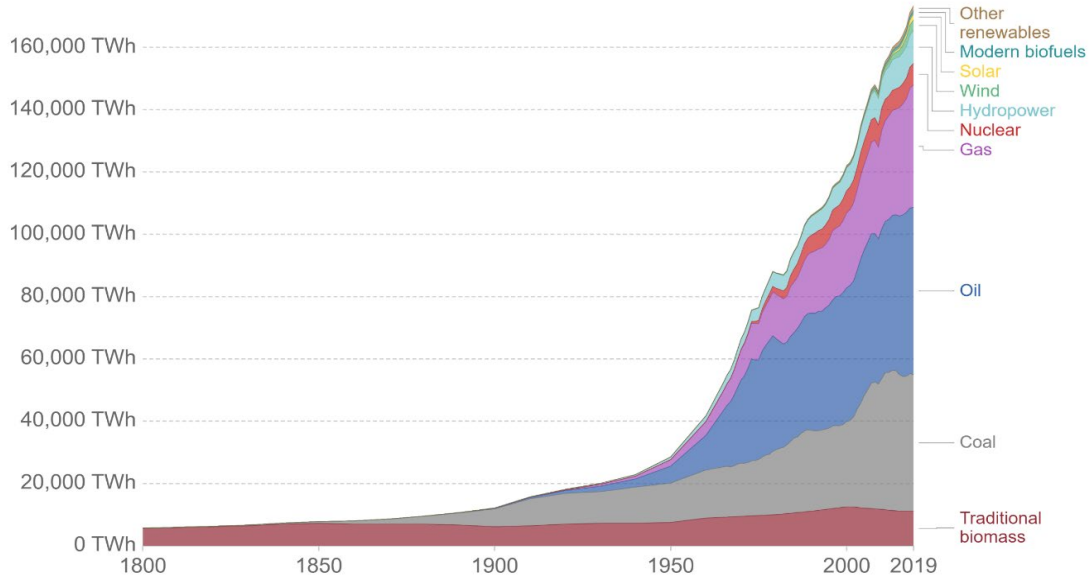

Figure 1. Global primary energy consumption by source. [1]

of greenhouse gas, CO_2. Increasing concentration of CO_2 in the atmosphere is one of the most important reasons of global warming that has worldwide environmental, economic and health consequences.

Renewable energy resources are suitable alternatives for fossil fuels and of all renewable energy sources, solar energy is the most abundant clean energy on the earth. Solar energy reaching the surface of the earth in one hour is more than the global energy consumption in one year which indicates the great potential of solar energy to satisfy increasing world energy demand[2]. Although the solar energy is abundant, low power density and intermittency have restricted its utilization. Storage of the solar energy is a method which helps to solve the solar power daily and seasonal variations. Giant batteries can be used to store solar energy but because of the high cost, poor performance or short life they are not an ideal option for large scale energy storage. Direct production of fuels using sunlight and storing the solar energy in chemical bonds is a promising large-scale solution to the intermittence nature of solar energy. Photoelectrochemical systems consist of light absorbing materials, catalysts, electrolyte and have special design to separate the products. All these components must operate simultaneously under mutually compatible conditions; Hence, there are many different variables that play role in developing high efficiency, cost effective and stable solar fuels systems.

1.2 Solar Driven Water Splitting

Artificial photosynthesis mimics the natural photosynthesis and enables storage of solar energy in chemical bonds and production of clean, high energy density and portable chemical fuels. Utilizing the solar energy to covert water molecules to oxygen and hydrogen is called solar driven water splitting[3-5]. Electrochemical water splitting consists

of two half-reactions, Oxygen evolution reaction (OER) and hydrogen evolution reaction (HER). In acidic electrolyte, oxidation and reduction reactions occur on anode and cathode respectively as:

$$HER: \quad 2H^+(aq) + 2e^- \rightarrow H_2(g); \quad E° = 0.00V \tag{1}$$

$$OER: \quad 2H_2O(l) + 4h^+ \rightarrow O_2(g) + 4H^+(aq); \quad E° = +1.23V \tag{2}$$

The 1.23 eV is the thermodynamic required energy to run the water splitting reaction. In photoelectrochemical systems, semiconductor photoelectrodes are used to absorb the energy of sunlight and drive the OER and HER reactions. Regarding the kinetic overpotentials at anode (220 mV on RuO_2), cathode (80 mV on Pt) and the solution resistance (100 mV), the photovoltage provided by semiconductors must be more than 1.63 eV to be able to run the reactions[6]. Semiconductors absorb the photons with energies higher than their band gap and upon absorption, electrons and holes are generated at the conduction band and valence band respectively. As shown in Figure 2, the conduction band minimum of an ideal semiconductor is more negative than water reduction potential (0 V

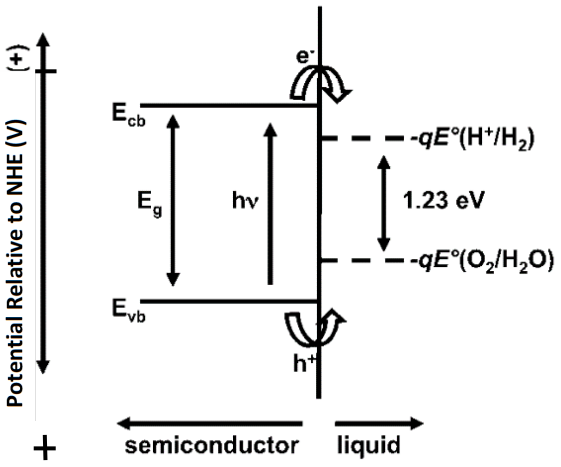

Figure 2. Ideal semiconductor with a band gap straddling OER and HER electrochemical potentials. [10]

vs NHE) and the valence band maximum is more positive than water oxidation potential (1.23 V vs NHE), therefore this single bandgap water splitting material drives both half reactions[7-9]. But not many semiconductors meet these criteria and can perform efficiently and stably under water splitting conditions and researchers strive to solve the problems of solar water splitting with focusing on the evaluation of new semiconductors for cathodic and anodic processes.

When a semiconductor is in contact with a liquid which contains redox couple (acceptor A, donor A^-) with electrochemical potential of $-qE°$, electrons will flow between the semiconductor and liquid until the fermi level is the same everywhere and equilibrium is reached. In solar driven water splitting systems, the redox couple for p-type semiconductor photocathode are H^+/H_2 couple and O_2/H_2O for n-type semiconductor photoanodes[10].

As a result of the charge transfer between semiconductor and liquid, an interfacial electric field form. Strength of the electric field depends on the initial difference between fermi level of the semiconductor and electrochemical potential of the redox couple in the solution. Ionized dopants in semiconductors spread over the depletion width which usually is in order of hundreds of nanometers and oppositely charge carriers are spread over Helmholz layer in the solution close to semiconductor which is usually much narrower. Band bending in semiconductor (Figure 3) resulted by the drop in strength of the electric field in solid directs the photo induced free minority charge carriers to move into the solution and run the oxidation/reduction half reactions. The photovoltage generated by semiconductor determines the photoelectrochemical reactions that can be driven by the system. As shown in Figure 3c, when semiconductor/liquid interface is under illumination,

electrons are excited from VB to CB and quasi-Fermi level of holes and electrons form. The difference between electron's and hole's quasi-Fermi level is called photovoltage and it should exceed 1.23 V for single semiconductor system with appropriate band positions to run the unassisted solar driven water splitting[10].

1.3 Photoanodes

In a n-type semiconductor photoanode with fermi level more positive than electrochemical potential of redox couples in solution, electrons flow from semiconductor to liquid until system reaches the equilibrium. Consequently, the photoanode's excess positive charge from ionized dopant atoms in semiconductor and solution's excess of negative charge result in an interfacial electric field. The band bending caused by electric field drop in the solid directs the photogenerated minority charge carries(holes) from VB towards the solution and drives the water oxidation reaction.

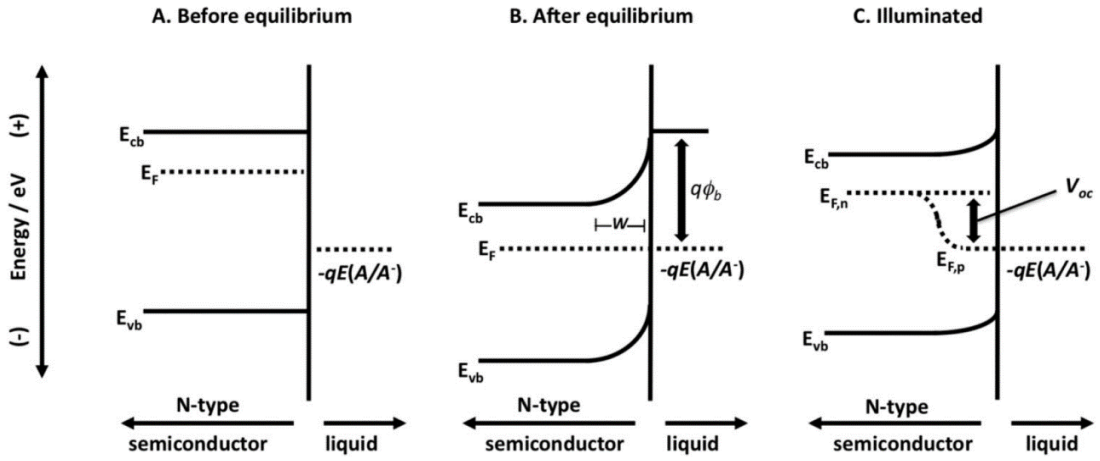

Figure 3. Semiconductor/liquid band energetics. (A) before equilibrium. (B) after equilibrium, in the dark. $q\Phi_b$ shows the barrier height. (C) in quasi-static equilibrium under illumination. $E_{F,n}$ and $E_{F,p}$ are electrons and holes quasi-Fermi level respectively. [10]

A n-type semiconductor photoanode for water oxidation reaction must have suitable band gap and band edge position, as well as suitable electrical properties such as dopant density and carrier mobility to be able to drive the reaction efficiently. In addition, photoanodes should be stable under oxidation conditions.

Metal oxide semiconductors have been vastly investigated as photoanode materials and they can oxidize water to O_2 in alkaline or acidic media. As shown in Figure 4[11], the valence band of most of the metal oxides such as TiO_2, WO_3, $BiVO_4$ are more positive than water oxidation potential (1.23V vs NHE) and they can be utilized as photoanodes. In addition, the self-oxidation potential (ϕ^{ox}) of these metal oxides are more positive than water oxidation potential and photogenerated minority carriers (holes) at VB prefer to drive

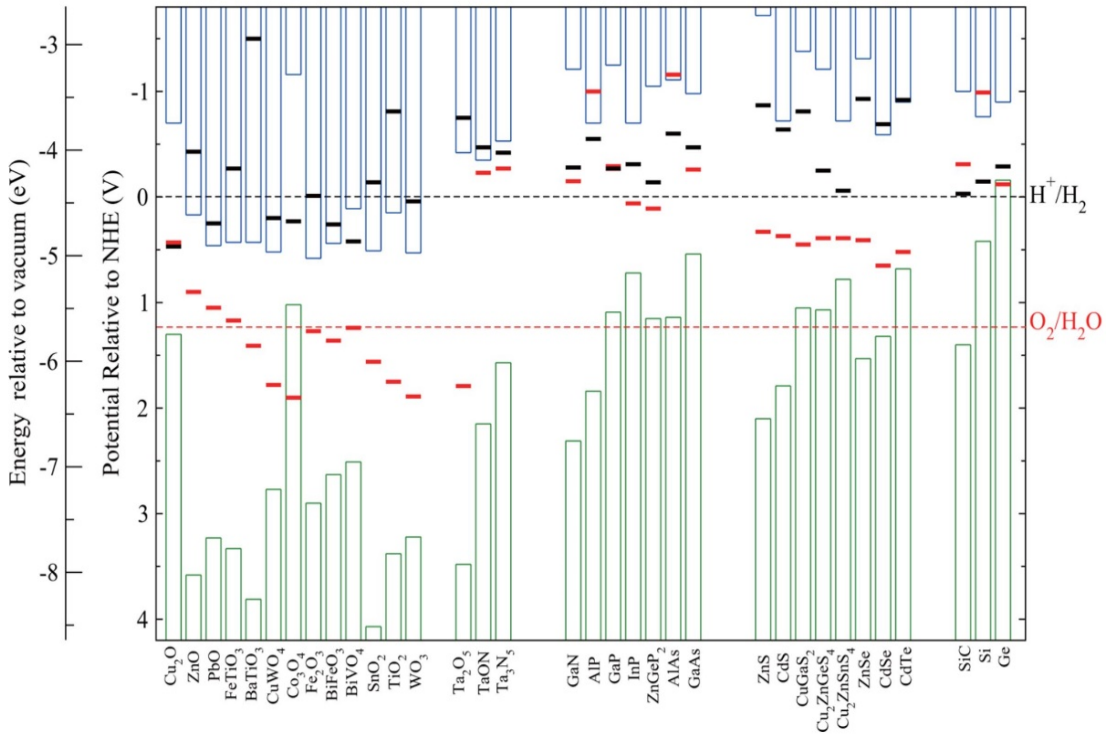

Figure 4. Calculated material oxidation potential (red bars) and reduction potential (black bars) relative to NHE in solution at pH = 0, room temperature, and 1 bar. The valence (green columns) and conduction (blue columns) band edge positions are also plotted. [11]

the OER rather than self-oxidation reaction which result in stability of metal oxides in oxidation conditions. However, they have been inefficient because of their too large band gaps and potential of VB around 3V which is much more positive than 1.23 V and the excess energy absorbed by the oxide will be wasted as thermal relaxation of excited electrons[10, 12-14]. The maximum theorical efficiency for these metal oxide semiconductors is less than 2%[10].

There are many other Semiconductors such as silicon (Si), gallium arsenide (GaAs) and gallium phosphide (GaP) with proper band gap and VB position for efficient solar driven water splitting, although these semiconductors are unstable in aqueous acidic or alkaline electrolytes and in anodic conditions. Self-oxidation potentials of these semiconductors are more negative than OER which leads to photopassivation or photocorrosion. Therefore, development of new semiconductors and strategies for safe, stable and efficient water splitting systems is of significant importance to realize the efficient solar hydrogen production.

1.4 III-V semiconductors

III-V semiconductors are alloys containing elements from group III and V in the periodic table. III-Vs are promising candidates for solar water splitting because of their superior electronic properties. III-V semiconductors offer significant photon-to-electron energy conversion in comparison to silicon-based systems. III-V based multijunction solar cells has the record efficiency of 47.1% while record efficiency of silicon-based systems are about 30%.[15-16] In addition, alloying of III-V semiconductors enables the tailoring of electronic properties like band gap and band edge position of the material for each particular system which can be very beneficial for PEC system. However, the fabrication

cost of high quality III-Vs is excessively high that limits the terrestrial use of III-V based photovoltaics. Instability and corrosion in aqueous solutions is another disadvantage of III-V semiconductors which makes them unsuitable for PEC systems. Hence, despite all advantages of III-V semiconductors there are still challenges that need to be addressed to make high efficiency, stable III-V based solar water splitting systems.

Striving for efficient water splitting systems, researchers have vastly investigated III-V semiconductors as single junction photoelectrodes and in tandem configuration.[16] For instance, n/p^+ GaAs, a III-V semiconductor with band gap of 1.42 eV and protective amorphous layer of TiO_2 was reported as a single photoanode with onset potential of 0.67 V (vs RHE), photocurrent density of 14.3 mA/cm^2 and over 25 hours of stability in alkaline electrolyte.[17]

In tandem configuration (multijunction cells), multiple photo absorbers are combined in a single device and each layer absorbs a specific spectral range of solar spectrum (Figure 5). Consequently, the absorption and thermalization losses are decreased resulting in improvement of sunlight energy conversion.

Band structure optimization in III-V semiconductors has led high solar to hydrogen (STH) efficiencies. Theorical calculations of STH efficiency of double junction cells show that combination of 1.6-1.9 eV (top-cell) and 0.9-1.2 eV (bottom-cell) results in STH efficiency more 25%.[18] For the first time, Khaselev and Turner designed a double junction cell with GaInP with band gap of 1.82 as top-cell and GaAs as bottom cell, they reported STH of 12.4%.[19] By then, many multijunction cells have been developed.[15-16, 20-21] For

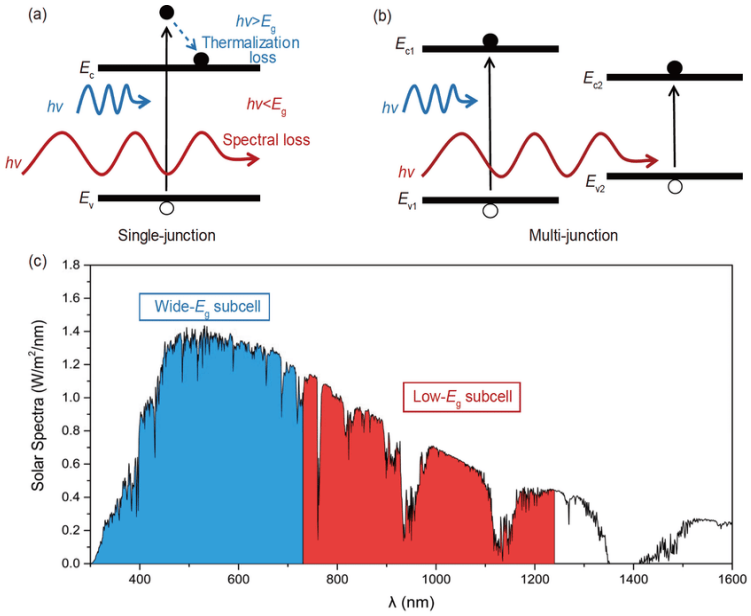

Figure 5. Schematics of light absorption in (a) single junction, (b) multijunction cell, (c) Absorption range of top-cell with higher band gap(blue,1.7eV) and bottom-cell with lower band gap (red, 1.1 eV).

instance, Cheng et al. have designed a monolithic photoelectrode, (GaInP/GaInAs)/TiO_2/Rh to run unassisted water splitting and this systems showed 19% of conversion efficiency and holds the record to date [22].

1.5 Stability of III-V semiconductors

III-V semiconductors suffer from severe corrosion and instability in acidic and alkaline solutions. As shown in Figure 4, oxidation potential of all III-V semiconductors is more negative than water oxidation level and self-oxidation reaction running by photogenerated holes are thermodynamically more favorable. Therefore, high quality and stable protection layers must be developed to avoid corrosion of III-V based photoelectrodes. The protection layers should be conductive to pass the photogenerated charge carriers to/from electrolyte.

To date, researchers have developed different types of protection layers and atomic layer deposition (ALD) of TiO_2 is the most common one that showed promising results. In 2014, Hu et al. reported deposition of relatively thick layer of defective amorphous TiO_2 (140 nm) utilizing ALD on n/p^+ GaAs photoanodes decorated with e-beam evaporated nickel catalyst. Electrically defective structure of amorphous TiO_2 allows the charge transfer through such a thick layer and simultaneously protects the surface of GaAs photoanode from corrosion over 25 hours in alkaline electrolyte.[17] However, ALD TiO_2 protection layers have been reported previously they were thin layers of crystalline TiO_2 (2-10 nm) to enable the charge transfer between the semiconductor and electrolyte.[23-24] Similar protection layer of amorphous TiO_2 has been applied to protect a multijunction photoanode of GaAs/GaInP and showed 80 hours of stable operation in 1 M KOH.[25]

Researchers have also reported deposition of MoS_2 on GaInP photocathode with stability of 80 hours. Metallic Mo used in the growth process can cause parasitic light absorption which limits the photoelectrochemical performance of the device.[26-27] Other protection strategies have also been studied such as electrodeposition of metal oxides, electroless deposition of noble metals, and coating of single layer graphene that protected III-V photoelectrode only for limited time.[28-31]However, some of the protection strategies have shown promising results, a single pin hole on the layer can lead to undercut etch pits and system failure. Development of protection strategies is thus still demanded to make III-V based photoelectrodes a viable technology for efficient water splitting systems.

It is worth noting that investigation and understanding of photocorrosion mechanisms is of great importance for solar fuels community and plays an important role in development of more stable systems. Researchers strive to design and deploy techniques

to provide deeper insight of corrosion mechanism which is discussed in more details in next chapter.

1.6 Overview of dissertation

This dissertation aims to study the photocorrosion mechanism of gallium based III-V semiconductor photoanodes in water splitting systems and introduces a novel in-situ technique to study corrosion of III-V photoelectrodes. A motivation to study III-V materials for water splitting systems is presented in chapter 1. It also includes an introduction to fundamentals of solar fuels, components of a water splitting systems, and properties of appropriate photoelectrode materials focusing on III-Vs. Challenges and system failure conditions such as photocorrosion are also discussed. Chapter 2 presents a thorough review on important in-situ techniques utilized for better understanding of corrosion and photocorrosion mechanism in electrocatalytic and photoelectrochemical systems. Chapter 3 introduces a novel in-situ UV-Vis spectroscopy technique to study photocorrosion of gallium phosphide (GaP) photoanodes including the design of the technique and experiments. Chapter 4 presents investigation of the photocorrosion on another gallium based III-V semiconductor gallium arsenide (GaAs) with in-situ UV-Vis spectroscopy in combination with other ex-situ techniques such as XPS. Chapter 4 provides more fundamental insights to the photocorrosion mechanism. In chapter 5, we have explored optical and electrical properties of a novel III-V ternary, $GaSb_xP_{(1-x)}$. Different characterization methods have been utilized to perform this study such as photoluminescence spectroscopy, X-ray diffraction spectroscopy and Hall effect measurement. The conclusion, challenges and recommended direction for future studies are also included in chapter 5.

We have performed a short, proof of concept study on plasma-assisted nitrogen reduction reaction for ammonia production which is not in line with other contents of this dissertation. We thus included the published work in appendix I.

CHAPTER 2

IN-SITU ANALYTICAL TECHNIQUES FOR THE INVESTIGATION OF MATERIAL STABILITY AND INTERFACE DYNAMICS IN ELECTROCATALYTIC AND PHOTOELECTROCHEMICAL APPLICATIONS

2.1 Introduction

Photoelectrolysis of water for carbon-free hydrogen production relies on semiconductors with appropriate bandgaps to absorb most of the solar spectrum while providing a total photovoltage in excess of ~1.6 V (the room-temperature thermodynamically required 1.23 V plus minimal anodic and cathodic overpotentials).

However, reaching appreciable rates for reduction at the cathode and oxidation at the anode in an electrolyte which is often highly corrosive or caustic

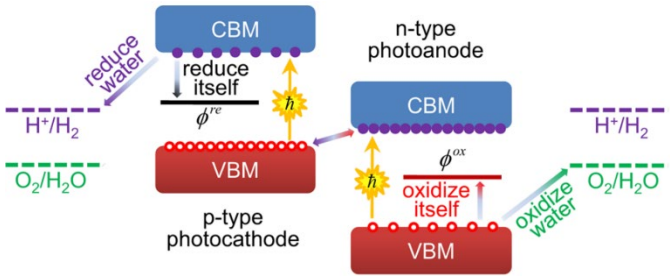

Figure 6. Band alignment of photoanode and photocathode semiconductors relative to water oxidation and reduction potentials and material self-oxidation and self-reduction potentials. [11]

gives rise to one of the grand challenges in the field of solar fuels: achieving material stability in harsh photoelectrochemical conditions. System components including catalysts, semiconductors, and conductive contact layers can all undergo corrosion or interfacial passivation processes which lead to device instability. The material stability can be succinctly conveyed using Pourbaix diagrams, which map the equilibrium material state as a function of pH and potential.[32] The electrochemical solid-aqueous equilibria can be computationally predicted to generate model Pourbaix diagrams.[33] Attaining chemical durability for efficient semiconductor photoelectrode materials in particular has been a major challenge. The electrode components can decompose via self-oxidation or self-reduction under anodic or cathodic potentials, respectively.[34-35] As illustrated in Figure 6, for the stability of a semiconductor photocathode, the material self-reduction potential, ϕ^{re}, should be more negative than the HER potential in order for conduction band electrons to kinetically prefer to drive water reduction rather than the self-reduction reaction. Likewise, for a photoanode the self-oxidation potential, ϕ^{ox}, should be more positive than the OER potential in order for valence band holes to kinetically prefer

to drive water oxidation rather than the oxidation of the semiconductor itself. Semiconductors which are thermodynamically stable in the dark may become unstable under illumination or applied bias when quasi-fermi level splitting gives sufficient energy to the electrons or holes to induce material self-reduction or oxidation, respectively.[7, 36-37]

In striving to develop efficient and stable materials for photoelectrolysis, several strategies have been devised to mitigate material instability. Researchers have had success protecting corrosion-prone electrodes by deposition of a very thin interfacial layer of a stable inorganic material via precise and conformal coating methods like atomic layer deposition (ALD).[17, 38-41] Titanium dioxide is the mostly widely used protection layer because it is stable across a wide potential and pH range, as evidenced by Figure 4 in which its self-reduction and self-oxidation potentials are well clear of the HER and OER potentials, respectively. For some semiconductors, most notably Si, chemical methods have enabled surface functionalization with organic groups which can also improve the robustness of the interface.[42-43] Modifications to semiconductor crystal structure and morphology, and the use of stabilizing redox couples which kinetically compete with corrosion reactions are some other strategies that scientists have employed for improved photoelectrochemical durability [34, 44-47]. For heterogeneous co-catalysts on the photoelectrode surface, there are a number of materials of competitive activity which are quite stable in alkaline conditions.[48] In strongly acidic electrolyte there are fewer options for stable active catalysts, especially at the anode for which rare element IrO_2 is one of the only viable materials. Researchers have primarily pursued mixed-

metal alloy compositions and modified material phases as strategies to enhance the durability of electrocatalysts.[49-51]

Despite the improved stability achieved with these methods, none have yet enabled the combination of high efficiency and long lifetime necessary for cost-effective commercial photoelectrochemical fuel production. For instance, ALD TiO_2 protective coatings have significantly improved durability for efficient III-V semiconductor photoelectrodes, but even a small pinhole will lead to corrosive undercutting of the protective layer and eventual device failure.[39] Therefore, a fundamental understanding of the corrosion and self-decomposition mechanisms remains of significant importance to the solar fuels community. Multiple conventional methods are routinely employed to investigate corrosion and photostability of electrodes, including electrochemical measurements (cyclic voltammetry and chronoamperometry/chronopotentiometry) to observe changes in PEC behavior, and ex-situ before and after analysis via techniques like scanning or transmission electron microscopy (SEM or TEM) and X-ray diffraction (XRD) to determine changes in morphology and/or crystal structure, X-ray photoelectron spectroscopy (XPS) to characterize changes in the interfacial chemical state, and inductively coupled plasma mass spectrometry (ICP-MS) to quantify dissolved elements.[17, 38, 52-56] Although these techniques are useful for describing post-mortem material degradation, the availability of a wider suite of in-situ material characterization methods is critical to enable researchers to gain deeper insight into the corrosion mechanism as it develops under realistic operation conditions.

The materials science community has invested significant effort into modifying many common analytical techniques to enable in-situ materials characterization during dark and/or photoelectrochemical operation. These methods make it possible to monitor the material corrosion, passivation, and restructuring in real-time. These in-situ methods range in sophistication and accessibility, as well as the information they provide. In presenting these techniques, we have broadly sorted them into three categories: (1) spectroscopy, (2) mass spectrometry, and (3) microscopy. Spectroscopy investigates spectra which result when matter interacts with electromagnetic radiation, and in-situ methods include UV-Vis spectroscopy, ambient-pressure X-ray photoelectron spectroscopy (APXPS), and Raman spectroscopy. Mass spectrometry ionizes chemical species and measures their mass-to-charge ratio, and methods including ICP-MS and differential electrochemical mass spectrometry (DEMS) have been utilized to investigate stability. Microscopy methods use different stimuli to produce spatial images of a variety of material properties, and include such techniques as in-situ transmission electron microscopy (TEM), electrochemical atomic force microscopy (EC-AFM), electrochemical scanning tunneling microscopy (EC-STM), and scanning electrochemical microscopy (SECM). This is not meant to be an exhaustive list, however, and other methods may exist with significant utility for monitoring material changes and interface dynamics.

Considering the significance of device stability in the solar fuels field, an overview of existing in-situ techniques along with highlighted reports of their implementation will be useful to the community and in particular to researchers with

an interest in understanding system degradation processes. In this review, each technique will be described beginning with a brief description of the corresponding conventional method as well as the required adjustments to convert it to an in-situ detection technique. Then, some representative example studies are highlighted to illustrate the capabilities, followed by discussion of the relative advantages and disadvantages of the technique.

2.2 Spectroscopy techniques

2.2.1 In-situ UV-Vis spectroscopy

Ultraviolet-Visible (UV-Vis) spectroscopy is a characterization method based on the absorbance, transmittance, and reflectance of materials in the UV-Vis spectral range (~170 – 800 nm). It is a relatively simple and inexpensive technique that is routinely employed for quantitative and qualitative measurements of solutions and solid-state samples. UV-Vis is mostly used to determine the concentration of a known solute or to identify functional groups and compounds. The measured absorbance at a particular wavelength corresponds to the energy difference between electronic states of a molecule, and commonly exhibited UV-Vis absorption bands include transitions involving double-bond or pi systems and nonbonding electrons as well as transitions between d-electron states of metals. The system photodetector measures the transmittance through the sample vs. wavelength, which is readily converted to absorbance. Absorbance can then be directly related to the optical path length, the species concentration, and the extinction coefficient via the Beer-Lambert Law.

UV-Vis spectroscopy can be employed in a spectroelectrochemical technique for the in-situ detection and time-resolved measurement of species concentrations

or thin film absorbance during reactions. Custom cell designs enable researchers to run electrochemical reactions in cuvettes and monitor the absorbance of ions in the electrolyte or on the surfaces of the working electrode under variable applied bias and reaction conditions.[57-59] Miniaturization of the cell components and the use of microelectrodes are generally required to enable full cell electrochemistry within a standard size UV-Vis cuvette while providing an unobstructed optical beam path for

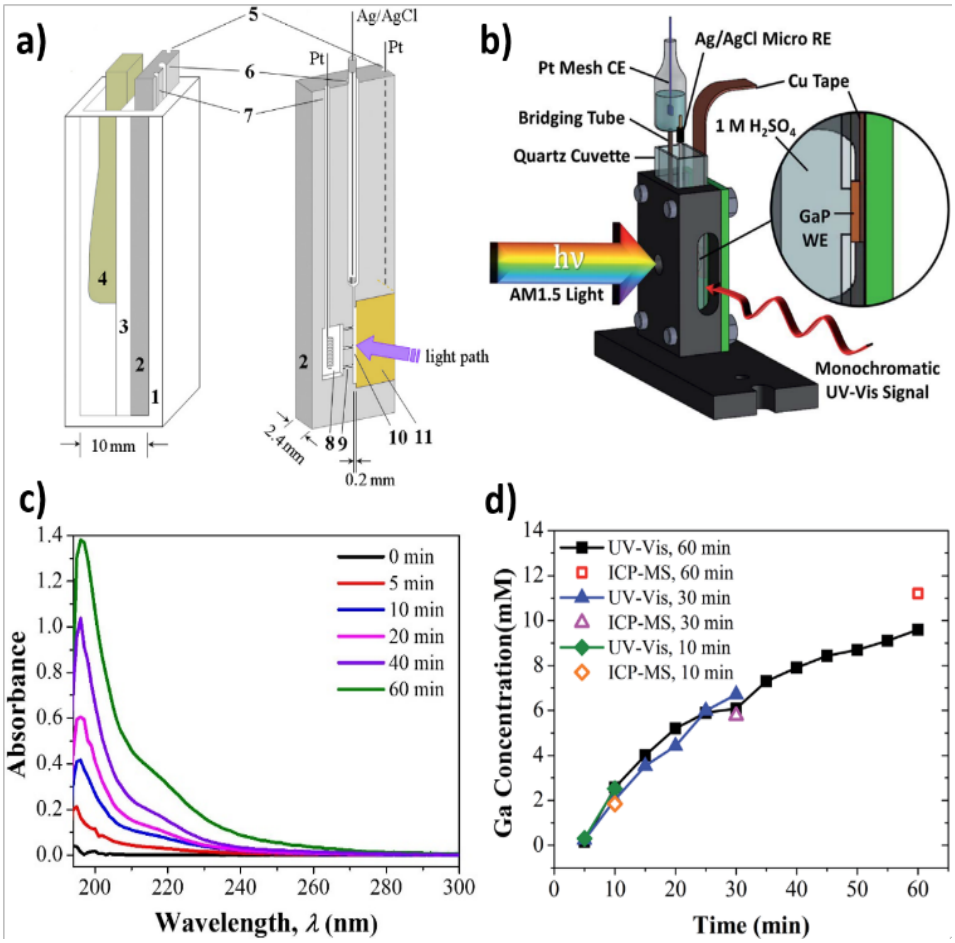

Figure 7. In-situ UV-Vis spectroscopy. (a) Schematic of a 3-electrode electrochemical thin-layer cuvette cell for a corrosion study of metallic electrodes.[63] The metal plate working electrode is #11 in the diagram. (b) Schematic of a 3-electrode cuvette cell for a photocorrosion study of illuminated semiconductor electrodes (n-GaP example). (c) Time-dependent absorbance spectra of electrolyte with illuminated n-GaP photoanode under applied bias. (d) Dissolved Ga concentration from (c) measured by in-situ UV-Vis compared to electrolyte aliquots measured by ICP-MS.[64]

analysis. As one example of the utility of in-situ UV-Vis spectroscopy in a photoelectrochemical application, Mandal et al. studied the band energetics of nanoparticle TiO_2 electrodes in KOH under applied bias. In monitoring the TiO_2 film, it was observed that the absorbance at the near bandgap excitation of 380 nm decreased at more negative potentials, which was attributed to filling of the low energy conduction band states which increasingly block the lowest energy transitions at greater negative applied bias [58].

Corrosion of materials under different electrochemical conditions is a topic that has been widely investigated by in-situ UV-Vis spectroscopy. The formation of complexes and compounds in the electrolyte during the corrosion reaction can be observed with UV-Vis spectroscopy by monitoring new peaks and changes in the intensity or position of the absorbance maximum[59-62]. For instance, the corrosion of metal electrodes in NaOH at different applied potentials has been studied by Li et al. Using a 3-electrode customized thin-layer spectroelectrochemical cell (Figure 7a), they found that sodium phytate significantly inhibited corrosion of brass in NaOH electrolyte. Absorbance spectra of the electrolyte at progressive times during the electrochemical reaction showed increased peak intensity corresponding to the dissolution of Zn^{2+} ions from the brass electrode, which was suppressed by the addition of the phytate anion.[63]

A similar UV-Vis in-situ method can be applied to operando investigations of photocorrosion of semiconductor electrodes. During the photocorrosion process for many semiconductors, material conversion at the semiconductor surface creates a species which can dissolve in the electrolyte. Therefore, monitoring the absorbance

of the electrolyte can provide qualitative and quantitative information about the decomposition process as it develops. Utilizing a custom electrochemical cuvette cell with an optical path for the UV-Vis signal through the electrolyte near the semiconductor and a simultaneous orthogonal white light AM1.5 illumination source on the electrode (Figure 7b), Pishgar et al. studied the photocorrosion of III-V GaP photoanodes at variable applied bias with and without a protective TiO_2 coating.[64] In this research, inductively coupled plasma mass spectrometry (ICP-MS) was used to calibrate the concentration of dissolved Ga and P in the 1 M H_2SO_4 electrolyte for quantification by UV-Vis absorbance peaks. Operando UV-Vis absorbance spectra vs. time (Figure 7c) could then be converted to a time-resolved measurement of the concentration of dissolved Ga and P in the electrolyte. The accuracy of the continuous UV-Vis data was confirmed by comparison to separate ICP-MS measurements on independent electrolyte aliquots (Figure 7d). This data was used to calculate the time-dependent corrosion reaction faradaic efficiency, which in conjunction with before and after SEM and XPS results was used to interpret the photocorrosion mechanism of the n-GaP photoanodes.[64] Klahr et al. utilized a similar setup to study the intermediate states formed on hematite photoelectrodes under illumination during water oxidation.[65] In this work, they monitored the absorbance of the hematite film vs. time and applied bias. The changing absorbance of the photoelectrode in conjunction with cyclic voltammetry and impedance spectroscopy data suggested the oxidation of a low valent Fe−H_2O or Fe−OH to a high valent Fe=O group at the surface.[65]

While useful for the real-time monitoring of dissolved species in the electrolyte or for photochromic or other absorbance changes in thin films, in-situ UV-Vis spectroscopy is not specifically surface sensitive nor is it straightforward to interpret for chemical information on unknown compounds. Solvation and pH effects can influence the absorbance spectra, making the unambiguous identification of unknown complexes challenging. For mechanistic interpretation, in-situ UV-Vis spectroscopy is most powerful when coupled with more informative techniques like XPS. Nevertheless, UV-Vis spectrometers are ubiquitous in most chemistry laboratories, making this one of the most widely accessible and cost-effective methods for the in-situ study of corrosion and material stability in electrochemical reactions. Also, unlike on-line ICP-MS, in-situ UV-Vis analysis can be done nondestructively in one static volume of electrolyte, allowing the monitoring of the evolution of corrosion in particulate slurry systems.

2.2.2 Ambient pressure X-ray photoelectron spectroscopy (APXPS)

X-ray photoelectron spectroscopy (XPS) is one of the most powerful techniques for studying the elemental composition and chemical states of the surface of materials. A sample is irradiated with X-rays which induce the emission of electrons via the photoelectric effect. A detector then measures the kinetic energy of these photoelectrons, which can be used to determine the binding energy of the respective orbitals. According to the Einstein relation, the binding energy of the photoelectron is given by the energy of the excitation photon, *hv*, minus the kinetic energy of the

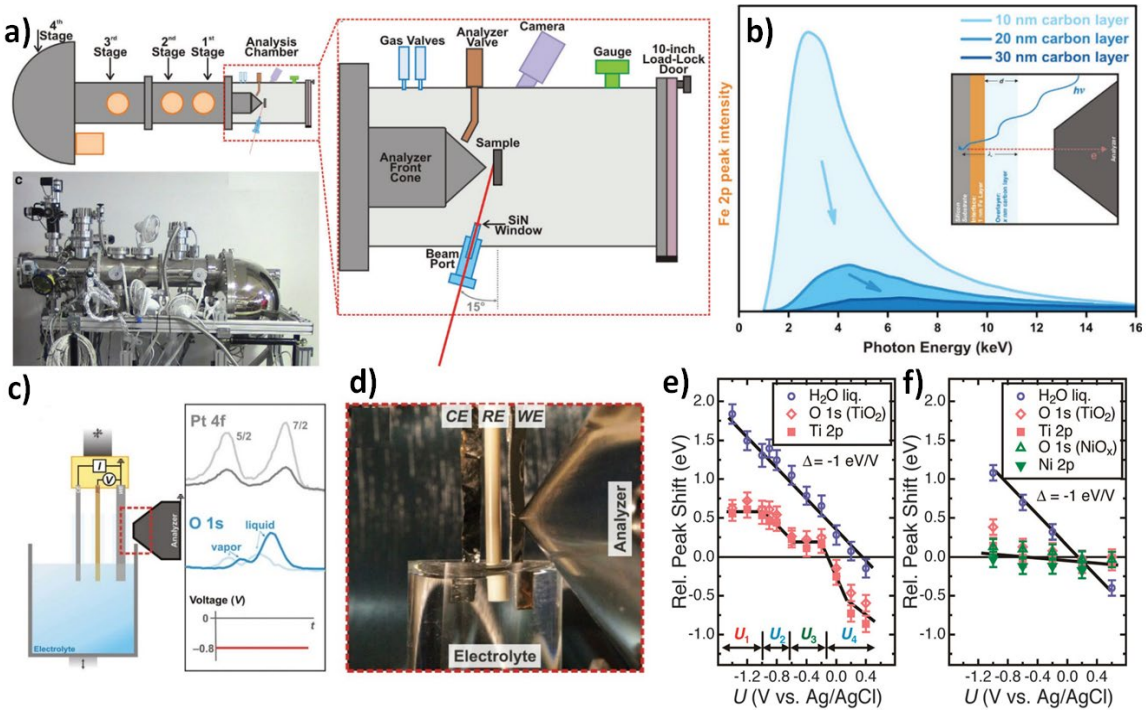

Figure 8. Ambient pressure X-ray photoelectron spectroscopy. (a) Instrumentation setup with multiple apertures using differential pumping system. (b) Simulated signal peak intensity vs. photon energy for a model system to find the optimal electrolyte thickness and photon energy for a 3-electrode cell in APXPS. (c) Schematic of a 3-electrode cell using the dip and pull method to create a thin electrolyte overlayer on the electrodes and corresponding XPS data vs. vapor-exposed electrodes. (d) Optical image of the 3-electrode cell under dip and pull method in XPS position.[67] (e-f) O 1s, Ti 2p, and Ni 2p signals as a function of applied bias (U) to a (e) bare p^+-Si/TiO_2 electrode and a (f) p^+-Si/TiO_2/Ni electrode in 1.0 M KOH(aq).[92]

photoelectron and the work function of the spectrometer. The binding energy of core electrons is characteristic of the individual atoms present and is indicative of the element as well as the oxidation state and chemical environment. In conventional XPS, using an irradiating soft X-ray source with a photon energy less than 2 keV limits the mean free path of the generated photoelectrons to less than 20 Å. Consequently, XPS is restricted to a purely surface sensitive characterization technique which requires an ultra-high-vacuum (UHV) condition to prevent electron scattering. The need for UHV inhibits XPS from being employed to investigate important chemical and physical processes under more realistic operation conditions.

To utilize XPS for the study of materials in liquid and gas environments, Siegbahn et al. introduced ambient pressure XPS (APXPS), which uses laboratory-based X-ray sources in near ambient pressure conditions[66]. In APXPS, the pressure of the sample chamber is elevated and connected to an electron analyzer through multiple apertures using a differential pumping system to protect the electron analyzer and minimize the path length of photoelectrons through the gas (Figure 8a).[67] Apertures with smaller sizes improve the differential pumping and reduce the path length of electrons through the high-pressure gas. Thus, a smaller size for the first aperture will lead to a higher upper pressure limit in APXPS measurements.

By applying this principle, researchers have strived to develop APXPS systems to study liquid-vapor[68-71] and solid-vapor[72-78] interfaces. This led to the development of a new generation of APXPS instruments with efficient differentially pumped electrostatic lens systems combined with a third generation synchrotron light source

at the Advanced Light Source (ALS) in Berkeley in 1999 [79-82]. As one example of the implementation of this system, Yamamoto et al. studied the mechanism of water adsorption on the surface of metals and oxides, such as Cu(110), Cu(111) and TiO_2(110).[83] They concluded that water adsorption happens on hydroxylated surfaces, and surface OH groups play an important role in this process. For a given material, the activation barrier for OH formation changes with the surface crystal structure, and thus the wettability depends on the surface crystal orientation.

APXPS is also a beneficial tool for the in-situ characterization of electrochemical and photoelectrochemical systems. The ambient pressure mode enables researchers to investigate in-situ solid-gas and solid-electrolyte interfaces at atomic and molecular levels, which has long been a challenge for the electrochemistry community [84]. X-ray synchrotron sources with higher energies (tender and hard X-rays) have been employed in APXPS to ensure that photoelectrons have enough energy to reach the interface of interest.[81-82, 85-86] Although X-ray sources with higher energies result in higher energy photoelectrons that can penetrate through thicker materials, these photoelectrons have less contribution from the interface region. In addition, increased photon energy causes a decrease in the ionization cross section, which leads to a lower signal-to-noise ratio. Hence, finding the optimal X-ray energy range is of great importance to the sensitivity and resolution of APXPS. Axnanda et al. simulated a model system to find the optimal photon energy and electrolyte thickness to maximize the peak intensity of the interface region.[67] This model consisted of a carbon layer of variable thickness to mimic a thin electrolyte layer, a 1 nm Fe layer to represent the interface region (the electrical double layer is typically

~ 1 nm), and a Si substrate. As shown in Figure 8b, the maximum signal-to-noise ratio happens in the tender X-ray region (2 – 7 keV) with less than 30 nm thick electrolytes[67].

Researchers have developed various instrumentation and cell designs inside the analysis chamber to accommodate the system of interest. For instance, Takagi et al. employed APXPS with a custom-design polymer electrolyte fuel cell with a membrane electrode assembly under a 3000 Pa vapor pressure of water to investigate the oxidation reaction on a Pt/C electrode under working conditions.[87-88] For in-situ electrochemical studies with the need for a reference electrode, like corrosion at interfaces, custom 3-electrode apparatuses have been designed in the analysis chamber of APXPS.[67, 89] As a practical method, the electrodes can be dipped into the electrolyte and then partially pulled out while a section of the electrodes are still in contact with the bulk electrolyte. This dip and pull method enables a thin layer of electrolyte (10-30 nm) to form on the electrodes as illustrated in Figure 8c-d and allows the direct analysis of surfaces under realistic electrochemical conditions.[67]

APXPS with the dip and pull method has been used to study fundamental interfacial phenomena in 3-electrode electrochemistry for a number of systems relevant to solar fuels. Utilizing this method, potential distributions of the electrolyte double layer and reaction mechanisms of catalyst surfaces have been studied as a function of applied potential in electrolytes of different pH.[90-91] Also, Lichterman et al. studied the solid-liquid interfaces of p^+-Si/TiO_2 and p^+-Si/TiO_2/Ni electrodes in 1.0 M KOH(aq) to verify that the energy-conversion behavior of semiconductor/liquid and semiconductor/metal junctions experimentally confirmed

theoretical calculations.[92] For this study, the working electrode was grounded to the electron analyzer to level their respective Fermi energies, and therefore binding energies of the core levels were referenced to this consistent Fermi level. In an ideal semiconductor/liquid junction, the core levels of bulk liquid water and the semiconductor should shift consistently with applied potential. As shown in Figure 8e, although the water O 1s peak shifted linearly with applied potential, TiO_2 O 1s and Ti 2p behaved differently, which are informative of the band bending conditions at each applied potential. The band bending and rectifying behavior of the semiconductor/liquid junction were complexly affected by the applied potential due to the presence of mid-gap surface or bulk electronic defect states which cause Fermi level pinning. After the deposition of Ni on TiO_2 electrodes, binding energies of the TiO_2 core level became almost independent of the corresponding electrolyte (Figure 8f). The Fermi level of TiO_2 was effectively pinned by the Ni layer, and the TiO_2/Ni and electrolyte displayed ohmic contact behavior. Using the APXPS data, these researchers calculated the density of electrochemically active defect states in the semiconductor using the non-ideal peak shifts of the semiconductor core levels and a model based on metal-oxide semiconductor solar cells.[92-93] Ali-Löytty et al. utilized a similar APXPS electrochemical setup and investigated a NiFe water oxidation electrocatalyst in 0.1 M KOH under anodic potentials. They reported an increase of the O:OH ratio upon increasing the applied potential from 0 to 0.3 V vs. Ag/AgCl, which was attributed to initial stages of the oxidation of $Ni(OH)_2$ to NiOOH.[94]

With its surface sensitivity and the chemical information it provides, ambient or near-ambient pressure XPS is well-situated to provide fundamental insights into

semiconductor photocorrosion and passivation processes for photoelectrodes in solar fuels. For instance, Zhang and Ptasinska studied the interaction of O_2 and H_2O with GaP under a range of pressures and temperatures.[95-96] They observed that for the O_2/GaP interface, the surface oxidized to a mixture of Ga_2O, Ga_2O_3, and $GaPO_m$ species. For the H_2O/GaP interface, the oxidation proceeded through a Ga_2O-like intermediate which then converted to O_n-Ga-$(OH)_{3-n}$ with a different extent of oxidation and hydroxylation depending on the pressure and temperature. Similarly, Starr et al. investigated $BiVO_4$ photoelectrodes in aqueous potassium phosphate electrolyte at different pressures and in the dark vs. under illumination.[97-98] With higher water vapor pressure, there was increased reduction of V^{5+} to V^{4+} at the surface. Under illumination with a 20 nm thick electrolyte, $BiPO_4$ was observed to form at the surface.

APXPS is a powerful tool which lets researchers study changes in the chemical state of the surfaces of electrodes in gas and liquid environments under operating conditions. This technique enables the experimental monitoring of interfacial oxidation states and band energetics as a function of applied potential in the electrolyte. It could therefore be one of the most comprehensive tools available for experimentally investigating the mechanism of chemical changes to material stability in solar fuels applications. However, disadvantages include low limits for the applied current density due to high ohmic losses in the thin electrolyte films and differences in the hydrophilicity of electrode surfaces, which leads to inconsistency in the electrolyte film thickness. Moreover, APXPS generally requires a synchrotron radiation source and a high level of technical sophistication and expertise to

implement, greatly reducing the accessibility of this technique for the average researcher.

2.2.3 In-situ Raman spectroscopy

Raman spectroscopy is a spectroscopic technique that can be used to probe vibrational, rotational, and low frequency modes of materials. A monochromatic electromagnetic radiation beam, usually a laser, interacts with molecular vibrations, or phonons, of a material resulting in inelastically scattered photons with different energy levels. The difference in photon energy between the incident and scattered beams contains useful information about the vibrational modes of molecules in a particular system, commonly referred to as the fingerprint of those materials [99-101]. This technique can be utilized for the understanding of interfacial structure and pathways of electrochemical reactions. There are different types of Raman spectroscopy, including surface-enhanced Raman spectroscopy,[99] tip-enhanced Raman,[102] resonance Raman,[103] stimulated Raman,[104] and transmission Raman.[105]

Surface-enhanced Raman spectroscopy (SERS) is commonly used for in-situ investigations of electrochemical systems. SERS, compared to other forms of Raman spectroscopy, is more useful and practical when studying electrochemical interfaces, especially systems with weak signals.[99] This technique utilizes enhanced inelastic light scattering (by a factor of 10^8 or even larger) of molecules adsorbed on roughened metal surfaces such as silver, gold, or copper.[106] The mechanism of signal enhancement in SERS is attributed to the excitation of localized surface plasmons, in which the oscillating electric field associated with the incident light interacts with the electron cloud in metal nanoparticles and amplifies the inelastic scattered light.[99]

Hence, selection of a proper signal-enhancing material (SERS substrate) and optical apparatus is of great importance for the generation of the enhanced Raman signal.[99]

Researchers have put significant effort into designing electrochemical Raman (EC-Raman) cells with high signal-to-noise ratios for in-situ measurements in liquid electrolyte. Fleischmann et al. designed one of the first EC-Raman cells containing a thick optical glass window and a thin layer of electrolyte to study the process of pyridine adsorption on a silver electrode, which resulted in the observation of SERS phenomena.[101] Another EC-Raman cell designed by Ren et al. was made of Teflon to study the oxidation of methanol on rough Pt electrodes.[107] In this cell, a quartz window over the thin electrolyte layer prevented corrosion of the objective lens and corresponding contamination of the electrolyte. Because the mismatch of refractive indices between the quartz window and the electrolyte causes a decay of the Raman signal from the working electrode, a thin electrolyte layer of 0.2 mm was chosen to enable a strong Raman signal while providing sufficient depth for a tolerable ohmic drop and to allow diffusion effects of the observed electrochemical species.[107] Detection efficiency of the Raman spectra has since been improved with windowless cell designs which eliminate refraction by the glass and induce a thin electrolyte meniscus at the working electrode (Figure 9a).[108] Zeng et al. also published a design of an EC-Raman cell incorporating a water immersion objective with a long working distance that facilitates the use of a thicker electrolyte layer (2 mm).[109] As illustrated in Figure 9b, the objective lens is connected to the cover glass through a droplet of water to account for the mismatch of refractive indices. In this work they investigated the effect of the cover glass and electrolyte

thicknesses on the in-situ Raman signal. By using the water immersion objective, the thickness of the electrolyte did not affect the Raman signal, although the signal did decrease with a thicker cover glass.[109]

EC-Raman cells developed for SERS have enabled researchers to study and monitor the molecular structure of catalysts during electrochemical reactions to provide insight for the design of more efficient and stable electrocatalytic systems.[110-114] For instance, Deng et al. monitored the surface structure of Cu, Cu_2O, CuO, and $Cu(OH)_2$ catalysts using in-situ EC-Raman spectroscopy during water oxidation in 0.1 M KOH. In-situ Raman spectra of the catalysts held at a potential of 1.7 V vs. RHE showed that Cu^{III} oxide (peak at 603 cm^{-1}), a metastable species, was only formed on CuO and $Cu(OH)_2$ electrodes and catalyzed water oxidation 10 times more efficiently than the other two electrodes (Figure 9c). This finding suggests that Cu^{III} species formed under bias are the catalytically active sites for the oxygen evolution reaction, an observation made possible by in-situ EC-Raman.[111] Similarly, Tang et al. used a windowless EC-Raman cell to study interfacial structural evolution during water oxidation of a NiFe electrocatalyst in aqueous 0.1 M KOH.[108] It was shown in this work that both layered double hydroxide and spinel oxide forms of the catalyst underwent a surface transformation to oxyhydroxides at

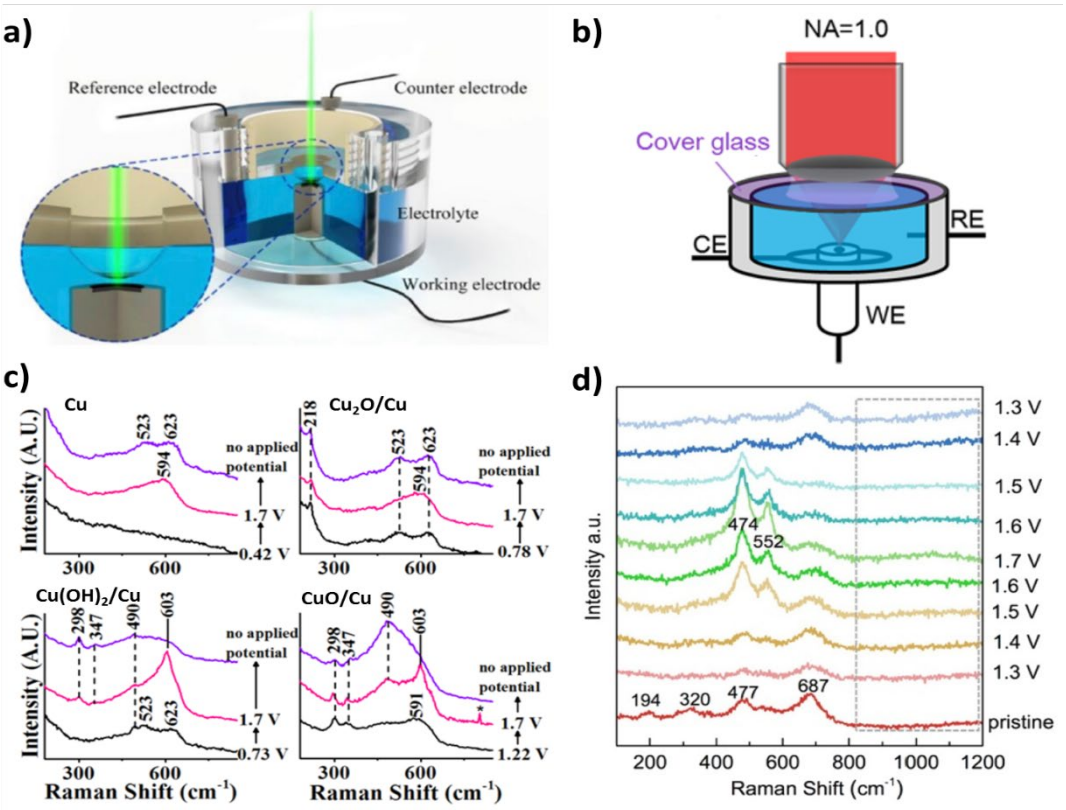

Figure 9. In-situ Raman spectroscopy for electrocatalysis. (a) Schematic of a windowless thin layer EC-Raman cell,[108] and (b) an EC-Raman cell with a water immersion objective (NA = numerical aperature).[109] (c) In-situ Raman spectra of Cu and different oxidized Cu surfaces under applied bias for water oxidation in 0.1 M KOH.[110] (d) In-situ Raman spectra of a Ni-Fe spinel catalyst during water oxidation at different potentials in 0.1 M KOH. (V vs. RHE)[108]

relevant oxygen evolution potentials, but the extent of the oxyhydroxide formation was lower on the NiFe spinel, accounting for its lower water oxidation activity (Figure 9d). Numerous other catalysts such as IrO_2,[112] CoO_x,[113] and MoS_x[114] have been studied with in-situ Raman spectroscopy to further the understanding of electrochemical reaction mechanisms by identifying adsorbed intermediates and reactive sites on the electrochemical interfaces. Also of interest to the solar fuels community, in-situ EC-Raman has been applied to investigate catalysts for the electrochemical reduction of CO_2, including investigations of the effect of species

adsorption and structural changes on the reaction mechanism at Ag,[115] Cu,[116] and SnO_2[117] electrodes. These fundamental insights provided by in-situ Raman spectroscopy help researchers develop better catalysts with higher efficiency and selectivity.

Electrochemical surface-enhanced Raman spectroscopy is also a powerful tool for the operando investigation of material stability in many applications relevant to solar fuels. In-situ EC-Raman has been used to study the potential dependence and chemical nature of the corrosion of metallic electrodes as well as the effectiveness of additives for corrosion inhibition.[118] Chen et al. used in-situ Raman to study the stability of $NiCo_2O_4$, a p-type transparent conductive oxide (p-TCO) that can be utilized as a protection layer for water oxidation photoanodes. They deposited $NiCo_2O_4$ on a Au substrate ideal for SERS measurements. The Raman spectra of $NiCo_2O_4$ showed the p-TCO was stable even after 16 hours of electrochemical cycling, with an absence of peaks for possible oxidation or phase segregation products and only modest broad peaks for some NiOOH [119].

Dynamic changes at the surface or interfaces of semiconductors have been explored with in-situ Raman spectroscopy as well. For instance, the technique has allowed the monitoring of the evolution of microstructural changes and phase formations in Si,[120] TiO_2,[121] $CuInSe_2$,[122] Cu_2ZnSnS_4,[123] and metal halide perovskite[124] photoabsorbers. In-situ Raman spectroscopy has also been enlightening for the study of chemical changes due to etching or corrosion processes for photoelectrodes. The photocorrosion process of CdS as a hydrogen evolution photocatalyst under visible light illumination has been studied in air vs. Ar

atmospheres via in-situ Raman spectroscopy.[125] Figure 10a shows the Raman spectra

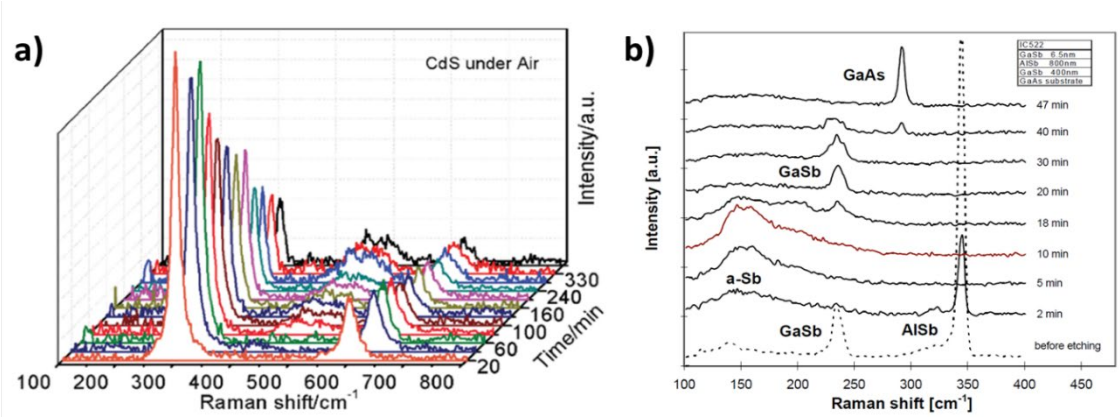

Figure 10. In-situ Raman spectroscopy for material stability. (a) Raman spectra of a CdS photocatalyst reacting in air under visible light illumination. [125] (b) Raman spectra of the chemical etching of a III-V semiconductor GaSb/AlSb/GaSb/GaAs heterostructure. Spectra were collected in situ through the stirred etchant, which was photoresist developer MF319. [129]

of CdS particles in air-saturated aqueous solution with Na_2S and Na_2SO_3 electron donors under visible light. The peak at ~500 cm^{-1} increased as the reaction progressed, indicating the substitution of surface S atoms with O and the formation of CdO, which was largely suppressed for CdS reacting under an Ar atmosphere as compared to an air atmosphere.[125] Balog et al. studied the optoelectronic properties of CuI photoelectrodes in 0.1 M Bu_4NPF_6/ dichloromethane and conducted in-situ Raman spectroscopy under applied potentials. Under these conditions, they found that the cathodic photocorrosion was kinetically hindered. A reversible gradual change was seen in the Raman spectra of the photoelectrodes that indicated increased disorder and changes in the density of states.[126] Other examples include the application of in-situ Raman spectroscopy to study the photocorrosion of WS_2[127] and CdSe[128] photoelectrodes. Photoelectrodes from III-V semiconductors are some of the most promising for solar fuels applications due to their high efficiency and tunable bandgaps, but photoelectrochemical instability has remained a major

challenge.[17] In-situ Raman spectroscopy could be useful for studying these processes as well, as highlighted by the work of Gatzke et al. on the etching of III-V semiconductor heterostructures. In their work, a photoresist developer was used to selectively etch antimonides. As revealed with real-time in-situ Raman monitoring, etching of AlSb led to a surface layer of amorphous Sb that slowed the etch rate whereas GaSb layers were etched without producing this residue layer (Figure 10b).[129] In-situ electrochemical Raman spectroscopy could thus realistically be expected to provide a wealth of information on operando photocorrosion for state-of-the-art photoelectrodes.

In-situ Raman spectroscopy has a number of advantages that make it a useful technique for studying material stability and reaction mechanisms in electrochemical systems. The inelastically scattered photons that make up the Raman signal probe several aspects of chemical bond states and provide a highly specific chemical fingerprint to identify a wide range of molecules. Because it is nondestructive, spectra can be acquired in seconds, and water is only a weak Raman scatterer, Raman spectroscopy can be modified for real-time monitoring in aqueous electrolytes. Besides molecular identification, the Raman signal can also be interpreted for changes in the material microstructure and crystallinity as well as lattice strain. By coupling with microscope optics, the Raman spectra can be collected with high spatial resolution. With appropriate choice of metallic substrate, a surface-enhanced Raman signal can enable highly surface sensitive measurements. However, leveraging the SERS effect can thus require depositing materials on a substrate other than the as-deposited electrode material under investigation. In

general, however, the Raman effect is very weak and detection requires sensitive and highly optimized instrumentation. Because of the sophisticated optics and high-powered laser, Raman spectroscopy is a fairly expensive technique, however it is available to many researchers through materials characterization user facilities.

2.2.4 Mass spectrometry techniques

2.2.4.1 On-line inductively coupled plasma mass spectrometry (ICP-MS)

ICP-MS is a quantitative elemental analysis technology capable of detecting a wide range of elements. This technique is multi-element and highly sensitive to low and ultra-low concentrations of analytes, even in the range of parts per trillion (ppt). In ICP-MS, a sample is usually dissolved in an acidic solvent and nebulized into the inductively coupled plasma, in which the analyte is atomized and ionized at a temperature of ~ 9000 K, then accelerated via an electric field and deflected via a magnetic field into a mass analyzer for isotopic and elemental analysis on the basis of the mass-to-charge ratio. Unlike most other forms of inorganic mass spectrometry, ICP-MS allows for time-resolved monitoring of species concentration. Continuous sampling is possible because the differential pumping through a series of vacuum stages separated by differential apertures permits the introduction of the analyte plasma at atmospheric pressure.[130]

The design of electrochemical or scanning flow cells coupled to ICP-MS enables researchers to conduct on-line monitoring of dissolved elements in the electrolyte during electrochemical measurements. Utilizing on-line ICP-MS, researchers can study the degradation through dissolution of electrocatalysts and

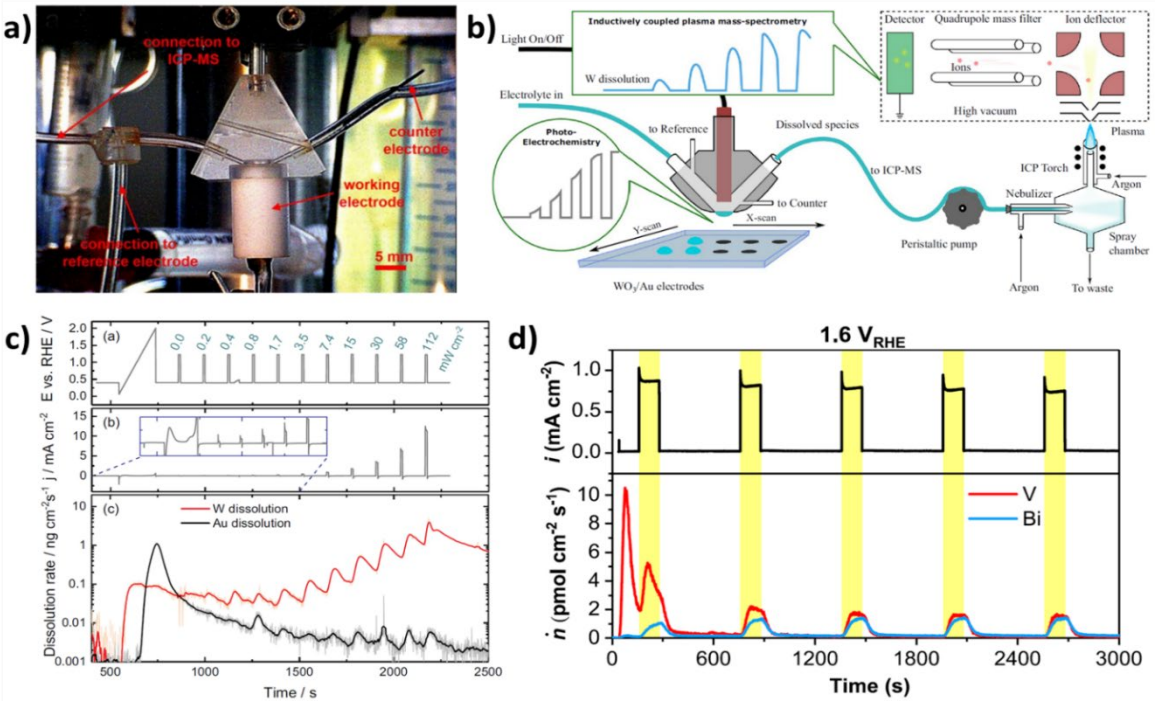

Figure 11. On-line inductively coupled plasma mass spectrometry. (a) Image of a scanning flow cell for real-time ICP-MS measurements. [132] (b) Schematic representation of a setup for an on-line photoelectrochemical ICP-MS system.[144] (c) Illuminated ICP-MS measurements for WO_3 on Au, with applied potential and illumination intensity (top), corresponding electrode photocurrent density (middle), and detected W and Au dissolution (bottom).[144] (d) Dissolution of Bi and V from a $BiVO_4$ photoanode at 1.6 V vs. RHE with pulses of illumination in yellow. [145]

photocatalysts and gain insight into the kinetics of material instability under operational conditions.[131] An example scanning flow cell connected to ICP-MS is shown in Figure 11a.[132] The electrolyte enters the cell through the inlet and flows sequentially across the counter, working, and then reference electrodes, respectively, before exiting to the ICP-MS for on-line analysis. Placing the working electrode downstream of the counter electrode limits possible back reactions of the dissolved analyte species.

On-line ICP-MS has been widely used to investigate the corrosion and dissolution of various metals and electrocatalysts.[131-135] Hochstrasser-Kurz et al., for

instance, used this technique to study corrosion of the metal matrix composite material WC-Co, also called cemented carbide, finding that increased pH led to the chemical dissolution of the WC while an anodic electrochemical route caused the dissolution of Co.[136] Klemm et al. used a similar setup to study electrochemical dissolution of copper in HCl.[137] The technique has also been demonstrated for the study of Pt dissolution behavior in nonaqueous organic vs. aqueous electrolytes.[138] On-line ICP-MS has been employed to evaluate the stability of many OER and HER electrocatalysts such as Ir/IrO_2,[139-141] Ru/RuO_2,[135, 139] and NiMo.[142] For example, Jovanovic et al. studied and compared the stability of thermally vs. electrochemically oxidized IrO_2 nanoparticles in acidic media. From time-resolved potential-dependent profiles of Ir dissolution, it was determined that Ir particles begin dissolving below the OER potential, but much less so for the thermally oxidized material. However, electrochemically pretreated Ir particles showed higher stability and activity under OER-relevant potentials due to an alternate corrosion mechanism.[140] For an on-line ICP-MS study in alkaline electrolyte of the hydrogen evolution catalyst Ni_xMo_{1-x}, the Mo leached out selectively at potentials more positive than -0.15 V vs. RHE and formed Ni-enriched surface sites.[142] The work concluded that the high HER activity of NiMo is likely attributable to the high surface area from electrochemical de-alloying during Mo dissolution rather than intrinsic properties of the binary alloy. Speck and Cherevko have extended the use of on-line ICP-MS to study the stability of Cu as an electrocatalyst for CO_2 reduction, finding that Cu dissolution was dependent on the applied potential and the pH of the electrolyte.[143] Results showed that long-term stability of Cu electrodes

is achievable by keeping the potential less than the Cu^0/Cu^I redox potential and maintaining an ideal pH between 9-10.

On-line ICP-MS measurements can also be employed in photoelectrochemical corrosion studies by introducing a light source to the scanning or electrochemical flow cell design. As illustrated in Figure 11b, flow cell designs have been created with LED illumination directed through the cell to the working electrode using a fiber optic cable.[144] Using this setup, the photoanodic dissolution of WO_3 on Au foil as a function of applied potential and light intensity was investigated in aqueous 0.1 M H_2SO_4 electrolyte. WO_3 was found to be stable in the dark across a wide potential range, but under illumination the W dissolution rate scaled to the photocurrent density, which was proportional to the light intensity (Figure 11c).[144] Similarly, this illuminated scanning flow cell approach was implemented to study the photocorrosion of $BiVO_4$ photoanodes in a buffered aqueous electrolyte at pH 7.[145] A significant initial dissolution of the surface V was observed upon contact with the electrolyte, after which the photoelectrochemical dissolution of both Bi and V was an order of magnitude higher than rates in the dark at the same potential (Figure 11d). The oxidation of Bi(III) was determined to be the main mechanism for PEC dissolution. These examples demonstrate that similar on-line photoelectrochemical ICP-MS setups can be utilized to study a wide range of photoelectrode materials and provide a better understanding of photocorrosion mechanisms, especially when implemented alongside other complementary characterization techniques.

There are clear pros and cons for on-line ICP-MS as a characterization technique. Its greatest strength is that it can provide quantitative multielemental concentration values for dissolved species in real time under operating conditions with very high sensitivity. Because it uses a mass spectrometer, isotopes can be distinguished, and the method is thus amenable to isotopic labeling studies. By

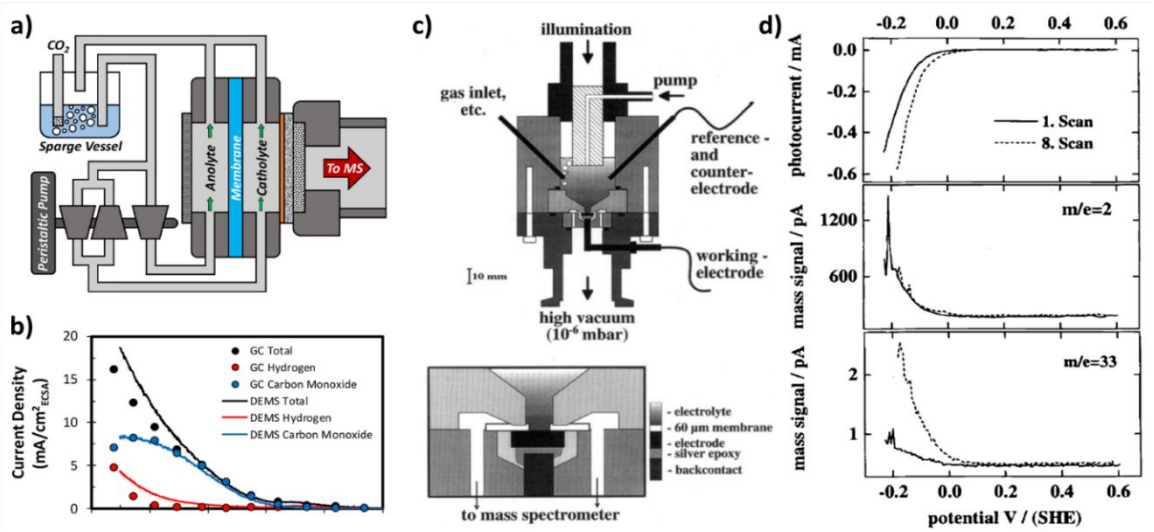

Figure 12. Differential electrochemical mass spectrometry. (a) Schematic of a two-chamber DEMS setup. [146] (b) Comparison of the CO_2 reduction activity of Ag measured via gas chromatograph and DEMS in aqueous 0.1 M $CsHCO_3$.[146] (c) Schematic of a DEMS cell modified for photoelectrochemistry (top) with a magnified view of the working electrode and inlet system.[155] (d) Photocurrent for p-InP (top) and simultaneously detected mass signals (middle: H_2, bottom, fragment of PH_3) in the first and eighth scan in 0.5 M H_2SO_4 under 1 Sun white light. [155]

monitoring the dissolution at open circuit, under applied potential, and with or without illumination, the technique enables a direct path to separate chemical from electrochemical from photoelectrochemical corrosion behavior. However, no information on chemical state or species solvation is provided, nor are any undissolved surface state changes detected. It also does not allow the study of spatial differentiation across non-uniform areas of the electrode.

2.2.4.2 Differential electrochemical mass spectrometry (DEMS)

Differential electrochemical mass spectrometry (DEMS) combines electrochemical methods with the powerful identification and quantification capabilities of mass spectrometry by connecting the electrolyte in the vicinity of the working electrode to the vacuum chamber of the mass spec with a thin permeable membrane (Figure 12a). This technique is also sometimes referred to as on-line electrochemical mass spectrometry (OLEMS). As with ICP-MS, the use of differential apertures through a series of vacuum stages enables the introduction of the analyte at higher pressures. Because of the short diffusion path from the working electrode surface to the vacuum chamber, DEMS allows the near-instantaneous detection of volatile and gaseous chemical species and correlation of their concentrations with the electrochemical conditions and applied potential in real time. As a mass spectrometry technique, products are identified by the detected mass-to-charge (m/z) ratio. A DEMS system can thus rapidly generate a product formation vs. applied potential curve which can be quantitative with careful calibration (Figure 12b).[146] It is thus effective for determining the onset potential for the formation of particular products and has become a favorite method for multiproduct electrochemical characterization of CO_2 reduction electrocatalysts.

DEMS has been used for a range of electrochemical applications.[147-149] In addition to the potential-dependent quantification of reaction products, DEMS has been utilized to study corrosion processes via dissolved electrode species. Researchers have investigated the anodic oxidative corrosion of carbon black as an electrocatalyst support material, reporting highly dynamic behavior in which the

oxidation rate depended on the history of applied potentials.[150-151] DEMS was also used to study degradation and aging mechanisms in CuO electrodes for batteries.[152] The stability of electrocatalysts such as Fe-N-C,[132] CoP_x,[153] Mo_2C,[154] and others have been investigated with DEMS, usually in conjunction with surface characterization techniques to correlate the observed dissolved species to electrode interfacial changes.

With modification of the electrochemical cell to permit illumination of the working electrode, DEMS can be applied to investigate in-situ photoelectrochemical stability (Figure 12c).[155] For example, Bogdanoff et al. used isotopically labeled ^{18}O-enriched TiO_2 to track the photocorrosion of thin layer anatase TiO_2 during the photooxidation of HCOOH and H_2O.[156] The m/z signal of the CO_2 and O_2 products was monitored throughout the experiment to determine that no ^{18}O from the photoelectrode was incorporated in the oxidation products. Photoelectrochemical DEMS has also been used to study the corrosion of p-InP(111) photocathodes for solar hydrogen evolution.[155] In this work, HER performance was tracked in comparison to photocorrosion by simultaneously monitoring the m/z = 2 signal for H_2 along with the m/z = 33 signal for the corrosion product phosphine, PH_3. As seen in Figure 12d, the H_2 product remained fairly steady with successive potential scans, but the p-InP corrosion to PH_3 increased markedly.[155] The photocorrosion process measured with the DEMS cell was corroborated with SEM images exhibiting a roughened surface as well as EDS measurements indicating a decrease in phosphorous content in the roughened area. In another photoelectrochemical DEMS study, both n-type and p-type (In,Ga)N nanowires were investigated as photoanodes

and photocathodes, respectively, in 0.5 M H_2SO_4.[157] DEMS showed that the n-type electrode anodic photocurrent led to N_2 evolution without O_2 evolution, indicating photocorrosion of the nitride semiconductor rather than water oxidation. The p-type nanowires, however, exhibited a cathodic photocurrent and produced primarily H_2 without significant corrosion byproducts, suggesting that p-(In,Ga)N is a suitable photocathode for hydrogen evolution in acid. These results display the utility of DEMS for studying the potential dependence of the photocorrosion of semiconductors simultaneously with characterization of the electrochemical product formation.

The major advantage of DEMS for both electrochemical product detection and corrosion monitoring is the ability to simultaneously measure current vs. potential behavior and the resulting evolution of gaseous or volatile products, which are readily identified by the mass-to-charge ratio. Mass spectrometric detection can also distinguish between isotopes to allow mechanistic studies via isotopic labeling. The product detection in DEMS is more immediate than on-line ICP-MS, allowing for observed variability during and between voltage scans. Unlike ICP-MS, the sample detection occurs without the need for plasma ionization, thus avoiding the breakdown of small molecules and allowing more chemical information on the products to be collected. However, precise quantification is challenging in DEMS wherein the diffusivity of each species, the electrochemical conditions, and the cell geometry can all affect the intensity of the respective m/z signal. Another drawback of DEMS is the inability to detect any species that are not volatile or gaseous. The requirement for a short distance between the electrode surface and permeable

membrane for sensitive product detection imposes limitations on the cell design to maintain low ohmic resistance while allowing illumination and versatile electrode materials. Lastly, because DEMS only reveals evolved products and does not probe changes at the electrode interface, it is a more powerful technique when used in complementary fashion with surface analysis tools

2.3 Microscopy techniques

2.3.1 In-situ transmission electron microscopy (TEM)

Transmission electron microscopy (TEM) uses an electron beam transmitted through an ultrathin (typically < 100 nm) section of a specimen to produce a high resolution image. The transmitted electrons that are unscattered produce an image on a fluorescent screen or via a charge coupled device (CCD) camera. The result is a combination of nanoscale or even atomic spatial resolution with sub-second temporal resolution. This powerful microscopic technique lets materials science researchers visualize morphology on a scale that can be directly connected to the atomic structure. TEM is widely used to observe the nanoscopic surface roughness, crystallinity, defects, porosity, composition, and internal structure of materials. Conventional ex-situ TEM, especially high voltage and high resolution systems, requires high vacuum levels to prevent electrical arcing and to minimize the collision frequency of electrons with gas atoms.

In-situ TEM has seen major advancements in the last few decades, enabling researchers to study the stability and structural changes of materials under gaseous or liquid environmental conditions at sub-nanometer resolution. Thus, in-situ TEM can provide greater insight into intrinsic mechanisms and catalyst structure-

reactivity relationships under real-world conditions as compared to samples under ultra-high vacuum in an ex-situ TEM.[158-161] In-situ electron microscopy experiments are made possible by utilizing differentially pumped sample chambers or specialized holders to contain the liquid media. For in-situ experiments, the TEM can be interfaced with sample holders capable of applying external stimuli, such as strain, heating/cooling, optical excitation, electrical bias, or reactive environments (i.e., liquid or gas reaction cells). In-situ TEM sample holders generally consist of Si microchips with a thin electron-transparent SiN window region.[162] Several microchip designs are commercially available, including sample holders with built-in microelectrodes for the biasing of samples to enable in-situ electrochemical TEM (EC-TEM).

In-situ TEM has been particularly useful for unraveling structure-reactivity relationships for catalysts. In one of the earliest high resolution in-situ TEM studies, Parkinson resolved lattice planes of a CeO_2 catalyst in a reactive gas.[163] Subsequent in-situ TEM studies have investigated the preparation, activation, and deactivation of various catalyst materials.[164-171] Furthermore, in-situ TEM has been implemented to investigate materials involved in electrochemical processes, which is essential for understanding the operando structure-modified mechanisms of electrocatalysts.[172-177] For instance, Zhu et al. used EC-TEM to gain deeper insight into the degradation mechanisms of Pt-Fe nanocatalysts.[172] They demonstrated that the coarsening processes of Pt-Fe electrocatalyst particles were not uniform, with the growth rate dependent on both the site and the applied potential. In another case, the structural evolution of nanoparticulate Co_3O_4 spinel electrocatalyst during the oxygen

evolution reaction was studied with EC-TEM using a commercial disposable miniaturized three-electrode cell from Protochips (Figure 13a-c).[173] The observations in this work demonstrated the irreversible formation of an amorphous surface layer

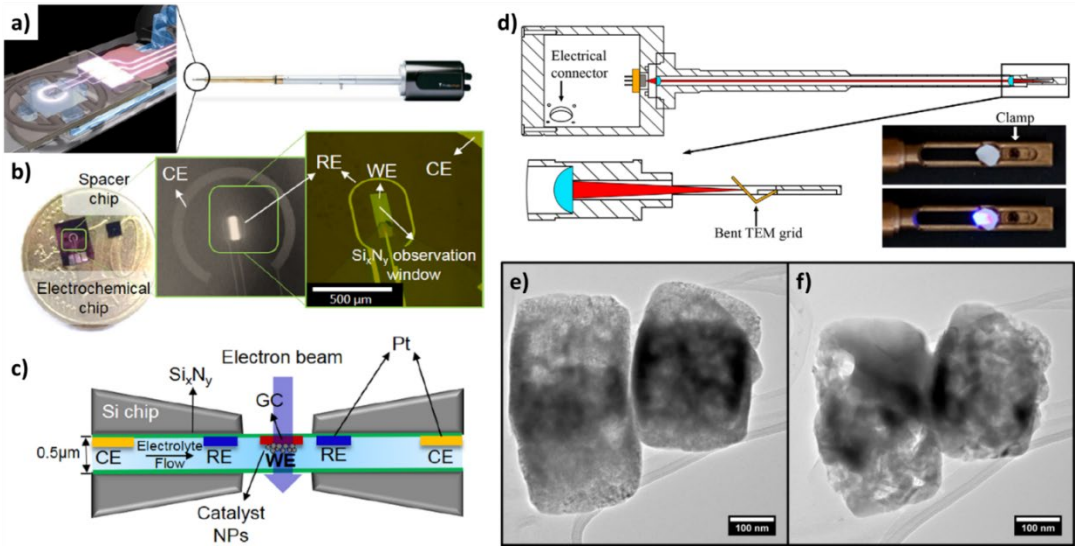

Figure 13. In-situ transmission electron microscopy. (a) In-situ liquid electrochemical TEM holder from Protochips. [173] (b) Disposable electrochemical chip and zoom-in showing the counter, reference, and working electrodes as well as the SiN window region. [173] (c) Transverse schematic of the assembled electrochemical TEM cell, where GC is the glassy carbon current collector for the catalyst particle working electrode. [173] (d) Schematic cross-section of an in-situ TEM holder for simultaneous illumination. A laser diode is focused through two lenses (in blue) onto the sample. Inset photo shows the tip with the illumination off (top) and on (bottom). [178]. (e, f) TEM images of Cu_2O nanocubes (e) before and (f) after the photodegradation reaction.[178]

of a cobalt (oxyhydr)oxide-like phase during OER which was affected by the pH and counterions in the electrolyte. EC-TEM also holds promise for providing insights on the complex effects of in-situ catalyst structural changes on the stability and mechanisms of CO_2 reduction. Vavra et al. used EC-TEM to study the reconstruction of Cu nanoparticle catalysts during the beginning phases of electrochemical CO_2 reduction.[174] As with similar EC-TEM studies, they used an electrochemical chip with a glassy carbon working electrode that provides a suitable

support for the nanoparticle catalyst. This worked indicated that Cu dissolution followed by redeposition, rather than coalescence, was the mechanism responsible for the observed size increase and morphological change of the electrocatalyst. The Cu ions responsible for redeposition arose from chemical dissolution of the Cu_2O phase at open circuit along with ions released during electrochemical reduction of the surface oxide.

Some research efforts have also investigated morphological changes occurring during photocatalytic reactions via monitoring by in-situ TEM with a built-in illumination source.[178-184] For in-situ TEM photochemistry studies, the sample holder design must permit illumination of the material while minimizing the disturbance of TEM imaging by the light. Furthermore, the interaction of the specimen with both light and accelerated electrons must be considered because the higher energy of the electrons can induce effects which are absent under illumination alone. Researchers should strive to distinguish the effects of the different irradiation from photon and electron sources, which may be attempted by correlating the observations to ex-situ studies. Cavalca et al. reported an adaptable specimen holder system that used a laser diode and built-in lenses to focus optical excitation on the sample during electron microscopy (Figure 13d).[178] Using this system, they directly monitored the structural transformation by photodegradation of Cu_2O nanoparticles in water vapor with in-situ TEM (Figure 13e-f). They also designed and conducted control experiments that allowed sample analysis after the reaction without electron beam-induced material changes. The particles were observed to considerably change shape and morphology during the light-induced reaction in the presence of water

vapor, which the authors explored and attributed to a light-driven proton-coupled electron-transfer pathway for the reduction of Cu_2O to Cu and CuO.[178] In other photocatalytic TEM work, Yoshida et al. visualized the in-situ decomposition process of hydrocarbons deposited on TiO_2 films on the atomic level and elucidated a mechanism of the decomposition process.[184] Later the same group investigated the photocatalytic nucleation of Au nanoparticles on TiO_2 under UV irradiation.[183] Zhang et al. used laser-excited in-situ TEM and photodetector tests to show that CdS/ZnO branched heterostructures had better performance than standard CdS nanobelts for optoelectronic applications.[182] The Crozier group has also contributed significantly to the atomic level observation of catalysts with in-situ TEM under various light-driven reaction conditions.[179-181] For instance, they employed atomic resolution in-situ TEM to study the structure of anatase TiO_2 nanoparticles exposed to 1 Torr of water vapor and broadband light illumination.[181] They reported that the crystalline titania surface converted to an amorphous phase 1 - 2 monolayers thick when exposed to light and water vapor at reaction conditions relevant to photocatalytic water-splitting. The heavily hydroxylated amorphous layer was stable and did not increase in thickness with time. Notably, little to no in-situ TEM work has been reported to date on the simultaneous inclusion of light and applied bias in liquid media to study the structural evolution in photoelectrochemical systems. The design of such cells would be challenging but not impossible, and the intersection of illuminated in-situ TEM with EC-TEM could provide significant insights for the solar fuels community, including structural observations of the potential-dependent photocorrosion process of semiconductor particles.

In-situ TEM is a remarkable and still advancing technology that provides materials scientists the unique capability to directly observe morphology changes in real-time at or near atomic resolution. Among its other advantages, the electron microscopy hardware can be interfaced with EDS and EELS for high-resolution elemental identification and mapping. However, there are several drawbacks to this technique, including the requirement for ultrathin samples which relegates specimens to nanoparticles or painstakingly prepared thin slices produced with microtome or focused ion beam (FIB) methods. In addition, under certain conditions the high energy electron beam can induce material changes that are not attributable to the in-situ process under investigation. For EC-TEM, the liquid environment poses challenges and generally reduces the achievable resolution. While commercially available disposable electrochemical microchips have greatly increased the accessibility of this technique, a high level of technical expertise is still required. Moreover, it can be challenging to achieve low-resistance ohmic contacts to semiconducting materials in this form factor. Overall, transmission electron microscopy, especially a novel in-situ approach, is an expensive and rather low-throughput analysis technique

2.3.2 Electrochemical atomic force microscopy (EC-AFM)

AFM is a scanning probe microscopy technique that can image the surface of a material through weak atomic forces between the sample and a probe mounted on a cantilever, as measured by observing the cantilever deflection with a reflected laser signal onto a photodiode detector. A three-dimensional depiction of the surface topography is generated by rastering the probe across the sample area, maintaining

a constant probe-sample interaction force, and plotting the cantilever deflection versus position. AFM has been used experimentally to visualize the surface roughness of materials as early as 1986.[185] Based on tip-sample interactions there are various available modes of operation, such as contact, non-contact, peak force tapping, intermittent tapping, and torsional resonance mode.[186] In contact mode, the tip is dragged across the surface at a depth to produce a repulsive force between the probe tip and the sample, which can cause damage to the material surface. In tapping mode, the cantilever oscillates with a constant set amplitude to image the surface through the force of the intermittent contacting, which helps prevent sticking of the probe tip when operating in ambient or liquid conditions. In non-contact mode, the cantilever oscillates at its resonant frequency and a control feedback loop along with a decrease in the frequency due to van der Waals forces near the surface act to maintain the probe tip just above the sample. Furthermore, the probe tip and/or system components can be modified in a number of ways to enable AFM techniques with additional functionality. In conductive AFM (C-AFM), the probe and sample are both electrodes in a circuit and the current passed through the sample at a set voltage can be measured to map DC conductivity simultaneously with the topography. Similarly, tunneling AFM (TUNA) can image currents through highly resistive samples, and photoconductive AFM (PC-AFM) can map material photoconductivity.

To utilize these capabilities for in-situ electrocatalysis and photoelectrochemical experiments, electrochemical atomic force microscopy (EC-AFM) puts a typical AFM probe within the liquid electrolyte to measure the

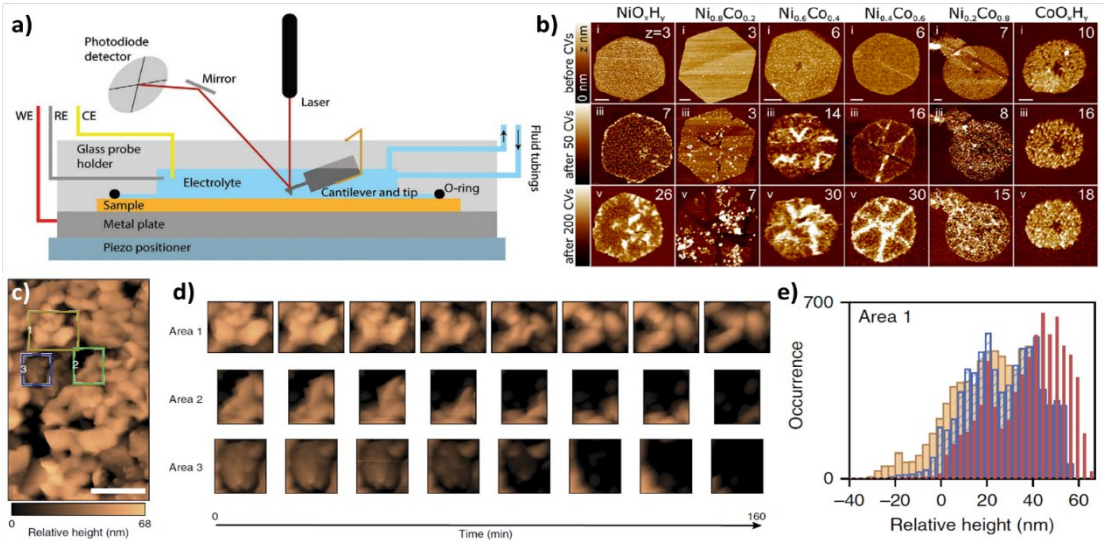

Figure 14. Electrochemical atomic force microscopy. (a) Schematic illustration of the working principle of EC-AFM. [187] (b) EC-AFM images of the evolution of $Ni_{1-\delta}Co_{\delta}O_xH_y$ nanosheets during 200 CV cycles in 0.1 M KOH. [198] (c) EC-AFM scan and (d) corresponding time-dependent scans of the three regions for a $BiVO_4$ film in 1 M potassium phosphate buffer at 1.23 V vs. RHE in the dark. [202] (e) Example histogram for relative height of the electrode features in part (d) area 1 during corrosion at 10 (red), 70 (blue), and 150 (orange) min. [202]

evolving topography of the solid-liquid interface of a sample working electrode under bias. Contact and intermittent tapping are the most commonly employed modes in EC-AFM. In a standard three-electrode setup, the probe tip is non-conductive and unbiased while monitoring the topography changes during electrolysis (Figure 14a).[187] This EC-AFM technique has been used extensively to observe changes in surface roughness during the corrosion of metals.[188-193] However, biasing an insulated conductive probe with only the tip exposed as a second independent working electrode in a four-electrode system enables scanning electrochemical microscopy (SECM) via the AFM tip.[194] This four-electrode EC-AFM can map the local electrochemical activity or potential at the electrode surface along with the topography at sub-100 nm resolution.[194-197]

EC-AFM has allowed researchers to monitor the potential-dependence of in-situ changes to electrocatalyst surface roughness at the nanoscale. Dette et al., for example, used EC-AFM to study how the addition of Co to nanosheets of the OER catalyst NiO_xH_y changed the porosity of the structure and enhanced its stability during electrochemical cycling.[198] In this work, the potential was repeatedly scanned between 1 and 1.7 V vs. RHE on catalyst-decorated highly oriented pyrolytic graphite (HOPG) working electrodes in 0.1 M KOH. Figure 14b shows the observed changes in morphology at different Co concentrations.[198] These transition metal (oxy)hydroxides tend to undergo high mechanical stress during redox cycling which causes a conversion to nanoparticle assemblies during CV sweeps. In-situ EC-AFM data, however, indicated that the Co-induced porosity reduced the stress and enhanced the structural stability of the catalyst under bias. The same group also used EC-AFM to study how the incorporation of Fe cations from the electrolyte into $Ni(OH)_2$ nanosheets can improve the OER activity.[199] The Fe integrated heterogeneously into the catalyst as a function of applied potential, leading to significant increases in catalyst volume and redox capacity. Deng et al. used EC-AFM to study the surface topography of Pt catalyst in sulfuric acid from reductive to oxidative bias conditions.[200] Under repeated potential cycling, the Pt surface coarsened and nanoparticles formed, which was attributed to the deposition of dissolved Pt from solution. Electrocatalysts have also been studied with EC-AFM in the four-electrode configuration using the probe tip as an electrode for SECM. Kolagatla et al., for instance, used this dual EC-AFM/SECM mode to

simultaneously map topography, oxygen reduction activity, and peroxide oxidation current on bare and Pt-nanoparticle-decorated HOPG electrodes.[201]

In-situ EC-AFM has also enabled the real-time monitoring of interfacial morphological changes due to corrosion and restructuring of semiconductor photoelectrodes under operation. Toma et al. employed EC-AFM to study the stability of $BiVO_4$ photoanodes and gain insight into the corrosion mechanism. A bias of 1.23 V vs. RHE was applied to the $BiVO_4$ working electrode in the dark while monitoring the morphology for over 160 min (Figure 14c-e).[202] They found that corrosion started at the solid/liquid boundary and that the voids in the inter-grain regions acted as spots for chemical attack. Furthermore, the observed corrosion was accelerated by illumination, increasing pH, and increased anodic bias. Photoelectrochemical researchers have also deployed modified versions of EC-AFM. For example, Nellist et al. developed a potential-sensing electrochemical AFM (PS-EC-AFM) in which the conductive tip of an otherwise electrically insulating cantilever is in contact with the sample, and the equilibrated tip and sample Fermi levels allow the surface potential to be probed.[196] They used this technique to measure the potential-dependent and thickness-dependent properties of CoPi catalyst on both Fe_2O_3 and $BiVO_4$ photoanodes, showing that the CoPi acts as both a hole collector and oxygen evolution catalyst.[195-196] The same group used PS-EC-AFM to study the operando photovoltage of an n-Si/Ni/NiOOH photoanode junction in 1 M KOH, and used it to explain how the size of the Ni catalyst on n-Si affected the interfacial barrier and improved the selectivity for holes. This technique

enabled the nanoscopic measurement of the pinch-off effect at each contact point of Ni on silicon.[203]

EC-AFM has a number of strengths that make it an ideal choice for in-situ surface studies for some applications. It works well in an ambient or liquid environment without the need for complex ancillary equipment or differential pumping, all while maintaining a high resolution down to the nanometer scale. Unlike electron microscopy, the data collected yields a three-dimensional picture of the sample surface. Moreover, the AFM cantilever can be utilized as an electrode to enable additional functionality such as conductive, potential-sensing, or dual-SECM modes. There are limitations for EC-AFM, though, including the need for corrosion-resistant materials for the AFM scanner and cantilever as well as high electrolyte transparency to maintain a strong detection of the laser signal. For electrolysis measurements, bubble formation can disrupt the probe-surface interaction, putting a practical limit on the allowable in-situ current density. While EC-AFM can monitor topography during electrochemical processes, it provides no chemical information, has relatively slow scan speeds, and is limited to small sample areas. However, AFM is a widely accessible technique and the modifications necessary for in-situ electrochemical measurements are modest.

2.3.3 Electrochemical scanning tunneling microscopy (EC-STM)

STM is a scanning probe technique that relies on the principle of quantum tunneling, in which a bias voltage applied between the sample and the probe tip allows electrons to tunnel across the gap and through the energy barrier between them. The tunneling current which results depends on the applied voltage, the local density of

states of the sample, and the nearest distance between the tip and sample surface. Typically, the tunneling current is on the order of nA to pA, and the resolution depends on the sharpness of the tip. Because the tunneling current decays exponentially with increasing tip-to-sample distance, most of the current can be confined to the one atom of the tip nearest the sample surface. This tunneling phenomenon allows angstrom-level resolution for true atomic imaging in the STM, as compared to nanometer-scale resolution for an AFM in which the surface force interaction is experienced over a number of atoms at the probe tip. With a piezoelectric positioning stage, the STM probe can be rastered across a small area to map the molecular topography. The basic system components include a probe and its motion sensor, scanner, electric controller, computer system, and a vibration isolation system. Standard ex-situ STM operates at ultra-high vacuum conditions to prevent ambient contaminants from adsorbing to the sample and interfering with the interface under investigation. Measurements are also typically done at very cold sample temperatures to minimize thermal vibrations that could degrade the atomic resolution. STM is usually operated in either constant current or constant height mode, although spectroscopic and manipulation modes also exist. In constant tunneling current mode, an electric controller will move the tip up and down, following the surface contour, to maintain the set current.[204] In constant height mode, the z-position of the tip is kept constant while the tunneling current is measured, which can allow faster scan rates. With the exponential dependence of the tunneling current on distance, this mode can lead to greater image contrast, but there is a risk of inadvertently crashing the tip into larger molecules or surface

features. In addition to topography, STM can provide information on spectroscopic properties and local variation of the work function.

Some of the earliest demonstrations of modifying an STM for operation in a liquid media were reported in 1986,[205] and thereafter adjusted for electrochemistry.[206] The principle behind in-situ EC-STM remains similar to ex-situ STM except that it requires a standard electrochemical cell with working, reference, and counter electrodes. With the sample as the working electrode, the tip of the probe is treated as a second independent working electrode with respect to the same reference in a four-electrode arrangement, and a bipotentiostat controls the applied potential and current flow (Figure 15a).[187] In EC-STM, the tip is coated with insulating materials, such as epoxy resin, exposing only about 0.01 μm^2 of electrochemically active surface area (ECSA) in order to reduce the tip-electrolyte interfacial reaction. This in-situ technique has been used to determine the surface reactivity of electrodes, study the dissolution and deposition of metals and semiconductors, and observe electrode surface reconstruction in various electrolytes at different potentials. EC-STM can also be used to study faradaic processes occurring at the substrate/electrolyte interface as well as monitor real-time morphological change at the electrode surface, such as passive film breakdown, while controlling the potential [207-213].

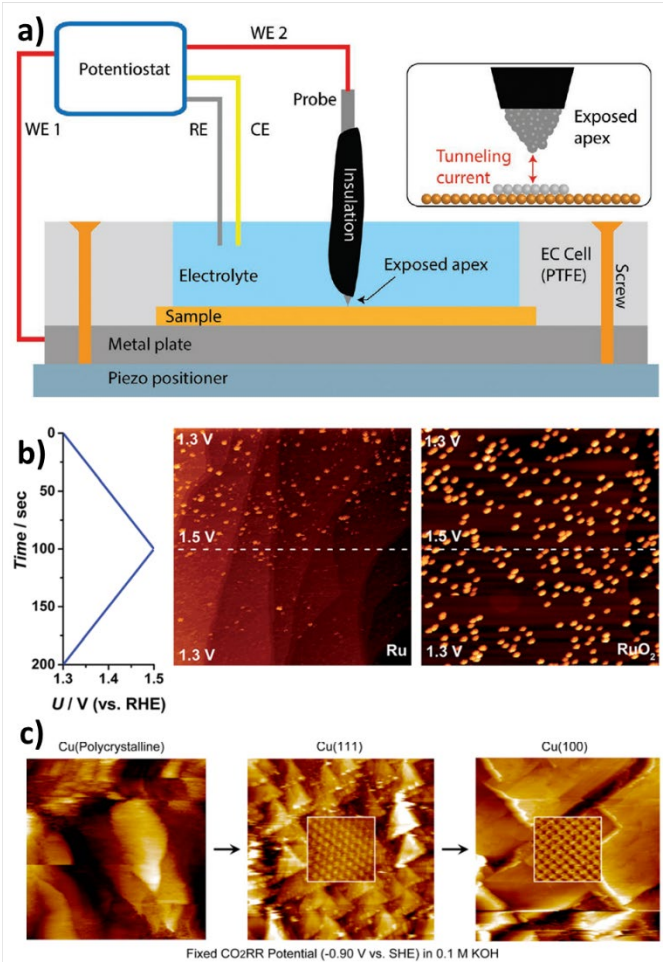

Figure 15. Electrochemical scanning tunnelling microscopy. (a) Schematic illustration of the working principle of EC-STM. [187] (b) Potentiodynamic EC-STM images with potential scanned between 1.3 and 1.5 V vs. RHE (left graph) in 0.05 M H_2SO_4 for as-deposited Ru nanoparticles (center image) and thermally oxidized RuO_2 nanoparticles (right image). [217] (c) Potentiostatic EC-STM images of initially polycrystalline Cu (left image) held at -0.9 V vs. SHE in 0.1 M KOH, converting to Cu(111) after 30 min (center image) and then Cu(100) after another 30 min (right image). [224]

Materials science researchers have applied EC-STM to study atomic surface structures and transformations on metals and electrocatalysts. Much of the early work focused on imaging the electrochemical deposition and dissolution processes for metals such as Cu,[214] Ag,[215] and Pt[216] on near-atomically flat surfaces such as single-crystal Au or HOPG substrates. Using similar methods, subsequent research

has monitored the in-situ dissolution of electrocatalysts under operation conditions. Paoli et al. used EC-STM to investigate the stability of RuO_2, an oxygen evolution electrocatalyst, by studying as-deposited sputtered Ru vs. thermally oxidized RuO_2 on a glassy carbon working electrode. As the potential was scanned from 1.3 V to 1.5 V vs. RHE and back again during rastering of the probe from the top to the bottom of the sample area, the as-deposited Ru nanoparticles disappeared from the image, indicating electrochemical dissolution (Figure 15b).[217] In contrast, the thermally oxidized RuO_2 exhibited no evidence of corrosion in the same potential range. EC-STM can also be utilized to map the catalytic activity of surfaces by intentionally employing faradaic current at the STM probe tip to study electrocatalytic reactions [218-222]. Hiesgen et al., for instance, used in-situ STM to investigate the local activity of a Pt nanoparticle catalyst for the oxygen reduction reaction [223]. Another application of this technique is for the investigation of electrocatalyst structure-composition-reactivity correlations. Kim and Baricuatro and coworkers have reported significant work using operando EC-STM to study Cu electrocatalyst surface restructuring and intermediate species adsorption for electrochemical CO_2 reduction.[224-228] During CO_2 reduction on Cu, the extent of hydrocarbon and alcohol formation depends on the crystal orientation of the electrocatalyst. It had previously been observed that polycrystalline Cu unexpectedly behaves like crystalline Cu(100) and generates ethylene as a major product. In their work, Kim et al. held a polycrystalline Cu working electrode at a constant potential of -0.9 V vs. SHE in 0.1 M KOH, in the vicinity of CO_2 reduction, and scanned the EC-STM in constant current mode to monitor the catalyst surface

topography. The images revealed that the polycrystalline Cu surface underwent a stepwise surface reconstruction to Cu(111) within 30 min followed by transformation to Cu(100) after another 30 min, explaining the observed structure-reactivity of polycrystalline Cu (Figure 15c).[224]

In-situ STM in liquid media has also been applied extensively to semiconductor surfaces, with much of the work focused on understanding chemical etching processes at the atomic level.[213] The corrosion of Si(111) in NH_4F and HF solutions, for instance, was observed to be potential-dependent with dissolution proceeding by a step-selective layer-by-layer mechanism in which pit corrosion mainly transpired on the terraces.[229-230] Yao et al. used EC-STM to characterize the surfaces of GaAs (001), (111)A and (111)B prepared via chemical etching and demonstrated that cathodic polarization of the electrodes prevented surface oxidation.[231] In-situ STM studies of etching reactions at the surfaces of GaP,[232] InSe,[233] and InP[234] semiconductor electrodes have also been conducted. Researchers have even demonstrated the feasibility of using EC-STM to study surface transformations invoked by photo-driven processes. Zhao et al. investigated the photooxidation of CdS particulate films in aqueous electrolyte.[235] Using white light coupled into an EC-STM with fiber optics, Eriksson et al. imaged the real-time anodic photocorrosion process for n-GaAs and observed anisotropic etching.[236] Also, an innovative EC-STM flow cell design was presented by Lay et al. which they used to monitor the electrochemical atomic layer epitaxy cycles of CdTe formation on Au(111) surfaces. Their setup modified the typical EC-STM cell by incorporating a peristaltic pump to flow solution onto the substrate and to the outlet

via an auxiliary compartment [237]. This flow technique could be extended for applications investigating the corrosion of photoelectrode materials.

EC-STM measurements enable researchers to better understand the conditions for electrocatalyst and photoelectrode degradation, including the crystal orientation yielding the highest stability and the adsorption/desorption of ions and molecules from the substrate. Thus, in-situ STM is a very advantageous method for uncovering fundamental atomic-level phenomena responsible for the structure-reactivity relationships at the interface. It provides the highest resolution available for in-situ imaging of electrochemical processes at the electrode surface. However, it can be a highly challenging technique, requiring expensive equipment and a high level of expertise to execute relatively low-throughput analysis. Probe tips must be meticulously fabricated to be atomically sharp, and sample areas should be extremely flat to mitigate the possibility of a tip crash. The probe must be corrosion resistant in the electrolyte at experimental conditions. Also, while most of the probe tip is insulated to minimize its electrochemically active surface area able to interact with the electrolyte, any unintentional faradaic current occurring at the STM tip is a disturbance to the tunneling current used for imaging.

2.3.4 Scanning electrochemical microscopy (SECM)

First introduced by Bard and Engstrom,[221, 222] scanning electrochemical microscopy (SECM) uses an ultramicroelectrode (UME) as a scanning probe to measure the in-situ current generated from electrochemical reactions near a substrate surface to investigate local electrochemical activity with high spatial resolution. The UME tip, a disk typically less than 25 μm in diameter and made of a conducting metal

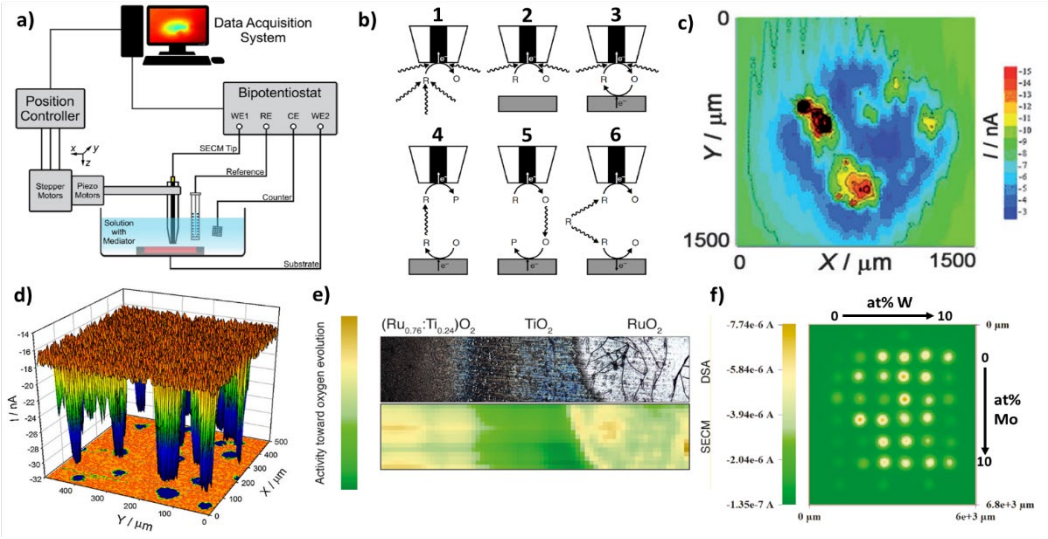

Figure 16. Scanning electrochemical microscopy. (a) Schematic of a conventional SECM instrument. [238] (b) Modes of SECM operation, including (1) feedback with the probe in the bulk electrolyte, (2) negative feedback with an insulating substrate, (3) positive feedback with a conductive substrate, (4) substrate generation-tip collection, (5) tip generation-substrate collection, and (6) redox competition modes. [240] (c) 2D SECM map of the reduction of dissolved Zn^{II} ions during corrosion of Zn immersed in 0.1 M NaCl for 24 h. [243] (d) 3D SECM map of corrosion activity at the surface of ductile cast iron using a custom pulse potential. Blue shaded areas represent graphite deposits in the cast iron. [246] (e) Optical microscopy image (top) and corresponding SECM map (bottom) of OER activity for pure phases and mixed-metal $Ru_xTi_{1-x}O_2$. [248] (f) Photoelectrochemical SECM image of a Bi/V/W/Mo oxide array with varying W and Mo doping levels as shown. [252]

surrounded with an insulator, interacts with the surface of a substrate via electrochemically active redox mediators [219]. Using a high resolution 3D positioning system and a bipotentiostat to independently control the sample and SECM tip working electrodes (Figure 16a), the UME probe can be scanned in the X-Y plane to generate a map of the substrate providing qualitative information on the charge-transfer rates and electrochemical activity.[238] In addition, the probe can be scanned in the Z direction to measure current as a function of tip distance from the electrode, generating an approach curve in which kinetic information can be obtained for the

substrate [239]. SECM is a powerful tool for the analysis of corrosion processes due to its ability to collect in-situ electrochemical and photoelectrochemical data in high spatial resolution, including local catalytic activity, kinetic rates, surface coverage, local pH, and opto-electronic properties. However, the overall resolution is limited by the dimensions of the UME, and the properties of the electrodes, electrolyte, and redox mediator can also affect SECM signal and resolution[219] .

SECM can be operated in several different modes, with the ideal arrangement depending on the process under investigation and the information desired. The most common modes of SECM operation are feedback, generation-collection, and redox competition modes. To operate in feedback mode, an electrochemically active redox mediator species must be present in the electrolyte. At a given potential and probe height in the bulk electrolyte, a steady-state diffusion current is obtained from the reduction (or oxidation) of the redox mediator species (Figure 16b, 1).[240] Starting the measurement with an approach curve, the measured current response is dependent upon the substrate conductivity. If the substrate is insulating, diffusion of the redox mediator is hindered as the probe approaches the surface by the short distance between the tip and substrate, thus decreasing the measured current and creating a negative feedback (Figure 16b, 2). If the substrate is conductive, the redox mediator can be regenerated at the substrate surface, thus increasing the measured current as the probe approaches the substrate surface and creating a positive feedback (Figure 16b, 3)[241]. Negative feedback thus provides topographical data while positive feedback provides electrochemical surface activity information, i.e., redox mediator heterogeneous reaction rates. In contrast to feedback mode, operating in a

generation-collection mode requires that the redox mediator species is not initially present in the electrolyte but is instead electrochemically generated once potentials are applied to the UME and substrate. In substrate generation-tip collection (SG-TC) mode, the redox mediator species is generated at the substrate and diffuses to the UME tip where it is reduced or oxidized (Figure 16b, 4). Conversely, in tip generation-substrate collection (TG-SC) mode, the mediator is generated at the UME tip then reduced or oxidized at the substrate (Figure 16b, 5). Generation-collection modes are used to measure the flux of the mediator species being generated, towards the substrate for TG-SC and away from the substrate for SG-TC.[240] In the redox competition mode, both the UME tip and the substrate compete for the same redox mediator species (Figure 16b, 6). As the tip and substrate are in close proximity, the decreased amount of redox mediator reacting at each interface leads to a decrease in current for the UME. The redox competition mode is useful for studying the ability of the substrate to consume a particular reactive species, such as dissolved oxygen.[240]

SECM has been used extensively to map the local electrochemical reactivity of metals and electrocatalysts to provide information on surface-feature-dependent corrosion processes.[242] For corrosion studies, the generation-collection SECM modes are most frequently employed due to their ability to directly probe locally dissolved ions from the corrosion reaction. For instance, Souto et al. investigated Zn corrosion in aqueous 0.1 M NaCl using a mercury-coated UME, which kinetically inhibited hydrogen evolution at strongly cathodic potentials while also preventing Zn nucleation and deposition on the UME from changing the electrochemically

active surface area.[243] Periodic SECM scans monitored the corrosion of the Zn substrate with time, with differences in the electrochemical activity attributed to evolving local characteristics of the metal corrosion process (Figure 16c).[243] Both anodic and cathodic corrosion sites were observed on the substrate, with anodic sites leading to higher UME cathodic current. These anodic sites shifted location over time as they became blocked by corrosion products and led to the formation of new anode areas. Bae et al. used a similar mercury-coated SECM tip strategy to investigate Pt dissolution during the oxygen reduction reaction.[244] During Pt dissolution, small Pt nanoparticles formed on the tip surface. The Pt nanoparticles catalyzed electrochemical oxidation of N_2H_4 which was dissolved in the electrolyte, leading to a current spike at the SECM tip which could be leveraged to detect the in-situ formation of Pt nanoparticles due to corrosion of the substrate. Ni et al. studied the corrosion of Fe in acidic solutions using SECM with a modified Pt UME by electrochemically polymerizing polyaniline at the tip in order to monitor pH changes at the electrode/electrolyte interface.[245] They observed current and corresponding pH oscillations which were attributed to a periodic formation and dissolution of the Fe oxide film. In another case, Nickchi et al. used a potential pulse method to monitor galvanic corrosion on a ductile cast iron substrate, which enabled a clearly resolved current map of oxidation/reduction processes displaying distinct behavior between iron and graphite regions (Figure 16d).[246]

One of the major strengths of SECM as a technique is its ability to readily image the local inhomogeneity of the electrocatalytic activity of a surface. Eckhard et al., for example, used the SECM redox competition mode to evaluate the oxygen

reduction kinetics of Pt and Au electrocatalysts and were able to image the difference in catalytic activity between the materials.[247] The activity of various compositions of mixed metal oxide oxygen evolution catalysts has been mapped with SECM as well. SECM of dimensionally stable anodes (DSA) of TiO_2 incorporated into RuO_2 films showed that the DSA catalyst was more stable and had higher OER activity than pure RuO_2.[248] SECM current maps and concurrent optical microscopy related the oxygen evolution activity to the mixed metal composition, while even allowing the researchers to identify cracks in the RuO_2 regions as the highest activity sites (Figure 16e). In another example, SECM was used to probe the spatial inhomogeneity of the anodic catalytic reaction in aqueous 3.5 M NaCl at Ti-Ru-Ir mixed metal oxides and investigate the spatial reactivity of the chlorine evolution reaction vs. oxygen evolution reaction.[249]

SECM can also be used in photoelectrochemical systems by adding a light source to induce photogenerated carriers near the region where the SECM probe is located. For instance, Lai et al. incorporated a fiber optic light source into an SECM system to investigate the kinetics of the photoetching reaction of n-GaAs in 0.5 M H_2SO_4.[250] Using Fe^{3+} as a redox mediator to accept the photogenerated electrons, the remaining positive holes led to GaAs oxidation and dissolution. SECM approach curves showed that the current, and corresponding interfacial charge-transfer rate, was dependent on the Fe^{3+} concentration and the illumination intensity as well as the tip-substrate distance. The researchers demonstrated that tuning these parameters enabled control of the photoetching rate which could be leveraged with the SECM for electrochemical micromachining of the semiconductor surface.[250] The Bard

group has reported many studies of spatially resolved photoelectrode activity enabled by light-coupled SECM.[251-259] They have pioneered the application of SECM as a screening technique for photoelectrocatalysts by imaging the illuminated activity of arrays of compositionally varied catalyst spots on a semiconductor[251] or varied doping of a photoelectrode (Figure 16f).[252] In another novel photoelectrochemistry application, Esposito et al. combined SECM with scanning photocurrent microscopy (SPCM) by fixing a laser beam immediately next to the UME tip, allowing them to map the rate of local light-driven H_2 evolution at Pt catalyst islands on p-Si photocathodes.[260] The effect of surface adsorbed species on photoelectrodes has also been investigated with SECM using a surface interrogation (SI-SECM) operation mode. SI-SECM is similar to TG-SC mode, however the species generated at the UME tip only reacts with the adsorbed species on the substrate. Zigah et al. used surface interrogation mode to detect and quantify the amount of adsorbed hydroxyl radicals photoelectrochemically generated on a nanostructured TiO_2 substrate.[261] By reacting the surface hydroxyl radicals with the redox pair $IrCl_6^{2-/3-}$, the surface coverage and decay kinetics of the hydroxyl radical were determined.[261] Similarly, Simpson et al. used SI-SECM to investigate the role of surface defects on n-doped $SrTiO_3$ photoelectrodes.[262] They created surface defects on the semiconductor by milling with a focused ion beam, then used SI-SECM with an $Fe^{3+/2+}$ redox mediator to identify changes in adsorbed oxygen species. By quantifying heterogenous rate constants between the adsorbed species and the mediator for milled and pristine samples, the researchers showed that surface

defects directly impacted the reactivity of photoelectrochemically generated surface adsorbates.[262]

SECM is inherently an in-situ electrochemical characterization technique, and the numerous available modes of operation make it highly versatile for characterization applications in energy, corrosion, biology, and catalysis. The main advantage of SECM is the ability to measure chemical reactivity at surfaces with high spatial resolution in a wide variety of electrochemical conditions. The resolution is limited by the size of the ultramicroelectrode, and while this does not yield spatial resolution at the scale of AFM or STM, efforts at probe miniaturization down to the nanoelectrode level offer the possibility of higher resolution. Moreover, combined AFM/SECM systems offer much of the same functionality at nanometer scale.[194] Compared to other in-situ electrochemical characterization techniques, SECM is quite affordable and relatively easy to use. It is also well-suited for mid- to high-level throughput studies, as it can be directly applied to generate reactivity maps for arrays of compositionally varied samples.[263]

2.4 Summary and Future Perspectives

In the last several decades, the research community has made major advancements in the development of analytical instruments and methods capable of the in-situ characterization of electrochemical processes and reactions occurring at the electrode interface. These powerful techniques, and their growing capabilities, have become indispensable tools for electrochemists interested in unraveling the fundamental phenomena underlying the behavior of electrocatalyst and photoelectrode materials under operational conditions. While by no means an

exhaustive list, many of the key techniques available for in-situ electrochemical investigations have been described herein along with highlighted examples of their application for studying material stability and other interfacial phenomena for electrocatalysts and photoelectrochemical systems. Table 1 provides a summary of each technique's core capabilities along with relevant advantages and disadvantages and a general gauge of the affordability of the instrumentation and its relative ease of use. Broadly speaking, more expensive systems tend to be rarer and more complicated, leading to a higher level of technical sophistication and expertise required to operate them for novel research. The ideal technique for a study will depend on the nature of the research and the desired information as well as the available resources and the required access to instruments. In-situ spectroscopy techniques are valuable for gaining insight into chemical changes confined to the solid electrode surface. In-situ microscopy is ideal for monitoring the evolution of material surface morphology and crystallinity. In particular, scanning probe methods offer an array of approaches to spatially resolve the non-uniformity of electrochemical properties across an electrode/electrolyte interface, which is helpful for relating reactivity and stability to material structures and composition. In-situ mass spectrometry techniques, while not directly probing the electrode, provide rapid and accurate analysis of species generated in the electrolyte as a result of the electrochemical process. Because they detect the mass-to-charge ratio of species, mass spectrometry methods can readily distinguish isotopes and are thus useful for labeling studies meant to clarify reaction mechanisms. For a thorough examination of an electrode material's reactivity, corrosion, and structural stability, a

complementary implementation of multiple techniques will yield the most informative result.

Table 1. Summarized comparison of in-situ analytical techniques for electrochemical applications

Technique	Capabilities	Advantages	Disadvantages	Affordability/ Ease of Use
In-situ UV-Vis	• Detection of dissolved species in electrolyte • Quantitative analysis of dissolution/faradaic efficiency of electrochemical corrosion by dissolution • Measurement of photochromic effects in thin films	• Nondestructive continuous monitoring of electrolyte • Low-cost widely available equipment	• No information provided about the electrode interface • Only detects species that absorb in the UV-vis spectral range • Peak overlaps must be deconvoluted • Does not allow spatially resolved study of dissolution from electrode area	High
APXPS	• Chemical oxidation state information at the interface under gas or liquid environment at applied bias	• Highly surface sensitive technique capable of detecting small chemical shifts • Experimental measure of interfacial band energetics under gas or liquid environment at applied bias	• Synchotron radiation generally required • Limited to thin electrolyte layer, so high ohmic resistance limits current density • Expensive and high technical expertise required	Low
In-situ Raman	• Measurement of electrode material bond vibration and rotational modes • Changes in the structure of the working electrode and new metastable species formed during the electrochemical reaction	• Nondestructive fast measurement for a specific chemical fingerprint that can identify molecules • Water does not significantly interfere with signal and samples can be analyzed through a glass or polymer covering • Can be collected with high spatial resolution	• Sometimes has weak signals requiring highly optimized instrumentation • SERS-enabling metal microstructure on sample necessary for surface sensitivity • Laser and optics equipment can be fairly expensive	Mid
On-line ICP-MS	• Real-time continuous detection and quantification of dissolved element concentrations during electrochemical operation • Quantitative analysis of dissolution/faradaic efficiency of electrochemical corrosion by dissolution	• Very low detection limits for elemental concentration • Detects multiple elements simultaneously • Isotopes can be distinguished for labeling studies	• Destructive measurement which consumes electrolyte • No information given about the chemical state of dissolved species or about the electrode interface • Does not allow spatially resolved study of dissolution from electrode area	Mid
DEMS	• Simultaneous correlation of current vs. potential behavior and the resulting evolution of gaseous or volatile products which are readily identified by the mass-to-charge ratio	• Near-instantaneous detection of molecular species upon change of current-voltage conditions • Rapid determination of faradaic efficiency vs. potential for multiple products is possible • Isotopes can be distinguished for labeling studies	• Quantification is challenging and dependent on cell geometry • Non-volatile species are not detected • Thin electrolyte layers can lead to high ohmic resistance • No information provided about the electrode interface • Does not allow spatial resolution of electrode area	Mid

Table 1. Continued,Summarized comparison of in-situ analytical techniques for electrochemical

Technique	Capabilities	Advantages	Disadvantages	Affordability/ Ease of Use
In-situ TEM	• Atomic scale imaging in gaseous or liquid environment for in-situ observation of dynamic processes • Microscopy under applied potential to image structural evolution during electrochemical operation	• Ability to directly observe structural changes and material stability under operating conditions at atomic resolution • Electron microscope can be coupled to EDS, EELS, and other techniques • Electrochemical microchips are commercially available	• Requires ultrathin samples • Electron beam can induce material changes • Material preparation and placement for in-situ electrochemical imaging can be challenging • Expensive and low-throughput technique requiring significant expertise	Low
EC-AFM	• Three-dimensional mapping of the electrode/electrolyte interface morphology under operation conditions • Monitoring of surface structure changes under applied bias	• High spatial resolution to the nm scale • Works well in an ambient or liquid environment without significant modification • Cantilever can be utilized as an electrode to enable additional functionality such as conductive, potential-sensing, or dual-SECM modes	• Requires corrosion-resistant materials for the AFM scanner and cantilever • Electrolyte should be highly transparent to maintain a strong detection of the laser signal • No information provided on chemical species • Slow scan speeds can limit rastering to a small sample area	Mid
EC-STM	• Atomic scale imaging of the molecular topography of the electrode/electrolyte interface under applied bias • Observation of electrode surface reconstruction under operation	• Highest resolution available for in-situ imaging of electrochemical processes at the electrode surface • Imaging of the adsorption/desorption of ions and molecules from the substrate • Observe fundamental atomic-level phenomena responsible for structure-reactivity relationships at the interface	• Probe tips must be atomically sharp and can be damaged during tip crash events • Probe must be corrosion resistant at experimental conditions • Unintentional faradaic current at the probe can disturb the image • Expensive and low-throughput technique requiring significant expertise	Low
SECM	• Measurement and mapping of electrode reactivity under operation conditions • Monitor temporal and spatial evolution of electrode corrosion by dissolution	• High spatial resolution to the µm scale • Can be used to determine kinetic rate constants and measure local pH changes • Numerous operational modes provide versatility for electrochemical studies • Well-suited for high-throughput screening • Affordable equipment and inherently in-situ technique	• Resolution limited by the size of the ultramicroelectrode • Chemical changes at the substrate which do not result in species in solution are not observed • Bubble generation interferes with imaging and necessitates limits on current density	High

Researchers continue to innovate in the area of in-situ characterization of electrochemical systems. For microscopy techniques, advancement is largely focused on enhancing the resolution in the presence of electrolyte while also

increasing the data collection speed. For the most complex methods, significant gains could be made by minimizing perturbations, increasing reproducibility and throughput, and easing the usability for the typical researcher. For APXPS, greater reproducibility of the thin electrolyte layer, along with higher tolerance for a thicker layer, would aid researchers. For EC-STM, controlled elimination of stray faradaic currents at the probe tip and the reduction of thermal and mechanical vibration remains a key pathway to improving the tunneling current image. In other cases, researchers are pushing the envelope by intentionally driving faradaic reactions at the probe tip in STM or AFM to enable SECM functionality at higher resolution with simultaneous topography mapping. Engineering innovations in modular cell designs are also helping to advance the convenience and reproducibility for some methods, as evidenced by the commercial availability of disposable electrochemical microchips for EC-TEM. While photoelectrochemical systems have been readily studied with most of these techniques, bringing an illumination source into the liquid sample holder to monitor photoelectrode structural changes under applied bias with EC-TEM has been challenging and is an opportunity for the advancement of in-situ photoelectrochemical characterization. Lastly, rather than technical breakthroughs, one of the most significant developments for improving the accessibility of these techniques has instead come through organizational and policy initiatives. For instance, the U.S. Department of Energy's HydroGEN Advanced Water Splitting Materials Consortium maintains a network of instrumentation resource nodes to make sophisticated national lab capabilities, including in-situ electrochemical characterization techniques, more accessible to academia and industry.[264-265] These

techniques will be critical to researchers' ongoing efforts to understand the fundamental source of catalyst and photoelectrode activity as well as to craft intelligent strategies for the long-term stability of materials.

CHAPTER 3

INVESTIGATION OF THE PHOTOCORROSION OF n-GaP PHOTOANODES IN ACID WITH IN-SITU UV-VIS SPECTROSCOPY

3.1 Introduction

III-V semiconductors including GaP are not stable in aqueous electrolyte at the anodic potentials necessary for water oxidation, and thus these materials anodically photocorrode or photopassivate.[17, 32, 36] In recent years researchers have successfully employed thin protective layers to stabilize corrosion-prone semiconductors, However, even a single pinhole can lead to corrosion, undercutting of the protective layer, and eventual device failure. Thus, there remains a significant need in the solar fuels field to investigate semiconductor degradation and mitigation strategies.

Several sophisticated research techniques exist for the in-situ investigation of electrochemical corrosion. In-situ electrochemical scanning tunnelling microscopy (ECSTM) can provide information on morphological and chemical changes at the

interface under bias.[215, 266-267] Other scanning probe methods such as in-situ electrochemical atomic force microscopy (AFM) can provide similar morphology data.[268] The evolution of the microstructure and physicochemical processes at the interface during corrosion can be observed with in-situ electrochemical TEM.[269] Ambient pressure x-ray photoelectron spectroscopy (AP-XPS) can also monitor the interfacial chemical changes in solution under applied bias.[270-271] These are powerful techniques for investigating material degradation processes, however, the expense and sophistication of the instruments as well as the degree of expertise required for their effective implementation serve as significant barriers to entry for new researchers.

Herein, we report the in-situ investigation of the photocorrosion of GaP photoanodes in acidic media using a simple and widely applicable method to monitor semiconductor dissolution during the reaction via UV-Vis spectroscopy. Spectroelectrochemical methods are well known for studying redox species and have seen some applications with semiconductors, including measurements of electrochromic behavior, but reports are slim on applying such techniques to in-situ photocorrosion quantification.[59, 272-274] Likewise, while there has been significant work reported on controlling the anodic surface etching of microporous GaP to influence the interfacial optical properties,[275-280] we are not aware of any in-situ studies of the photocorrosion process. By designing an electrochemical cell for operation within the spectrometer, and introducing white light illumination orthogonal to the monochromatic UV-Vis signal (Figure 17), PEC performance was monitored herein while simultaneously observing the time-dependent evolution of

dissolved semiconductor elements. Coupled with electron microscopy and ex-situ XPS measurements, this is an informative technique for studying semiconductor corrosion with commonly available laboratory facilities. Within the detection limits, the dissolved Ga and P concentration and faradaic efficiency of the electrochemical oxidation of GaP in acid is reported as a function of time and applied potential and interpreted in conjunction with SEM and XPS data.

3.2 Experimental

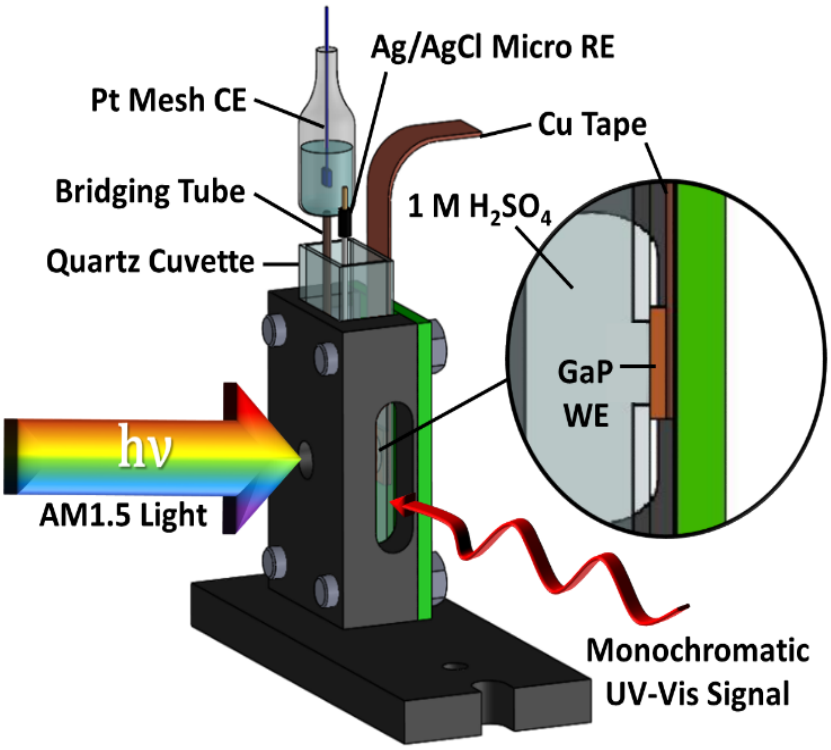

Figure 17. Schematic of the quartz cuvette cell for PEC measurements with in-situ UV-Vis spectroscopy, with a GaP working electrode (WE), Pt mesh counter electrode (CE), and Ag/AgCl micro-reference electrode (RE).

3.2.1 Electrode fabrication

Working electrodes used semiconductor wafers of either n-GaP ((111), S-doped to $4x10^{17}$ cm^{-3}, 0.14 Ω-cm resistivity, University Wafer, Inc.) or p^+-GaP ((100), Zn-doped to $5.4x10^{18}$ cm^{-3}, 0.028 Ω-cm resistivity, University Wafer, Inc.). Back contact was made by scribing Ga/In eutectic onto the back of the wafer followed by connecting to Cu tape. Some GaP electrodes also had a protective coating of TiO_2 grown by atomic layer deposition (ALD). Immediately prior to ALD, the GaP surface was etched by 9 M HCl for 30 s and then thoroughly rinsed with deionized water. TiO_2 films were deposited at 150 °C using a Cambridge Nanotech S200 ALD system. Each ALD cycle consisted of a 0.015 s pulse of H_2O, followed by a 0.10 s pulse of tetrakisdimethylamidotitanium (TDMAT, Sigma-Aldrich, 99.999%, used as received). A 20 s purge under a constant 0.02 L min^{-1} flow of research-grade N_2 was performed between each precursor pulse. TiO_2 films on the GaP electrodes reported herein were the result of 400 ALD cycles, corresponding to a thickness of ~20 nm from calibration measurements. Some of the GaP/TiO_2 wafers, when specified, were further annealed for 30 min at 500 °C in 1 atm N_2. Some electrodes were further decorated with an IrO_x oxygen evolution reaction co-catalyst by spin-coating (500 rpm for 20 s) a 40 mM iridium acetylacetonate solution in isopropyl alcohol and allowing to dry. This was repeated three times before annealing for 20 min at 480 °C in 1 atm N_2.

3.2.2 Photoelectrochemical measurements

A custom cell was developed for simultaneous photoelectrochemical measurements and UV-Vis spectroscopy (Figure 17). A quartz cuvette with 4 clear polished sides had a 5-mm-diameter holed drilled on one vertical side to permit contact between the electrolyte and the semiconductor working electrode. The quartz cell was mounted in a 3D-printed plastic holder in front of the UV-Vis detector, with the working electrode pressed to the outside of the cell against the drilled hole with a Teflon tape gasket to prevent electrolyte leakage. Aqueous 1.0 M H_2SO_4 (99.99%, VWR) was used as the electrolyte for all measurements. A minimal electrolyte volume of 1.25 mL was used to maximize dissolved species concentration for UV-Vis sensitivity while still fully submerging the exposed working electrode. A leak-free, 1-mm-diameter Ag/AgCl micro reference electrode (Innovative Instruments, Inc.) was placed in solution out of the illumination path. A Pt mesh counter electrode was immersed in a small secondary electrolyte container and connected to the main quartz cell electrolyte with an electrolyte-filled 2-mm-diameter bridging tube with a glass frit (KZT-2 tube, Innovative Instruments, Inc.). This approach kept the counter electrode and corresponding hydrogen bubbles out of the illumination path and prevented any dissolved species from redepositing on the Pt.

The UV-Vis input illumination signal passed through the electrolyte parallel to the GaP working electrode surface. White light illumination entered the electrolyte through the cell window opposite the hole and orthogonal to the UV-Vis beam. This simulated sunlight at normal incidence to the working electrode was generated with a 300 W Xe lamp (Newport 6258) coupled with an AM1.5 global

filter (Newport 81094) and calibrated for intensity with a Si photodiode (Thorlabs FDS100-CAL). A 2.0 Sun intensity was used for illuminated n-GaP experiments to increase the current density and subsequent dissolved species concentrations and corresponding UV-Vis sensitivity. A shroud around the quartz cell prevented the AM1.5 light from impinging on most of the cell or the UV-Vis detector, while a small hole in the shroud permitted light to pass through to the working electrode. An Autolab PGSTAT 128N (Metrohm) potentiostat was used for all electrochemical measurements. The results are reported versus the reversible hydrogen electrode (RHE) scale according to $V_{RHE} = V_{Ag/AgCl} + 0.197 + 0.059\text{pH}$, where the electrolyte pH was 0.

3.2.3 In-situ UV-Vis spectroscopy

All absorbance measurements were performed with an Agilent Cary 60 UV-Vis spectrophotometer in background correction mode, using blank 1.0 M H_2SO_4 as the background. In-situ UV-Vis absorbance data was calibrated to dissolved Ga and P concentrations using inductively coupled plasma mass spectrometry (ICP-MS, Agilent 7900). Separate calibration curves of Ga and P concentration vs. absorbance were measured for n-GaP and p^+-GaP (appendix II, Fig. S2), with a ~ 1:1 ratio of Ga:P measured in each case. The dissolved Ga concentration was used to calculate the estimated faradaic efficiency of the GaP corrosion reaction by determining the charge required to oxidize the GaP to produce the observed quantity of dissolved Ga (assuming either 3 or 6 e^- per molecule of GaP)[36, 280] and dividing this by the total

charge passed during the potentiostatic measurement at the time of the absorbance measurement.

3.2.4 Materials characterization

The electrode surfaces were characterized with scanning electron microscopy (SEM) using a NOVA FEI microscope at an accelerating voltage of ~ 10 – 15 kV. Surface elemental analysis was performed using X-ray photoelectron spectroscopy (XPS) with a VG Scientific Multilab 3000 custom-built ultra-high vacuum system with Al-Kα radiation. XPSPEAK 4.1 software was used for peak deconvolution and the XPS data analysis.

3.3 Results and discussion

3.3.1 Photoelectrochemical energy-conversion behavior

The photoelectrochemical current density vs. potential (*J-E*) behavior for n-GaP photoanodes is shown in Figure 18. Under 1 Sun, the polished n-GaP wafer initially reached a light-limited current density of ~4.1 mA cm^{-2}, increasing to ~ 8.3 mA cm^{-2} at 2 Suns. Under continued photoanodic operation in acid, the n-GaP surface transitioned from a mirror-like polished surface to a more matte appearance, which was indicative of the shift from specular to diffuse reflectance as the surface roughness increased with etching. The 2 Suns light-limited current density increased as a result of the etching-induced anti-reflection effect, eventually reaching ~12.5 mA cm^{-2} (appendix II, Fig. S1). Large increases in the current density of GaP photoanodes have been reported previously due to the etching of triangular pores at

the surface, with the increase attributed to enhanced separation of photogenerated charge-carriers in addition to the reduced surface reflectance.[276, 281]

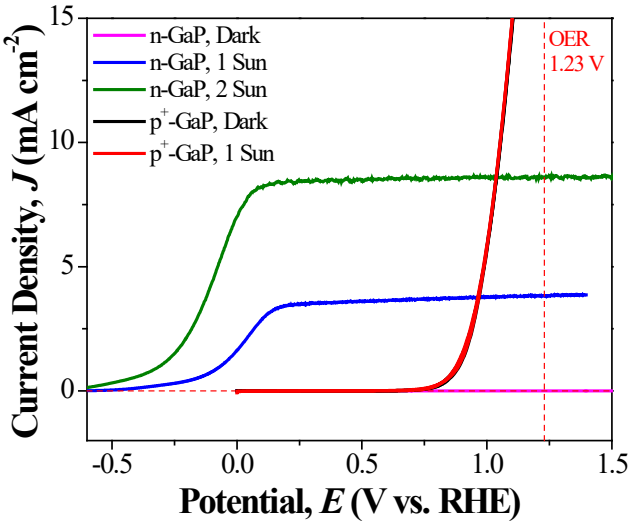

Figure 18. Current density vs. potential (*J-E*) behavior for GaP photoanodes in the dark and under AM1.5 illumination in 1 M H_2SO_4. The oxygen evolution reaction (OER) is marked at 1.23 V vs. RHE.

The 2-Sun-illuminated n-GaP photoanodes displayed an onset potential near -0.5 V vs. RHE with a maximum power point at ~0.06 V vs. RHE. Relative to the oxygen evolution reaction (OER) at 1.23 V vs. RHE, this is would be a very high photovoltage for water oxidation considering the GaP bandgap and the fact that the photovoltage must overcome the OER activation overpotential as well. In the dark, the semiconductor/liquid junction diode inhibits oxidative charge flow, which prevents a direct measurement of the dark electrocatalytic Butler-Volmer behavior. However, a degenerately doped p-type electrode with high conductivity allows the unimpeded transfer of majority-carrier holes to measure the dark catalytic behavior. Degenerate p^+-GaP electrode *J-E* behavior is shown in Figure 18, with no noticeable change in the presence of illumination as expected for a material of metallic character. For p^+-GaP, the exponential increase in oxidative current

happened with an early onset, reaching 10 mA cm^{-2} at 1.0 V vs. RHE, below the standard OER potential. Previous modelling indicates that the GaP self-oxidation potential occurs at a significantly lower potential than OER,[36] and we thus ascribe this current to electrochemical corrosion processes. For the n-GaP photoanodes, the early onset potential is similarly attributed to corrosion and the semiconductor photo-oxidation is expected to occur in kinetic competition with water oxidation.

3.3.2 In-situ UV-Vis spectroscopy method

Continuous UV-Vis absorbance measurements of the electrolyte with simultaneous potentiostatic photoanodic operation of the GaP was used to monitor the

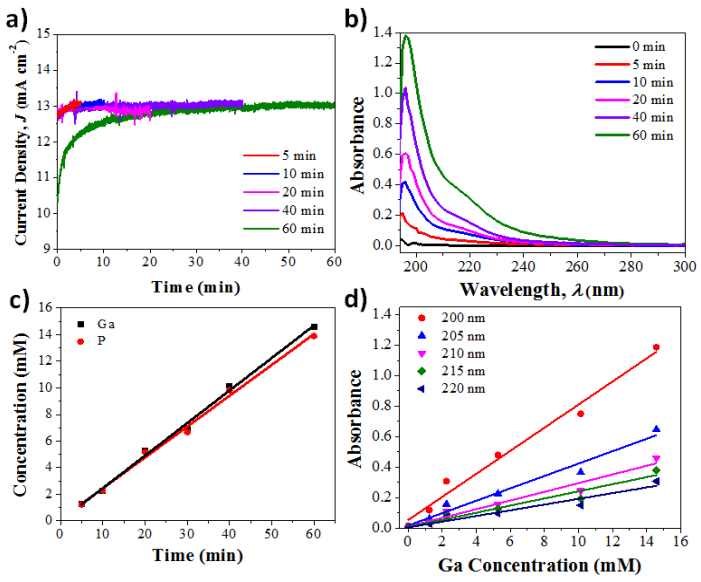

Figure 19. Calibration for n-GaP in-situ UV-Vis spectroscopy. (a) Current density vs. time for n-GaP photoanodes at 1.4 V vs. RHE at 2 Suns in 1 M H_2SO_4 and corresponding (b) absorbance vs. wavelength data. (c) Concentration of dissolved Ga and P in the electrolyte as measured by ICP-MS. (d) Resulting absorbance vs. Ga concentration calibration data.

semiconductor corrosion and dissolution. Figure 19 shows some of the data used to calibrate the absorbance measurements to dissolved Ga and P. For illuminated n-GaP photoanodes, we measured the absorbance spectra from 5 to 60 min, and analyzed the corresponding electrolyte aliquots with ICP-MS to establish definitive concentrations of elemental Ga and P atoms. ICP-MS, however, does not provide information on the chemical state of these atoms. Across all time periods measured, the dissolved Ga to P ratio was observed to be 1:1 within experimental error (Figure 19c). Thus, while only Ga concentration trends are reported herein, P concentrations are predicted to display the same behavior. Absorbance values vs. Ga concentration at wavelengths near the absorbance peak displayed linear behavior in the measured concentration range (Figure 19d). Subsequent ICP-MS measurements indicated that an average of the 200 and 205 nm wavelength absorbance data provided the most accurate calibration curve, and thus all reported UV-Vis-measured Ga concentrations herein used that approach.

Interestingly, the absorbance values for p^+-GaP operation displayed a different trend with concentration and required a second calibration (appendix II, Fig. S2). Dissolved Ga and P concentrations for p^+-GaP were still measured to be 1:1. Thus, we attributed the different trend in absorbance with concentration relative to n-GaP to a change in the species and/or complexation which affects the UV-Vis absorbance. Indeed, the absorbance peaks displayed a shoulder at ~ 217 nm which was more prominent relative to the main peak for the p^+-GaP data. The exact nature of the species resulting in absorbance in this shoulder region is unclear at present. A theoretically calculated Pourbaix diagram for GaP indicates that the stable phases at

pH 0 for potentials of interest in this work are Ga^{3+} and H_3PO_4 (appendix II, Fig. S3). Control measurements of UV-Vis absorbance for Ga_2SO_4 and H_3PO_4 in 1 M H_2SO_4, however, did not indicate strong absorbance in this shoulder region. We speculate that the observed absorbance at ~217 nm may correspond to a dissolved partially oxidized state of GaP which is not fully decomposed. The strongly different electrical properties and different wafer surface crystal orientation relative to the n-GaP (due to limited options for quality commercial p^+-GaP) may affect the exact degradation mechanism and result in this discrepancy in the two calibration curves.

Additional control experiments were performed to establish the validity and limits of the in-situ UV-Vis spectroscopic technique (appendix II, Fig. S4). At open-circuit for the GaP, the absorbance spectra in the presence of 2 Suns AM1.5 illumination was indistinguishable from the spectra in the dark, indicating that the white light did not appreciably affect the UV-Vis detector. Similarly, the absorbance spectra for n-GaP at 1.8 V vs. RHE in the dark did not change over time from its initial value, clearly indicating that the observed absorbance peaks in photoelectrochemical measurements were correlated to the photocurrent. Finally, the absorbance spectra vs. time for the cell under illumination without GaP was monitored, resulting in a variability in the absorbance at 200 nm of ~ 0.18. We attribute this small absorbance drift to heating effects and changes to the 1 M H_2SO_4 baseline. Thus for low concentrations (< 4 mM) resulting in absorbance values in this range, the error is expected to be higher. Values below this threshold, which also correspond to low total charge passed, were therefore excluded from subsequent calculations of corrosion faradaic efficiency due to their unreliable accuracy.

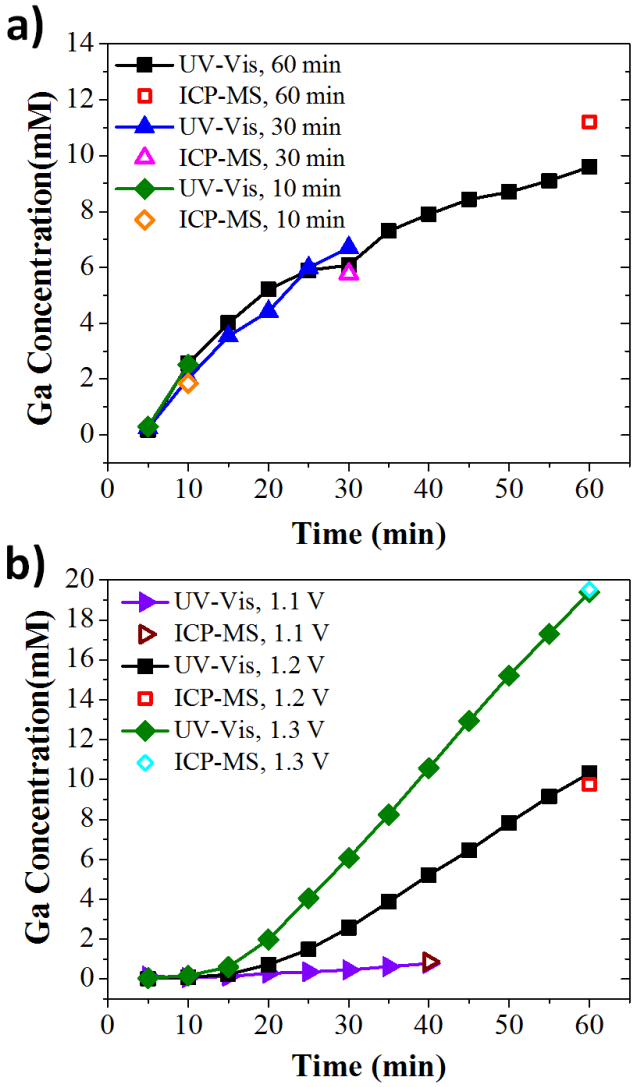

Figure 20. Comparing Ga concentration vs. time measured with calibrated in-situ UV-Vis absorbance and ICP-MS. (a) n-GaP under 2 Sun illumination at 1.8 V vs. RHE in three different runs. (b) p^+-GaP measured without illumination, listed voltages are the applied bias vs. RHE.

With the calibration established, additional ICP-MS measurements were made and compared to the concentrations determined by in-situ UV-Vis spectroscopy to gauge the accuracy and reproducibility of the technique. Three equivalent n-GaP experiments showed good reproducibility in Ga concentration over equivalent time periods and agreed well with

the corresponding ICP-MS values (Figure 20a). For p^+-GaP, the agreement in concentration values was high between UV-Vis and ICP-MS methods for different amounts of charge passed (Figure 20b). While ICP-MS is a destructive batch method, the in-situ absorbance measurement can provide similar data throughout the experiment without perturbing the electrolyte.

3.3.3 Corrosion of n-GaP photoanodes

The GaP photocorrosion and dissolution behavior as a function of time and applied bias was explored by employing in-situ UV-Vis spectroscopic analysis. Figure 21 shows the resulting trends in the dissolved Ga concentration with time, the

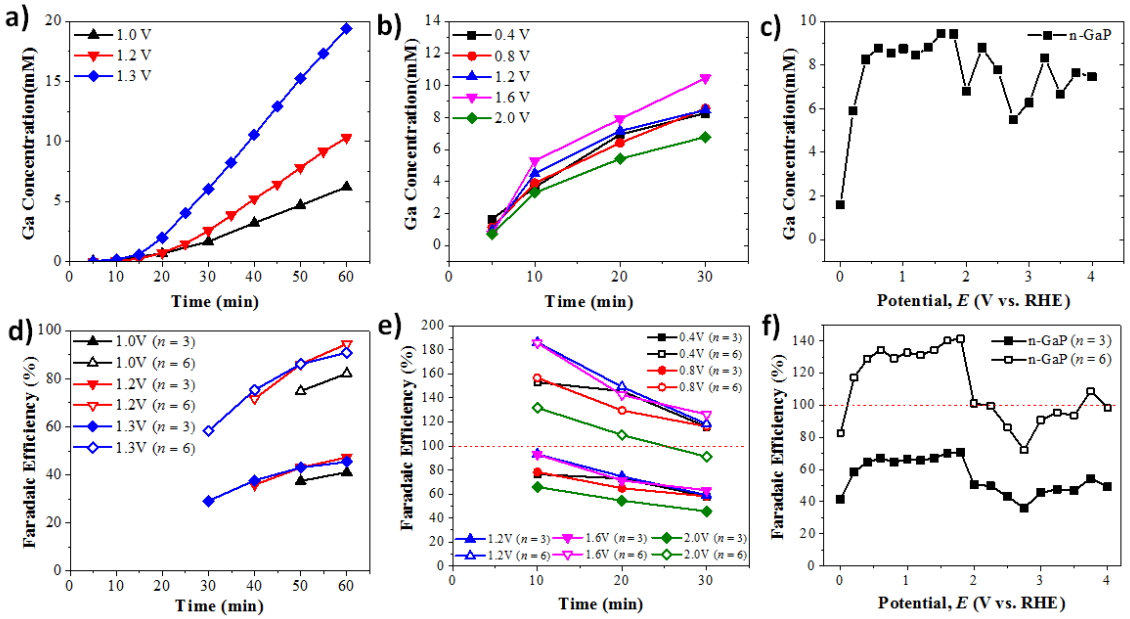

Figure 21. In-situ UV-Vis spectroscopic measurements of (a-c) Ga concentration and (d-f) corresponding GaP corrosion faradaic efficiency. (a, d) The behavior of p^+-GaP in the dark vs. time. The behavior of n-GaP at 2 Suns AM1.5 illumination (b, e) at various applied potentials vs. time, and (c,f) at 30 min vs. applied potential. All listed potentials are vs. RHE.

corresponding GaP corrosion faradaic efficiency, and the related bias-dependent

behavior after 30 min. Corresponding time-dependent absorbance data for n-GaP is reported in appendix II, Fig. S5. Interestingly, p^+-GaP and n-GaP displayed a different initial time dependence for the Ga concentration. For p^+-GaP the dissolved Ga concentration was initially slow to rise but then increased to a steady-state dissolution rate after ~ 20 min (Figure 21a). In contrast, at each applied bias for n-GaP, the initial increase in Ga concentration was steep at short times (< 10 min) before gradually reaching a steady, linear concentration increase with time (Figure 21b). This difference in electrochemical corrosion behavior is consistent with the observed morphology changes to the p^+-GaP and n-GaP after anodic operation.

Photoelectrochemical operation of n-GaP in acid results in the electrochemical etching of porous triangular arrays at the surface of GaP (111).[278] GaP etches anisotropically, with the (111) surface breaking down and dissolving preferentially to expose the (110) surface planes and leading to the triangular pores.[281] For GaP's zinc blende crystal structure, the (100) and (111) surface consists of only one species, either Ga or P. Due to the ionic character of binary GaP, this arrangement creates a dipole moment perpendicular to the surface which makes this orientation less energetically favorable and thus less stable. The (110) surface, by contrast, is occupied by both atom types and thus has no perpendicular surface dipole moment, leading to higher stability.[279] Although the initial n-GaP surface was smooth and relatively featureless, triangular pores of ~0.5 – 3 μm appeared after operation in acid, with the smaller pores eventually growing together into 3 – 5 μm pores. (Figure 22a-c). The Ga concentration thus rises rapidly at first as the (111) surface decomposes before reaching a lower, pseudo-steady-state rate when the

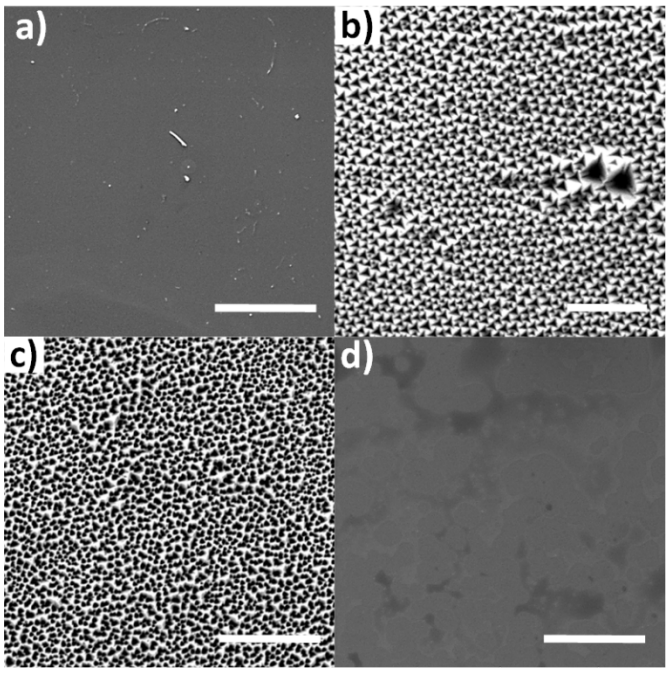

Figure 22. SEM images of the photoanode surface for (a) unetched n-GaP, (b) n-GaP after 30 min etch, (c) n-GaP after 60 min etch, and (d) p^+-GaP after 60 min etch. The scale bar is 50 µm in (a, c, d) and 5 µm in (b).

more slowly etching (110) orientation dominates the exposed surface. The etching of pores in n-GaP is in contrast to the uniform dissolution which is usually observed with p-type material.[277] Indeed, the etched p^+-GaP surface remained very flat and highly reflective without the microscopic triangular surface roughening of the n-GaP (Figure 22d). The initially slow rate of observable dissolved Ga is consistent with a delay as the p^+-GaP surface layer is fully oxidized, dissolved, and diffused throughout the electrolyte.

The difference in the etch process with doping type can be understood by considering the effect of the band energetics on the anodic oxidation of the semiconductor.[275] GaP oxidation is driven by hole-transfer across the semiconductor/electrolyte interface. For p-type material at oxidative potentials,

there is an abundance of majority-carrier holes to transfer, resulting in relatively uniform etching across the surface. For n-GaP, light absorption is necessary to generate minority-carrier holes in the valence band and permit appreciable oxidative current in reverse bias. Interfacial defect sites introduce energy states within the band gap (i.e., surface trap states) which are more likely to be populated with a hole. These defect sites can thus selectively promote semiconductor oxidation, leading to pits and subsequent pore formation.[275, 279]

With data for the dissolved Ga concentration vs. time and corresponding cumulative charge passed, the faradaic efficiency for the GaP oxidation reaction can be calculated. However, the calculation assumes a known and constant number of electrons transferred, n, to fully decompose one molecule of GaP. Several studies for GaP in acid have assumed a value of 6 charge-carriers required to oxidize one GaP unit.[276-277] This value appears to have been derived from a colorimetric measurement which assumed no side reactions, in a batch-method approach which would not capture transient behavior.[280] The proposed anodic half-reaction is:

$$GaP + 3H_2O \rightarrow Ga^{3+} + H_3PO_3 + 3H^+ + 6e^- \quad (3)$$

However, the same study reported that only 3 charge-carriers were required to oxidize GaP in alkaline conditions.[280] Similarly, a more recent computational study proposed that the most energetically favorable route to GaP oxidation in acid would require 3 charge-carriers per GaP unit, in which the anodic half-reaction would be:[36]

$$2GaP + 3H_2O \rightarrow Ga_2O_3 + 2P + 6H^+ + 6e^- \quad (4)$$

Thus, the calculated GaP oxidation faradaic efficiency is plotted in Figure 21 using either $n = 3$ or $n = 6$, and assuming the Ga_2O_3 fully dissolves. For the p^+-GaP, the

corrosion faradaic efficiency increased with time and approached a limiting value of ~90% or higher for n = 6 (Figure 21d). These potentials are at or below the thermodynamic potential for OER, and thus in the dark none of the charge is expected to be directed to water oxidation. The n = 6 reaction is therefore likely the dominant corrosion route for p^+-GaP, with the balance attributable to surface oxides that have yet to dissolve.

The observed corrosion faradaic efficiency behavior was quite different for illuminated n-GaP. As the rise in Ga concentration slowed, the n-GaP photocurrent density typically increased as a result of the surface-etched anti-reflection effect discussed above (appendix II, Fig. S1). Therefore, at longer times, more charge passed resulted in proportionally less total Ga and P in solution. As a consequence, the calculated electrochemical GaP oxidation faradaic efficiency decreased with time (Figure 21e). Moreover, a value of n = 6 for the corrosion reaction resulted in faradaic efficiencies greater than 100% at shorter times, and therefore this cannot be the dominant reaction pathway for the initial stage of etching on illuminated n-GaP. Instead, we attribute the initial behavior to the n = 3 route being dominant in the early stages of etching, though a combination of reaction mechanisms is possible. At longer times, the n-GaP oxidation faradaic efficiency approached a value of ~40% for n = 3, ~ 80% for n = 6 (appendix II, Fig. S6). Measuring O_2 in the gaseous headspace by GC for illuminated n-GaP resulted in faradaic efficiency values for OER of 5 – 20%, averaged over 2 h (appendix II, Fig. S7). If the n = 6 corrosion route is dominant at longer times, this value for OER represents most of the balance of charge. Some portion of the charge may also be assigned to undissolved or

incomplete oxidation of the semiconductor surface. X-ray photoelectron spectroscopy indicated a significant surface oxide phase developing over time under applied bias (see Surface characterization, Figure 26). While the evolution of the n-GaP corrosion process appears convoluted and could benefit from further study, the existing data could be interpreted as the reaction branching ratio changing over time as the surface and crystal orientation change, from the $n = 3$ route during initial pore formation and selective (111) etching, to $n = 6$ at longer times.

Although the dissolved Ga concentration and resulting n-GaP photocorrosion faradaic efficiency were time-dependent, Figure 21c-f highlight the role of applied bias by analyzing the electrolyte after 30 min of potentiostatic operation. At < 0.4 V vs. RHE, the dissolved Ga concentration was low because *J-E* energy-conversion behavior had not yet reached the light-limited photocurrent density (appendix II, Fig. S1). Below 2 V vs. RHE, the dissolved Ga concentration was fairly steady at the 30 min point, resulting in a consistent n-GaP corrosion faradaic efficiency (n = 3, ~65 – 70%) (Figure 21f). Above 2 V vs. RHE, the dissolved Ga concentration was less steady but resulted in a noticeable drop in the corrosion faradaic efficiency ($n = 3$, 35 – 50%). We partially attribute this drop in corrosion faradaic efficiency to a shift in the oxidation pathway. After extended operation above 2 V, a yellow film developed on the GaP surface, indicating significant charge was directed to form this layer which did not dissolve and was therefore not quantified by UV-Vis absorbance (see Surface characterization, Figure 26). For electrodes above 2 V vs. RHE, XPS indicated significantly more intense peaks corresponding to a GaP oxide phase as well as the formation of a peak assigned to a sulfur oxide phase, which we

attribute to an oxidative breakdown of the H_2SO_4 acid anion. In H_2SO_4 solution, the HSO_4^- anion is known to oxidize via a hole-transfer process to $S_2O_8^{2-}$ at a standard redox potential of 2.12 V vs. NHE, which can be kinetically competitive with water oxidation in the absence of effective OER catalysis.[282-283]

3.3.4 Effect of TiO_2 protective layer

The solar fuels research community has had success in recent years employing thin, conformal surface protection layers to mitigate semiconductor corrosion, including increasing the lifetime of GaP photoanodes in alkaline conditions.[17, 39-40, 284] The in-situ UV-Vis spectroscopy method was therefore extended to investigate the effect of thin ALD-grown TiO_2 protective layers on n-GaP in acid. In previous work, thick TiO_2 layers (up to > 100 nm) provided robust corrosion resistance, and when this layer was unannealed it had a high density of electronic defect states which made it a leaky dielectric and permitted low charge-transfer resistance at a photoanode surface.[17] Reproducing this effect with pinhole-free, conformal TiO_2 proved highly challenging, and n-GaP with an unannealed TiO_2 layer via ALD in our own labs as

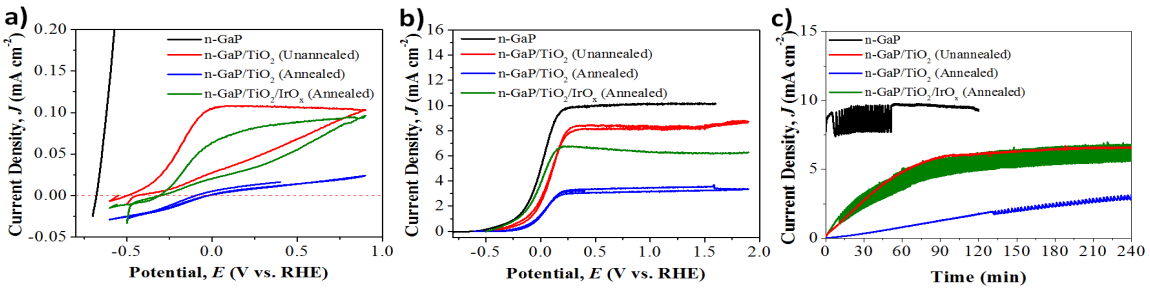

Figure 23. Photoelectrochemical energy-conversion behavior for n-GaP photoanodes with different surface protection layers. Current density vs. potential (*J-E*) under 2 Suns illumination (a) before and (b) after extended operation at 0.2 V vs. RHE. (c) Current density vs. time at 0.2 V vs. RHE for each type of electrode. TiO_2 was grown by ALD to 20 nm thickness.

well as via ALD from an outside university lab both showed strongly reduced photocurrent behavior indicative of a strong interfacial tunnelling barrier inhibiting charge transfer. appendix II, Fig. S8 shows some of the resulting data for different thicknesses of TiO_2. At 4 nm, the light-limited current density for the *J-E* behavior was significantly reduced at first, but rapidly increased with each successive cycling of potential. This behavior indicated a high density of pinholes permitting a fast degradation of the interface and failure of the TiO_2 protective layer. A thicker 20 nm TiO_2 layer was therefore chosen for more robust protection on a longer time scale amenable to study by the in-situ UV-Vis spectroscopic method.

With an unannealed 20 nm layer of ALD-grown TiO_2, the initial light-limited current density at 2 Suns was reduced to ~ 0.1 mA cm^{-2} (Figure 23a) relative to ~ 8.3 mA cm^{-2} for bare n-GaP (Figure 18). When held at 0.2 V vs. RHE, the n-GaP/TiO_2 (Unannealed) photocurrent density gradually increased over 90 min to reach a steady light-limited current density of ~ 8.2 mA cm^{-2} (Figure 23). Unannealed ALD-grown TiO_2 is known to be largely nonstoichiometric and amorphous with significant structural disorder.[17] While the ALD film in this case did slow corrosion over a few hours, it did not provide longer term stability and the structure presented a significant impediment to charge transfer. It was thus an imperfect electronically leaky dielectric in which the acid was still able to penetrate the layer via pinholes and/or a hydrous amorphous phase. Thermal annealing of the TiO_2 layer was performed to reduce the defect states and produce stoichiometric crystalline films.[17] As expected, the annealing step led to a more insulating interfacial barrier with even lower initial photocurrent, but it did provide more robust

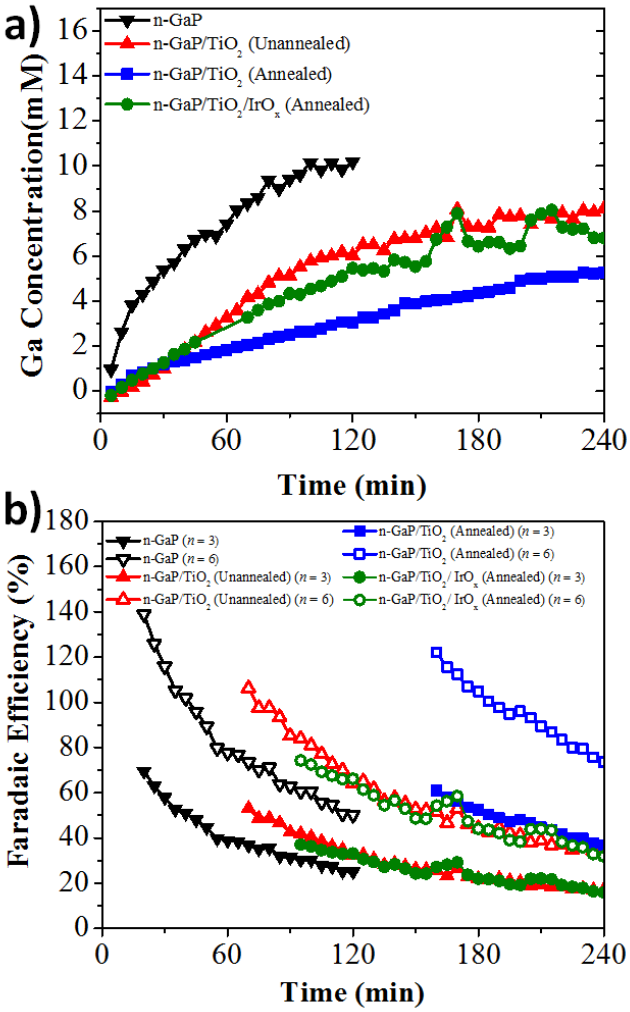

Figure 24. In-situ UV-Vis spectroscopic measurements of (a) Ga concentration and (b) corresponding GaP corrosion faradaic efficiency for n-GaP photoanodes with different surface protection layers under 2 Suns at 0.2 V vs. RHE. TiO_2 was grown by ALD to 20 nm thickness.

protection by resulting in a slower drift in the current density vs. time under potentiostatic operation (Figure 23). An IrO_x co-catalyst layer was added as well to see if the kinetic promotion of OER would affect the stability. The n-GaP/TiO_2/IrO_x (Annealed) photocurrent was increased relative to the uncatalyzed annealed electrode, but its photocurrent was no more stable over time than the n-GaP/TiO_2

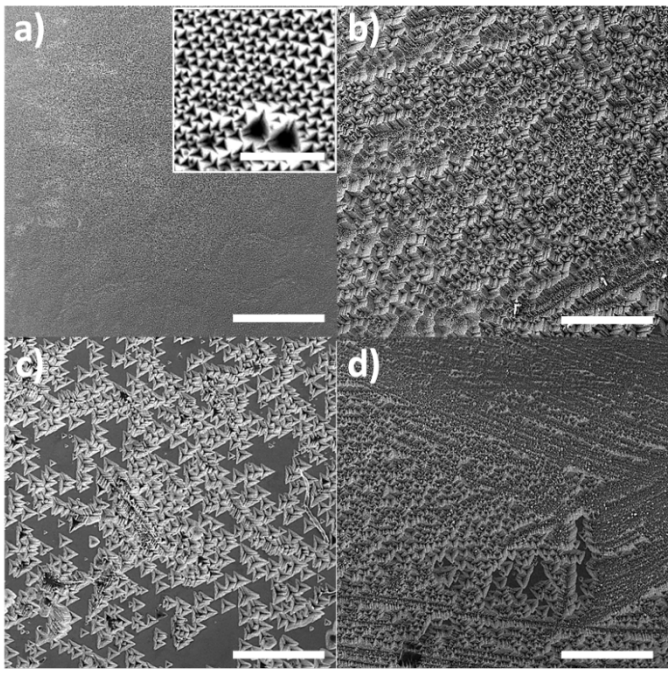

Figure 25. SEM images of the photoanode surface after the extended measurement at 0.2 V vs. RHE in Fig. 6 for (a) n-GaP, (b) n-GaP/TiO_2 (Unannealed), (c) n-GaP/TiO_2 (Annealed), and (d) n-GaP/TiO_2/IrO_x (Annealed). The scale bar is 500 μm in each image and 5 μm for the inset in (a).

(Unannealed) electrode (Figure 23). The oscillations in the Figure 23c current density vs. time curves corresponded to bubble formation and release on the GaP active area.

Figure 24 shows the dissolved Ga concentration and corresponding GaP corrosion faradaic efficiency vs. time for the n-GaP photoanodes with different surface protection layers. Corresponding absorbance data is presented in appendix II, Fig. S9. Each electrode was operated potentiostatically at 0.2 V vs. RHE, a potential chosen to be near the least oxidative potential that still reached the light-limited current density. The unannealed TiO_2 succeeded in reducing the rate of semiconductor dissolution, with the annealed TiO_2 layer leading to even lower Ga concentration. After four hours of operation, each TiO_2-protected photoanode

displayed less GaP dissolution than the bare n-GaP after two hours. However, this was attributed primarily to the low initial current density of the TiO_2-coated electrodes as a result of interfacial charge-transfer resistance. A comparison of the calculated electrochemical corrosion faradaic efficiency, which accounts for the amount of charge passed, showed that the electrodes exhibited similar trends in faradaic efficiency but offset by a period of time. Again, we have omitted calculated faradaic efficiency values corresponding to Ga concentrations below 4 mM, where the absorbance error over time leads to insufficient accuracy (appendix II, Fig. S4). Moreover, the low charge passed at these early times further contributes to higher error in the faradaic efficiency calculation. In each case, the faradaic efficiency again starts out high and gradually decreases toward a pseudo-steady-state value, consistent with the behavior discussed above for bare n-GaP (111) photoanodes etching the (111) surface at a high rate to expose more slowly etching (110) surfaces (Figure 21e). The TiO_2-protected electrodes took longer for the faradaic efficiency to decrease to similar values, consistent with an initially slower etch confined to areas of exposed GaP (111) (i.e., pinholes). Although the TiO_2-coated photoanodes took longer to decompose, the initially high calculated corrosion faradaic efficiency indicates that most of the early charge transfer across the interface is likely passing through pinholes rather than the contigous regions of TiO_2. With the TiO_2 layer presenting a significant interfacial barrier to charge transport leading to initially low current density, pinholes and weak spots in the protective layer represent low-resistance shunt pathways that would be favored for interfacial hole transport. This behavior would lead to selective etching at pinholes, high corrosion faradaic

efficiency at low current density, undercutting of the TiO_2, and accelerated corrosion across the electrode surface, which is consistent with the morphology observed by SEM after operation in acid (Figure 25).

3.3.5 GaP electrode surface characterization

In addition to in-situ UV-Vis spectroscopic analysis, SEM and XPS characterization of the semiconductor surface was performed before and after operation in acid to provide further insight into the GaP corrosion process. Figure 25 shows the electrode surfaces after the potentiostatic operation at 0.2 V vs. RHE as presented in Figure 23c. The n-GaP surface before electrochemical measurements was flat and unremarkable other than occasional dust particles. After photoanodic operation in acid, the bare n-GaP surface was microscopically roughened but fairly uniform at the 500 μm scale (Figure 25a). Zooming in to the 5 μm scale, however, the etched triangles corresponding to pores with (110) side walls were readily apparent (Figure 25a inset). This surface is consistent with previously reported n-GaP photoanode etching behavior in which nucleation sites lead to the simultaneous etching of parallel pores across the entire wafer surface.[281] In contrast, the n-GaP/TiO_2 (Unannealed) surface was noticeably macroscopically roughened with pyramidal features at the 500 μm scale (Figure 25b). The change in post-etching surface morphology from bare n-GaP is consistent with the TiO_2 layer reducing the density of etching nucleation sites, with variable size pinholes leading to faster and slower triangular pit growth which undercut the TiO_2. As these etch pits expand, they grow into each other, resulting in pyramidal surface structures after sufficient etch time.

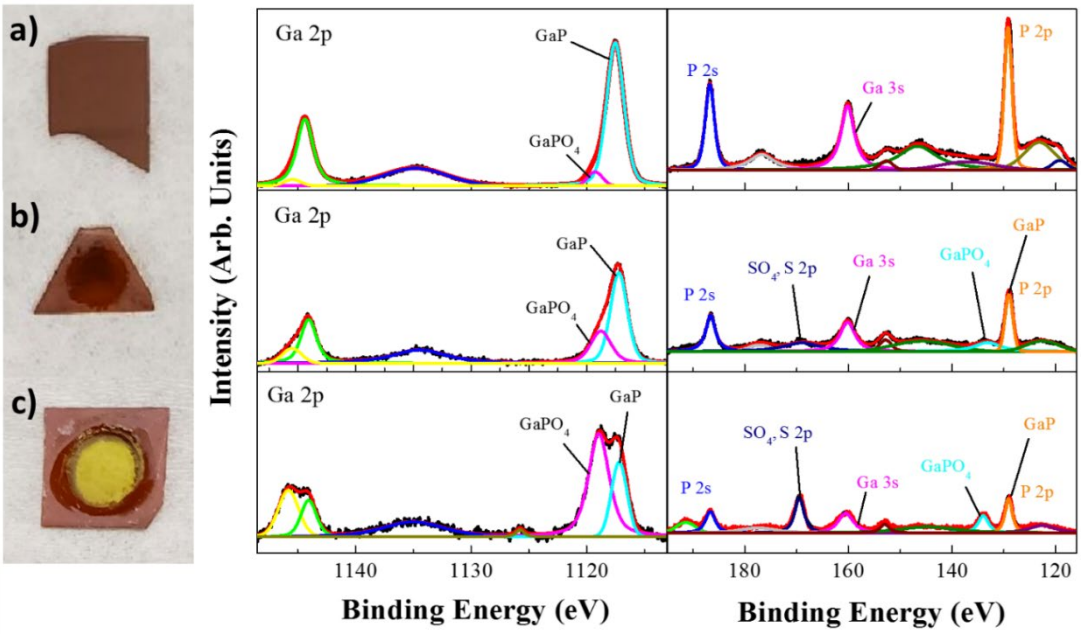

Figure 26. Photographs (left) and corresponding XPS spectra (right) for (a) pristine n-GaP, and n-GaP after > 2 h at (b) < 2 V vs. RHE and (c) > 2 V vs. RHE.

The n-GaP/TiO_2 (Annealed) surface supports this interpretation of the etch process. With an annealed TiO_2-coating, the large triangular etch pits are visible in different stages of growth, including some growing together and beginning to form the pyramidal surface (Figure 25c). Large sections of the n-GaP/TiO_2 (Annealed) surface appear intact and etch-free, which is evidence that the crystalline TiO_2 layer was robust with a lower pinhole density than the unannealed layer. appendix II, Fig. S10 shows the n-GaP/TiO_2 (Annealed) surface at a higher magnification along with energy dispersive x-ray spectroscopy (EDS) elemental maps. The n-GaP/TiO_2/IrO_x (Annealed) surface displayed more advanced etching and pyramidal structures similar to the n-GaP/TiO_2 (Unannealed) electrode (Figure 25d), which is consistent with these two electrodes passing a similar amount of charge and resulting in a comparable dissolved Ga concentration (Figure 24).

XPS characterization provided information on the chemical structure of the interface before and after etching. Figure 26 shows optical images of pristine n-GaP, n-GaP after etching at < 2 V vs. RHE and n-GaP after etching at > 2 V vs. RHE along with corresponding XPS spectra for the Ga 2p and P 2p regions. Peak assignments were made according to the NIST binding energy database and previous literature reports.[285-286] After etching n-GaP for a few hours at < 2 V vs. RHE, a corroded ring of less reflective roughened material was visible to the eye where the GaP wafer was exposed to the electrolyte. By XPS, a shoulder peak appeared at 134 eV next to the GaP P 2p peak, which is attributable to a gallium orthophosphate, $GaPO_4$.[285] Similarly, the GaP Ga 2p3/2 developed a shoulder at 1118 eV. This peak was also attributed to $GaPO_4$ but could also include Ga_2O_3. These undissolved oxide phases at the interface represent additional charge directed towards GaP corrosion and highlight that the calculated faradaic efficiencies above are a lower limit only representative of the dissolved Ga and P species. The observed oxide phase is consistent with a previous etching study which found that n-GaP undergoes a surface passivation effect which slows the etch rate in acid.[287] At potentials > 2 V vs. RHE, a yellow film became visible on the GaP wafer in the exposed area. XPS spectra show that this film corresponds to sharp increases in the relative intensity of the $GaPO_4$ (and/or Ga_2O_3) peaks. In addition, a new peak arose prominently at 169 eV, which is not readily attributable to any Ga or P phases. Instead, we attribute this to a sulfate state (e.g., Ga_2SO_4), with similar metal sulfates giving S 2p binding energy peaks in the same region.[288-289] Oxidation of the H_2SO_4 electrolyte becomes feasible

beyond 2 V vs. RHE,[282] and we attribute the rise of this surface sulfur oxide peak and the formation of the yellow film to such a route.

XPS spectra for the n-GaP photoanodes with different protective layers were also measured before and after extended potentiostatic operation. Figure 27 shows the resulting binding energy peaks for the Ti 2p and P 2p regions, with the Ga 2p and O 1s given in appendix II, Fig. S11. The Ti 2p peak intensity decreased significantly for the n-GaP/TiO_2 (Unannealed) and n-GaP/TiO_2/IrO_x (Annealed) electrodes, consistent with their steadied photocurrent density (Figure 23c) and etched surface across nearly all the electrode area (Figure 25) indicating that there was little of the TiO_2 barrier layer remaining. Less change in the Ti 2p peak intensity was measured for the n-GaP/TiO_2 (Annealed) electrode, which was attributed to the ALD-grown TiO_2 layer remaining intact on significant portions of the electrode area which were unetched (Figure 25c).

The behavior of peaks in the P 2p binding energy region was more complex. For bare n-GaP, the GaP P 2p peak at 129 eV and P 2s peak at 187 eV were strongly reduced in intensity after extended photoanodic operation, consistent with the result from Figure 26. Relative to the GaP peaks, the $GaPO_x$ peaks at 134 eV and 192 eV were more significant after electrochemical operation. Likewise, the Ga 3s peak at 160 eV was also reduced in intensity. The bare n-GaP spectra thus indicate a surface oxide layer formed during photoanodic measurements which reduced the signal from the underlying pure GaP. For the unetched TiO_2-coated electrodes, little to no signal was observed at the binding energies corresponding to pure GaP. Instead, the observable P signal was restricted to the prominent peaks at the binding energies for

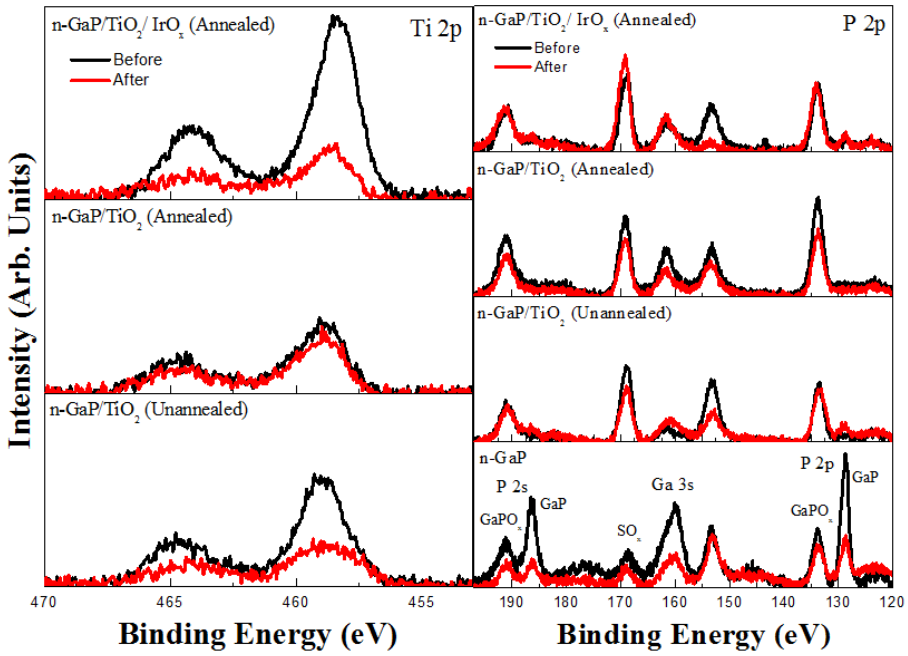

Figure 27. XPS spectra for the n-GaP with and without protective layers before (black) and after (red) extended potentiostatic operation at 0.2 V vs RHE under 2 Suns for the Ti 2p (left) and P 2p (right) regions.

$GaPO_x$. With 20 nm of ALD-grown TiO_2, the minimal XPS excitation occurring in the GaP through the TiO_2 must still be in the interfacial region where it was in a chemically oxidized form. In addition, pinholes of GaP that may be exposed through the TiO_2 layer were still exposed to the ALD growth conditions, including water vapor at elevated temperature, so these regions may have a strong $GaPO_x$ surface layer as well. Even after 4 h of photoanodic operation, the most extensively etched electrodes, the n-GaP/TiO_2 (Unannealed) and the n-GaP/TiO_2/IrO_x (Annealed), displayed only a weak signal for the pure GaP P 2p and P 2s. The lack of pure GaP signal indicates that the undercutting and removal of the TiO_2 was accompanied by surface $GaPO_x$ layer growth which was thick enough to minimize XPS detection of the underlying pure GaP. Lastly, it is interesting to note that the binding energy peak at 169 eV attributed to a sulfate state was prominently observed for all TiO_2-coated

electrodes. The Before data was actually collected from a region of the sample just outside the active etch area, but on a wafer surface that had been exposed to the 1 M H_2SO_4 electrolyte. We thus speculate that the TiO_2 phase absorbed some sulfate counterions even in the absence of applied bias.

3.4 Conclusions

The evolution of the photocorrosion on GaP anodes in acid was studied with a novel spectroelectrochemical in-situ UV-Vis absorption technique to monitor the dissolved Ga and P concentration in solution as a function of time and applied bias. Degenerate p^+-GaP electrodes dissolved uniformly, leading to a steady rise in electrolyte Ga concentration and a semiconductor oxidation faradaic efficiency rising to more than 90%, assuming the $n = 6$ corrosion half-reaction. In contrast, illuminated n-GaP photoanodes displayed a decreasing rate of dissolution with declining semiconductor corrosion faradaic efficiency values, which possibly depend on a changing combination of $n = 3$ and $n = 6$ GaP oxidation half-reactions. The difference between n- and p^+-GaP corrosion mechanisms was attributed to anisotropic crystal etching and the semiconductor band energetics which lead to the etching of triangular micropores on the n-GaP surface. Moreover, the tested ALD-grown TiO_2 protective coatings failed to achieve low interfacial charge-transfer resistance, and consequently led to steady but slower GaP dissolution via shunts through pinholes in the TiO_2 layer. The in-situ UV-Vis spectroscopy confirmed a consistent mechanism for the n-GaP corrosion with varying protective layers by displaying a similar evolution to the GaP oxidation faradaic efficiency, just offset by a period of time. The protective layers did, however, lead to variations in the

surface etch morphology, as pinhole nucleation sites led to (111) pyramidal etch sites that undercut the TiO_2 layer and eventually grew into one another. The results demonstrate the capability and versatility of the in-situ UV-Vis spectroscopy technique to investigate semiconductor photocorrosion, enabling researchers to learn about transient corrosion phenomena in operando without the requirement for sophisticated, expensive, low-throughput, and training-intensive facilities.

CHAPTER 4

INVESTIGATION OF n-GaAs PHOTOANODE CORROSION IN ACIDIC MEDIA WITH VARIOUS THIN Ir CO-CATALYST LAYERS

4.1 Introduction

Gallium arsenide (GaAs) plays an important role in high-efficiency solar fuels systems, although it suffers from rapid photocorrosion resulting in formation of an insulating oxide layer or dissolution of the photoelectrode. Different methods have been developed to improve the stability of GaAs photoanodes such as deposition of thin layer of noble metals (Au, Pt, Rh) and polymers like polypyrrole that prevented the photocorrosion of n-GaAs only for limited time.[290-295] In addition, atomic layer deposition (ALD) of TiO_2 coupled with a catalyst have been vastly investigated for stabilization of Si and III-V semiconductors like GaAs and GaP.[17, 296-299] GaAs photoanodes protected with ALD amorphous TiO_2 in combination with Ni catalyst showed stability for about 24 hours.[297,300] Researchers also have studied the effect of a monolayer of graphene and in-

situ electrodeposited nickel-borate on the stability of GaAs photoanodes which provided limited protection in aqueous electrolyte.[28, 295]

Improving practical and cost-effective corrosion protection strategies and understanding of process of photo-corrosion are still demanded in order to design high efficiency and long-term stable PEC systems. Galvanic displacement of metals on semiconductors is a simple, cost effective and high through-put method that have been investigated to create metal semiconductor contacts. Galvanic displacement of noble metals on n-GaAs have been studied intermittently and the reports show the formation of nanoparticles and thin films of Au, Ag and Pt on n-GaAs using galvanic displacement method.[301-303] Recently, P. Buabthong has reported electroless deposition of gold on a-TiO_2 protected p^+-GaAs electrodes as a failure detection method of protection layer.[304] In this case, Au^{3+} ions are reduced on the bare semiconductor surface (pin holes on a-TiO_2) and Au seeds are nucleated on GaAs surface. According to the reduction potential of different noble metals in respect to valence band of GaAs, iridium, an oxygen evolution catalyst, can be deposited on n-GaAs by galvanic displacement method.[305-306] Investigation of the catalytic behaviour and protective properties of electroless deposited Ir on n-GaAs can be a promising route to develop inexpensive and high efficiency protection strategies of photoelectrodes.

Researchers have studied the mechanism of photocorrosion of GaAs photoanodes and proposed corrosion reaction pathways that result in dissolution of Ga and As in acidic and alkaline electrolytes and formation of oxide layers on n-GaAs electrodes in neutral electrolytes that is discussed in more details in this chapter.[307-310] Herein, we have studied the effect of electroless deposition of Ir on stability of n-GaAs photoanodes under applied

bias and in acidic electrolyte. Photocorrosion of electrodes have been studied via in-situ UV-Vis spectroscopy method that we reported in our previous work[64]. We investigated the photocorrosion of n-GaAs photoanodes with galvanic displacement of Ir and spin-coated Ir. Surface of photoelectrodes were characterized by SEM and X-ray photoelectron spectroscopy (XPS).

4.2 Experimental

4.2.1 Electrode fabrication

n-GaAs wafers ((111), Si-doped to 1 – 5 x 10^{18} cm^{-3}, Precision Micro-Optics) were used as the working electrodes in all experiments unless stated otherwise. One other commercial source of comparable n-GaAs wafers ((111B), Si-doped to 2.2 – 2.8x10^{17} cm^{-3}, University Wafer, Inc.) was tested for its photoelectrochemical performance, as shown in Figure 28a. Ohmic contacts were made to the working electrodes by lightly scratching Ga/In eutectic onto the back of the wafer followed by attaching copper tape as a current collector.

Some of the electrodes were further decorated with Ir or IrO_x oxygen evolution reaction co-catalyst. A thin layer of electrolessly deposited iridium (hereafter referred to as Ir(el)) was produced via a galvanic displacement method to deposit iridium catalyst on n-GaAs substrates. The n-GaAs was pre-treated by immersion in 3 M HCl for 3 min and then thoroughly rinsed with 18 MΩ-cm water. GaAs samples were subsequently immersed in a solution of 1 mM hydrogen hexachloroiridate(IV) hydrate, $H_2IrCl_6 \cdot xH_2O$ (99%, Alfa Aesar), in 1 M H_2SO_4 for 24 hours followed by a thorough rinse. In some other samples, IrO_x was deposited by a spin-coating method using one of two different iridium precursors. In one case, a solution of 40 mM iridium (III) chloride, $IrCl_3$ (99.8%, Alfa Aesar), in

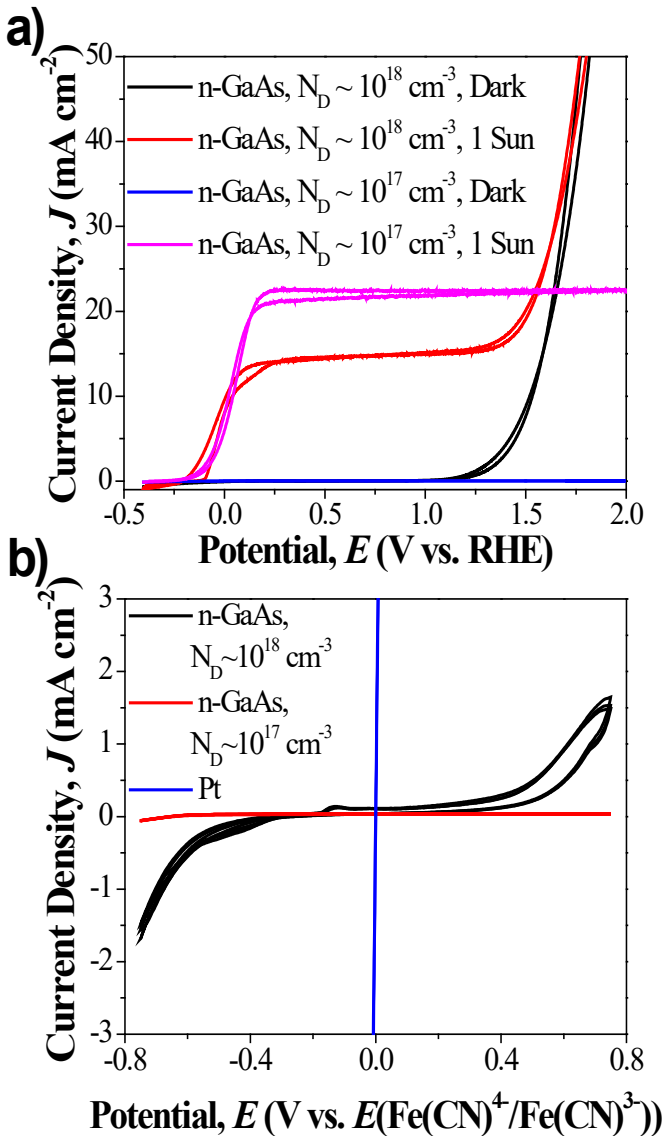

Figure 28. Bare n-GaAs electrochemical behavior. (a) Current density vs. potential (*J*-*E*) in 1 M H_2SO_4 in the dark and under 1 Sun AM1.5 illumination for GaAs wafers of two different doping densities. (b) Current density vs. potential (*J*-*E*) behavior in 0.5 M $K_4Fe(CN)_6$ – 0.05 M $K_3Fe(CN)_6$(aq) for (black line) n-GaAs of $N_D \sim 10^{18}$ cm^{-3}, (red line) n-GaAs of $N_D \sim 10^{17}$ cm^{-3}, and (blue line) a Pt electrode.

isopropanol was used to make a thin Ir layer (hereafter referred to as Ir(ch)). In the second case, a solution of 40 mM iridium (III) acetylacetonate, $Ir(acac)_3$ (98%, Strem Chemicals, Inc.), in chloroform was used to make the thin Ir layer (hereafter referred to as Ir(ac)). In both cases, 40 µL of solution was applied while the substrate was rotating at 200 rpm, then

the substrate rotation rate was increased to 2000 rpm and spun for 60 s. The substrates were then heated at 60 °C for 5 min to evaporate any residual solvent before annealing them in a preheated furnace at 250 °C for 2 h under ambient air.[54]

4.2.2 Photoelectrochemical measurements

Photoelectrochemical measurements were conducted in a quartz cuvette simultaneously with UV-Vis spectroscopy of the electrolyte for in-situ photocorrosion detection as reported in our previous work.[52] Briefly, a 5-mm diameter hole was drilled on one vertical face of the cuvette for electrolyte contact with the n-GaAs working electrode. The n-GaAs was pressed against the outside of the cell at the drilled hole using a thin Teflon gasket to prevent electrolyte leakage. The 1.0 M H_2SO_4 electrolyte volume was kept low (1.25 mL) to promote a higher concentration of dissolved electrode species to maximize the UV-Vis detection sensitivity. The 1-mm diameter leak-free micro Ag/AgCl (Innovative Instruments, Inc.) was used as the reference electrode. The Pt mesh counter electrode was confined to a secondary small container connected to the cuvette electrolyte through a 2-mm diameter bridging tube with a glass frit (KZT-2 tube, Innovative Instruments, Inc.). The counter electrode was separated from the main cell to avoid Pt contamination of the working electrode, to prevent any back reactions of the dissolved semiconductor species at the counter, and to keep hydrogen bubbles generated at the counter from obscuring the illumination pathway. Illumination consisted of 1-Sun AM1.5 white light (300 W Xe lamp, Newport 6258 with AM1.5 global filter) directed through the electrolyte normal to the working electrode and orthogonal to the UV-Vis input beam passed through the electrolyte parallel to working electrode surface. A Si photodiode (Thorlabs, FDS100-CAL) was used

to calibrate the intensity of the simulated sunlight. All electrochemical measurements were performed using an Autolab PGSTAT 100N (Metrohm) potentiostat. The results are reported versus the reversible hydrogen electrode (RHE) scale according to $V_{RHE} = V_{Ag/AgCl} + 0.197 + 0.059pH$, where the electrolyte pH was 0.

4.2.3 Characterization methods

In-situ UV-Vis spectroscopy measurements were performed with an Agilent Cary 60 spectrophotometer in background correction mode with 1.0 M H_2SO_4 as the background. Absorbance data was calibrated to dissolved Ga and As concentrations using inductively coupled plasma mass spectrometry (ICP-MS, Agilent 7900). Separate calibration curves were measured for GaAs at 1.0 and 1.5 V vs. RHE (appendix III, Fig. S3). The dissolved Ga concentration was used to calculate the estimated faradaic efficiency of the GaAs corrosion reaction by determining the charge required to oxidize GaAs to produce the observed quantity of dissolved Ga (assuming 6 e^- per molecule of GaAs) and dividing this by the total charge passed during the potentiostatic measurement at the time of the absorbance measurement.

The electrode surfaces were imaged with scanning electron microscopy (SEM) using a NOVA FEI microscope or Thermo-Fisher Scientific Apreo C LoVac FESEM at an accelerating voltage of 20 kV. Surface elemental analysis was conducted using X-ray photoelectron spectroscopy (XPS) with a VG Scientific Multilab 3000 custom-built ultra-high vacuum system with Al-Kα radiation. XPSPEAK 4.1 software was used for peak deconvolution and the XPS data analysis.

4.3 Results and discussion

4.3.1 Bare n-GaAs photocorrosion behavior

Photoanodes of (111)-oriented GaAs doped n-type with Si donors were used throughout the experiments. The majority of samples available for study were doped to $N_D \sim 10^{18}$ cm^{-3}. The measured dark and 1-Sun photoelectrochemical energy conversion behavior of bare n-GaAs photoanodes in 1 M H_2SO_4 is shown in Figure 28a. These photoanodes had an onset potential under illumination of -0.24 V vs. RHE and a light-limited current density of 12-13 mA cm^{-2}. A typical high-quality GaAs photoactive layer has a photovoltage of ~ 1 V or less, which is not sufficient to split water on its own. Thus, the photocurrent at voltages negative of 0 V vs. RHE is primarily indicative of electrochemical GaAs photocorrosion. Notably, the oxidative current increased exponentially at potentials > 1.2 V vs. RHE. The exponential increase at more anodic potentials was similarly observed in the dark and can be attributed to electrocatalytic Butler-Volmer kinetics. Again, the onset in the dark of this behavior at potentials less that the oxygen evolution reaction (OER at 1.23 V vs. RHE) indicates that the charge passed is contributing to semiconductor corrosion rather than water oxidation. Cycling the potential to values beyond 1.5 V vs. RHE led to high anodic currents, rapid and visible pitting and etching of the semiconductor surface, and corresponding irreversible decreases in the light-limited current density with successive voltage scans (appendix III, Fig. S1).

In an ideal semiconductor-liquid photoelectrochemical junction for a photoanode, increasing anodic potential puts the diode into reverse bias which leads to stronger band bending in the depletion region. The resulting energy barrier across

the depletion region inhibits majority-carrier transfer from the semiconductor bulk, leading to one-way charge flow and a flat current profile which prevents the type of exponential current increase exhibited by the n-GaAs ($N_D \sim 10^{18}$ cm^{-3}) anodes in the dark. Indeed, some samples of similar n-GaAs at a lower doping ($N_D \sim 10^{17}$ cm^{-3}) from a different commercial source were obtained and measured for comparison. As shown in Figure 28a, these photoanodes exhibited higher light-limited current density (~22 mA cm^{-2}) and did not display the Butler-Volmer-type exponential current increase in the dark or under illumination at higher potentials.

The observed energy-conversion behavior for the more highly doped n-GaAs electrodes of a photodiode response conflated with dark electrocatalytic Butler-Volmer kinetics has frequently been reported for metal oxide photoanodes, especially in the presence of a co-catalyst. In some of those cases, the exponential current increase at higher potentials was attributed to shunt pathways for charge-transfer across the electrode interface to bypass the reverse bias energy barrier, thus allowing dark electrocatalytic behavior to occur in parallel with the illuminated photodiode behavior.[283] This possibility was tested for the n-GaAs photoanodes in this work using the kinetically fast one-electron redox couple ferro-/ferricyanide. As shown in Figure 28b, the lower doped n-GaAs electrodes appeared highly resistive in the ferro-/ferricyanide solution, due to the band bending produced by the difference between the redox couple potential and the semiconductor Fermi level. A metallic Pt electrode, in contrast, exhibited highly ohmic behavior with low resistance. If the dark Butler-Volmer exponential response in the higher doped GaAs anodes was attributed to parallel shunt pathways for charge flow, a similar low-

resistance ohmic response would be expected.[283] However, the $N_D \sim 10^{18}$ cm^{-3} doped n-GaAs electrodes did not exhibit ohmic behavior but instead showed rectifying behavior less resistive than the $N_D \sim 10^{17}$ cm^{-3} doped n-GaAs. The exponential increase in dark anodic current for the higher doped GaAs was therefore not attributed to shunt pathways for charge-carriers to bypass the band bending.

The electrochemical energy-conversion behavior exhibited by the higher doped n-GaAs is instead consistent with the onset of degenerate-like semiconductor properties. This finding is supported by literature reports that the low effective mass of electrons in GaAs leads to degenerate properties at a relatively low n-type doping of $5x10^{17} – 1x10^{18}$ cm^{-3}.[311] Strongly degenerate semiconductors are so highly doped that the excess majority carriers and sharply bent bands lead to metallic characteristics and photo-inactive properties. The decreased light-limited photocurrent for the $N_D \sim 10^{18}$ cm^{-3} doped n-GaAs relative to the $N_D \sim 10^{17}$ cm^{-3} doped n-GaAs is consistent with the onset of degeneracy as charge-carriers can increasingly tunnel through the sharply bent bands in a narrow depletion region. This interpretation is further in agreement with past reports of increased anodic dark current for GaAs with increasing N_D owing to electrons tunnelling a barrier which becomes thinner with doping density.[312-314] Specifically, Allongue et al. proposed a GaAs corrosion mechanism in which Ga and As surface atoms partially bonded to the lattice and to species of the solution give rise to interface states within the GaAs bandgap, and injection of electrons from these states into the GaAs bulk leads to oxidative corrosion by holes at that site.[312] Thus, the exponential increase of corrosion current for higher doped n-GaAs beyond 1.2 V vs. RHE (Figure 28a) could

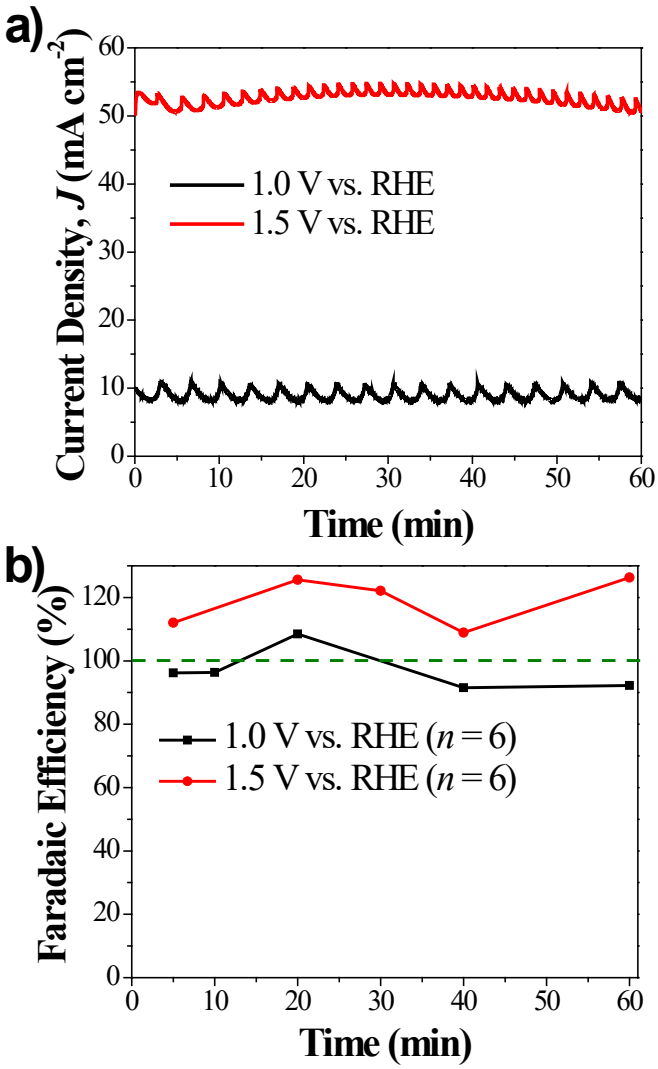

Figure 29. (a) Illuminated chronoamperometric behavior and (b) corresponding faradaic efficiency for the corrosion reaction for n-GaAs of $N_D \sim 10^{18}$ cm^{-3} in the UV-Vis cuvette reactor. The FE was determined assuming six electrons ($n = 6$) per detected Ga atom.

reasonably be interpreted as electrons from these interface states increasingly tunnelling through the narrow energy barrier of a quasi-degenerate semiconductor resulting in rapidly increasing surface corrosion with increased anodic bias.

The bare n-GaAs photoanodes were measured under 1 Sun AM1.5 conditions at potentiostatic conditions in a quartz cuvette reactor cell with simultaneous in-situ

UV-Vis spectroscopic analysis of the electrolyte, as reported in our previous work.[52] Control measurements and ICP-MS calibration data for the in-situ UV-Vis spectroscopy for GaAs are reported in appendix III, Figure S2 and Figure S3, respectively. Figure 29 shows the corresponding current density vs. time curves for the n-GaAs at 1.0 and 1.5 V vs. RHE. The oscillations in these curves were observed to correspond to bubble formation and release from the exposed wafer in the 5-mm diameter hole in the cuvette. By comparing the detected concentration of dissolved Ga ions to the charge passed over the same time period, the faradaic efficiency for the GaAs corrosion reaction was plotted over the course of a 60-min measurement (Figure 29b). This calculation assumed that six holes are required to dissolve each molecule of GaAs. Although literature reports vary on the resulting byproducts and the species state of the dissolved As upon GaAs oxidative corrosion in acidic media, a value of n = 6 for the required number of charges passed per GaAs has been consistently identified.[312, 315-316] The overall corrosion reaction in acid is proposed to follow a two-step process in which Ga is selectively etched first, leaving behind As^0 metal which is subsequently electrochemically oxidized and dissolved:

$$\mathbf{GaAs + 3h^+ \rightarrow Ga^{3+} + As^0} \quad (5)$$

$$\mathbf{As^0 + 3h^+ + 2H_2O \rightarrow HAsO_2 + 3}\boldsymbol{H^+} \quad (6)$$

$$\mathbf{GaAs + 6h^+ + 2H_2O \rightarrow Ga^{3+} + HAsO_2 + 3}\boldsymbol{H^+} \quad (7)$$

Using the overall reaction in Equation 7, the faradaic efficiency for GaAs corrosion was determined to be > 95% at 1.0 V vs. RHE (Figure 29b). This result is an indication that six holes per GaAs molecule is accurate under these conditions and that the semiconductor oxidative corrosion reaction is strongly kinetically favored

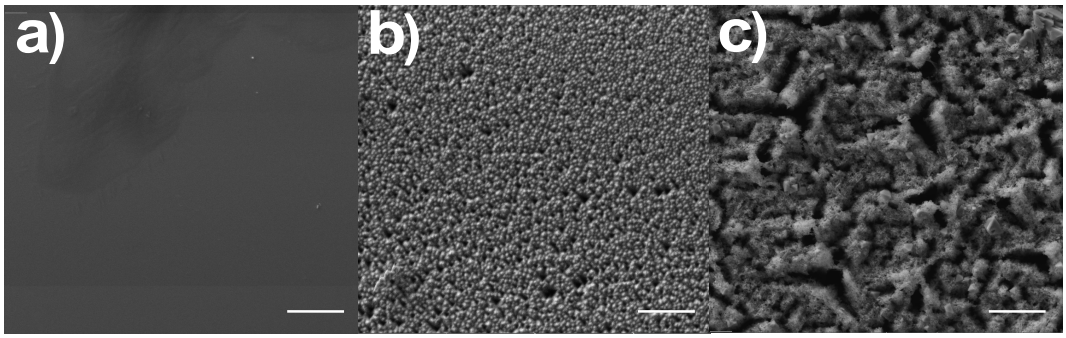

Figure 30. SEM images for bare n-GaAs photoanodes (a) pristine, (b) after 2 h at 1.0 V vs. RHE, and (c) after 2 h at 1.5 V vs. RHE. Scale bar is 20 μm in all panels.

at this potential relative to the oxygen evolution reaction, which would reduce the faradaic efficiency for GaAs dissolution.

Interestingly, at the higher current density under 1.5 V vs. RHE, the calculated faradaic efficiency for GaAs corrosion was 115 – 122% (Figure 29b). Clearly, greater than 100% faradaic efficiency is not possible, and this is an indication that the assumption of six holes per molecule of dissolved GaAs no longer holds at this condition. If a value of $n = 5$ is assumed instead, the corrosion faradaic efficiency is reduced to ~ 95 – 101%. It is possible that the mechanism for corrosion at 1.5 V vs. RHE on the $N_D \sim 10^{18}$ cm^{-3} doped n-GaAs, in which significant current can pass in the dark as theorized above via electron tunnelling of the band bending, is distinctly different from the corrosion route at 1.0 V vs. RHE which would be dominated by the transfer of photogenerated holes from the valence band to the corroding surface sites. A competing corrosion reaction requiring less than six holes per GaAs could thus account for the observed faradaic efficiency at 1.5 V vs. RHE. Furthermore, while no macroscopic particles or precipitates were observed in the electrolyte, we also cannot entirely rule out the possibility that under the rapid etching conditions at 1.5 V vs. RHE some unreacted microparticulates of GaAs may

be released from the surface and quantified by ICP-MS, leading to a higher detected concentration of Ga ions than could be attributed to the electrochemical dissolution alone. SEM images of the GaAs surface after extended operation at these potentials highlight the feasibility of this explanation (Figure 30). While operation at 1.0 V vs. RHE led to micron-scale etch pits and pock marks across the surface, operation at 1.5 V vs. RHE led to deep etching with some much larger pits and valleys as well as flaky material and particles at the surface (appendix III, Fig. S4). One other possible explanation considered was that the reactions of Equations 5-7 might remain the dominant pathway for the electrochemical corrosion, but the significantly increased current density observed at 1.5 V vs. RHE could conceivably lead to kinetic constraints causing an imbalance in the rates of the reactions in Equations 5 and 6. In this case with preferential electrochemical etching of the Ga site,[312] the excess As^0 would need to be chemically dissolved to maintain the ~1:1 Ga:As ratio for dissolved atoms that was measured by ICP-MS (appendix III, Fig. S3). However, it has been reported that under strongly acidic conditions, chemical etching of GaAs preferentially etches Ga sites leaving an As-rich surface.[312] This finding has been confirmed with XPS using a UHV chamber coupled with the electrochemical cell to enable surface analysis before ambient oxidation of the elemental As^0 layer.[317-318] The As^0 layer is thus considered thermodynamically stable at pH 0,[312] making the chemical dissolution of this layer an unlikely explanation for the calculated > 100% faradaic efficiency observed at 1.5 V vs. RHE. We thus attribute this result to one or both of the previous two explanations.

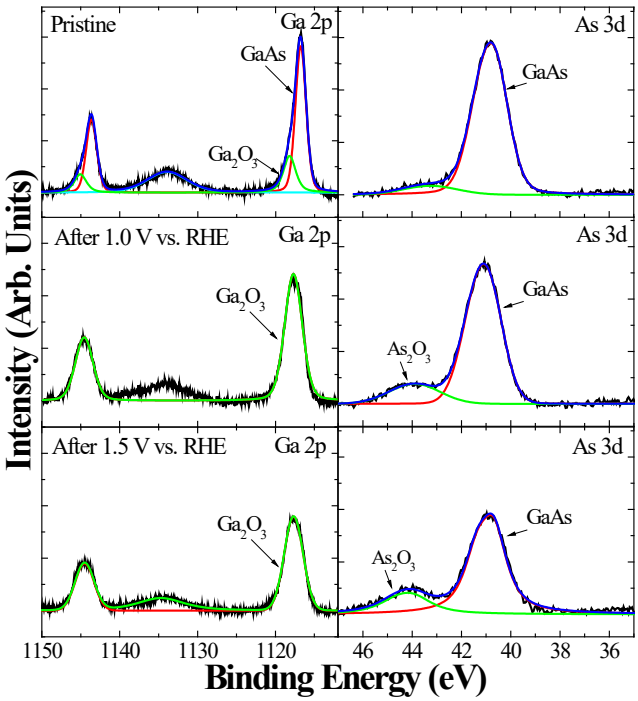

Figure 31. XPS spectra of bare n-GaAs photoanodes. Samples are (top) pristine, and after 2 h at 1 Sun in 1 M H_2SO_4 at either (middle) 1.0 V vs. RHE or (bottom) 1.5 V vs. RHE.

Surface analysis of the bare n-GaAs by XPS after operation at 1.0 V and 1.5 V vs. RHE are reported in Figure 31. For pristine samples, the Ga 2p and As 3d peaks were dominated by the GaAs phase with only a minor shoulder peak attributed to the native surface oxide phases Ga_2O_3 and As_2O_3. Following oxidative corrosion in aqueous acid and exposure to air, the Ga 2p peak position shifted and was primarily assigned to Ga_2O_3. For the As 3d peaks, a significantly stronger As_2O_3 shoulder peak developed which was most intense relative to the GaAs peak for the 1.5 V vs. RHE condition. Elemental As^0 As 3d peaks occur within 0.5 eV of the GaAs peak binding energy and were not readily resolved in the measured spectra.[319-320] Given the highly porous nature of the As^0 layer formed during acidic etching

observed here (Figure 30) and reported elsewhere,[321] it is not surprising that this layer was primarily converted to As_2O_3 after exposure to air.

4.3.2 Thin layer Ir-coated n-GaAs photocorrosion behavior

One strategy that has had success at limiting the photocorrosion of n-GaAs in aqueous media is to use chalcogenide redox couples which provide stabilization by being kinetically easier to oxidize than the semiconductor itself.[322] However, to use this material as a water-splitting photoanode, the holes should be directed to the oxygen evolution reaction (OER). The decoration of a photoanode with a low OER overpotential co-catalyst has been shown to improve the OER kinetics enough to promote water oxidation to the dominant reaction pathway in other acidic systems.[283] The GaAs self-oxidation potential is thermodynamically negative of the OER potential, however, so OER kinetic improvements alone are not predicted to stabilize the GaAs surface.[36] To prevent oxidative corrosion while still maintaining photoelectrochemical water oxidation, the Ga and As sites should be physically protected from reaction with the acidic aqueous media with a thermodynamically stable layer. This approach was the premise for studying n-GaAs photocorrosion with thin layers of the acid-stable OER catalyst IrO_x. While a thick layer is more likely to provide robust coverage and protection, it would also absorb more light and detrimentally affect the band bending at the photoelectrochemical junction.

Three methods of thin-layer Ir application were tested as described above: electroless deposition (Ir(el)), spin-coated $IrCl_3$ (Ir(ch)), and spin-coated $Ir(acac)_3$ (Ir(ac)). The uniform formation of an Ir layer through the electroless method was confirmed via SEM and EDS mapping (appendix III, Fig. S5). The effect of the Ir layer on the n-GaAs

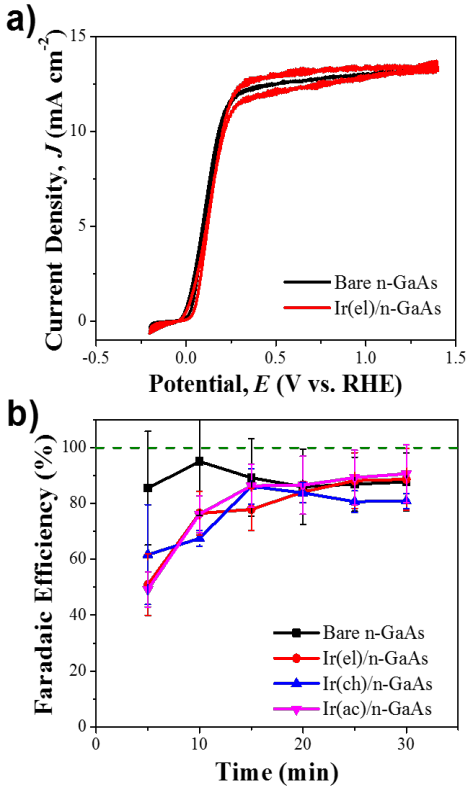

Figure 32. (a) Current density vs. potential behavior for bare n-GaAs and 24 h electrolessly deposited iridium, Ir(el), on n-GaAs under 1 Sun in 1 M H_2SO_4. (b) Faradaic efficiency for GaAs photocorrosion as measured by in-situ UV-Vis spectroscopy on bare n-GaAs and Ir-coated n-GaAs prepared by electroless iridium deposition (Ir(el)), spin-coating iridium chloride (Ir(ch)), or spin-coating iridium acetylacetonate (Ir(ac)). Error bars represent the deviation over three duplicate measurements

current density vs. potential behavior in each case was minimal. A representative example showing the Ir(el)/n-GaAs *J-E* curve is shown in Figure 32a. The potential range of operation for these electrodes was intentionally maintained below 1.5 V vs. RHE to avoid the rapid etching observed at more anodic potentials. The time-dependent faradaic efficiency of the GaAs corrosion reaction was then monitored at the light-limited current density at 1.0 V vs. RHE using in-situ UV-Vis spectroscopy (Figure 32b). Unfortunately, none of the thin co-catalyst surface layers had a dramatic effect on the corrosion faradaic efficiency profile, with each Ir/n-GaAs photoanode reaching comparable behavior to a bare n-GaAs after 15 – 20 min. Before 15 min a modest decrease in the corrosion faradaic

efficiency was detected for all three Ir deposition approaches, though it was not measured less than ~ 50%.

Materials characterization of the Ir/n-GaAs samples after operation in acid provides some additional insights on the physical differences between the electrodes by the method of Ir deposition. Figure 33 shows SEM images of the electrode surfaces after 10 min at 1.0 V vs. RHE, long enough for corrosion to cause morphological changes but during the critical early stage when some effect on the faradaic efficiency was still detectable. The Ir(el)/n-GaAs sample after 10 min showed only the small beginnings of etch pits with fairly uniform distribution. After 2 h of photoetching, these sites grew into deeper triangular pits approximately 5 μm across which fully covered the surface of the exposed area (appendix III, Fig. S6). The Ir(ch)/n-GaAs electrode, in contrast, displayed sizable 3 – 5 μm triangular etch pits even after only 10 min, although these etch pits were much less dense and nonuniformly distributed (Figure 33b). Moreover, for these etch pits, the SEM images show the rougher Ir(ch) surface layer disturbed near the edge of the triangular pits, in some cases appearing to spill over into the pit. This morphology is consistent with corrosion proceeding through pinholes in the Ir(ch) layer, leading to faster etching through the limited pinhole area and creating larger pits which start to undercut the Ir(ch) layer beside the

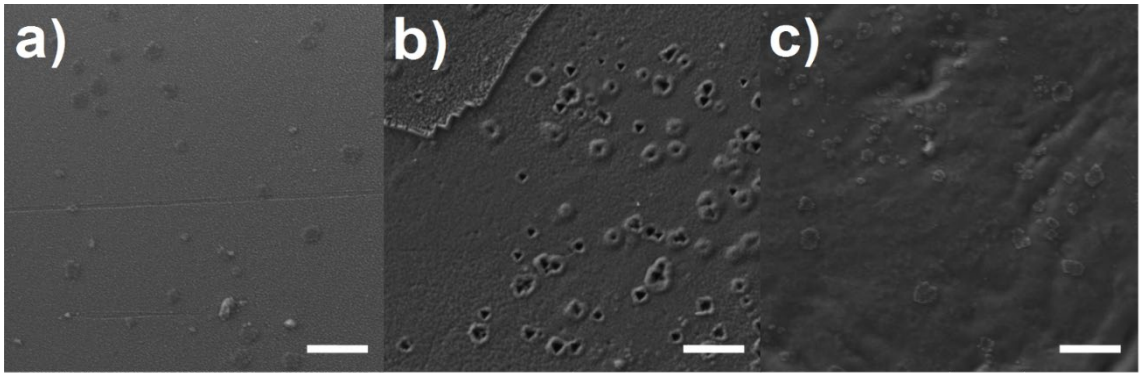

Figure 33. SEM images for Ir-coated GaAs after 10 min at 1.0 V vs. RHE for (d) Ir(el), (e) Ir(ch), and (f) Ir(ac). Scale bar is 20 μm in all panels.

pinhole. In some cases, flaking and lift-off of the Ir(ch) compact surface layer was observed in the vicinity of an etch pit (appendix III, Fig. S7). The uniform, slower growing etch pits on the Ir(el)/n-GaAs indicate etching occurring across the entire surface area rather than via isolated pinholes. The mechanism for preferential formation of triangular etch pits on these surfaces is likely similar to the process we described previously for n-GaP in acid.[52] Photogenerated minority-carrier holes from the valence band are most likely to populate surface states within the band gap, leading to accelerated oxidative corrosion at interface defects which become nucleation sites for etch pits. Because of the different energy density required to break the bonds in different crystal orientations, anisotropic etching can occur. The (111) Ga-terminated surface in particular has the fastest kinetics for surface corrosion in acid, and this selective etching leads to pyramidal etch pits on the GaAs(111) wafers used in this work.[312, 323] Interestingly, for the Ir(ac)/n-GaAs no obvious etch pits were observed but the surface layer, which appeared more amorphous than the other electrode types, did develop noticeable contours which were not present in the flat pristine sample. We speculate that the electrode may permeate this more amorphous IrO_x layer and lead to corrosion underneath areas of the film.

Surface analysis of the Ir/n-GaAs also indicates notable differences between electrode interfaces that may affect the corrosion process. XPS spectra for the Ga 2p, As 3d, and Ir 4f regions are plotted in Figure 34 for the three types of Ir-coated n-GaAs photoanodes before and after operation at 1.0 V vs. RHE. For the Ir(el)/n-GaAs photoanode, the significantly higher intensity of the As 3d peak for As_2O_3 relative to the peak for GaAs distinguishes this electrode type from the bare n-GaAs and the other Ir-coated photoanodes. Importantly, the enhancement of the As_2O_3 peak is present even on

the pristine Ir(el)/n-GaAs before photoelectrochemical operation. The prevalence of As_2O_3 at the surface is attributable to the mechanism of electroless iridium deposition via galvanic displacement. In a galvanic displacement reaction, a noble metal ion in solution can be reduced to its metal form and replace the surface layer of a substrate if the noble metal/metal ion redox couple has a standard electrochemical potential greater than that of the substrate metal/metal ion potential. If the material and pH conditions allow a stable substrate oxide, then the noble metal deposition may coincide with surface oxidation as well.[306] In this case, the hexachloroiridate ion/iridium redox standard potential is positive of the GaAs valence band as well as the GaAs corrosion potentials.[305] Metal deposition on the semiconductor surface occurs via local anode and cathode sites, in which electrons from the valence band reduce the $IrCl_6^{2-}$ to plate Ir^0 on the surface at a cathode site while a local anode site undergoes GaAs oxidation resulting in an As_2O_3-rich surface. With co-located anode and cathode sites, metal deposits produced by galvanic displacement are usually porous.[324] Thus, acidic electrolyte contact with the semiconductor surface remains possible leading to the fairly uniform distribution of small etch pits seen after 10 min of operation. After 2 h under illumination at 1.0 V vs. RHE, the etch pits became deeper, undercutting the Ir surface layer and growing into each other. Despite the highly roughened surface of Ir(el)/n-GaAs after 2 h (appendix III, Fig. S6), the XPS still shows significant although decreased Ir 4f peaks corresponding to IrO_2. The presence of IrO_2 after 2 h indicates that some areas of the surface were well protected and had not yet been removed by undercutting.

An additional experiment was performed to investigate the possibility of using in-situ electroless Ir deposition as an ongoing surface repair mechanism, allowing the co-

catalyst to redeposit during operation and perhaps protect the surface in the etch pits. In this experiment, a normally prepared Ir(el)/n-GaAs photoanode in 1 mM H_2IrCl_6, 1 M H_2SO_4 was cycled for 10 min between 10 s at 1.0 V vs. RHE under 1 Sun followed by 10 s at the open-circuit voltage (OCV) in the dark (appendix III, Fig. S8). The iridium deposition bath as electrolyte was too strongly light-absorbing to utilize in-situ UV-Vis characterization, but ICP-MS measurements of the dissolved semiconductor elements indicated that the corrosion faradaic efficiency remained high (> 90% at 10 min). Thus, whether the Ir(el) layer is too porous to be sufficiently protective, or the electroless deposition was too slow to be beneficial on the 10 s pulse time scale, or the galvanic displacement mechanism itself contributes too much surface corrosion, it was clear the thin Ir(el) layer did not provide sufficient stabilization to the n-GaAs surface to enable durable photoanodic water oxidation in acidic.

For the spin-coated Ir layers on GaAs, XPS results showed differences in the interfacial chemical state as well (Figure 34). Ir(ch)/n-GaAs had significant As_2O_3 present on the pristine surfaces. Although not as dominant as for the Ir(el) samples, the As 3d As_2O_3 peak for Ir(ch) was more intense relative to the GaAs peak than observed for bare n-GaAs (Figure 31). This was attributed to surface oxidation during the catalyst annealing step to make IrO_2. The Ir 4f peaks for Ir(ch)/n-GaAs were entirely assigned to IrO_2 and were much more intense than the corresponding peaks for Ir(el)/n-GaAs owing to the thicker, more compact Ir film that resulted from spin-coating. Although a slight decrease in IrO_2 peak intensity was observed after 2 h at 1.0 V vs. RHE, the signal remained strong, which indicates that much of the surface was protected from corrosion. Instead, the charge passed by photogenerated holes was primarily directed through isolated pinholes in the

Ir(ch) to form larger and fewer etch pits (Figure 33b). The Ir(ac) film, in contrast, did not display as much As_2O_3 on the pristine surface (Figure 34). The Ir 4f peaks were also present at lower binding energy than the other Ir films and were deconvoluted and assigned to a combination of IrO_2 and Ir. The SEM of the Ir(ac) suggests a more amorphous layer which may thus be an incompletely oxidized IrO_x film (Figure 33c). Incomplete oxidation of the layer during the anneal step could also have prevented greater oxidation of the underlying GaAs surface, accounting for the decreased As_2O_3 in the pristine state. After 2 h of operation at 1.0 V vs. RHE, the Ir(ac)/n-GaAs Ir 4f peak intensities were almost unchanged, indicating much of the surface was still covered with the Ir(ac) layer. However, the post-operation As 3d As peak did significantly increase, which confirms that surface corrosion occurred to an appreciable extent.

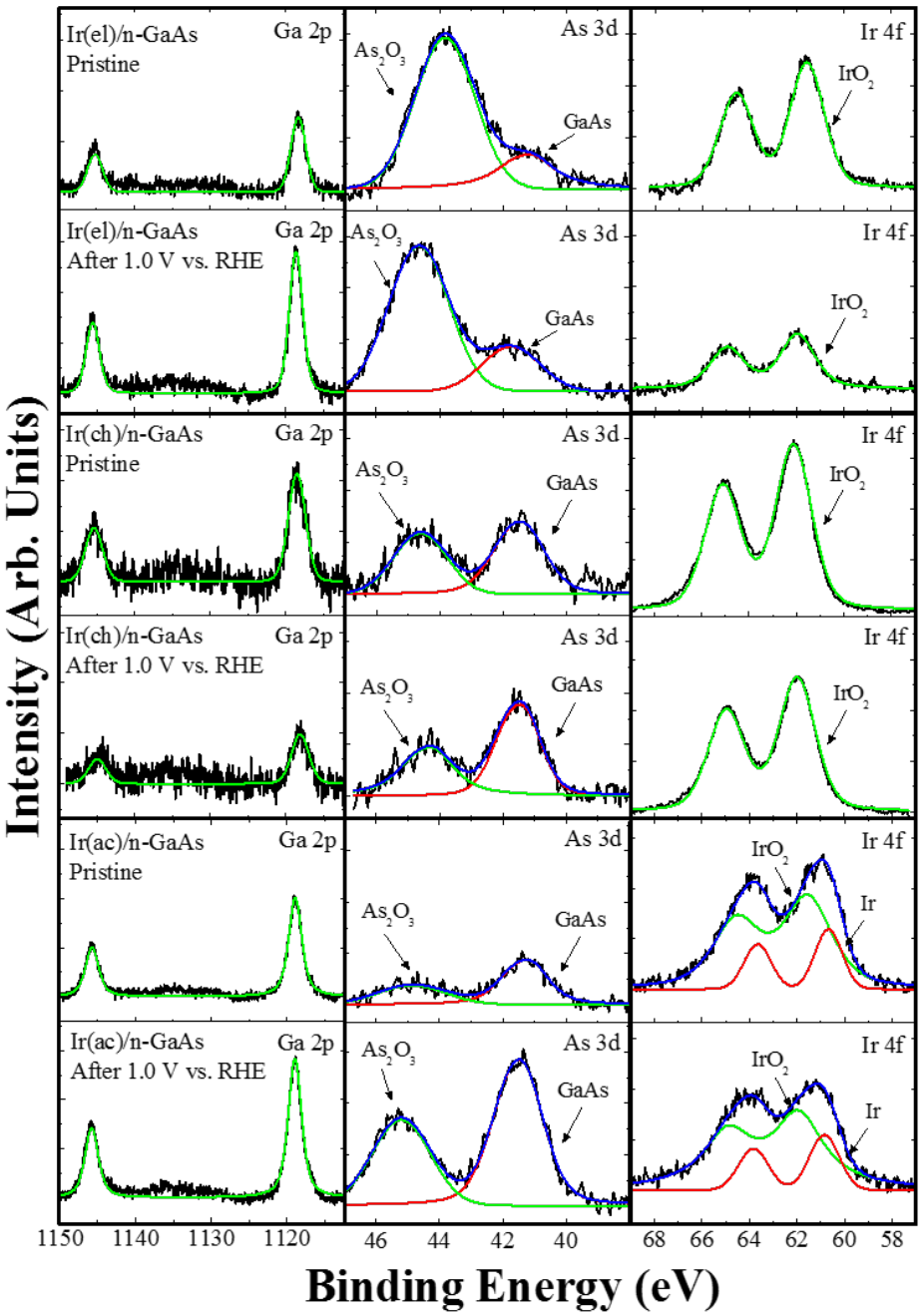

Figure 34. XPS spectra of Ir-coated n-GaAs (Micro Optics) photoanodes. Samples are (top two rows) 24 h electroless iridium (Ir(el)), (middle two rows) spin-coated iridium chloride (Ir(ch)), and (bottom two rows) spin-coated iridium acetylacetonate (Ir(ac)) coated GaAs. For each Ir type, the top row is pristine as-deposited and the bottom row is after 2 h under 1 Sun at 1.0 V vs. RHE in 1 M H_2SO_4. The binding energy ranges are for the (left column) Ga 2p, (middle column) As 3d, and (right column) Ir 4f regions.

4.4 Conclusions

GaAs is notoriously unstable under photoelectrochemical oxidative conditions. The photocorrosion mechanism is complex and depends on the pH, crystal orientation, band energetics, and the doping. As seen herein, a slight increase in the n-GaAs doping density led to dramatically different current density vs. potential behavior, with $N_D \sim 10^{18}$ cm^{-3} doped material displaying the beginnings of degenerate behavior which enabled charges to tunnel through the band bending energy barrier and pass significant current to corrosion even in the dark. Moreover, quantification of Ga and As atoms in solution to determine the corrosion faradaic efficiency showed a shift in the dissolution pathway at the higher potential.

Three types of OER co-catalyst Ir layers were tested in this work to investigate their effect on the GaAs photocorrosion. As determined by in-situ UV-Vis spectroscopy, each Ir thin layer modestly decreased the corrosion faradaic efficiency over the first 15 min. Self-limiting surface coverage with electroless deposition of Ir provided a thin uniform layer, but the nature of the galvanic displacement process left the GaAs vulnerable to electrochemical attack. Thicker compact Ir layers produced by spin-coating and annealing Ir precursors more effectively protected a greater area of the surface, but rapid etching via pinholes in the catalyst film still eventually led to most of the charge being directed to corrosion. Thus, stabilizing this type of III-V semiconductor under relevant solar water-splitting conditions is an exceptionally difficult materials challenge. Even a single pinhole can result in a corrosion nucleation site which will grow and degrade the protection layer. Thicker catalyst layers are thus ideal for minimizing pinholes, but such metal layers can lead to Fermi-level pinning and impede the photoelectrochemical junction. Using a buried

p-n semiconductor junction to control the band bending, the photovoltage can be maintained despite a thick catalyst surface layer, but parasitic light absorption in the film is an issue. Thus a pinhole-free, compact thin film is still desirable. Graphene is an ideal material for such a layer which has been shown to add durability to GaAs photoelectrodes, but it still degrades rapidly in aqueous media.[295] ALD protective coatings of inert materials with favorable interfacial charge-transfer properties have had the most success, but pinholes remain problematic.[39] Thus, despite the difficulty many laboratories have had synthesizing and reproducing thick pinhole-free ALD layers of "leaky" TiO_2,[17] this strategy currently remains the state-of-the-art for the protection of III-V photoanodes like GaAs.

CHAPTER 5

EXPLORATORY STUDIES OF NOVEL GaSbP PHOTOANODES AND FUTURE DIRECTIONS

5.1 Introduction

Finding the appropriate photoabsorber is the most important part of structure of a photovoltaic and photoelectrochemical water splitting system. To develop high efficiency and stable water splitting systems new semiconductor materials with appropriate band gap, band edge positions, charge carrier mobility and chemical stability are still demanded. To date, the best photoabsorbers are III-V semiconductors resulting in the most efficient solar cells and PEC systems.[7, 15, 19-20, 25]

Among all III-V semiconductors GaP is of particular interest because of indirect band gap of 2.26 eV, appropriate band alignment for water splitting and low lattice mismatch with silicon leading to more economic growth of GaP on Si substrates.[325-328] However, the indirect band gap of GaP results in large absorption depth which is not favorable for photoelectrodes in water splitting systems. Synthesis of ternary III-V alloys enable us to tune the band gap of III-V semiconductor with changing the compositions which can lead

to indirect to direct band gap transition.[329] Several III-V ternary alloys of GaP such as GaInP, GaPN and GaPAs are reported to undergo indirect to direct band gap transition.[330-331]

Herein we explored a novel III-V ternary alloy $GaSb_xP_{(1-x)}$, synthesized in Conn Center for Renewable Energy Research by Halide Vapor Phase Epitaxy (HVPE) method. HVPE is a high throughput process with growth rates in the order of hundreds of microns per hour which allows optimization of the processing time and lowers the capital costs.[332] HVPE uses elemental metallic sources such as Gallium that costs less than trimethylgallium used in metalorganic chemical vapor deposition (MOCVD) systems. HVPE uses gas phase precursors of V element species, typically hydrides and gaseous halide species of the III group of the periodic table to grow III-V semiconductors. The species are transported in vertical or horizontal hot wall chambers and reach a single crystal substrate where they get adsorbed and react forming the solid film.

According to the report by Conn Center,[333] a quartz tube with a volume of 1.2 L fitted in a two-zone furnace was used to grow $GaSb_xP_{(1-x)}$ films. The two-zone furnace is equipped with an additional zone with a graphite susceptor to hold and inductively heat the silicon substrate [111]. Two gas lines that mix before the entrance are connected to the reactor. One of them carry 100 sccm of hydrogen previously flown though a bubbler containing phosphorous trichloride (kept at constant temperature of 35 °C) and the other one carry 125 sccm of hydrogen. Metallic precursors, 5 g of antimony powder and 10 g of gallium in quartz boats are placed in each of reactor. Gallium zone and antimony zone were kept at 970 °C and 750 °C respectively and the pressure inside the reactor was 500 torr. The substrate temperature was varied between 400 °C and 725 °C which affects the

growth rate and quality of the film. Figure 35 shows the P&ID of the experimental system.[333]

We have investigated the optical and electrical characteristics of this new ternary III-V, $GaSb_xP_{(1-x)}$ films, via different techniques. Diffuse reflectance spectroscopy (DRS) and photoluminescence spectroscopy (PL) have been used to study the band gap of $GaSb_xP_{(1-x)}$ films. Crystal structure and antimony concentration of films are investigated by x-ray diffraction (XRD) analysis.

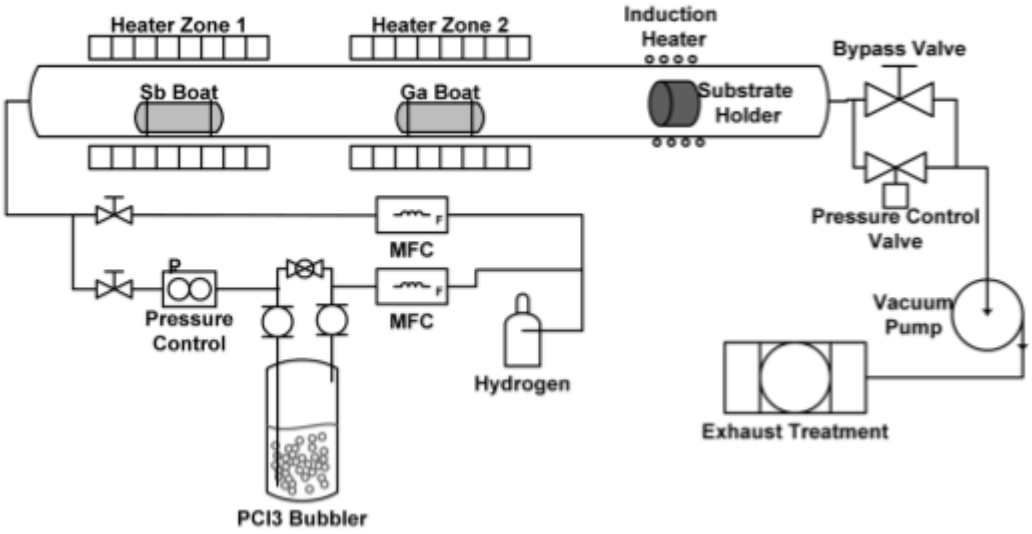

Figure 35. P&ID of HVPE reactor [333]

Surface morphology of $GaSb_xP_{(1-x)}$ films are characterized via SEM. In addition, EDS and x-ray photoelectron spectroscopy (XPS) have been used for elemental composition studies. 4-point probe and Hall effect measurements are performed to understand the electrical properties of this new material such as surface/bulk resistance and Hall mobility.

We have also tested the photoelectrochemical behavior of $GaSb_xP_{(1-x)}$ free standing samples under illumination and acidic electrolyte to evaluate its performance in water splitting systems as photoanode.

5.2 Band gap

Addition of antimony to gallium phosphide can result in lowering the band gap via a phenomenon known as band gap bowing.[329] Moreover, addition of antimony at low concentrations leads to transformation of band gap of GaP from an indirect to a direct transition. According to previous fundamental studies using the BAC model, interaction between the localized Sb states and the extended states of the semiconductor matrix results in reduction of the band gap.[334] Here we have used DRS and PL analysis to investigate the affect of Sb addition on band gap of GaP semiconductor.

5.2.1 Diffuse reflectance spectroscopy

When a surface is illuminated, two types of reflection can happen, specular and diffuse reflection. Regular or specular reflection usually occurs on smooth, polished surfaces like mirror and diffuse reflection is from mat or dull surfaces textured like powders. In the case of ideal diffuse reflection, the angular distribution of the reflected radiation is independent of the angle of incidence. When a dull or matt sample is illuminated, results in combination of reflection, refraction and diffraction. It also can absorb the incident light at selected wavelengths.[335] One of the well-known theories which is most often used to interpret the diffuse reflectance theory is the Kubelka-Munk theory.[336] One assumption in Kubelka-Munk theory is that the sample is infinitely thick and none of the irradiating light penetrates to the bottom of the sample holder. The function derived by Kubelka and Munk is

$$F(R_\infty) = \frac{(1-R_\infty)^2}{2R_\infty} = \frac{K}{S} \quad (8)$$

where $R_\infty = \frac{R_{sample}}{R_{standard}}$ is reflectance of an infinitely thick specimen, K is the absorption coefficient and S is scattering coefficient. Later in 1966, Tauc proposed a method of estimating the band gap of semiconductors using optical absorption spectra. Tauc method assumes that the energy-dependent absorption coefficient α is expressed by equation 9:

$$(\alpha.h\upsilon)^{1/\gamma} = B(h\upsilon - E_g) \quad (9)$$

where h is the planck constant, υ is the incident photon's frequency, E_g is the band gap energy, and B is a constant. The factor of γ depends on the nature of transition of the electron and is equal to $1/2$ or 2 for the direct and indirect transition band gaps respectively. In the case of samples that the scattering component cannot be neglected, we can use analogous Tauc plot using DRS. In this version, α is replaced with Kubelka-Munk function as shown in equation 10.

$$(F(R_\infty).h\upsilon)^{1/\gamma} = B\left(h\upsilon - E_g\right) \quad (10)$$

According to equation 10, if we draw $(F(R_\infty).h\upsilon)^{1/\gamma}$ vs $h\upsilon$ (eV), the x-axis intersection point of the linear fit of the Tauc plot gives an estimate of the band gap energy.[336] We have used diffuse reflectance spectra of $GaSb_xP_{(1-x)}$ samples to calculate the Kubelka-Munk function and draw the Tauc plots to estimate the band gap energy.[337] We have stablished our method on commercial standard sample of gallium phosphide (GaP) single crystal wafer which is the closest material to compare with $GaSb_xP_{(1-x)}$ samples. As show in Figure 36, the indirect band gap of GaP is estimated about 2 eV which agrees with 2.26 eV indirect band gap of GaP reported in literature.

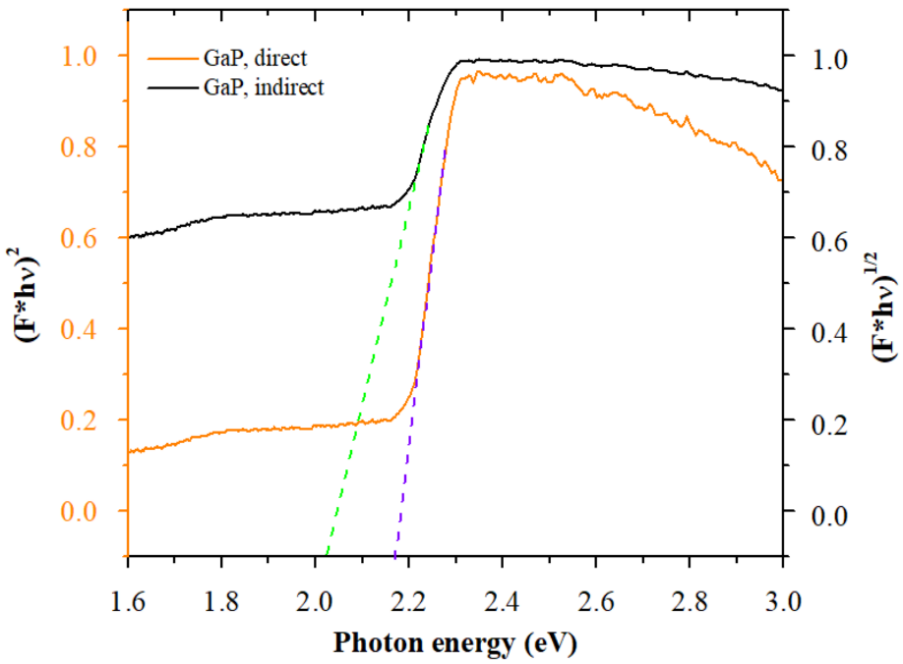

Figure 36. Tauc plot of commercial GaP wafer

a)

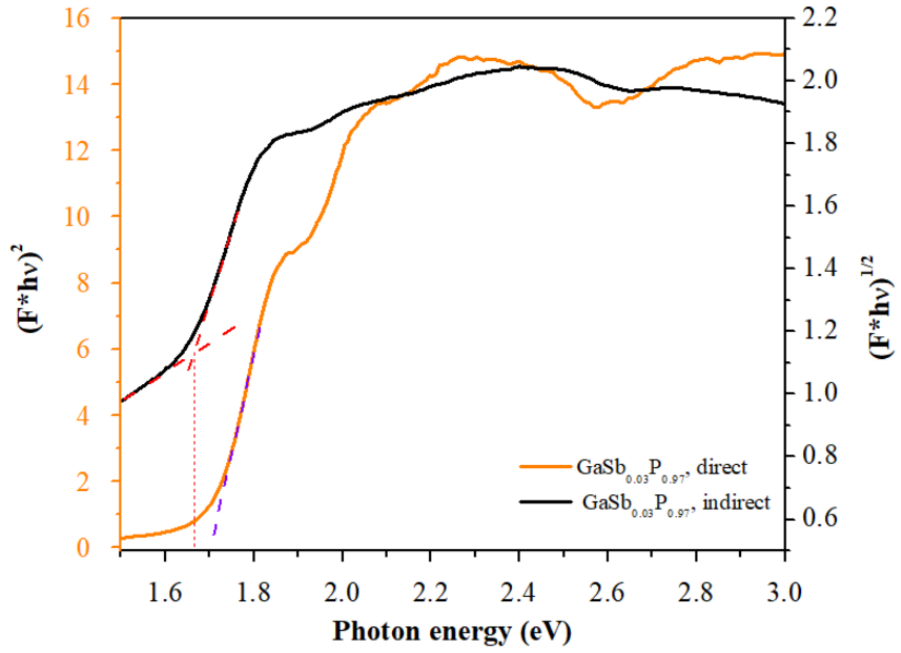

b)

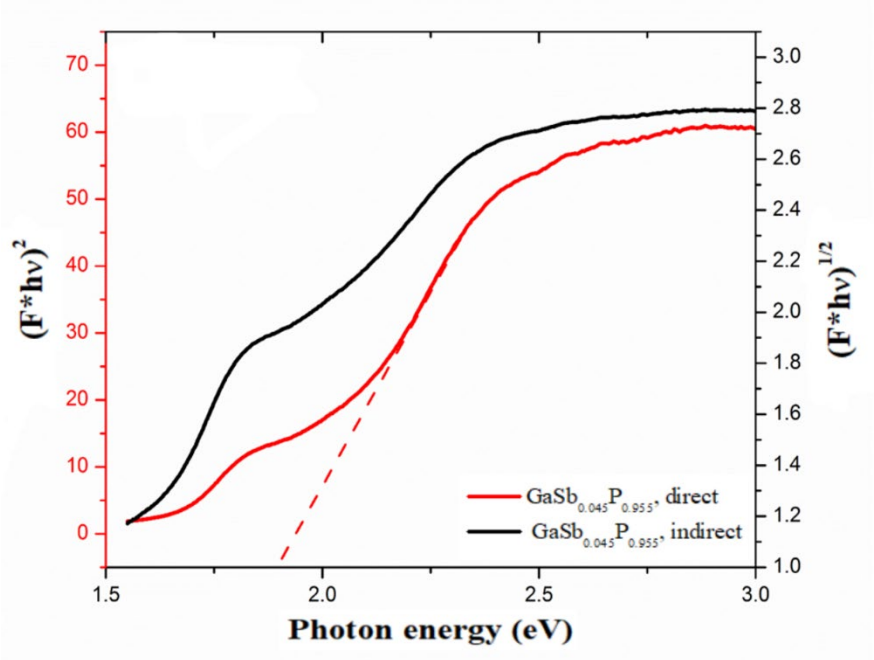

Figure 37. Tauc plot of (a) $GaSb_{0.03}P_{0.97}$, (b) $GaSb_{0.045}P_{0.0955}$

Figure 37a shows the direct and indirect band gap of close to 1.7 eV for select $GaSb_{0.03}P_{0.97}$ sample which confirms the band gap reduction due to addition of Sb to the lattice of GaP. Since the direct band gap of GaP is underestimated in the Tauc plot, we

suspect that similar phenomenon occurred for $GaSb_{0.03}P_{0.97}$, however the reduction in the band gap is confirmed. Tauc plot of another sample with 4.5% of antimony is shown in Figure 37b that indicates the direct band gap of 1.8-2.2 eV and indirect band gap of 1.6-1.8 eV for a sample with 4.5% of antimony. Similar to the sample with 3% antimony the band gap energy is decreased in comparison to GaP standard sample.

Using diffuse reflectance spectroscopy and Kubelka-Munk theory to estimate the band gap of material requires precise methods of sample preparation. Ideal samples are packed powders, and the scattering coefficient must be kept constant from sample to sample to perform quantitative diffuse reflectance measurement. For this purpose, two important parameters must remain constant from sample to sample: particle size and sample packing. In addition, there are many assumptions to derive Kubelka-Munk function such as: 1) The thickness of sample should be greater than the penetration depth of the beam to fulfill the infinitely thick sample criteria. 2) size of the particles in the sample should be much smaller than the thickness of sample. 3) To avoid optical effects that are not due to the sample, the sample diameter should be much greater than the focus of the incident beam. Considering all these assumptions and the importance of sample preparation, we can conclude that this method can only give us a rough estimation of band gap and should be employed along with other techniques such as photoluminescence spectroscopy and photocurrent spectroscopy for further information about the band gap energy.

5.2.2 Photoluminescence spectroscopy

Photoluminescence is a contactless and non-destructive method to study the electronic and optical properties of material. In this method, sample is illuminated with a monochromatic light and photoexcitation can occur. Then photoexcited electrons undergo quantized transitions from higher energy levels to empty lower energy levels which could be through radiative or nonradiative recombination (Figure 38). In the radiative recombination, the energy difference between two energy states is emitted as electromagnetic wave and it is called photoluminescence. Studying the PL spectrum of semiconductors provide useful information about the quality, band structure and defect states of these materials.[329, 334, 338]

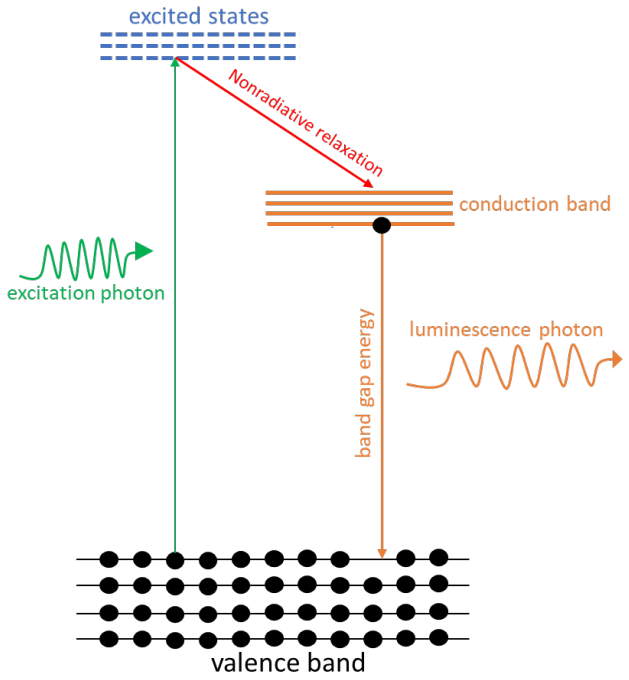

Figure 38. Energy diagram showing photoluminescence emission process

Figure 39 shows the PL spectra of standard commercial GaP wafer at different temperatures. We have measured PL of standard GaP as a control to better understand the spectra of indirect band gap semiconductor.

Excitons play an important role in optical properties of semiconductors. When the incident photon does not have enough energy to excite the electrons from valence band to conduction band, the missing energy can be taken from binding energy of excitons. Consequently, PL peaks of excitons are often dominant at energies just below the band gap. This phenomenon is more detectable at low temperatures, as stable excitons form when the thermal energy of the phonons in the material are lower than binding energy of excitons. As shown in Figure 39, there is a peak at 2.25 eV that increases while the temperature decreases, and it can be attributed to PL peak of excitons just below the indirect band gap of GaP. In addition, the PL peak position can change with the temperature and is described by Varshni equation:

$$E_g(T) = E_g(T = 0K) - \alpha \frac{T^2}{T+\beta} \tag{11}$$

where α and β are materials specific constants. According to equation 11 we expect to see a blue shift in PL peak position while temperature decreases. A slight blue shift in PL peak position of GaP is detected in Figure 39. There is also a peak at 2.7 eV with very low intensity which can show the direct band gap of GaP. However, it does not show a temperature-dependent behavior as expected.

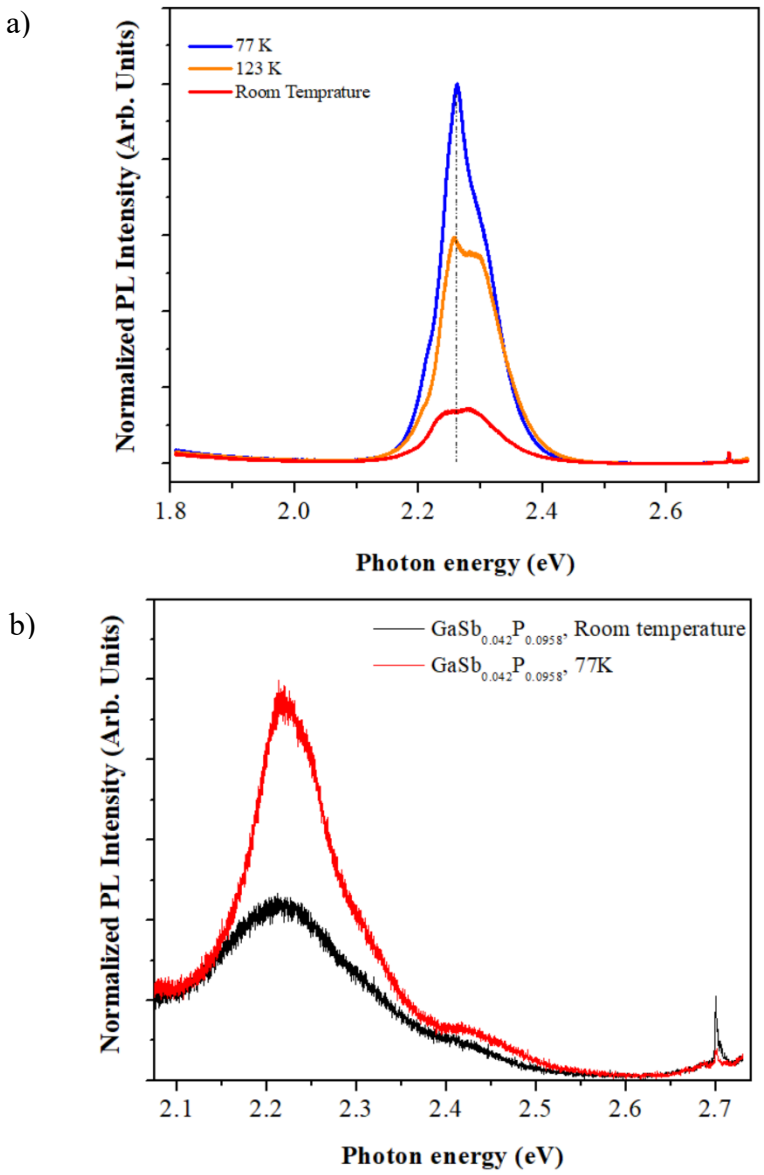

Figure 39. (a) PL spectra of commercial GaP wafer at different temperatures,
(b) PL spectra of select GaSbP sample

Figure 39b shows PL spectra of select $GaSb_{0.042}P_{0.0958}$ sample with a peak at about 2.22 eV increasing at lower temperature. This peak can attribute to PL peak of excitons just below the band gap or direct energy band of $GaSb_{0.042}P_{0.958}$. In a direct gap semiconductor, band gap PL peak increases at low temperatures and shows a blue shift.

Due to the addition of 4.2% of antimony to GaP, we expect to see the indirect to direct transition of band gap although it requires more investigation and complementary measurements to validate this phenomenon. Room temperature PL spectra of another sample of $GaSb_{0.045}P_{0.955}$ is shown in Figure 40. The PL peak at 1.78 eV and lack of peak at 2.7 eV can indicate the indirect to direct band gap transition of this sample that is in accordance with Tauc plot shown in Figure 37b.

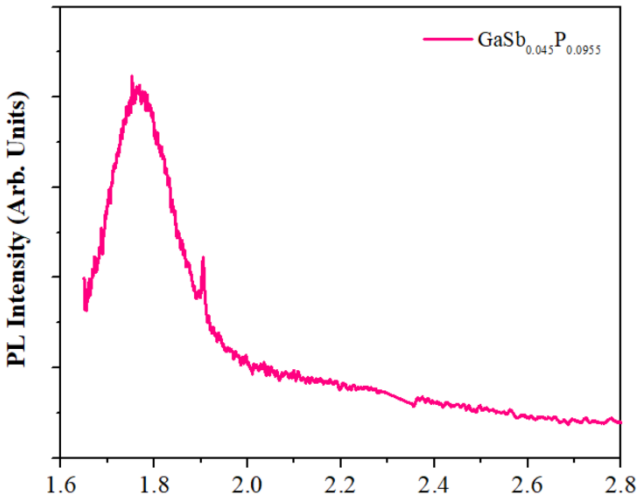

Figure 40. PL spectra of $GaSb_{0.045}P_{0.0955}$

The difference in the PL spectra of sample with 4.2% (Figure 39b) and Figure 40 indicates that the quality of materials grown in HVPE reactor is not very consistent and contribution of Sb to the lattice of GaP may be different in different samples which is predictable due to the complexity of the reactor and various controlling factors. However, these preliminary data on HVPE-grown GaSbP samples shows that this method can be a promising route to synthesize semiconductors with appropriate band gap for solar fuels systems.

5.3 Crystal orientation and Antimony concentration

In order to understand the crystallographic structure and composition of HVPE-grown $GaSb_xP_{(1-x)}$ alloys we have studied them with X-ray diffraction spectroscopy (XRD) (a Bruker Discovery D8 system, with Cu Kα radiation (0.154 nm)). Utilizing the X-ray diffractograms we can get useful information about the crystal orientation, lattice parameter and antimony percentage in the films. In this analysis, we have also measured commercial GaP wafer as a control.

5.3.1 X-ray diffraction analysis

XRD is a technique used for phase identification of crystalline materials and can provide information on unit cell dimensions. This technique could be very useful to study $GaSb_xP_{(1-x)}$ films, since the addition of Sb to the lattice structure of GaP changes the unit cell dimension and consequently the peak positions in X-ray diffractogram are changed. Figure 41 represents the X-ray diffractograms of standard GaP wafer and select samples of $GaSb_xP_{(1-x)}$. Red dashed lines correspond to the peak positions of pure GaP from PDF (00-012-0191) with lattice parameter of 5.448 A°. In the X-ray diffractogram of $GaSb_xP_{(1-x)}$ films, we can observe that there is a set of peaks similar to pure GaP but slightly shifted to lower angles. We know that GaP has cubic zinc blende structure and single crystal commercial GaP shows 2 peaks corresponding to (111) and (222) crystal planes in Figure 41a. Using the Bragg's law and the equation 12 we can calculate the lattice parameter of as-grown $GaSb_xP_{(1-x)}$ samples and compare it with standard GaP lattice parameter. Peak shift to lower angles means that lattice parameter of $GaSb_xP_{(1-x)}$ films are larger than GaP as expected.

$$d_{hkl} = \frac{a}{\sqrt{h^2 + k^2 + l^2}} \tag{12}$$

According to Vegard's law which says that at constant temperature there is a linear relation between the crystal lattice constant of an alloy and the concentrations of the constituent elements (equation 13); we have calculated the antimony concentration in $GaSb_xP_{(1-x)}$ films.[330, 339]

$$a_{GaSb_xP_{(1-x)}} = xa_{GaSb} + (1-x)a_{GaP} \tag{13}$$

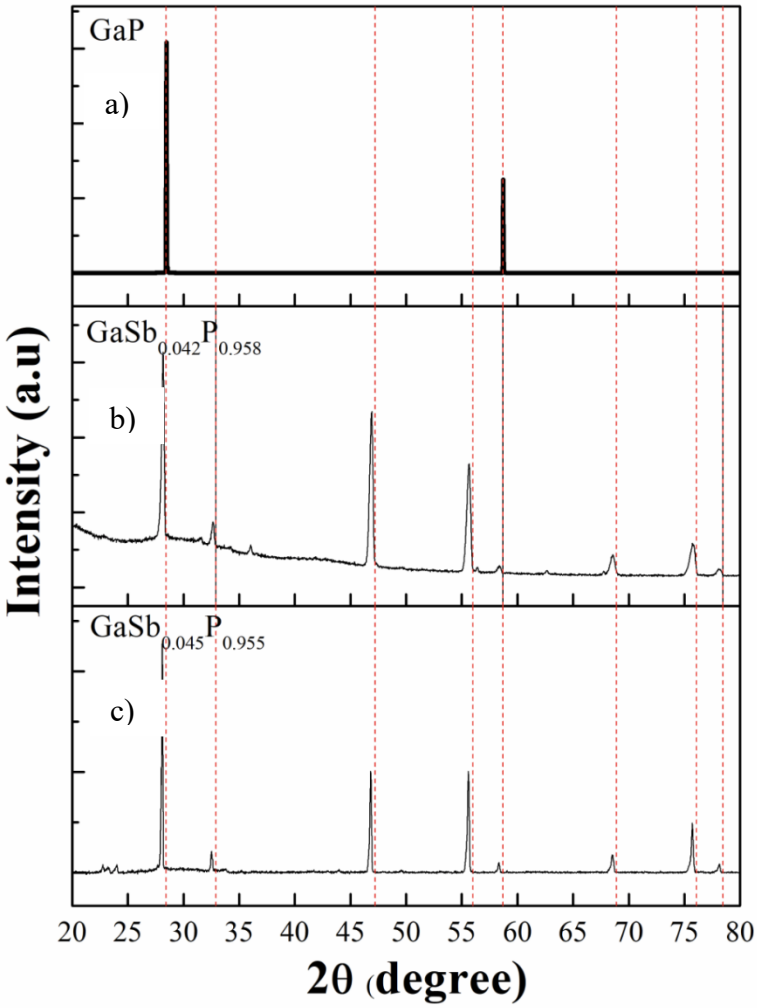

Figure 41. XRD of (a) GaP, (b) $GaSb_{0.042}P_{0.958}$, (c) $GaSb_{0.045}P_{0.955}$

Table 2 shows the peak shift, lattice parameter and Sb concentration calculated for select $GaSb_xP_{(1-x)}$ films. If the peak shifts are due to addition of sb to the lattice, they should be greater at higher angles; we can observe that peak shift increases with angles however there are some exceptions.

Table 2. Sb concentration, lattice parameter, and peaks shift of select GaSbP samples using XRD

sample	Sb concentration (x)	lattice constant (a)	Δθ $GaSb_{0.042}P_{0.958}$	Δθ $GaSb_{0.034}P_{0.965}$
$GaSb_{0.042}P_{0.958}$	4.28	5.480	0.21	0.11
			0.22	0.20
			0.28	0.26
			0.46	0.42
$GaSb_{0.034}P_{0.965}$	3.49	5.475	0.45	0.42
			0.44	0.33
			0.57	0.32
			0.55	0.47

Utilizing Vegard's law can be a useful method to calculate the concentration of Sb contributed to the lattice of III-V alloy, however it should be used preciously, and it can result it wrong interpretations. The peak positions of XRD can be shifted due to displacement of specimen. In this case, the peak shift follows a cosθ behavior, so peak shift might change direction over a large angular range. Some research reports that not all III-V alloys follow the Vegard's law, and the relation between the Sb concentration and lattice parameter may not be perfectly linear which causes error in numbers we have reported.[340]

5.4 SEM/EDS

To study the surface morphology and elemental composition of as-grown $GaSb_xP_{(1-x)}$ films we have used scanning electron microscope (SEM) and energy dispersive X-ray spectroscopy (EDS). Surface of all samples were characterized with TESCAN VEGA3

SB-EASYPROBE SEM and images and elemental mapping result of select samples are discussed.

Figure 42a shows SEM image of the cross section of $GaSb_xP_{(1-x)}$ with x=0.044 (calculated from XRD). We can observe that crystal grain sizes of this sample are 5-10 µm. EDS spectrum and mapping of same spot is shown (Figure 42 b,c,d). The peak at 3.6 KeV conforms the existence of Sb and it is shown in the yellow map that Sb is spread all over the sample. Sharper yellow sections indicate agglomeration of Sb at some spots. Sb concentration utilizing EDS data is 0.0556 which is slightly higher than the number acquired by XRD and it can be the result of more Sn at the surface of samples.

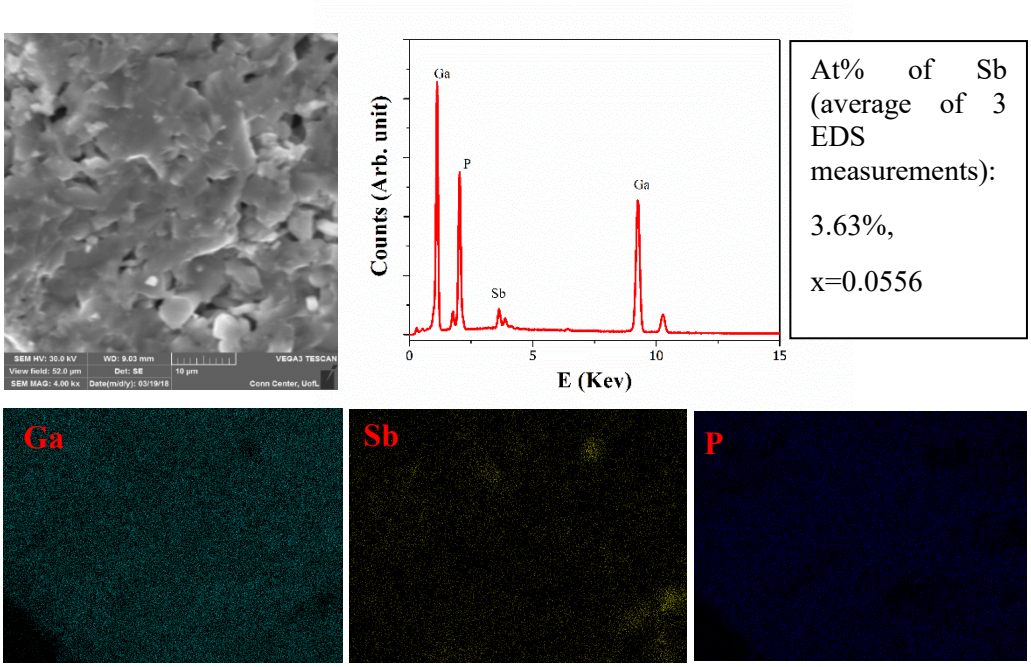

Figure 42. SEM image and EDS mapping of cross section of select $GaSb_{0.044}P_{0.956}$ sample.

SEM and EDS characterization of another $GaSb_xP_{(1-x)}$ sample is shown in Figure 43. Antimony concentration of this sample is determined as x=0.0349 using XRD. Crystal grain sizes of $GaSb_{0.034}P_{0.965}$ are about 5-10 μm and EDS maps shows that sb and P are agglomerated at same spots at surface of sample. Sb concentration is determined as x=0.0304 which is in accordance with XRD data. By analysis of EDS maps of different samples grown in HVPE reactor, we can conclude that Sb and P agglomeration occur at the surface of some samples and growth process needs to be optimized for more uniform and homogenous film growth. However, comparing the antimony concentration acquired by EDS and XRD indicates that Sb contributes to the lattice of GaP and makes a ternary alloy of GaSbP.

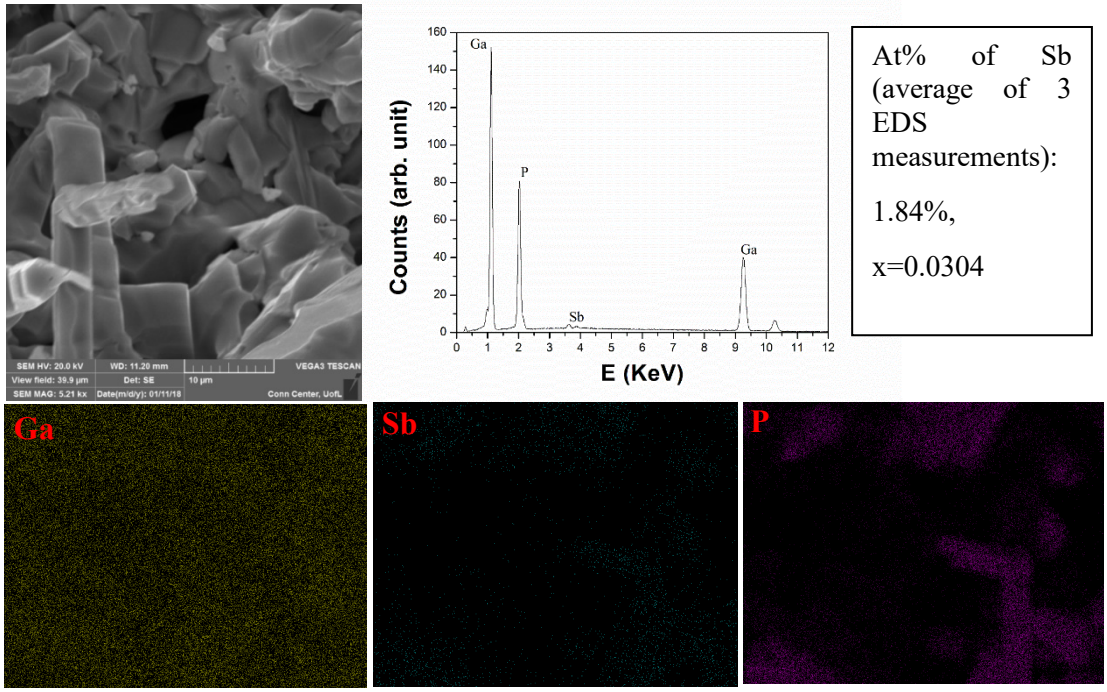

Figure 43. SEM image and EDS mapping of cross section of select $GaSb_{0.034}P_{0.965}$ sample

5.5 Photoelectrochemical measurements

As discussed before, ternary III-V alloys are of great interest for photoelectrochemical water splitting systems. We have investigated the photoelectrochemical behavior of limited number of $GaSb_xP_{(1-x)}$ films as photoanodes in acidic media under chopped 1 sun illumination. These photoanodes are made of free standing $GaSb_xP_{(1-x)}$ films. Ga/In eutectics is applied to the back of the films to form the ohmic contact and then a coiled copper wire is attached to the back of the sample using silver paste as current collector. A Loctite epoxy is utilized to cover the edges and back of the film and define the area of the photoelectrode to be exposed to electrolyte and 1 sun illumination (Figure 44a). According to the current vs potential curves shown in Figure 44b the onset potential for 3 different samples with about the same Sb concentration are between -0.6- to -0.4 V vs RHE and similar to standard n-GaP photoanode. Different onset potential of these samples can be due to different quality of the films, defect states, incorporation of antimony in the lattice and band gap of the alloy. We observe a positive

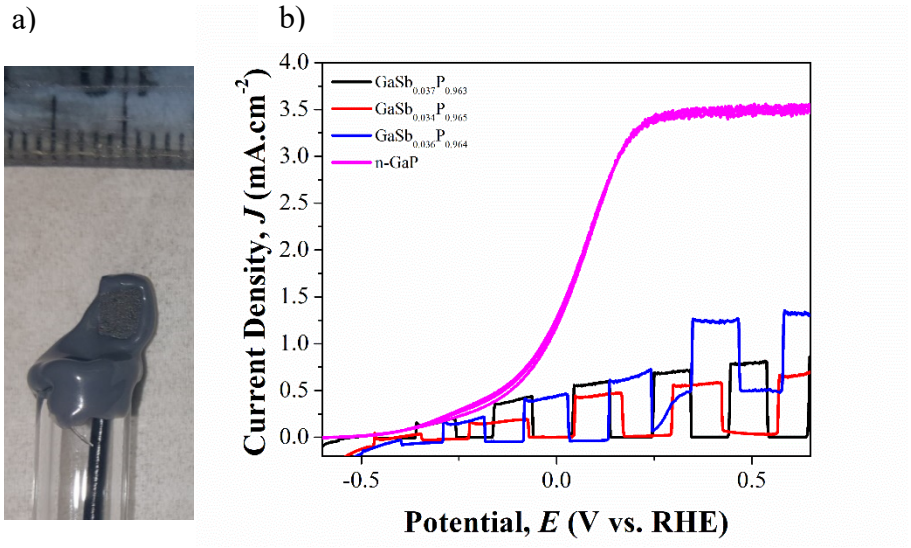

Figure 44. (a) Image of a $GaSb_xP_{(1-x)\ electrode}$, (b) Current vs time behavior of select GaSbP films

current at 0 V applied bias which can be due to oxidation of water (OER) or self-oxidation of sample. We have not performed a corrosion detection measurement for these samples, however based on our corrosion studies on GaAs and GaP we suggest that most part of the photocurrent at 0 V runs the self-oxidation of the sample rather than running the oxygen evolution reaction.[64]

5.6 Hall effect measurement

Hall effect measurement is a well-known method to measure the carrier concentration, carrier type and mobility of materials. This method can be used to characterize a wide range of materials, such as semiconductors. In Hall effect measurement, a uniform current density flows through the material in presence of a perpendicular applied magnetic field and consequently a voltage difference (Hall voltage) is developed perpendicular to the current and magnetic field as shown in Figure 45[341] this measurement can be performed in 2 different common geometries: 1) long, narrow Hall bar and 2) nearly square or circular van der Pauw geometries. Regarding the size and shape of HVPE-grown $GaSb_xP_{(1-x)}$ films, we have used van der Pauw geometry in square shape samples and the NIST method has been followed in all measurements.[342] We have performed this measurement on standard n-GaP as control.

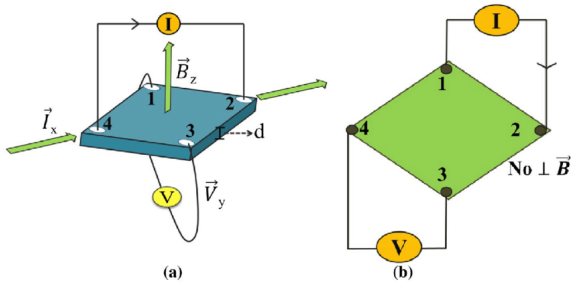

Figure 45. Schematics of Hall effect measurement. (a) van der Pauw geometry. (b) resistivity measurements.[341]

For this measurement, 4 ohmic contacts were deposited on the corners of n-GaP and $GaSb_xP_{(1-x)}$ films with square shape using thermal evaporation of 50 nm of Sn and 100 nm of Au. Then, samples were annealed at 450°C for 30 minutes in nitrogen atmosphere. As shown in Figure 46 samples were mounted on an electrical chip with 4 fine gold wires which are connected to sample using conducting silver paint.

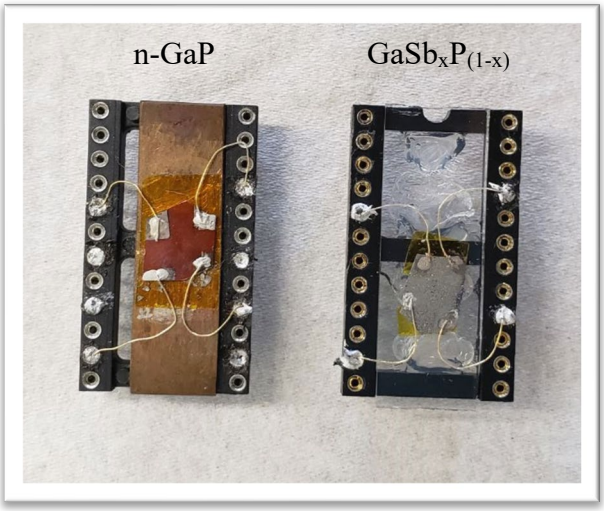

Figure 46. Image of n-GaP and $GaSb_xP_{(1-x)}$ samples mounted on electrical chip for Hall effect measurements.

Electrical properties of standard n-GaP wafer were measured to compare with the numbers reported by the vendor company and literature. Figure 47 shows the resistivity of n-GaP wafer measured at different temperatures. Heating and cooling curve is acquired when sample was under vacuum with 20 μA of current passing 2 adjacent contacts. As we expect for the semiconductors the resistivity of n-GaP has increased exponentially at very low temperatures called freeze out region (inset diagram in Figure 47). With increasing the temperature, the resistivity has decreased but we do not see further decrease in resistivity (intrinsic region) at high temperatures due to high dopant density of the wafer which is $4.1x\ 10^{17}\ cm^{-3}$. For the n-type semiconductors, ionization energy of donors is small, and

electrons are all ionized to the conduction band at room temperature. At low temperatures, the thermal energy becomes too small to cause electron excitation and all of them falls into the donor level and resistivity of samples increase dramatically which we observe in Figure 47. Equation 14 defines the dependence of resistivity to temperature [343]:

$$\log \rho = F(T)\exp\left(\frac{E_d}{2k_B T}\right) \tag{14}$$

Where E_d is the binding energy of donor and we can calculate it by finding the slope of the resistivity vs 1/T curve as shown in Figure 48. Donor binding energy calculated for n-GaP wafer is 0.12 eV which is in accordance with literature.[344]

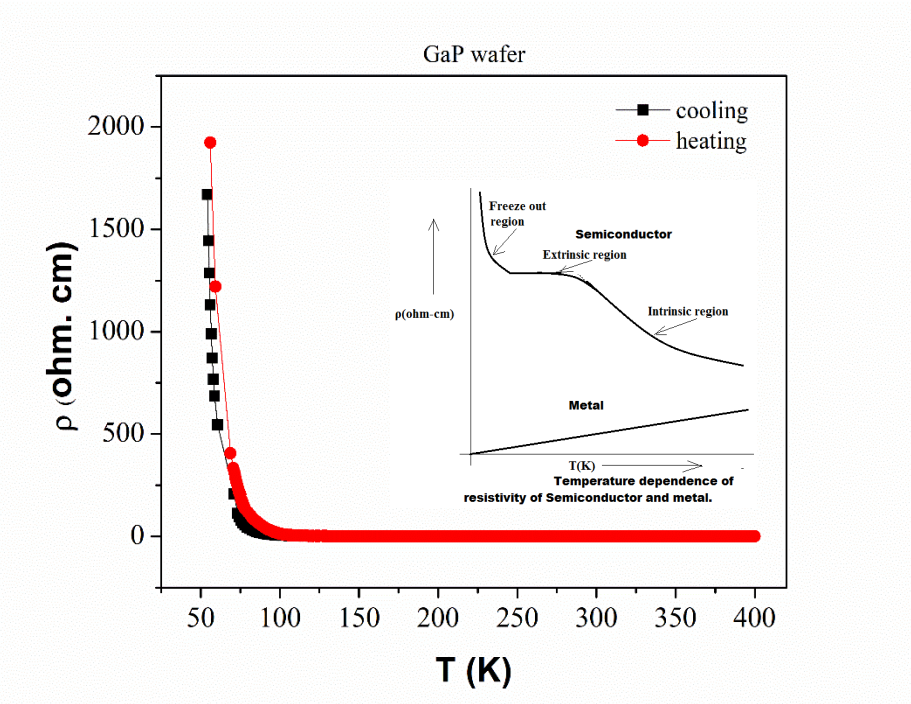

Figure 47. Resistivity vs temperature measurement of n-GaP wafer, inset graph shows the resistivity behavior of a semiconductor at different

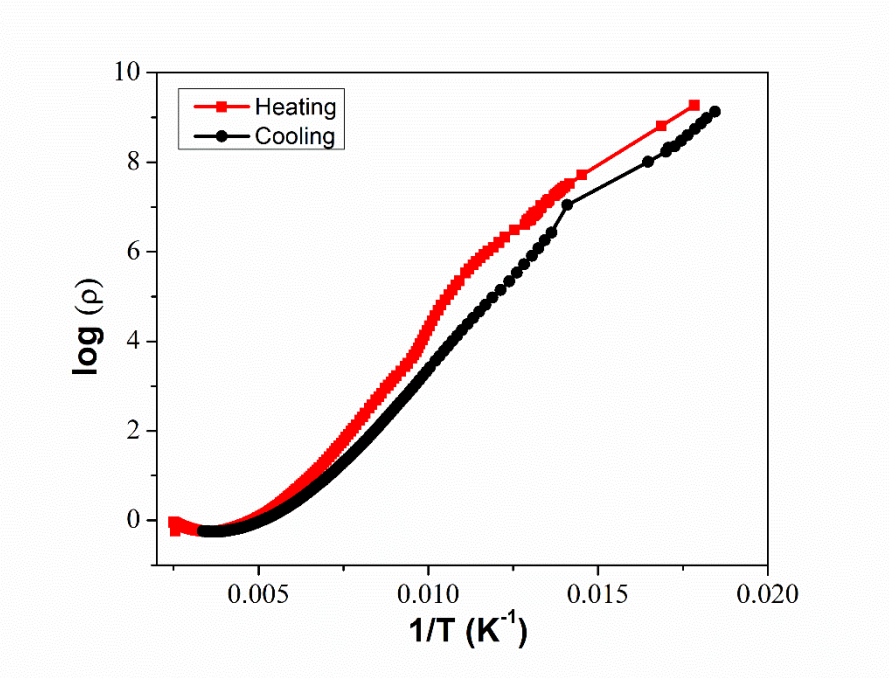

Figure 48. log(ρ) vs 1/T of n-GaP wafer

We also can calculate the mobility of carriers at different temperatures by knowing the dopant density of the commercial n-GaP wafer utilizing the equation 15 and results are shown in Figure 49.

$$\mu_e = \frac{1}{en_d\rho} \tag{15}$$

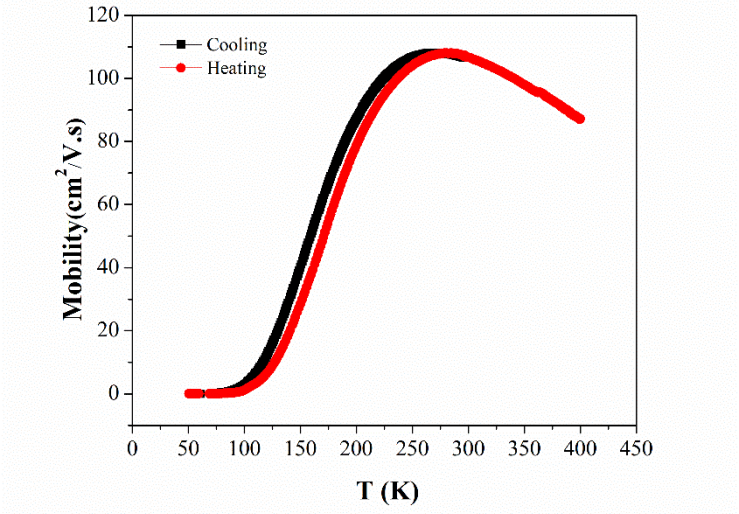

Figure 49. Mobility vs temperature of n-GaP

There are two main types of scattering that affect the mobility of electrons in a semiconductor, 1) lattice scattering and 2) impurity scattering. Lattice vibrations increases at higher temperatures and result in decrease of mobility of electrons. At low temperatures, electrons move slower and have more time to interact with charged impurities and as a result mobility decreases and we see a maximum for n-GaP mobility at about 250 K.[343]

After establishment of our method on 4-point probe measurements we moved on to measure the Hall effect by exposing the sample to a perpendicular magnetic field of 0.52 T. Preparing the HVPE-grown $GaSb_xP_{(1-x)}$ samples for 4-point probe measurements are very challenging due to several reasons: 1) $GaSb_xP_{(1-x)}$ films are very brittle; handling them in thermal evaporation for deposition of ohmic contacts and mounting them on the electrical chip with 4 wires increases the chance of creation of cracks on the film that even may not be visible by eye. 2) deposited Sn/Au ohmic contacts on $GaSb_xP_{(1-x)}$ films are not visible to eye after annealing although we see a clear deposition before annealing the

Figure 50. $GaSb_xP_{(1-x)}$ with 4 thermally evaporated Sn/Au contacts before annealing.

samples at 450°C (Figure 50); Hence we suspect diffusion of Sn and Au particles through the film.

Due to these reasons, we used two commercial standard n-GaP samples that were doped with Sb by thermal diffusion in 500°C for 24 h and 62 h. Samples were prepared at Advanced Energy Materials group in Conn Center. Hall effect measurement was performed on n-GaP and Sb doped n-GaP by passing 10 μA of current through diagonal contacts at presence of perpendicular magnetic field of 0.52 T following the NIST method. Using the resistivity and Hall measurement data we have calculated sheet/bulk resistance, sheet/bulk carrier density and hall mobility. Bulk carrier density reported for standard n-GaP by company is $4.1x10^{17}$ which agrees with numbers acquired in this measurement. The results show that Hall mobility of Sb doped n-GaP is higher than n-GaP and dopant density decreased (Table 3). With the addition of sb to the lattice of the Si doped n-GaP may have introduced some acceptor states (vacancy, defects) and also it might have caused displacement of Si atomes to P sites resulting in dreacreasing of the donor dopant density.

Table 3. Electrical properties of n-GaP and Sb doped n-GaP from Hall measurement

	Sheet Resistance R_s(Ω)	**Bulk Resistivity (Ω.cm)**	**Sheet Carrier Density (n_s)**	**Bulk Carrier Density(cm^{-3})**	**Hall Mobility(cm^2/V.s)**
n-GaP	3.12	0.12	1.37E+16	3.44E+17	145.57
n-GaP(Sb doped for 24h)	14.05	0.56	2.67E+15	6.67E+16	166.57
n-GaP(Sb doped for 62h)	16.04	0.68	1.45E+15	3.62E+16	268.65

Optical measurements on the novel $GaSb_xP_{(1-x)}$ films synthesized by HVPE reactor shows that the band gap of the materials has decreased in comparison with III-V semiconductor

GaP. XRD results on select $GaSb_xP_{(1-x)}$ samples indicate that Sb incorporated in GaP lattice and the lattice parameter is increased due to addition of Sb.

Electrical measurements of sb-doped commercial n-GaP show that mobility of the charge carriers increases with Sb concentration.

Characterization of new materials have always been challenging and conclusive measurements require samples with consistent quality. Growth of III-V semiconductors with HVPE reactor can be a promising alternative for expensive high-quality methods such as metalorganic chemical vapor deposition (MOCVD), however, it still requires improvement to synthesize crystalline III-Vs with consistent quality.

CHAPTER 6

CONCLUSION AND FUTURE DIRECTION

This dissertation is focused on investigation of photocorrosion of gallium based III-V semiconductors. The evolution of the photocorrosion on GaP anodes in acid was studied with a novel spectroelectrochemical in situ UV-Vis absorption technique. n-GaP and P^+-GaP showed different corrosion behaviors. Dissolution rate of Ga and P decreased on illuminated n-GaP while the p^+-GaP electrodes dissolved uniformly. The difference between n- and p^+-GaP corrosion mechanisms, was attributed to anisotropic crystal etching and the semiconductor band energetics which lead to the etching of triangular micropores on the n-GaP surface. ALD-grown TiO_2 protective layer on n-GaP affects the surface etch morphology. Pin holes on protective layer act as corrosion nucleation sites and etch pits undercut the TiO_2 layer end grow into one another over time. Results demonstrated that in situ UV-Vis spectroscopy technique is a versatile and viable tool to study semiconductor photocorrosion, while it is a high-throughput, inexpensive and relatively simple method. One recommendation to improve the method is to find chelating agents to sensitize Ga at different visible light wavelengths for better quantification and deconvolution of electrolyte absorption spectrum.

GaAs is one of the most well-developed and efficient III-V semiconductors, however it suffers from severe corrosion under photoelectrochemical oxidative conditions. We have tested three types of OER co-catalyst Ir layers to investigate their effect on the GaAs photocorrosion. Thin layers of Ir decreased the GaAs dissolution faradaic efficiency to a small degree over the first 15 minutes. Surface etch pits provided a favorable pathway to direct charge to corrosion reaction. Although electroless deposision of Ir provided an uniform thin layer on n-GaAs, the porous nature of the layer left the GaAs surface vulnerable to photocorrosion. The photocorrosion mechanism of III-Vs such GaAs is complex and the pH, crystal orientation, band energetics and the dopant density affect this process. As reported in chapter 4, the current density vs. potential behavior of n-GaAs with increased dopant density ($N_D \sim 10^{18}$ cm^{-3}) is different than n-GaAs with lower dopant density and it shows the beginnings of degenerate behavior and pass significant current to corrosion even in the dark. Thus, protection of III-V semiconductors has still remained one of the difficult challenges of the field. To date, ALD protective coatings of stable materials such as TiO_2 have had the most success, but pinholes remail problematic.

Electrodeposition of metal oxides on corrosion-prone substrates as protective layer and OER catalyst is another method that has been investigated for the stability of photoanodes under alkaline and acidic conditions.[345-346] Some research showed that if the potential required for electrodeposition of metal oxide is smaller than water oxidation potential (1.23 V vs RHE), the system benefits from self-healing process. Re-oxidation of dissolved metal ions in the electrolyte affords a self-repair route for metal oxide film to stay stable during OER. Electrodeposited MnO_2 and Co-OEC on FTO showed self-healing

feature at pH>0 and 5, respectively.[347-348]However, future studies are needed to extend these findings to catalyst nucleation and growth on semiconductor substrates.

As we reported, electroless deposition of Ir on n-GaAs provided a uniform but porous layer which is not sufficient to protect the surface of semiconductor. However, this method can be used to block the pinholes of ALD protective coatings on semiconductors. As noble metal reduction occur at uncovered surface of the semiconductor, this method can potentially block the corrosion nucleation sites (in-situ) and affect the corrosion. It is recommended to study the effect of electroless deposition of iridium or gold (Au) on n-GaAs with protective layer of TiO_2 and investigate the electrochemical dissolution of Ga and As while the sample is kept in electroless deposition bath.

Characterization of HVPE-grown $GaSb_xP_{(1-x)}$ films showed that with incorporation of Sb into the GaP lattice we can alter the band gap of the semiconductor and optimize the band energy edges according to the water splitting system requirements. However deeper investigation and characterization of this novel material is required. It is recommended to stablish the characterization methods on commercial n-GaP samples that are doped with Sb by thermal diffusion method as a better control before moving on to the novel HVPE-grown $GaSb_xP_{(1-x)}$ films. More work on the growth process is required to improve the reproducibility and uniformity of growth. Systematic growth of $GaSb_xP_{(1-x)}$ films with different Sb incorporation can help to gain a better understanding of this material. In addition, we recommend to do a doping dependence study of the properties to find consistent trends which requires controlled, intentional doiping of $GaSb_xP_{(1-x)}$ films during the growth process.

REFERENCES

1. Smil, V., ed., Vol., 2017.
2. Jiang, C.; Moniz, S. J. A.; Wang, A.; Zhang, T.; Tang, J., *Chemical Society Reviews* 2017, *46* (15), 4645-4660.
3. Fujishima, A.; Honda, K., *Nature* 1972, *238* (5358), 37-38.
4. Heller, A., *Accounts of Chemical Research* 1981, *14* (5), 154-162.
5. Turner, J. A., *Science* 1999, *285* (5428), 687.
6. Döscher, H.; Geisz, J. F.; Deutsch, T. G.; Turner, J. A., *Energy & Environmental Science* 2014, *7* (9), 2951-2956.
7. Ager, J. W.; Shaner, M. R.; Walczak, K. A.; Sharp, I. D.; Ardo, S., *Energy & Environmental Science* 2015, *8* (10), 2811-2824.
8. Guo, L.-J.; Luo, J.-W.; He, T.; Wei, S.-H.; Li, S.-S., *Physical Review Applied* 2018, *10* (6), 064059.
9. Li, Z.; Luo, W.; Zhang, M.; Feng, J.; Zou, Z., *Energy & Environmental Science* 2013, *6* (2), 347-370.
10. Walter, M. G.; Warren, E. L.; McKone, J. R.; Boettcher, S. W.; Mi, Q.; Santori, E. A.; Lewis, N. S., *Chemical Reviews* 2010, *110* (11), 6446-6473.
11. Chen, S.; Wang, L.-W., *Chemistry of Materials* 2012, *24* (18), 3659-3666.
12. Nozik, A. J.; Memming, R., *The Journal of Physical Chemistry* 1996, *100* (31), 13061-13078.
13. Matsumoto, Y., *Journal of Solid State Chemistry* 1996, *126* (2), 227-234.
14. Yang, Y.; Niu, S.; Han, D.; Liu, T.; Wang, G.; Li, Y., *Advanced Energy Materials* 2017, *7* (19), 1700555.
15. Geisz, J. F.; France, R. M.; Schulte, K. L.; Steiner, M. A.; Norman, A. G.; Guthrey, H. L.; Young, M. R.; Song, T.; Moriarty, T., *Nature Energy* 2020, *5* (4), 326-335.
16. Tournet, J.; Lee, Y.; Karuturi, S. K.; Tan, H. H.; Jagadish, C., *ACS Energy Letters* 2020, *5* (2), 611-622.
17. Hu, S.; Shaner, M. R.; Beardslee, J. A.; Lichterman, M.; Brunschwig, B. S.; Lewis, N. S., *Science* 2014, *344* (6187), 1005-1009.
18. Hu, S.; Xiang, C.; Haussener, S.; Berger, A. D.; Lewis, N. S., *Energy & Environmental Science* 2013, *6* (10), 2984-2993.
19. Khaselev, O.; Turner, J. A., *Science* 1998, *280* (5362), 425.
20. Young, J. L.; Steiner, M. A.; Döscher, H.; France, R. M.; Turner, J. A.; Deutsch, Todd G., *Nature Energy* 2017, *2* (4), 17028.
21. Wang, Y.; Schwartz, J.; Gim, J.; Hovden, R.; Mi, Z., *ACS Energy Letters* 2019, *4* (7), 1541-1548.

22. Cheng, W.-H.; Richter, M. H.; May, M. M.; Ohlmann, J.; Lackner, D.; Dimroth, F.; Hannappel, T.; Atwater, H. A.; Lewerenz, H.-J., *ACS Energy Letters* 2018, *3* (8), 1795-1800.
23. Scheuermann, A. G.; Prange, J. D.; Gunji, M.; Chidsey, C. E.; McIntyre, P. C., *Energy & Environmental Science* 2013, *6* (8), 2487-2496.
24. Chen, Y. W.; Prange, J. D.; Dühnen, S.; Park, Y.; Gunji, M.; Chidsey, C. E.; McIntyre, P. C., *Nature materials* 2011, *10* (7), 539-544.
25. Verlage, E.; Hu, S.; Liu, R.; Jones, R. J. R.; Sun, K.; Xiang, C.; Lewis, N. S.; Atwater, H. A., *Energy & Environmental Science* 2015, *8* (11), 3166-3172.
26. Britto, R. J.; Benck, J. D.; Young, J. L.; Hahn, C.; Deutsch, T. G.; Jaramillo, T. F., *The Journal of Physical Chemistry Letters* 2016, *7* (11), 2044-2049.
27. Ben-Naim, M.; Britto, R. J.; Aldridge, C. W.; Mow, R.; Steiner, M. A.; Nielander, A. C.; King, L. A.; Friedman, D. J.; Deutsch, T. G.; Young, J. L.; Jaramillo, T. F., *ACS Energy Letters* 2020, *5* (8), 2631-2640.
28. Jiang, C.; Wu, J.; Moniz, S. J. A.; Guo, D.; Tang, M.; Jiang, Q.; Chen, S.; Liu, H.; Wang, A.; Zhang, T.; Tang, J., *Sustainable Energy & Fuels* 2019, *3* (3), 814-822.
29. Yang, F.; Nielander, A. C.; Grimm, R. L.; Lewis, N. S., *The Journal of Physical Chemistry C* 2016, *120* (13), 6989-6995.
30. Xu, Y.; Ahmed, R.; Zheng, J.; Hoglund, E. R.; Lin, Q.; Berretti, E.; Lavacchi, A.; Zangari, G., *Small* 2020, *16* (39), 2003112.
31. Kamimura, J.; Budde, M.; Bogdanoff, P.; Tschammer, C.; Abdi, F. F.; van de Krol, R.; Bierwagen, O.; Riechert, H.; Geelhaar, L., *Solar RRL* 2020, 2000568.
32. Pourbaix, M., Pergamon Press: Oxford, 1966.
33. Persson, K. A.; Waldwick, B.; Lazic, P.; Ceder, G., *Physical Review B* 2012, *85* (23), 235438.
34. Weng, B.; Qi, M. Y.; Han, C.; Tang, Z. R.; Xu, Y. J., *ACS Catal.* 2019, *9* (5), 4642-4687.
35. Chen, S.; Huang, D. L.; Xu, P. A.; Xue, W. J.; Lei, L.; Cheng, M.; Wang, R. Z.; Liu, X. G.; Deng, R., *J. Mater. Chem. A* 2020, *8* (5), 2286-2322.
36. Chen, S. Y.; Wang, L. W., *Chem. Mater.* 2012, *24* (18), 3659-3666.
37. Walter, M. G.; Warren, E. L.; McKone, J. R.; Boettcher, S. W.; Mi, Q. X.; Santori, E. A.; Lewis, N. S., *Chem. Rev.* 2010, *110* (11), 6446-6473.
38. Chen, Y. W.; Prange, J. D.; Duehnen, S.; Park, Y.; Gunji, M.; Chidsey, C. E. D.; McIntyre, P. C., *Nature Materials* 2011, *10* (7), 539-544.
39. Liu, R.; Zheng, Z.; Spurgeon, J.; Yang, X., *Energy Environ. Sci.* 2014, *7* (8), 2504-2517.
40. Hu, S.; Lewis, N. S.; Ager, J. W.; Yang, J. H.; McKone, J. R.; Strandwitz, N. C., *J. Phys. Chem. C* 2015, *119* (43), 24201-24228.
41. Lichterman, M. F.; Shaner, M. R.; Handler, S. G.; Brunschwig, B. S.; Gray, H. B.; Lewis, N. S.; Spurgeon, J. M., *J. Phys. Chem. Lett.* 2013, *4* (23), 4188-4191.
42. Wong, K. T.; Lewis, N. S., *Acc. Chem. Res.* 2014, *47* (10), 3037-3044.
43. Buriak, J., *Chem. Rev.* 2002, *102* (5), 1271-1308.
44. Tan, M. X.; Laibinis, P. E.; Nguyen, S. T.; Kesselman, J. M.; Stanton, C. E.; Lewis, N. S., In *Progress in Inorganic Chemistry, Vol 41*ed., Vol. 41, 1994, pp 21-144.
45. Lang, D.; Xiang, Q. J.; Qiu, G. H.; Feng, X. H.; Liu, F., *Dalton Transactions* 2014, *43* (19), 7245-7253.

46. Li, W.; Sheehan, S. W.; He, D.; He, Y. M.; Yao, X. H.; Grimm, R. L.; Brudvig, G. W.; Wang, D. W., *Angew. Chem.-Int. Edit.* 2015, *54* (39), 11428-11432.
47. Xie, Y. P.; Yu, Z. B.; Liu, G.; Ma, X. L.; Cheng, H. M., *Energy Environ. Sci.* 2014, *7* (6), 1895-1901.
48. McCrory, C. C. L.; Jung, S.; Ferrer, I. M.; Chatman, S. M.; Peters, J. C.; Jaramillo, T. F., *J. Am. Chem. Soc.* 2015, *137* (13), 4347-4357.
49. Moreno-Hernandez, I. A.; MacFarland, C. A.; Read, C. G.; Papadantonakis, K. M.; Brunschwig, B. S.; Lewis, N. S., *Energy Environ. Sci.* 2017, *10* (10), 2103-2108.
50. Kumari, S.; Ajayi, B. P.; Kumar, B.; Jasinski, J. B.; Sunkara, M. K.; Spurgeon, J. M., *Energy Environ. Sci.* 2017, *10* (11), 2432-2440.
51. Kwong, W. L.; Lee, C. C.; Shchukarev, A.; Bjorn, E.; Messinger, J., *J. Catal.* 2018, *365*, 29-35.
52. Pishgar, S.; Strain, J. M.; Gulati, S.; Sumanasekera, G.; Gupta, G.; Spurgeon, J. M., *J. Mater. Chem. A* 2019, *7* (44), 25377-25388.
53. Gulati, S.; Hietsoi, O.; Calvary, C. A.; Strain, J. M.; Pishgar, S.; Brun, H. C.; Grapperhaus, C. A.; Buchanan, R. M.; Spurgeon, J. M., *Chem. Commun.* 2019, *55* (64), 9440-9443.
54. Ben-Naim, M.; Palm, D. W.; Strickler, A. L.; Nielander, A. C.; Sanchez, J.; King, L. A.; Higgins, D. C.; Jaramillo, T. F., *ACS Appl. Mater. Interfaces* 2020, *12* (5), 5901-5908.
55. Chen, X. G.; He, Y. Q.; Zhang, Q.; Li, L. J.; Hu, D. H.; Yin, T., *J. Mater. Sci.* 2010, *45* (4), 953-960.
56. Tan, C. S.; Kemp, K. W.; Braun, M. R.; Meng, A. C.; Tan, W. L.; Chidsey, C. E. D.; Ma, W.; Moghadam, F.; McIntyre, P. C., *Sustain. Energ. Fuels* 2019, *3* (6), 1490-1500.
57. Lichterman, M. F.; Sun, K.; Hu, S.; Zhou, X. H.; McDowell, M. T.; Shaner, M. R.; Richter, M. H.; Crumlin, E. J.; Carim, A. I.; Saadi, F. H.; Brunschwig, B. S.; Lewis, N. S., *Catal. Today* 2016, *262*, 11-23.
58. Mandal, D.; Hamann, T. W., *PCCP* 2015, *17* (17), 11156-11160.
59. Su, L. Y.; Dai, Q.; Lu, Z. H., *Spectrochim Acta A* 1999, *55* (11), 2179-2185.
60. Boras, C. A.; Romagnoli, R.; Lezna, R. O., *Electrochim. Acta* 2000, *45* (11), 1717-1725.
61. Itagaki, M.; Hori, F.; Watanabe, K., *Anal. Sci.* 2000, *16* (4), 371-375.
62. Yi, Y. M.; Weinberg, G.; Prenzel, M.; Greiner, M.; Heumann, S.; Becker, S.; Schlogl, R., *Catal. Today* 2017, *295*, 32-40.
63. Li, Y.; He, J. B.; Zhang, M.; He, X. L., *Corros. Sci.* 2013, *74*, 116-122.
64. Pishgar, S.; Strain, J. M.; Gulati, S.; Sumanasekera, G.; Gupta, G.; Spurgeon, J. M., *Journal of Materials Chemistry A* 2019, *7* (44), 25377-25388.
65. Klahr, B.; Hamann, T., *J. Phys. Chem. C* 2014, *118* (19), 10393-10399.
66. Siegbahn, H., *J. Phys. Chem.* 1985, *89* (6), 897-909.
67. Axnanda, S.; Crumlin, E. J.; Mao, B. H.; Rani, S.; Chang, R.; Karlsson, P. G.; Edwards, M. O. M.; Lundqvist, M.; Moberg, R.; Ross, P.; Hussain, Z.; Liu, Z., *Scientific Reports* 2015, *5*, 09788.
68. Moberg, R.; Bokman, F.; Bohman, O.; Siegbahn, H. O. G., *J. Am. Chem. Soc.* 1991, *113* (10), 3663-3667.

69. Moberg, R.; Bokman, F.; Bohman, O.; Siegbahn, H. O. G., *J. Chem. Phys.* 1991, *94* (7), 5226-5232.
70. Siegbahn, H.; Lundholm, M., *J. Electron. Spectrosc. Relat. Phenom.* 1982, *28* (2), 135-138.
71. Siegbahn, H.; Svensson, S.; Lundholm, M., *Journal of Electron Spectroscopy and Related Phenomena* 1981, *24* (2), 205-213.
72. Aulich, H.; Nemec, L.; Chia, L.; Delahay, P., *J. Electron. Spectrosc. Relat. Phenom.* 1976, *8* (4), 271-289.
73. Nemec, L.; Gaehrs, H. J.; Chia, L.; Delahay, P., *J. Chem. Phys.* 1977, *66* (10), 4450-4458.
74. Ballard, R. E.; Gunnell, G. G.; Hagan, W. P., *J. Electron. Spectrosc. Relat. Phenom.* 1979, *16* (6), 435-440.
75. Joyner, R. W.; Roberts, M. W.; Yates, K., *Surf. Sci.* 1979, *87* (2), 501-509.
76. Watanabe, I.; Flanagan, J. B.; Delahay, P., *J. Chem. Phys.* 1980, *73* (5), 2057-2062.
77. Ruppender, H. J.; Grunze, M.; Kong, C. W.; Wilmers, M., *Surf. Interface Anal.* 1990, *15* (4), 245-253.
78. Starr, D. E.; Liu, Z.; Havecker, M.; Knop-Gericke, A.; Bluhm, H., *Chem. Soc. Rev.* 2013, *42* (13), 5833-5857.
79. Bluhm, H.; Andersson, K.; Araki, T.; Benzerara, K.; Brown, G. E.; Dynes, J. J.; Ghosal, S.; Gilles, M. K.; Hansen, H. C.; Hemminger, J. C.; Hitchcock, A. P.; Ketteler, G.; Kilcoyne, A. L. D.; Kneedler, E.; Lawrence, J. R.; Leppard, G. G.; Majzlan, J.; Mun, B. S.; Myneni, S. C. B.; Nilsson, A.; Ogasawara, H.; Ogletree, D. F.; Pecher, K.; Salmeron, M.; Shuh, D. K.; Tonner, B.; Tyliszczak, T.; Warwick, T.; Yoon, T. H., *J. Electron. Spectrosc. Relat. Phenom.* 2006, *150* (2-3), 86-104.
80. Ogletree, D. F.; Bluhm, H.; Hebenstreit, E. D.; Salmeron, M., *Nucl. Instrum. Methods Phys. Res. Sect. A-Accel. Spectrom. Dect. Assoc. Equip.* 2009, *601* (1-2), 151-160.
81. Grass, M. E.; Karlsson, P. G.; Aksoy, F.; Lundqvist, M.; Wannberg, B.; Mun, B. S.; Hussain, Z.; Liu, Z., *Rev. Sci. Instrum.* 2010, *81* (5), 053106.
82. Ogletree, D. F.; Bluhm, H.; Lebedev, G.; Fadley, C. S.; Hussain, Z.; Salmeron, M., *Rev. Sci. Instrum.* 2002, *73* (11), 3872-3877.
83. Yamamoto, S.; Bluhm, H.; Andersson, K.; Ketteler, G.; Ogasawara, H.; Salmeron, M.; Nilsson, A., *J. Phys.-Condes. Matter* 2008, *20* (18).
84. Miller, D. J.; Oberg, H.; Kaya, S.; Casalongue, H. S.; Friebel, D.; Anniyev, T.; Ogasawara, H.; Bluhm, H.; Pettersson, L. G. M.; Nilsson, A., *Phys. Rev. Lett.* 2011, *107* (19), 195502.
85. Salmeron, M.; Schlogl, R., *Surface Science Reports* 2008, *63* (4), 169-199.
86. Crumlin, E. J.; Bluhm, H.; Liu, Z., *J. Electron. Spectrosc. Relat. Phenom.* 2013, *190*, 84-92.
87. Takagi, Y.; Wang, H.; Uemura, Y.; Ikenaga, E.; Sekizawa, O.; Uruga, T.; Ohashi, H.; Senba, Y.; Yumoto, H.; Yamazaki, H.; Goto, S.; Tada, M.; Iwasawa, Y.; Yokoyama, T., *Appl. Phys. Lett.* 2014, *105* (13).
88. Takagi, Y.; Uruga, T.; Tada, M.; Iwasawa, Y.; Yokoyama, T., *Acc. Chem. Res.* 2018, *51* (3), 719-727.

89. Lichterman, M. F.; Richter, M. H.; Hu, S.; Crumlin, E. J.; Axnanda, S.; Favaro, M.; Drisdell, W.; Hussain, Z.; Brunschwig, B. S.; Lewis, N. S.; Liu, Z.; Lewerenz, H. J., *J. Electrochem. Soc.* 2016, *163* (2), H139-H146.
90. Lichterman, M. F.; Richter, M. H.; Brunschwig, B. S.; Lewis, N. S.; Lewerenz, H. J., *J. Electron. Spectrosc. Relat. Phenom.* 2017, *221*, 99-105.
91. Favaro, M.; Yang, J. H.; Nappini, S.; Magnano, E.; Toma, F. M.; Crumlin, E. J.; Yano, J.; Sharp, I. D., *J. Am. Chem. Soc.* 2017, *139* (26), 8960-8970.
92. Lichterman, M. F.; Hu, S.; Richter, M. H.; Crumlin, E. J.; Axnanda, S.; Favaro, M.; Drisdell, W.; Hussain, Z.; Mayer, T.; Brunschwig, B. S.; Lewis, N. S.; Liu, Z.; Lewerenz, H. J., *Energy Environ. Sci.* 2015, *8* (8), 2409-2416.
93. Lewerenz, H. J.; Lichterman, M. F.; Richter, M. H.; Crumlin, E. J.; Hu, S.; Axnanda, S.; Favaro, M.; Drisdell, W.; Hussain, Z.; Brunschwig, B. S.; Liu, Z.; Nilsson, A.; Bell, A. T.; Lewis, N. S.; Friebel, D., *Electrochim. Acta* 2016, *211*, 711-719.
94. Ali-Loytty, H.; Louie, M. W.; Singh, M. R.; Li, L.; Casalongue, H. G. S.; Ogasawara, H.; Crumlin, E. J.; Liu, Z.; Bell, A. T.; Nilsson, A.; Friebel, D., *J. Phys. Chem. C* 2016, *120* (4), 2247-2253.
95. Zhang, X. Q.; Ptasinska, S., *Top. Catal.* 2016, *59* (5-7), 564-573.
96. Zhang, X. Q.; Ptasinska, S., *PCCP* 2015, *17* (5), 3909-3918.
97. Favaro, M.; Abdi, F. F.; Lamers, M.; Crumlin, E. J.; Liu, Z.; van de Krol, R.; Starr, D. E., *J. Phys. Chem. B* 2018, *122* (2), 801-809.
98. Starr, D. E.; Favaro, M.; Abdi, F. F.; Bluhm, H.; Crumlin, E. J.; van de Krol, R., *J. Electron. Spectrosc. Relat. Phenom.* 2017, *221*, 106-115.
99. Schlucker, S., *Angew. Chem.-Int. Edit.* 2014, *53* (19), 4756-4795.
100. Joya, K. S.; Sala, X., *PCCP* 2015, *17* (33), 21094-21103.
101. Fleischmann, M.; Hendra, P. J.; McQuillan, A. J., *Chem. Phys. Lett.* 1974, *26* (2), 163-166.
102. Pettinger, B.; Schambach, P.; Villagomez, C. J.; Scott, N., In *An. Rev. Phys. Chem.*ed., Vol. 63; Johnson, M. A.; Martinez, T. J., Eds., 2012, pp 379-399.
103. Efremov, E. V.; Ariese, F.; Gooijer, C., *Anal. Chim. Acta* 2008, *606* (2), 119-134.
104. Prince, R. C.; Frontiera, R. R.; Potma, E. O., *Chem. Rev.* 2017, *117* (7), 5070-5094.
105. Buckley, K.; Matousek, P., *J. Pharm. Biomed. Anal.* 2011, *55* (4), 645-652.
106. Langer, J.; de Aberasturi, D. J.; Aizpurua, J.; Alvarez-Puebla, R. A.; Auguie, B.; Baumberg, J. J.; Bazan, G. C.; Bell, S. E. J.; Boisen, A.; Brolo, A. G.; Choo, J.; Cialla-May, D.; Deckert, V.; Fabris, L.; Faulds, K.; de Abajo, F. J. G.; Goodacre, R.; Graham, D.; Haes, A. J.; Haynes, C. L.; Huck, C.; Itoh, T.; Ka, M.; Kneipp, J.; Kotov, N. A.; Kuang, H.; Le Ru, E. C.; Lee, H. K.; Li, J. F.; Ling, X. Y.; Maier, S. A.; Mayerhofer, T.; Moskovits, M.; Murakoshi, K.; Nam, J. M.; Nie, S.; Ozaki, Y.; Pastoriza-Santos, I.; Perez-Juste, J.; Popp, J.; Pucci, A.; Reich, S.; Ren, B.; Schatz, G. C.; Shegai, T.; Schlucker, S.; Tay, L. L.; Thomas, K. G.; Tian, Z. Q.; Van Duyne, R. P.; Vo-Dinh, T.; Wang, Y.; Willets, K. A.; Xu, C.; Xu, H.; Xu, Y.; Yamamoto, Y. S.; Zhao, B.; Liz-Marzan, L. M., *ACS Nano* 2020, *14* (1), 28-117.
107. Ren, B.; Li, X. Q.; She, C. X.; Wu, D. Y.; Tian, Z. Q., *Electrochim. Acta* 2000, *46* (2-3), 193-205.
108. Tang, F.; Liu, T.; Jiang, W. L.; Gan, L., *J. Electroanal. Chem.* 2020, *871*.

109. Zeng, Z. C.; Hu, S.; Huang, S. C.; Zhang, Y. J.; Zhao, W. X.; Li, J. F.; Jiang, C. Y.; Ren, B., *Anal. Chem.* 2016, *88* (19), 9381-9385.
110. Deng, Y. L.; Yeo, B. S., *ACS Catal.* 2017, *7* (11), 7873-7889.
111. Deng, Y. L.; Handoko, A. D.; Du, Y. H.; Xi, S. B.; Yeo, B. S., *ACS Catal.* 2016, *6* (4), 2473-2481.
112. Pavlovic, Z.; Rajan, C.; Gao, Q.; van Gastel, M.; Schlogl, R., *ACS Catal.* 2016, *6* (12), 8098-8105.
113. Yeo, B. S.; Bell, A. T., *J. Am. Chem. Soc.* 2011, *133* (14), 5587-5593.
114. Li, Y. M.; Nakamura, R., *Chin. J. Catal.* 2018, *39* (3), 401-406.
115. Schmitt, K. G.; Gewirth, A. A., *J. Phys. Chem. C* 2014, *118* (31), 17567-17576.
116. Jiang, S.; Klingan, K.; Pasquini, C.; Dau, H., *J. Chem. Phys.* 2019, *150* (4).
117. Dutta, A.; Kuzume, A.; Rahaman, M.; Vesztergom, S.; Broekmann, P., *ACS Catal.* 2015, *5* (12), 7498-7502.
118. Sherif, E. M.; Erasmus, R. M.; Comins, J. D., *Electrochim. Acta* 2010, *55* (11), 3657-3663.
119. Chen, L.; Yang, J. H.; Klaus, S.; Lee, L. J.; Woods-Robinson, R.; Ma, J.; Lum, Y.; Cooper, J. K.; Toma, F. M.; Wang, L. W.; Sharp, I. D.; Bell, A. T.; Ager, J. W., *J. Am. Chem. Soc.* 2015, *137* (30), 9595-9603.
120. Muthmann, S.; Kohler, F.; Meier, M.; Hulsbeck, M.; Carius, R.; Gordijn, A., *Phys. Status Solidi-Rapid Res. Lett.* 2011, *5* (4), 144-146.
121. Rigby, S. J.; Al-Obaidi, A. H. R.; Lee, S. K.; McStay, D.; Robertson, P. K. J., *Appl. Surf. Sci.* 2006, *252* (22), 7948-7952.
122. Wang, D. L.; Cao, Y. S.; Wan, L., *J. Mater. Res.* 2009, *24* (7), 2373-2377.
123. Awadallah, O.; Cheng, Z., *Sol. Energy Mater. Sol. Cells* 2018, *176*, 222-229.
124. Liao, M. L.; Shan, B. B.; Li, M., *J. Phys. Chem. Lett.* 2019, *10* (6), 1217-1225.
125. Ma, L. J.; Liu, M. C.; Jing, D. W.; Guo, L. J., *J. Mater. Chem. A* 2015, *3* (10), 5701-5707.
126. Balog, A.; Samu, G. F.; Kamat, P. V.; Janaky, C., *J. Phys. Chem. Lett.* 2019, *10* (2), 259-264.
127. Sourisseau, C.; Cruege, F.; Gorochov, O., *J. Electroanal. Chem.* 1991, *308* (1-2), 239-253.
128. Detacconi, N. R.; Myung, N.; Rajeshwar, K., *J. Phys. Chem.* 1995, *99* (16), 6103-6109.
129. Gatzke, C.; Webb, S. J.; Fobelets, K.; Stradling, R. A., *Semicond. Sci. Technol.* 1998, *13* (4), 399-403.
130. Profrock, D.; Prange, A., *Appl. Spectrosc.* 2012, *66* (8), 843-868.
131. Kasian, O.; Geiger, S.; Mayrhofer, K. J. J.; Cherevko, S., *Chem. Rec.* 2019, *19* (10), 2130-2142.
132. Choi, C. H.; Baldizzone, C.; Grote, J. P.; Schuppert, A. K.; Jaouen, F.; Mayrhofer, K. J. J., *Angew. Chem.-Int. Edit.* 2015, *54* (43), 12753-12757.
133. Lee, W. H.; Nong, H. N.; Choi, C. H.; Chae, K. H.; Hwang, Y. J.; Min, B. K.; Strasser, P.; Oh, H. S., *Applied Catalysis B-Environmental* 2020, *269*.
134. Ahluwalia, R. K.; Papadias, D. D.; Kariuki, N. N.; Peng, J. K.; Wang, X. P.; Tsai, Y. F.; Graczyk, D. G.; Myers, D. J., *J. Electrochem. Soc.* 2018, *165* (6), F3024-F3035.

135. Hodnik, N.; Jovanovic, P.; Pavlisic, A.; Jozinovic, B.; Zorko, M.; Bele, M.; Selih, V. S.; Sala, M.; Hocevar, S.; Gaberscek, M., *J. Phys. Chem. C* 2015, *119* (18), 10140-10147.
136. Hochstrasser-Kurz, S.; Reiss, D.; Suter, T.; Latkoczy, C.; Gunther, D.; Virtanen, S.; Uggowitzer, P. J.; Schmutz, P., *J. Electrochem. Soc.* 2008, *155* (8), C415-C426.
137. Klemm, S. O.; Topalov, A. A.; Laska, C. A.; Mayrhofer, K. J. J., *Electrochem. Commun.* 2011, *13* (12), 1533-1535.
138. Ranninger, J.; Wachs, S. J.; Moller, J.; Mayrhofer, K. J. J.; Berkes, B. B., *Electrochem. Commun.* 2020, *114*.
139. Cherevko, S.; Geiger, S.; Kasian, O.; Kulyk, N.; Grote, J. P.; Savan, A.; Shrestha, B. R.; Merzlikin, S.; Breitbach, B.; Ludwig, A.; Mayrhofer, K. J. J., *Catal. Today* 2016, *262*, 170-180.
140. Jovanovic, P.; Hodnik, N.; Ruiz-Zepeda, F.; Arcon, I.; Jozinovic, B.; Zorko, M.; Bele, M.; Sala, M.; Selih, V. S.; Hocevar, S.; Gaberscek, M., *J. Am. Chem. Soc.* 2017, *139* (36), 12837-12846.
141. Weber, T.; Ortmann, T.; Escalera-Lopez, D.; Abb, M. J. S.; Mogwitz, B.; Cherevko, S.; Rohnke, M.; Over, H., *ChemCatChem* 2020, *12* (3), 855-866.
142. Schalenbach, M.; Speck, F. D.; Ledendecker, M.; Kasian, O.; Goehl, D.; Mingers, A. M.; Breitbach, B.; Springer, H.; Cherevko, S.; Mayrhofer, K. J. J., *Electrochim. Acta* 2018, *259*, 1154-1161.
143. Speck, F. D.; Cherevko, S., *Electrochem. Commun.* 2020, *115*.
144. Knoppel, J.; Zhang, S. Y.; Specle, F. D.; Mayrhofer, K. J. J.; Scheu, C.; Cherevko, S., *Electrochem. Commun.* 2018, *96*, 53-56.
145. Zhang, S. Y.; Rohloff, M.; Kasian, O.; Mingers, A. M.; Mayrhofer, K. J. J.; Fischer, A.; Scheu, C.; Cherevko, S., *J. Phys. Chem. C* 2019, *123* (38), 23410-23418.
146. Clark, E. L.; Bell, A. T., *J. Am. Chem. Soc.* 2018, *140* (22), 7012-7020.
147. Baltruschat, H., *J. Am. Soc. Mass. Spectrom.* 2004, *15* (12), 1693-1706.
148. Herl, T.; Matysik, F. M., *Chemelectrochem* 2020, *7* (12), 2498-2512.
149. Oberacher, H.; Pitterl, F.; Erb, R.; Plattner, S., *Mass Spectrom. Rev.* 2015, *34* (1), 64-92.
150. Moller, S.; Barwe, S.; Masa, J.; Wintrich, D.; Seisel, S.; Baltruschat, H.; Schuhmann, W., *Angew. Chem.-Int. Edit.* 2020, *59* (4), 1585-1589.
151. Ashton, S. J.; Arenz, M., *J. Power Sources* 2012, *217*, 392-399.
152. Klein, F.; Pinedo, R.; Berkes, B. B.; Janek, J.; Adelhelm, P., *J. Phys. Chem. C* 2017, *121* (16), 8679-8691.
153. Goryachev, A.; Gao, L.; Zhang, Y.; Rohling, R. Y.; Vervuurt, R. H. J.; Bol, A. A.; Hofmann, J. P.; Hensen, E. J. M., *Chemelectrochem* 2018, *5* (8), 1230-1239.
154. Garcia, G.; Roca-Ayats, M.; Guillen-Villafuerte, O.; Rodriguez, J. L.; Arevalo, M. C.; Pastor, E., *J. Electroanal. Chem.* 2017, *793*, 235-241.
155. Bogdanoff, P.; Friebe, P.; Alonso-Vante, N., *J. Electrochem. Soc.* 1998, *145* (2), 576-582.
156. Bogdanoff, P.; Alonso-Vante, N., *J. Electroanal. Chem.* 1994, *379* (1-2), 415-421.
157. Kamimura, J.; Bogdanoff, P.; Lahnemann, J.; Hauswald, C.; Geelhaar, L.; Fiechter, S.; Riechert, H., *J. Am. Chem. Soc.* 2013, *135* (28), 10242-10245.
158. Crozier, P. A.; Hansen, T. W., *MRS Bull.* 2015, *40* (1), 38-45.

159. Taheri, M. L.; Stach, E. A.; Arslan, I.; Crozier, P. A.; Kabius, B. C.; LaGrange, T.; Minor, A. M.; Takeda, S.; Tanase, M.; Wagner, J. B.; Sharma, R., *Ultramicroscopy* 2016, *170*, 86-95.
160. Tao, F.; Crozier, P. A., *Chem. Rev.* 2016, *116* (6), 3487-3539.
161. Gai, P. L., *Top. Catal.* 2002, *21* (4), 161-173.
162. Ring, E. A.; Peckys, D. B.; Dukes, M. J.; Baudoin, J. P.; de Jonge, N., *J. Microsc.* 2011, *243* (3), 273-283.
163. Parkinson, G. M., *Catal. Lett.* 1989, *2* (5), 303-307.
164. Beermann, V.; Holtz, M. E.; Padgett, E.; de Araujo, J. F.; Muller, D. A.; Strasser, P., *Energy Environ. Sci.* 2019, *12* (8).
165. Lawrence, E. L.; Crozier, P. A., *ACS Appl. Nano Mater.* 2018, *1* (3), 1360-1369.
166. Goncalves, R. H.; Leite, E. R., *Energy Environ. Sci.* 2014, *7* (7), 2250-2254.
167. Peng, Z. M.; Somodi, F.; Helveg, S.; Kisielowski, C.; Specht, P.; Bell, A. T., *J. Catal.* 2012, *286*, 22-29.
168. Jeangros, Q.; Faes, A.; Wagner, J. B.; Hansen, T. W.; Aschauer, U.; Van herle, J.; Hessler-Wyser, A.; Dunin-Borkowski, R. E., *Acta Mater.* 2010, *58* (14), 4578-4589.
169. Gai, P. L.; Boyes, E. D.; Helveg, S.; Hansen, P. L.; Giorgio, S.; Henry, C. R., *MRS Bull.* 2007, *32* (12), 1044-1050.
170. Sharma, R., *J. Mater. Res.* 2005, *20* (7), 1695-1707.
171. Helveg, S.; Lopez-Cartes, C.; Sehested, J.; Hansen, P. L.; Clausen, B. S.; Rostrup-Nielsen, J. R.; Abild-Pedersen, F.; Norskov, J. K., *Nature* 2004, *427* (6973), 426-429.
172. Zhu, G. Z.; Prabhudev, S.; Yang, J.; Gabardo, C. M.; Botton, G. A.; Soleymani, L., *J. Phys. Chem. C* 2014, *118* (38), 22111-22119.
173. Pena, N. O.; Ihiawakrim, D.; Han, M.; Lassalle-Kaiser, B.; Carenco, S.; Sanchez, C.; Laberty-Robert, C.; Portehault, D.; Ersen, O., *ACS Nano* 2019, *13* (10), 11372-11381.
174. Vavra, J.; Shen, T. H.; Stoian, D.; Tileli, V.; Buonsanti, R., *Angew. Chem.-Int. Edit.* 2021, *133*, 1367-1374.
175. Gocyla, M.; Kuehl, S.; Shviro, M.; Heyen, H.; Selve, S.; Dunin-Borkowski, R. E.; Heggen, M.; Strasser, P., *ACS Nano* 2018, *12* (6), 5306-5311.
176. Dong, H.; Xu, F.; Sun, Z. Q.; Wu, X.; Zhang, Q. B.; Zhai, Y. S.; Tan, X. D.; He, L. B.; Xu, T.; Zhang, Z.; Duan, X. F.; Sun, L. T., *Nature Nanotechnology* 2019, *14* (10), 950-+.
177. Su, Q. M.; Wang, S. X.; Yao, L. B.; Li, H. J.; Du, G. H.; Ye, H. Q.; Fang, Y. Z., *Scientific Reports* 2016, *6*.
178. Cavalca, F.; Laursen, A. B.; Kardynal, B. E.; Dunin-Borkowski, R. E.; Dahl, S.; Wagner, J. B.; Hansen, T. W., *Nanotechnology* 2012, *23* (7).
179. Levin, B. D. A.; Haiber, D.; Liu, Q. L.; Crozier, P. A., *Microsc. Microanal.* 2020, *26* (1), 134-138.
180. Zhang, L. X.; Liu, Q. L.; Aoki, T.; Crozier, P. A., *J. Phys. Chem. C* 2015, *119* (13), 7207-7214.
181. Zhang, L. X.; Miller, B. K.; Crozier, P. A., *Nano Lett.* 2013, *13* (2), 679-684.
182. Zhang, C.; Tian, W.; Xu, Z.; Wang, X.; Liu, J. W.; Li, S. L.; Tang, D. M.; Liu, D. Q.; Liao, M. Y.; Bando, Y.; Golberg, D., *Nanoscale* 2014, *6* (14), 8084-8090.

183. Yoshida, K.; Nozaki, T.; Hirayama, T.; Tanaka, N., *J. Electron Microsc.* 2007, *56* (5), 177-180.
184. Yoshida, K.; Yamasaki, J.; Tanaka, N., *Appl. Phys. Lett.* 2004, *84* (14), 2542-2544.
185. Binnig, G.; Quate, C. F.; Gerber, C., *Phys. Rev. Lett.* 1986, *56* (9), 930-933.
186. Garcia, R.; Perez, R., *Surf. Sci. Rep.* 2002, *47* (6-8), 197-301.
187. Liang, Y.; Pfisterer, J. H. K.; McLaughlin, D.; Csoklich, C.; Seidl, L.; Bandarenka, A. S.; Schneider, O., *Small Methods* 2019, *3* (8), 1800387.
188. Chen, H. B.; Qin, Z. B.; He, M. F.; Liu, Y. C.; Wu, Z., *Materials* 2020, *13* (3), 668.
189. Zheng, L.; Shim, H. J.; Cui, Y.; Gao, Y.; Lee, K. W.; Hahn, S. J.; Pyo, S. G., *J. Nanosci. Nanotechnol.* 2019, *19* (3), 1242-1247.
190. Li, Y.; Cheng, Y. F., *Appl. Surf. Sci.* 2017, *396*, 144-153.
191. Kreta, A.; Rodosek, M.; Perse, L. S.; Orel, B.; Gaberscek, M.; Vuk, A. S., *Corros. Sci.* 2016, *104*, 290-309.
192. Zhang, S. D.; Liu, Z. W.; Wang, Z. M.; Wang, J. Q., *Corros. Sci.* 2014, *83*, 111-123.
193. Padhy, N.; Paul, R.; Mudali, U. K.; Raj, B., *Appl. Surf. Sci.* 2011, *257* (11), 5088-5097.
194. Yu, W. L.; Fu, H. J.; Mueller, T.; Brunschwig, B. S.; Lewis, N. S., *J. Chem. Phys.* 2020, *153* (2).
195. Nellist, M. R.; Qiu, J. J.; Laskowski, F. A. L.; Toma, F. M.; Boettcher, S. W., *ACS Energy Letters* 2018, *3* (9), 2286-2291.
196. Nellist, M. R.; Laskowski, F. A. L.; Qiu, J. J.; Hajibabaei, H.; Sivula, K.; Hamann, T. W.; Boettcher, S. W., *Nature Energy* 2018, *3* (1), 46-52.
197. Izquierdo, J.; Eifert, A.; Kranz, C.; Souto, R. M., *Electrochim. Acta* 2017, *247*, 588-599.
198. Dette, C.; Hurst, M. R.; Deng, J.; Nellist, M. R.; Boettcher, S. W., *ACS Applied Materials & Interfaces* 2019, *11* (6), 5590-5594.
199. Deng, J.; Nellist, M. R.; Stevens, M. B.; Dette, C.; Wang, Y.; Boettcher, S. W., *Nano Lett.* 2017, *17* (11), 6922-6926.
200. Deng, X.; Galli, F.; Koper, M. T. M., *J. Am. Chem. Soc.* 2018, *140* (41), 13285-13291.
201. Kolagatla, S.; Subramanian, P.; Schechter, A., *Chemsuschem* 2019, *12* (12), 2708-2714.
202. Toma, F. M.; Cooper, J. K.; Kunzelmann, V.; McDowell, M. T.; Yu, J.; Larson, D. M.; Borys, N. J.; Abelyan, C.; Beeman, J. W.; Yu, K. M.; Yang, J. H.; Chen, L.; Shaner, M. R.; Spurgeon, J.; Houle, F. A.; Persson, K. A.; Sharp, I. D., *Nat. Commun.* 2016, *7*, 12012.
203. Laskowski, F. A. L.; Oener, S. Z.; Nellist, M. R.; Gordon, A. M.; Bain, D. C.; Fehrs, J. L.; Boettcher, S. W., *Nature Materials* 2020, *19* (1), 69-76.
204. Hansma, P. K.; Tersoff, J., *J. Appl. Phys.* 1987, *61* (2), R1-R23.
205. Sonnenfeld, R.; Hansma, P. K., *Science* 1986, *232* (4747), 211-213.
206. Liu, H. Y.; Fan, F. R. F.; Lin, C. W.; Bard, A. J., *J. Am. Chem. Soc.* 1986, *108* (13), 3838-3839.
207. Gentz, K.; Wandelt, K., *Chimia* 2012, *66* (1-2), 44-51.
208. Kolb, D. M., *Angew. Chem.-Int. Edit.* 2001, *40* (7), 1162-1181.
209. Magnussen, O. M., *Chem-Eur J* 2019, *25* (56), 12865-12883.

210. Magnussen, O. M.; Gross, A., *J. Am. Chem. Soc.* 2019, *141* (12), 4777-4790.
211. Mudali, U. K.; Padhy, N., *Corros. Rev.* 2011, *29* (1-2), 73-103.
212. Zhang, J. D.; Kuznetsov, A. M.; Medvedev, I. G.; Chi, Q. J.; Albrecht, T.; Jensen, P. S.; Ulstrup, J., *Chem. Rev.* 2008, *108* (7), 2737-2791.
213. Itaya, K., *Prog. Surf. Sci.* 1998, *58* (3), 121-247.
214. Hachiya, T.; Honbo, H.; Itaya, K., *J. Electroanal. Chem.* 1991, *315* (1-2), 275-291.
215. Itaya, K.; Tomita, E., *Surf. Sci.* 1988, *201* (3), L507-L512.
216. Itaya, K.; Sugawara, S., *Chem. Lett.* 1987, (10), 1927-1930.
217. Paoli, E. A.; Masini, F.; Frydendal, R.; Deiana, D.; Schlaup, C.; Malizia, M.; Hansen, T. W.; Horch, S.; Stephens, I. E. L.; Chorkendorff, I., *Chem. Sci.* 2015, *6* (1), 190-196.
218. Koper, M. T. M., *Nanoscale* 2011, *3* (5), 2054-2073.
219. Esposito, D. V.; Baxter, J. B.; John, J.; Lewis, N. S.; Moffat, T. P.; Ogitsu, T.; O'Neil, G. D.; Pham, T. A.; Talin, A. A.; Velazquez, J. M.; Wood, B. C., *Energy Environ. Sci.* 2015, *8* (10), 2863-2885.
220. Meier, J.; Friedrich, K. A.; Stimming, U., *Faraday Discuss.* 2002, *121*, 365-372.
221. Strmcnik, D. S.; Tripkovic, D. V.; van der Vliet, D.; Chang, K. C.; Komanicky, V.; You, H.; Karapetrov, G.; Greeley, J.; Stamenkovic, V. R.; Markovic, N. M., *J. Am. Chem. Soc.* 2008, *130* (46), 15332-15339.
222. Wolfschmidt, H.; Weingarth, D.; Stimming, U., *ChemPhysChem* 2010, *11* (7), 1533-1541.
223. Hiesgen, R.; Eberhardt, D.; Aleksandrova, E.; Friedrich, K. A., *J. Appl. Electrochem.* 2007, *37* (12), 1495-1502.
224. Kim, Y. G.; Baricuatro, J. H.; Javier, A.; Gregoire, J. M.; Soriaga, M. P., *Langmuir* 2014, *30* (50), 15053-15056.
225. Kim, Y. G.; Javier, A.; Baricuatro, J. H.; Torelli, D.; Cummins, K. D.; Tsang, C. F.; Hemminger, J. C.; Soriaga, M. P., *J. Electroanal. Chem.* 2016, *780*, 290-295.
226. Kim, Y. G.; Baricuatro, J. H.; Soriaga, M. P., *Electrocatalysis* 2018, *9* (4), 526-530.
227. Baricuatro, J. H.; Kim, Y. G.; Korzeniewski, C. L.; Soriaga, M. P., *Catal. Today* 2020, *358*, 210-214.
228. Baricuatro, J. H.; Kim, Y. G.; Tsang, C. F.; Javier, A. C.; Cummins, K. D.; Hemminger, J. C., *J. Electroanal. Chem.* 2020, *857*.
229. Yau, S. L.; Fan, F. R. F.; Bard, A. J., *J. Electrochem. Soc.* 1992, *139* (10), 2825-2829.
230. Kaji, K.; Yau, S. L.; Itaya, K., *J. Appl. Phys.* 1995, *78* (9), 5727-5733.
231. Yao, H.; Yau, S. L.; Itaya, K., *Appl. Phys. Lett.* 1996, *68* (11), 1473-1475.
232. Carlsson, P.; Holmstrom, B.; Kita, H.; Uosaki, K., *Surf. Sci.* 1990, *237* (1-3), 280-290.
233. Uosaki, K.; Koinuma, M., *J. Electroanal. Chem.* 1993, *357* (1-2), 301-306.
234. Yao, H.; Itaya, K., *J. Electrochem. Soc.* 1998, *145* (9), 3090-3094.
235. Xiao, K. Z.; McCormick, L.; Fendler, J. H., *Chem. Mater.* 1991, *3* (5), 922-935.
236. Eriksson, S.; Carlsson, P.; Holmstrom, B.; Uosaki, K., *J. Electroanal. Chem.* 1991, *313* (1-2), 121-128.
237. Lay, M. D.; Sorenson, T. A.; Stickney, J. L., *J. Phys. Chem. B* 2003, *107* (38), 10598-10602.

238. Polcari, D.; Dauphin-Ducharme, P.; Mauzeroll, J., *Chem. Rev.* 2016, *116* (22), 13234-13278.
239. Mirkin, M. V.; Nogala, W.; Velmurugan, J.; Wang, Y. X., *PCCP* 2011, *13* (48), 21196-21212.
240. Payne, N. A.; Stephens, L. I.; Mauzeroll, J., *Corrosion* 2017, *73* (7), 759-780.
241. Pust, S. E.; Maier, W.; Wittstock, G., *Z. Phys. Chemie-Int. J. Res. Phys. Chem. Chem. Phys.* 2008, *222* (10), 1463-1517.
242. Niu, L.; Yin, Y.; Guo, W.; Lu, M.; Qin, R.; Chen, S., *J. Mater. Sci.* 2009, *44* (17), 4511-4521.
243. Souto, R. M.; Gonzalez-Garcia, Y.; Battistel, D.; Daniele, S., *Chem-Eur J* 2012, *18* (1), 230-236.
244. Bae, J. H.; Brocenschi, R. F.; Kisslinger, K.; Xin, H. L.; Mirkin, M. V., *Anal. Chem.* 2017, *89* (23), 12618-12621.
245. Ni, W.; Shao, Y.; Qi, J.; Yuan, B.; Li, L.; Wang, C., *Int. J. Electrochem. Sci.* 2020, *15* (4), 3315-3326.
246. Nickchi, T.; Rostron, P.; Barsoum, I.; Alfantazi, A., *J. Mater. Sci.* 2019, *54* (12), 9213-9221.
247. Eckhard, K.; Chen, X. X.; Turcu, F.; Schuhmann, W., *PCCP* 2006, *8* (45), 5359-5365.
248. Naslund, L.-A.; Sanchez-Sanchez, C. M.; Ingason, A. S.; Backstrom, J.; Herrero, E.; Rosen, J.; Holmin, S., *J. Phys. Chem. C* 2013, *117* (12), 6126-6135.
249. Zeradjanin, A. R.; Menzel, N.; Schuhmann, W.; Strasser, P., *PCCP* 2014, *16* (27), 13741-13747.
250. Lai, J. H.; Yuan, D.; Huang, P.; Zhang, J.; Su, J. J.; Tian, Z. W.; Zhan, D. P., *J. Phys. Chem. C* 2016, *120* (30), 16446-16452.
251. Ye, H.; Park, H. S.; Bard, A. J., *J. Phys. Chem. C* 2011, *115* (25), 12464-12470.
252. Park, H. S.; Kweon, K. E.; Ye, H.; Paek, E.; Hwang, G. S.; Bard, A. J., *J. Phys. Chem. C* 2011, *115* (36), 17870-17879.
253. Kim, J. Y.; Ahn, H. S.; Bard, A. J., *Anal. Chem.* 2018, *90* (5), 3045-3049.
254. Lee, H. C.; Cho, S. K.; Park, H. S.; Nam, K. M.; Bard, A. J., *J. Phys. Chem. C* 2017, *121* (33), 17561-17568.
255. Nam, K. M.; Park, H. S.; Lee, H. C.; Meekins, B. H.; Leonard, K. C.; Bard, A. J., *J. Phys. Chem. Lett.* 2013, *4* (16), 2707-2710.
256. Leonard, K. C.; Nam, K. M.; Lee, H. C.; Kang, S. H.; Park, H. S.; Bard, A. J., *J. Phys. Chem. C* 2013, *117* (31), 15901-15910.
257. Cho, S. K.; Park, H. S.; Lee, H. C.; Nam, K. M.; Bard, A. J., *J. Phys. Chem. C* 2013, *117* (44), 23048-23056.
258. Bhattacharya, C.; Lee, H. C.; Bard, A. J., *J. Phys. Chem. C* 2013, *117* (19), 9633-9640.
259. Cong, Y. Q.; Park, H. S.; Wang, S. J.; Dang, H. X.; Fan, F. R. F.; Mullins, C. B.; Bard, A. J., *J. Phys. Chem. C* 2012, *116* (27), 14541-14550.
260. Esposito, D. V.; Levin, I.; Moffat, T. P.; Talin, A. A., *Nature Materials* 2013, *12* (6), 562-568.
261. Zigah, D.; Rodriguez-Lopez, J.; Bard, A. J., *PCCP* 2012, *14* (37), 12764-12772.
262. Simpson, B. H.; Rodriguez-Lopez, J., *J. Am. Chem. Soc.* 2015, *137* (47), 14865-14868.

263. Fernandez, J. L.; Walsh, D. A.; Bard, A. J., *J. Am. Chem. Soc.* 2005, *127* (1), 357-365.
264. Vickers, J. W.; Dinh, H. N.; Randolph, K.; Weber, A. Z.; McDaniel, A. H.; Boardman, R. D.; Ogitsu, T.; Colon-Mercado, H.; Peterson, D.; Miller, E., *ECS Trans.* 2018, *85* (11), 3-14.
265. https://www.h2awsm.org/, *HydroGEN Advanced Water Splitting Materials*.
266. Zamborini, F. P.; Crooks, R. M., *Langmuir* 1997, *13* (2), 122-126.
267. Kim, Y.-G.; Baricuatro, J. H.; Javier, A.; Gregoire, J. M.; Soriaga, M. P., *Langmuir* 2014, *30* (50), 15053-15056.
268. Bearinger, J. P.; Orme, C. A.; Gilbert, J. L., *Surf. Sci.* 2001, *491* (3), 370-387.
269. Song, Z.; Xie, Z.-H., *Micron* 2018, *112*, 69-83.
270. Lichterman, M. F.; Richter, M. H.; Hu, S.; Crumlin, E. J.; Axnanda, S.; Favaro, M.; Drisdell, W.; Hussain, Z.; Brunschwig, B. S.; Lewis, N. S.; Liu, Z.; Lewerenz, H.-J., *J. Electrochem. Soc.* 2016, *163* (2), H139-H146.
271. Yamamoto, S.; Bluhm, H.; Andersson, K.; Ketteler, G.; Ogasawara, H.; Salmeron, M.; Nilsson, A., *Journal of Physics-Condensed Matter* 2008, *20* (18).
272. Zhai, Y.; Zhu, Z.; Zhou, S.; Zhu, C.; Dong, S., *Nanoscale* 2018, *10* (7), 3089-3111.
273. Dunsch, L., *J. Solid State Electrochem.* 2011, *15* (7-8), 1631-1646.
274. Nayak, S.; Biedermann, P. U.; Stratmann, M.; Erbe, A., *Electrochim. Acta* 2013, *106*, 472-482.
275. Schuurmans, F. J. P.; Vanmaekelbergh, D.; van de Lagemaat, J.; Lagendijk, A., *Science* 1999, *284* (5411), 141-143.
276. Erne, B. H.; Vanmaekelbergh, D.; Kelly, J. J., *J. Electrochem. Soc.* 1996, *143* (1), 305-314.
277. Tjerkstra, R. W.; Rivas, J. G.; Vanmaekelbergh, D.; Kelly, J. J., *Electrochemical and Solid State Letters* 2002, *5* (5), G32-G35.
278. Tiginyanu, I. M.; Kravetsky, I. V.; Monecke, J.; Cordts, W.; Marowsky, G.; Hartnagel, H. L., *Appl. Phys. Lett.* 2000, *77* (15), 2415-2417.
279. Muller, K.; Wloka, J.; Schmuki, P., *J. Solid State Electrochem.* 2009, *13* (5), 807-812.
280. Memming, R.; Schwandt, G., *Electrochim. Acta* 1968, *13*, 1299-1310.
281. Zhu, C.; Zheng, M.; Xiong, Z.; Li, H.; Shen, W., *Int. J. Hydrogen Energy* 2014, *39* (21), 10861-10869.
282. Mi, Q. X.; Zhanaidarova, A.; Brunschwig, B. S.; Gray, H. B.; Lewis, N. S., *Energy Environ. Sci.* 2012, *5* (2), 5694-5700.
283. Spurgeon, J. M.; Velazquez, J. M.; McDowell, M. T., *PCCP* 2014, *16* (8), 3623-3631.
284. Kargar, A.; Sukrittanon, S.; Zhou, C.; Ro, Y. G.; Pan, X. Q.; Dayeh, S. A.; Tu, C. W.; Jin, S., *Small* 2017, *13* (21).
285. Franke, R.; Chasse, T.; Streubel, P.; Meisel, A., *J. Electron. Spectrosc. Relat. Phenom.* 1991, *56* (4), 381-388.
286. Nefedov, V. I.; Salyn, Y. V.; Domashevskaya, E. P.; Ugai, Y. A.; Terekhov, V. A., *J. Electron. Spectrosc. Relat. Phenom.* 1975, *6* (3), 231-238.
287. Zhang, J.; Lai, J. H.; Wang, W.; Huang, P. C.; Jia, J. C.; Han, L. H.; Tian, Z. W.; Tian, Z. Q.; Zhan, D. P., *J. Phys. Chem. C* 2017, *121* (18), 9944-9952.

288. Yu, X. R.; Liu, F.; Wang, Z. Y.; Chen, Y., *J. Electron Spectrosc. Relat. Phenom.* 1990, *50*, 159-166.
289. Shalvoy, R. B.; Reucroft, P. J., *Journal of Vacuum Science & Technology* 1979, *16* (2), 567-569.
290. Allongue, P.; Souteyrand, E.; Allemand, L., *Journal of The Electrochemical Society* 1989, *136* (4), 1027-1033.
291. Frese, K. W.; Madou, M. J.; Morrison, S. R., *Journal of The Electrochemical Society* 1981, *128* (9), 1939-1943.
292. Madou, M. J.; Frese, K. W.; Morrison, S. R., *Journal of The Electrochemical Society* 1980, *127* (4), 987-989.
293. Menezes, S.; Heller, A.; Miller, B., *Journal of The Electrochemical Society* 1980, *127* (6), 1268-1273.
294. Noufi, R.; Tench, D.; Warren, L. F., *Journal of The Electrochemical Society* 1980, *127* (10), 2310-2311.
295. Yang, F.; Nielander, A. C.; Grimm, R. L.; Lewis, N. S., *J. Phys. Chem. C* 2016, *120* (13), 6989-6995.
296. Hendricks, O. L.; Tang-Kong, R.; Babadi, A. S.; McIntyre, P. C.; Chidsey, C. E. D., *Chemistry of Materials* 2018, *31* (1), 90-100.
297. Hu, S.; Shaner, M. R.; Beardslee, J. A.; Lichterman, M.; Brunschwig, B. S.; Lewis, N. S., *Science* 2014, *344* (6187), 1005.
298. Ros, C.; Andreu, T.; Hernandez-Alonso, M. D.; Penelas-Perez, G.; Arbiol, J.; Morante, J. R., *ACS Appl Mater Interfaces* 2017, *9* (21), 17932-17941.
299. Scheuermann, A. G.; Prange, J. D.; Gunji, M.; Chidsey, C. E. D.; McIntyre, P. C., *Energy & Environmental Science* 2013, *6* (8).
300. Alqahtani, M.; Ben-Jabar, S.; Ebaid, M.; Sathasivam, S.; Jurczak, P.; Xia, X.; Alromaeh, A.; Blackman, C.; Qin, Y.; Zhang, B.; Ooi, B. S.; Liu, H.; Parkin, I. P.; Wu, J., *Opt Express* 2019, *27* (8), A364-A371.
301. Sayed, S. Y.; Daly, B.; Buriak, J. M., *The Journal of Physical Chemistry C* 2008, *112* (32), 12291-12298.
302. Pham, N. D.; Park, S. J.; Lee, J. P.; Oh, I., *Journal of Chemistry* 2014, *2014*, 784824.
303. Hormozi Nezhad, M. R.; Aizawa, M.; Porter Jr, L. A.; Ribbe, A. E.; Buriak, J. M., *Small* 2005, *1* (11), 1076-1081.
304. Buabthong, P.; Ifkovits, Z. P.; Kempler, P. A.; Chen, Y. K.; Nunez, P. D.; Brunschwig, B. S.; Papadantonakis, K. M.; Lewis, N. S., *Energy Environ. Sci.* 2020, *13* (11), 4269-4279.
305. Frese, K. W.; Madou, M. J.; Morrison, S. R., *J. Electrochem. Soc.* 1981, *128* (9), 1939-1943.
306. Papaderakis, A.; Mintsouli, I.; Georgieva, J.; Sotiropoulos, S., *Catalysts* 2017, *7* (3).
307. Allongue, P.; Blonkowski, S., *Journal of Electroanalytical Chemistry and Interfacial Electrochemistry* 1991, *317* (1), 77-99.
308. Khader, M. M.; Hannout, M. M.; El-Dessouki, M. S., *International Journal of Hydrogen Energy* 1991, *16* (12), 797-803.
309. Lai, J.; Yuan, D.; Huang, P.; Zhang, J.; Su, J.-J.; Tian, Z.-W.; Zhan, D., *The Journal of Physical Chemistry C* 2016, *120* (30), 16446-16452.

310. Sharma, H.; Moumanis, K.; Dubowski, J. J., *The Journal of Physical Chemistry C* 2016, *120* (45), 26129-26137.
311. Schlesinger, T. E., In *Encyclopedia of Materials: Science and Technology*ed., Vol.; Elsevier Ltd., 2001, pp 3431-3435.
312. Allongue, P.; Blonkowski, S., *J. Electroanal. Chem.* 1991, *317* (1-2), 77-99.
313. Allongue, P.; Blonkowski, S., *J. Electroanal. Chem.* 1991, *316* (1-2), 57-77.
314. Allongue, P.; Blonkowski, S., *Electrochim. Acta* 1993, *38* (7), 889-895.
315. Khader, M. M.; Hannout, M. M.; Eldessouki, M. S., *Int. J. Hydrogen Energy* 1991, *16* (12), 797-803.
316. Schroder, K.; Memming, R., *Berichte Der Bunsen-Gesellschaft-Physical Chemistry Chemical Physics* 1985, *89* (4), 385-392.
317. Solomun, T.; McIntyre, R.; Richtering, W.; Gerischer, H., *Surf. Sci.* 1986, *169* (2-3), 414-424.
318. Huang, Y.; Luo, J. L.; Ivey, D. G., *Mater. Chem. Phys.* 2005, *93* (2-3), 429-442.
319. King, D. E.; Fernandez, J. E.; Swartz, W. E., *Appl. Surf. Sci.* 1990, *45* (4), 325-339.
320. Contour, J. P.; Massies, J.; Saletes, A., *Japanese Journal of Applied Physics Part 2-Letters* 1985, *24* (7), L563-L565.
321. Sharma, H.; Moumanis, K.; Dubowski, J. J., *J. Phys. Chem. C* 2016, *120* (45), 26129-26137.
322. Ellis, A. B.; Bolts, J. M.; Kaiser, S. W.; Wrighton, M. S., *J. Am. Chem. Soc.* 1977, *99* (9), 2848-2854.
323. Kohl, P. A.; Wolowodiuk, C.; Ostermayer, F. W., *J. Electrochem. Soc.* 1983, *130* (11), 2288-2293.
324. Djokic, S. S., In *Encyclopedia of Interfacial Chemistry*ed., Vol.; Wandelt, K., Ed.; Elsevier, 2018, pp 161-173.
325. Alqahtani, M.; Ben-Jabar, S.; Ebaid, M.; Sathasivam, S.; Jurczak, P.; Xia, X.; Alromaeh, A.; Blackman, C.; Qin, Y.; Zhang, B.; Ooi, B. S.; Liu, H.; Parkin, I. P.; Wu, J., *Opt. Express* 2019, *27* (8), A364-A371.
326. Kargar, A.; Sukrittanon, S.; Zhou, C.; Ro, Y. G.; Pan, X.; Dayeh, S. A.; Tu, C. W.; Jin, S., *Small* 2017, *13* (21), 1603574.
327. Kotulak, N. A.; Diaz, M.; Barnett, A.; Opila, R. L., *Thin Solid Films* 2014, *556*, 236-240.
328. Nozik, A. J., *Applied Physics Letters* 1976, *29* (3), 150-153.
329. Shan, W.; Walukiewicz, W.; Yu, K. M.; Wu, J.; Ager, J. W.; Haller, E. E.; Xin, H. P.; Tu, C. W., *Applied Physics Letters* 2000, *76* (22), 3251-3253.
330. Deutsch, T. G.; Koval, C. A.; Turner, J. A., *The Journal of Physical Chemistry B* 2006, *110* (50), 25297-25307.
331. Tietjen, J. J.; Amick, J. A., *Journal of The Electrochemical Society* 1966, *113* (7), 724.
332. Simon, J.; Young, D.; Ptak, A., In *2014 IEEE 40th Photovoltaic Specialist Conference (PVSC)*ed., Vol., 2014, pp 0538-0541.
333. Calero-Barney, S. J.; Paxton, W.; Ortiz, P.; Sunkara, M. K., *Solar Energy Materials and Solar Cells* 2020, *209*, 110440.
334. Shan, W.; Walukiewicz, W.; Ager, J. W.; Haller, E. E.; Geisz, J. F.; Friedman, D. J.; Olson, J. M.; Kurtz, S. R., *Physical Review Letters* 1999, *82* (6), 1221-1224.
335. Mirabella, F. M., John Wiley & Sons: 1998.

336. Makuła, P.; Pacia, M.; Macyk, W., ed., Vol.; ACS Publications, 2018.
337. Russell, H.; Andriotis, A.; Menon, M.; Jasinski, J.; Martinez-Garcia, A.; Sunkara, M., *Scientific reports* 2016, *6* (1), 1-9.
338. Gilliland, G., *Materials Science and Engineering: R: Reports* 1997, *18* (3-6), 99-399.
339. Martinez-Garcia, A.; Russell, H. B.; Paxton, W.; Ravipati, S.; Calero-Barney, S.; Menon, M.; Richter, E.; Young, J.; Deutsch, T.; Sunkara, M. K., *Advanced Energy Materials* 2018, *8* (16), 1703247.
340. Murphy, S.; Chroneos, A.; Jiang, C.; Schwingenschlögl, U.; Grimes, R., *Physical Review B* 2010, *82* (7), 073201.
341. Muthusamy, K.; Hussain, S.; Gopalakrishnan, R.; Vishista, k., *Materials Technology* 2017, *33*, 1-7.
342. Philips'Gloeilampenfabrieken, O., *Philips Res. Rep* 1958, *13* (1), 1-9.
343. Kittel, C., 1976.
344. Montgomery, H.; Feldmann, W., *Journal of Applied Physics* 1965, *36* (10), 3228-3232.
345. Lee, S. A.; Lee, T. H.; Kim, C.; Choi, M.-J.; Park, H.; Choi, S.; Lee, J.; Oh, J.; Kim, S. Y.; Jang, H. W., *ACS Catalysis* 2020, *10* (1), 420-429.
346. Loget, G.; Fabre, B.; Fryars, S.; Mériadec, C.; Ababou-Girard, S., *ACS Energy Letters* 2017, *2* (3), 569-573.
347. Huynh, M.; Bediako, D. K.; Nocera, D. G., *Journal of the American Chemical Society* 2014, *136* (16), 6002-6010.
348. Surendranath, Y.; Lutterman, D. A.; Liu, Y.; Nocera, D. G., *Journal of the American Chemical Society* 2012, *134* (14), 6326-6336.
349. Giddey, S.; Badwal, S. P. S.; Kulkarni, A., *Int. J. Hydrogen Energy* 2013, *38* (34), 14576-14594.
350. Kordali, V.; Kyriacou, G.; Lambrou, C., *Chem. Commun.* 2000, (17), 1673-1674.
351. Sclafani, A.; Augugliaro, V.; Schiavello, M., *J. Electrochem. Soc.* 1983, *130* (3), 734-735.
352. Chen, S. M.; Perathoner, S.; Ampelli, C.; Mebrahtu, C.; Su, D. S.; Centi, G., *Angew. Chem.-Int. Edit.* 2017, *56* (10), 2699-2703.
353. Lan, R.; Irvine, J. T. S.; Tao, S. W., *Scientific Reports* 2013, *3*.
354. Lan, R.; Tao, S. W., *Rsc Advances* 2013, *3* (39), 18016-18021.
355. Deng, J.; Iñiguez, J. A.; Liu, C., *Joule* 2018, *2* (5), 846-856.
356. Abghoui, Y.; Garden, A. L.; Hlynsson, V. F.; Bjorgvinsdottir, S.; Olafsdottir, H.; Skulason, E., *PCCP* 2015, *17* (7), 4909-4918.
357. Abghoui, Y.; Garden, A. L.; Howat, J. G.; Vegge, T.; Skulason, E., *ACS Catal.* 2016, *6* (2), 635-646.
358. Xu, G.; Liu, R.; Wang, J., *Science in China Series B-Chemistry* 2009, *52* (8), 1171-1175.
359. Guo, C. X.; Ran, J. R.; Vasileff, A.; Qiao, S. Z., *Energy Environ. Sci.* 2018, *11* (1), 45-56.
360. Zhou, F. L.; Azofra, L. M.; Ali, M.; Kar, M.; Simonov, A. N.; McDonnell-Worth, C.; Sun, C. H.; Zhang, X. Y.; MacFarlane, D. R., *Energy Environ. Sci.* 2017, *10* (12), 2516-2520.

361. Suryanto, B. H. R.; Kang, C. S. M.; Wang, D. B.; Xiao, C. L.; Zhou, F. L.; Azofra, L. M.; Cavallo, L.; Zhang, X. Y.; MacFarlane, D. R., *Acs Energy Letters* 2018, *3* (6), 1219-1224.
362. McEnaney, J. M.; Singh, A. R.; Schwalbe, J. A.; Kibsgaard, J.; Lin, J. C.; Cargnello, M.; Jaramillo, T. F.; Norskov, J. K., *Energy Environ. Sci.* 2017, *10* (7), 1621-1630.
363. Richmonds, C.; Witzke, M.; Bartling, B.; Lee, S. W.; Wainright, J.; Liu, C.-C.; Sankaran, R. M., *J. Am. Chem. Soc.* 2011, *133* (44), 17582-17585.
364. Richmonds, C.; Sankaran, R. M., *Appl. Phys. Lett.* 2008, *93* (13).
365. Neyts, E. C.; Ostrikov, K.; Sunkara, M. K.; Bogaerts, A., *Chem. Rev.* 2015, *115* (24), 13408-13446.
366. Mizushima, T.; Matsumoto, K.; Ohkita, H.; Kakuta, N., *Plasma Chem. Plasma Process.* 2007, *27* (1), 1-11.
367. Mehta, P.; Barboun, P.; Herrera, F. A.; Kim, J.; Rumbach, P.; Go, D. B.; Hicks, J. C.; Schneider, W. F., *Nature Catalysis* 2018, *1* (4), 269-275.
368. Deng, X. L.; Nikiforov, A. Y.; Vanraes, P.; Leys, C., *J. Appl. Phys.* 2013, *113* (2).
369. Rumbach, P.; Bartels, D. M.; Sankaran, R. M.; Go, D. B., *J. Phys. D-Appl. Phys.* 2015, *48* (42).
370. Spurgeon, J. M.; Lewis, N. S., *Energy Environ. Sci.* 2011, *4* (8), 2993-2998.
371. Kumari, S.; White, R. T.; Kumar, B.; Spurgeon, J., *Energy Environ. Sci.* 2016, *9*, 1725-1733.
372. Ma, S.; Siroma, Z.; Tanaka, H., *J. Electrochem. Soc.* 2006, *153* (12), A2274-A2281.
373. Whitehead, J. C., *J. Phys. D-Appl. Phys.* 2016, *49* (24).
374. Snoeckx, R.; Bogaerts, A., *Chem. Soc. Rev.* 2017, *46* (19), 5805-5863.
375. Wang, W. Z.; Patil, B.; Heijkers, S.; Hessel, V.; Bogaerts, A., *Chemsuschem* 2017, *10* (10), 2145-2157.
376. www.materialsproject.org.
377. Jain, A.; Ong, S. P.; Hautier, G.; Chen, W.; Richards, W. D.; Dacek, S.; Cholia, S.; Gunter, D.; Skinner, D.; Ceder, G.; Persson, K. A., *Apl Materials* 2013, *1* (1).

APPENDIX I

SYNERGISTIC PLASMA-ASSISTED ELECTROCHEMICAL REDUCTION OF NITROGEN TO AMMONIA

Ammonia, NH_3, is a key component in fertilizer and is commercially synthesized at large scale through the Haber-Bosch process. Due to the energy intensive nature of this process and the use of steam reforming of natural gas to provide the hydrogen feedstock, the ammonia synthesis industry is a major emitter of CO_2 (over 200 million tons of CO_2 per year).[349] About 80% of the ammonia currently produced worldwide is used for nitrogen-based fertilizer production, making NH_3 a critical molecule in global agricultural output. For this reason there has been increasing research interest in the electrochemical nitrogen reduction reaction (NRR) to ammonia driven by renewable electricity. In addition to cleaner fertilizer production, electrochemical NH_3 production can also provide a carbon-free energy-dense fuel which is liquid at near-ambient pressure.[349]

Electrochemical nitrogen reduction in aqueous media has proven very challenging, with low electrolysis performance and low faradaic efficiency for NH_3 formation.[349-354] The primary limitation in this system is kinetic competition at the cathode from the hydrogen evolution reaction (HER). Because the reversible potential for HER (0 V vs. NHE) is close to that for NRR (0.097 V vs. NHE) both can occur at applied voltages sufficient for electrolysis.[355] Moreover, the high dissociation energy of the triply bonded nitrogen molecule presents a significant activation barrier, which manifests in the electrolysis reaction as additional cathodic overpotential needed to drive NRR to ammonia.[349] Recent research in ambient-condition NH_3 electrosynthesis has thus pursued novel electrocatalysts to selectively promote NRR[356-359] and electrolysis strategies to suppress HER, with promising results reported for studies using a high-N_2-solubility ionic liquid electrolyte[360-361] and another study employing a three-step lithium cycling process to circumvent HER.[362]

Herein we explore an alternate approach to promote electrochemical NRR with aqueous electrolyte at ambient temperature and pressure in which a plasma is utilized to provide a high flux of energetically excited N_2 species in the vicinity of the electrolyzer cathode catalyst. While plasma-assisted electrochemistry is an underexplored area of research, microplasmas have been used in electrochemical reactions for a few fundamental studies[363] and for particle deposition.[364] Plasma-driven NH_3 synthesis from a mixed N_2/H_2 gas has been demonstrated for non-electrochemical reactions,[365-367] but to our knowledge has not been employed in electrochemical NRR. N_2 plasmas can produce ionized nitrogen species as well as

numerous excited N_2 states.[368] While sufficiently energetic nitrogen species can directly produce NH_3 in the presence of water or hydrogen, the weaker plasma-induced vibrational excitations which are not energetic enough to drive the reaction are still theoretically predicted to decrease the N_2 dissociation barrier.[367] Thus, if a high flux of vibrationally excited N_2 species are provided to the cathode catalyst surface in an aqueous electrolyzer, it is feasible that NRR could be promoted relative to HER and enable greater NH_3 production than either individual plasma-driven or electrochemical bias-driven processes.

A first-generation four-electrode N_2 plasma-assisted proton exchange membrane (PEM) electrolyzer was fabricated to test this concept as shown in Fig. 1. Many reports of plasma-assisted electrochemistry have been performed in a two-electrode configuration, in which the plasma is a gaseous electrolyte conducting charge in the circuit and is capable of creating solvated electrons which drive reactions at the plasma/liquid interface.[369] Because of the high voltage needed to generate a plasma, a two-electrode system thus leads to prohibitively low efficiency for electrolysis. A four-electrode configuration (two for plasma ignition and two for the electrolyzer) was pursued instead to permit electrochemical NRR at a more conventional voltage range. Detailed experimental methods are reported in the ESI. Briefly, an AC power source was used to generate a plasma from a flow of 2.5 L min^{-1} of 1:1 N_2:He gas by volume, in which inert He was supplied to aid in plasma ignition and steady operation. The power supply was operated at the minimum power setting required for plasma ignition. The PEM electrolyzer was a commercially available unit with a Nafion membrane and carbon-supported Pt

catalyst particles on the cathode side of the membrane electrode assembly (MEA). Liquid water was continuously circulated through the anode chamber while the N_2/He gas was introduced to the cathode chamber through the plasma jet electrode

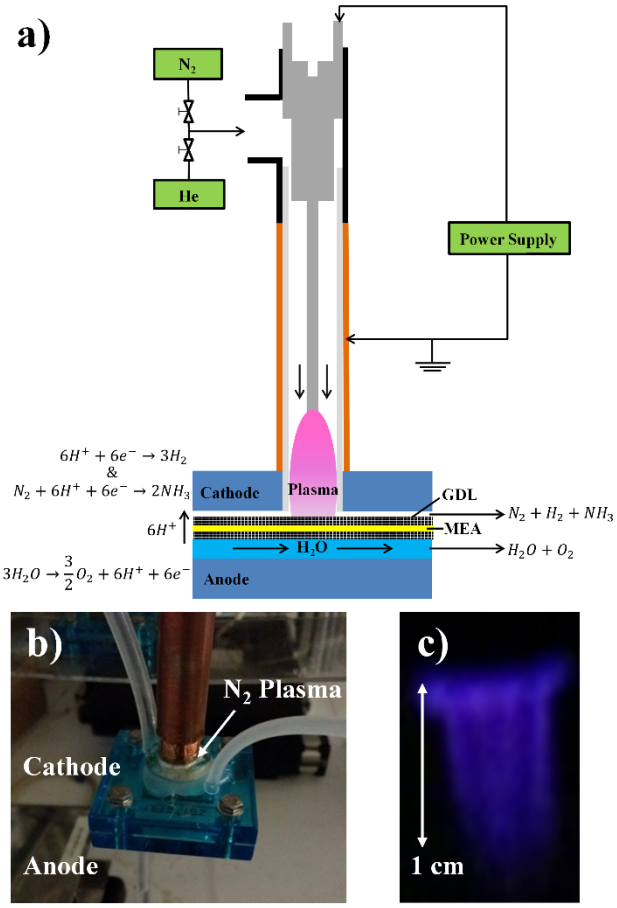

Figure1. (a) Schematic of the N_2 plasma jet impinging on a gas diffusion layer (GDL) on the cathode side of a membrane electrode assembly (MEA) in an electrolyzer. (b) Image of the plasma-assisted electrolyzer and (c) dark room image of the plasma jet plume when disconnected from the electrolyzer.

fitted through the electrolyzer end plate. The cathode gas output was bubbled through an aqueous solution with an indicator dye used to quantify NH_3 production via UV/vis colorimetry.

The initial PEM electrolyzer current density vs. voltage (*J-V*) behavior is shown in Fig. 2. The current density was determined relative to the active area (5

cm^2) of the membrane electrode assembly (MEA). Under steady state conditions with liquid water circulating through the anode but no active gas flow through the cathode, the electrolysis current density steadily increased with the applied voltage beyond 1.5 V and did not reach a limiting value within the measured range up to 4 V. At steady state under active gas flow at the cathode, however, the current density was observed to decrease at higher voltages. This limitation on the current was attributed to dehydration of the membrane surface near the cathode side due to the dry gas convection, which can reduce the membrane conductivity and increase the

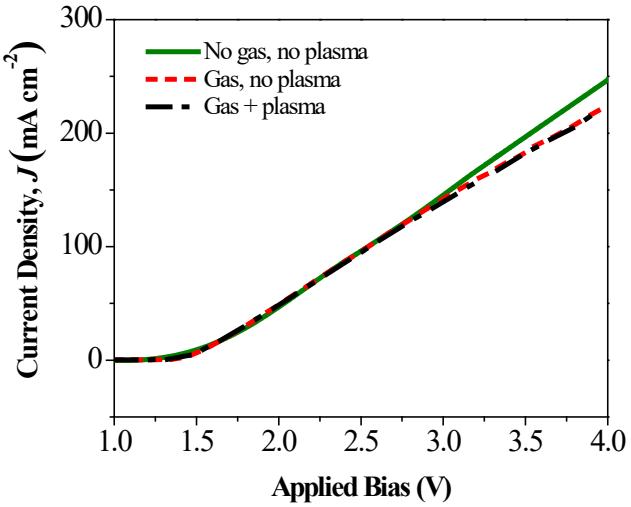

Figure 2. Current density vs. applied bias (*J-V*) behavior for the electrolyzer at various operating conditions.

ohmic resistance across the MEA.[370-371] Membrane conductivity was observed to decrease under gas flow as determined by an AC measurement technique,[371-372] with the conductivity recovering to its initial value after several minutes of water circulation without gas flow. The electrolyzer *J-V* behavior with the active N_2/He plasma impinging on the cathode side of the MEA was not significantly distinct from the behavior with gas flowing without plasma ignition. The plasma flux thus did not appear to have any immediate short-term detrimental effects on the

functioning of the MEA. After a 1 h potentiostatic measurement under plasma conditions for NH_3 quantification, the electrolyzer was slower to recover the full *J-V* performance upon stopping the cathode gas flow.

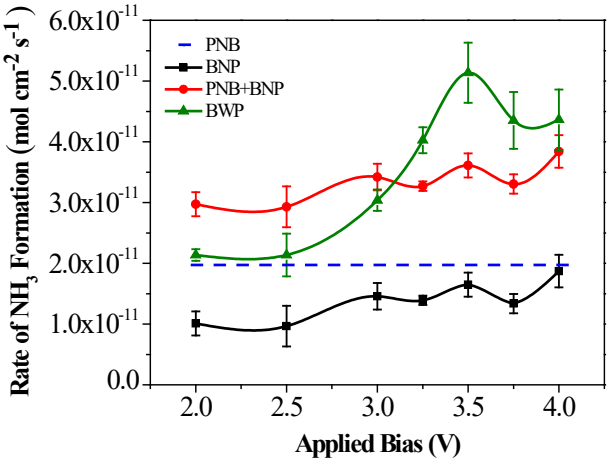

Figure 3. Ammonia production rate vs. applied bias for conditions of plasma with no bias (PNB), bias with no plasma (BNP), combined BNP+PNB, and simultaneous bias with plasma (BWP).

To determine if there is any synergistic effect from the presence of excited N_2 species at the cathode electrocatalyst, the rate of NH_3 formation under bias with plasma (BWP) conditions was measured as a function of applied bias to the electrolyzer and compared to the rate for plasma with no bias (PNB), bias with no plasma (BNP), and the combination of individual PNB and BNP cases (Fig. 3). Even for the PNB case, with minimal power for plasma ignition and no electrochemical reaction, there was an average rate of ammonia synthesis of 1.95 x 10^{-11} mol cm^{-2} s^{-1}. This NH_3 is formed from excited nitrogen species dissociating water molecules at the Nafion membrane surface and is not due to an electrochemical reaction. Because this is a contributing route to NH_3 synthesis in the BWP case that does not result from faradaic processes, we are unable to unequivocally deconvolute the direct plasma synthesis portion to determine a faradaic efficiency for electrolysis in the

presence of the plasma. Total NH_3 molar production rates are reported instead in Fig. 3 with each point representing the average of three independent 1 h potentiostatic measurements with several hours between each measurement at steady state conditions without plasma to reduce variability.

In the absence of plasma, an applied bias from 2 V to 4 V resulted in an NH_3 production rate of 1.0 x 10^{-11} to 1.9 x10^{-11} mol cm^{-2} s^{-1}, respectively. This is the total two-electrode applied bias to the electrolyzer cell and thus reflects the required thermodynamic potential for ammonia formation and/or water-splitting as well as overpotentials from ohmic losses, water oxidation at the anode, and NRR/HER at the cathode. This NH_3 formation rate compares favorably to a rate of ~3.1 x 10^{-12} mol cm^{-2} s^{-1} reported by Kordali, et al. under similar conditions at room temperature.[350] The combined rate of NH_3 formation from individual cases of PNB and BNP is plotted in Fig. 3 as well to show a baseline level of ammonia formation that might be predicted if the electrochemical reduction and plasma dissociation processes operate together without influencing each other. Interestingly, for the simultaneous BWP condition, the rate of ammonia formation was observed to be modestly less than the BNP+PNB combination for an applied bias ≤ 3 V, and notably higher for > 3 V. For the peak at 3.5 V, an NH_3 rate of 5.3 x 10^{-11} mol cm^{-2} s^{-1} was achieved, which was ~47% higher than the 3.6 x 10^{-11} mol cm^{-2} s^{-1} measured for the BNP+PNB combination. Note also that the rate of NH_3 formation for all points in Fig. 3 is relative to the MEA active area (5 cm^2) while the current reactor design had a plasma glow discharge impinging directly on only a fraction of that area (~1 cm^2), which may limit the observed plasma/electrocatalyst interaction since only ~20% of

catalyst sites would have direct exposure to excited nitrogen states, though convection could allow these molecules to react with a larger area of the MEA.

Plasma reactions are generally non-equilibrium in nature, and while plasma catalysis is a field of growing interest, there are still many fundamental aspects which are poorly understood.[50, 365, 373] The interactions of a plasma in an electrochemical system are even less well-described. Interpreting the bias-dependence and synergistic interaction in the BWP ammonia production case is thus rather speculative at this stage. The reduced NH_3 formation rate for BWP relative to BNP+PNB at ≤ 3 V may be attributable to further dehydration of the membrane near the cathode surface due to the incident plasma and resulting direct dissociation of H_2O, which would be in addition to the convective drying effect of the cathode gas flow in the absence of the plasma. This reduced hydration near the membrane surface would slow the rate of electrochemical NRR while maintaining similar direct plasma-driven NH_3 synthesis, which is consistent with the observed rate for BWP being greater than PNB but less than BNP+PNB.

At > 3 V total cell voltage, the BWP NH_3 rate exceeded the BNP+PNB combination, demonstrating the synergy of plasma and electrochemical bias for NRR. This result is consistent with plasma-induced vibrational excitations of N_2, which are insufficiently energetic to spontaneously react with protons at the MEA to form ammonia, leading to a decrease in the Gibb's free energy between reactants and products as well as a reduced dissociation activation energy. Reducing vibrationally excited nitrogen, $N_2^{(v)}$, to NH_3 would thus have a concomitant reduction in the overpotential for NRR relative to the overpotential for HER. The

effect on the NRR half-reaction at an electrochemical cathode would be analogous to that at a heterogeneous thermally catalysed reaction on a metal surface, in which it was modelled and experimentally demonstrated that $N_2^{(v)}$ states led to increased kinetics for NH_3 synthesis by breaking the intermediate reaction-step scaling relations and selectively enhancing the rate-limiting N_2 dissociation step.[367] It is also possible that the increased NH_3 production in the BWP case may be partially attributable to improved direct plasma-driven synthesis by reaction of excited nitrogen states with H_2 gas produced electrochemically by HER at the cathode. At > 3.5 V, the enhancement in NH_3 production of the BWP relative to BNP+PNB decreased. A similar peaking of the NH_3 production along with a decreasing rate at greater applied potentials has been reported for electrochemical nitrogen reduction.[350-351] This behavior was attributed to competitive adsorption of nitrogen and hydrogen species on the cathode surface. Perhaps a similar competition for catalyst binding sites between $N_2^{(v)}$ and electrochemically generated H_2 limits the NRR in the presence of plasma at higher electrolyzer applied bias.

While the reactor used in this work demonstrates a proof-of-concept for conditions that enable the synergistic enhancement of ammonia formation through plasma-assisted electrochemical NRR, the present design has several drawbacks which could be targeted for more optimized NH_3 production. A commercial PEM water electrolyzer MEA was used in which the cathode electrocatalyst was Pt with highly active HER kinetics. A more selective catalyst for NRR, such as Ru metal[350] or even a metal nitride[357] could improve the NH_3 formation rate. However, for thermally catalysed NH_3 synthesis, vibrationally excited N_2 was predicted to shift

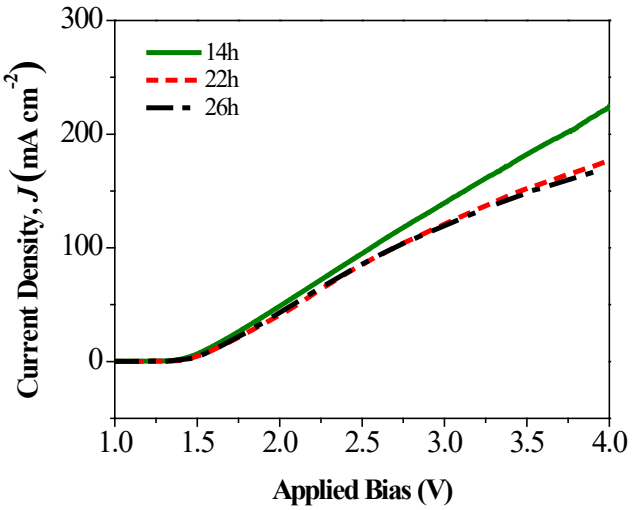

Figure 4. Current density vs. applied bias (*J-V*) behavior for the electrolyzer under plasma with bias conditions after cumulative exposure of the MEA to the N_2/He plasma for a time as shown in the legend. Up to 14 h, the performance was observed to be near its maximum but demonstrated decreasing performance thereafter.

the peak of the catalyst activity volcano curve to Co metal, with a similar effect possible for the electrochemical reaction.[367] Likewise, the integration of the plasma into the electrochemical cell and the corresponding transport of excited nitrogen states to the catalyst sites is still far from optimized. As mentioned above, the cross-sectional area of the plasma discharge was less than the active area of the MEA, which left portions of the electrode unlikely to benefit from the plasma-assisted effect. Also, the gas flow rate and distance between the plasma jet electrode and the MEA were not varied, both of which could affect the distribution of excited states and their flux to the electrocatalyst surface. The plasma power and method of excitation could also be adjusted for better performance. A similar AC power source N_2 plasma was estimated to have at most 37% of the molecules in an excited state.[367] Microwave[374] or gliding arc discharge[375] plasmas instead are known to create a greater density of high-energy vibrational states. In addition, the direct plasma dissociation of water was observed to lead to appreciable byproduct formation, with

indicator dyes confirming significant nitrate formation and small quantities of nitrite and hydrazine. The replacement of Nafion with a different membrane material less dependent on water permeation for proton conductivity could limit water exposure to the plasma and minimize energy loss to byproduct formation.

A practical electrolyzer for industrial use should be stable for thousands of hours. Although the PEM electrolyzer used in this work maintained its *J-V* performance for up to 14 h of cumulative exposure of the MEA to the N_2/He plasma, it subsequently experienced irreversible degradation. The electrolyzer *J-V* curves of Fig. 4 show that the current density at 3.5 V applied bias decreased 13% after 26 h of operation with plasma impinging on the cathode. The measured steady state membrane ionic conductivity did not appreciably change during this period, so we instead attribute this loss of performance to degradation of the catalyst. High-energy excited molecules and ions impacting the catalyst particles and carbon supports may induce gradual degradation via a sputtering mechanism.[365] Improving the electrolyzer stability, by catalyst protection or an altered plasma discharge with fewer high-energy states, would be necessary to harness the plasma-assisted electrochemical process in a practical device.

Conclusions

Novel strategies are needed to greatly increase the kinetics of electrochemical nitrogen reduction relative to the competing hydrogen evolution reaction if ambient-condition electrolytic synthesis of ammonia from air and water is to have a chance of competing with the established Haber-Bosch process of NH_3 synthesis. By impinging a non-thermal plasma on the cathode of a PEM electrolyzer, a flux of

vibrationally excited N_2 species were given the opportunity to electrochemically react with H^+ atoms crossing the membrane from water oxidation at the anode. The response for the bias-with-plasma operation was convoluted, but a proof-of-concept for a synergistic enhancement to NH_3 synthesis was observed at ~3.5 V. The measured ~47% increase in the ammonia production rate for the simultaneous bias with plasma (BWP) condition relative to the combined bias with no plasma (BNP) and plasma with no bias (PNB) conditions does not yet represent an optimized system, and there are many possible routes to improve the interaction of plasma and electrocatalyst sites as discussed above. Also, while a greater understanding of plasma-assisted electrochemical reactions are worthwhile in their own right, a practical application for NH_3 synthesis would need to eventually demonstrate sufficiently enhanced nitrogen reduction efficiency to justify the energy consumption required to sustain the plasma.

Supporting information

Experimental Methods

Plasma Operation

A custom-built plasma jet reactor was fabricated consisting of a 3.2-mm-diameter stainless steel rod electrode in the center of a 10-mm-inner-diameter (13 mm outer diameter) quartz tube fitted inside a 13-mm-inner-diameter (16 mm outer diameter) copper tube electrode (Fig. 1a). The inner quartz tube extended ~ 5 mm beyond the end of the copper tube electrode. High purity N_2 (99.99%, Welder Supply) and He (99.99% Welder Supply) were mixed at a 1:1 volumetric ratio and flowed through

the quartz tube at a total rate of 2.5 std L min^{-1}. The plasma was driven by an AC power supply (PVM500) using a sinusoidal waveform at ~20 kHz. All reported plasma measurements were performed at an applied power of 8.4 W. The power supply ground was also connected to the copper tube, which along with the high gas flow rate prevented plasma arcing to the electrolyzer electrode. Under these conditions, the visible plasma glow discharge was observed to extend ~ 1 cm beyond the end of the quartz tube exit (Fig. 1c). The plasma jet reactor was inserted through a machine-milled hole fit to the diameter of the quartz tube in the end plate of the electrolyzer cathode side, with the copper electrode just outside the electrolyzer end plate. The plasma reactor tube was secured and sealed gas-tight with epoxy. The distance from the tip of the stainless steel rod electrode to the surface of the electrolyzer membrane electrode assembly was 1.7 cm.

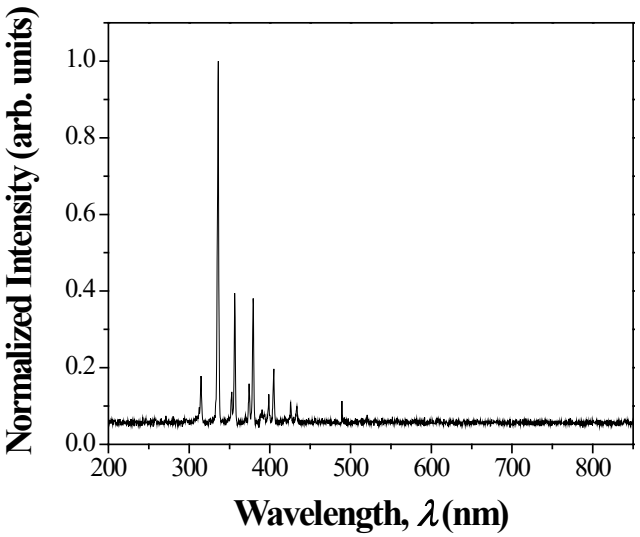

Figure S151. Optical emission spectra of the AC plasma discharge for N_2/He flow.

Electrochemical Measurements

Commercially available PEM reversible fuel cells (Horizon, FCSU-023) were used in electrolyzer mode in this work. The electrolyzer consisted of two stainless steel

grids (one for the anode and one for the cathode), two carbon Toray paper sheets as gas diffusion layers, and one membrane electrode assembly (MEA) with catalyst particles on either side of a sulfonated polytetrafluoroethylene (i.e., Nafion) proton-exchange membrane. The particulate catalyst material was the same for both electrodes (Pt/C), and was dispersed on the MEA following standard hot press methods. The projected active area of the MEA was 5 cm^2. Deionized liquid water (18 MΩ-cm) was circulated through the anode chamber at 35 mL min^{-1} for the duration of all experiments and for > 1 h prior to measurements. The N_2/He gas was flowed through the plasma reactor through the cathode chamber for > 1 h prior to measurements, though the actual plasma was ignited only ~ 1 min before measurements under plasma conditions. An SP-200 model Bio-Logic potentiostat was used to apply DC bias to the electrolyzer MEA and to measure current, through pins in contact with the current collector metal grids at either electrode. The *J-V* behavior was measured by sweeping the voltage at a scan rate of 5 mV s^{-1}. The current density was determined using the full projected area of the active part of the MEA (5 cm^2). During NH_3 production measurements, the applied bias to the electrolyzer was held constant for 1 h while the cathode gas output was bubbled through a 50 mL reservoir of deionized water. To improve reproducibility, the

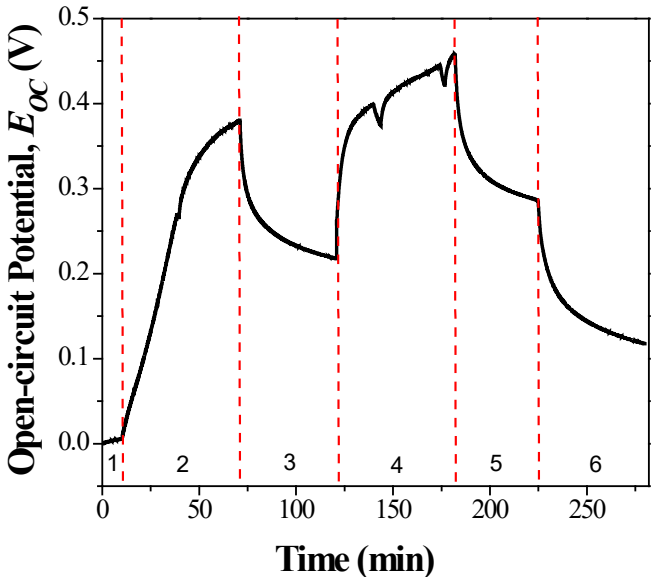

Figure S2. Open-circuit potential for the PEM electrolyzer vs. time for various operating conditions: (1) gas flow to cathode, no plasma, (2) gas flow to cathode, plasma on, (3) gas flow to cathode, no plasma, (4) gas flow to cathode, plasma on, (5) gas flow to cathode, no plasma, (6) no gas flow to cathode, no plasma. Liquid water was circulated at the anode for all conditions.

electrolyzer was left under idle conditions for > 3 h between ammonia production measurements.

Ammonia Detection

A common colorimetric method for the detection and quantification of ammonia was employed by mixing 16 drops (8 drops from each bottle of the indicator kit) of an ammonia indicator dye (API Ammonia Test Kit) in a sample of 10 mL from the cathode output reservoir solution after each 1 h measurement. The electrolyzer cathode gas output was bubbled through this solution during the experiment, and the presence of dissolved ammonia changed the indicator dye color. A second reservoir in series with the gas output from the first reservoir confirmed that effectively all the ammonia was captured in the first reservoir. To quantify ammonia production, the absorbance of a sample of the reservoir indicator dye solution was measured with a UV/vis spectrometer (PerkinElmer Lambda 950) within 10 min of the

completion of the 1 h potentiostatic measurement. An external calibration was produced using variable concentrations of NH_4Cl to correlate the absorbance peak intensity to the mg L^{-1} of dissolved ammonia. The ammonia production rate at each condition was determined by the average of at least three separate measurements. Additional indicator dyes were also used in separate measurements to test for the presence of nitrates (API Nitrate Test Kit), nitrites (API Nitrite Test Kit), and hydrazine (Hach 184900 Model HY-2). For electrolyzer bias in the absence of plasma, none of these byproducts were detected. With the plasma on, appreciable amounts of nitrate (but less than the ammonia) and small amounts of nitrite and hydrazine were detected.

Optical emission spectroscopy (OES) was performed on the N_2/He plasma by detaching the plasma jet electrode from the PEM electrolyzer and positioning the optical probe perpendicular against the inner glass tube of the plasma jet electrode at the tip of the device near the plasma discharge. An optical fiber connected to an Ocean Optics S2000 spectrometer recorded the emission data. Figure S1 shows characteristic spectra for the plasma at operating conditions. The spectra is similar to that reported for a DC N_2 plasma jet discharge, with peaks in the 300 – 400 nm range attributed to the second positive system of the nitrogen molecule (N_2 ($C^3\Pi_u$-$B^3\Pi_g$)), and peaks in the 380 – 440 nm range attributed to the first negative system of the nitrogen molecular ion (N_2^+ ($B^2\Sigma_u$-$X^2\Sigma_g$)).[368] However, unlike the reported DC plasma, notable peaks of the first positive system of the nitrogen molecule (N_2 ($B^3\Pi_g$-$A^3\Pi_u$)) in the 500 – 800 nm range were not observed, nor were NO emissions observed in the 250 – 300 nm range, since the AC plasma emission herein was

measured in the glass tube before exposure to air.[1] The emission peaks in the 580-710 nm range were not clearly observed either, likely because of these emissions is much less than the nitrogen emission peaks.[2]

Electrolyzer Open-circuit Potential

The open-circuit potential, E_{oc}, of the PEM electrolyzer was monitored as a function of time for different operating conditions as shown in Figure S2. Prior to starting measurements, the electrolyzer was allowed to reach steady-state conditions with water flowing to the anode and gas flow to the cathode in the absence of plasma. At this condition, the steady-state E_{oc} was ~ 0 V (Fig. S2, zone 1). Upon plasma ignition at the cathode, the PEM electrolyzer E_{oc} began to steadily rise before slowing its increase, and reached 0.37 V after 1 h of active plasma impinging on the electrolyzer cathode (Fig. S2, zone 2). All ammonia detection measurements over the course of this study were performed for 1 h, making the E_{oc} during this period the most relevant to the experimental conditions. Upon turning off the plasma, the E_{oc} decreased rapidly at first before slowly declining (Fig. S2, zone 3). Turning the plasma back on led to a rapid rise in E_{oc} followed by a slow increase to as high as 0.45 V after another hour of active plasma at the cathode (Fig. S2, zone 4). The dips in E_{oc} during this period corresponded to brief interruptions in the anode water circulation. Turning the plasma off again led to an initial rapid drop in E_{oc} followed by a slow decline (Fig. S2, zone 5). Stopping the gas flow to the cathode caused a further drop in E_{oc} (Fig. S2, zone 6).

Current Density vs. Time Performance

For electrolysis conditions of simultaneous applied bias with plasma (BWP), the PEM electrolyzer current density was observed to decrease sharply over the first ~ 5 min of plasma operation and then settle to a fairly stable value as shown in Figure S3. This initial decline in current density at a constant applied bias was attributed to additional dehydration of the membrane surface from plasma dissociation of water and charging of the membrane surface from charged plasma states. The brief spikes in the chronoamperometric data at 3.75 and 4 V corresponded to brief interruptions in the anode water circulation.

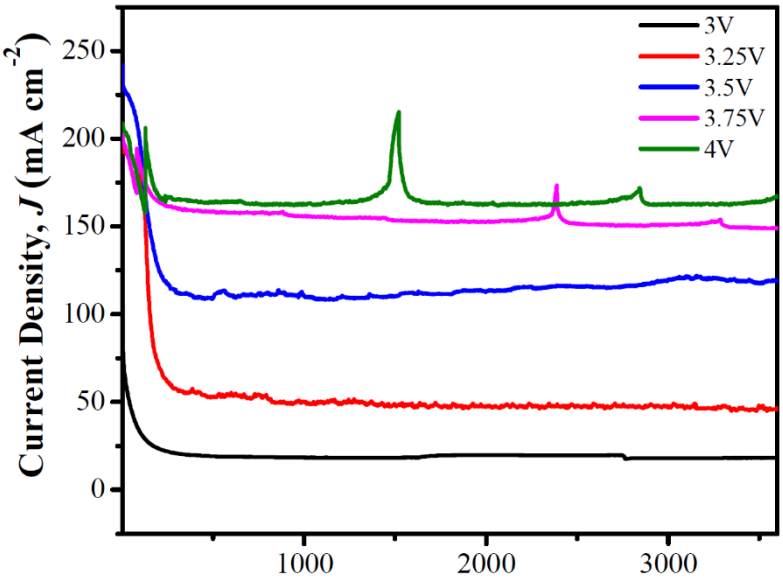

Figure S3. Current density vs. time (*J-t*) behavior for a constant applied bias for the electrolyzer under bias with plasma (BWP) conditions.

Energetics of Excited N_2 States and the Dissociation Barrier for Reaction

To further elucidate the proposed origin of the synergistic enhancement for ammonia formation through plasma-assisted electrochemical NRR, some simplified conceptual schematics are presented in Figure S4. Fig. S4a shows a simplified Frank-Condon diagram for nitrogen (not all energy levels and configurations are

represented). Above ~ 6 eV, the N_2 molecule is sufficiently energetic to enter electronic states (e.g., $A^3S_u^+$, B^3P_g, C^3P_u) in which electron relaxation leads to photon emission which can be observed by optical emission spectroscopy (Fig. S1). From the ground state to ~ 6 eV, N_2 is excited through vibrational states such as the $X^1S_g^+$ system, which are not directly observable by OES. Fig. S4b shows a schematic of potential energy vs. reaction coordinate to show the N_2 excited state effect on the dissociation barrier for the reaction. Here only the first intermediate step to break the triple bond of the N_2 reactant to form two adsorbed N^* atoms at the catalyst sites is represented.[367] Sufficiently energetic electronic states of N_2 (e.g., $N_2(B^3P_g)$) may have enough potential energy to yield a negative change in free energy upon dissociation to adsorbed N^* and thus yield a spontaneous reaction which can produce ammonia in the presence of water. This type of route leads to NH_3 in the reactor condition for plasma with no bias (PNB). Conversely, in the bias with no plasma (BNP) operational condition, the N_2 molecules are generally in the ground state and the nitrogen dissociation reaction is energetically uphill, requiring applied potential to overcome the activation energy, E_a, to drive NRR. Nitrogen molecules in plasma-induced vibrationally excited states, $N_2^{(v)}$, on the other hand, may not have sufficient potential energy to spontaneously lead to N_2 dissociation and subsequent NH_3 formation, but these states do reduce the activation energy for NRR and thus enable

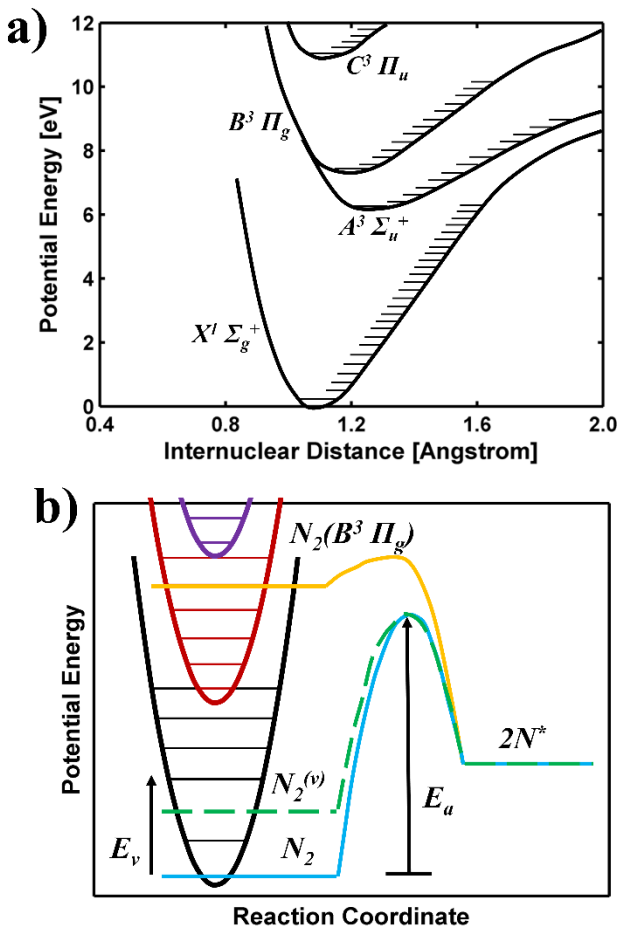

Figure S4. Schematic conceptual diagram of the energetics of excited N_2 states and the dissociation barrier for reaction. (a) Simplified Frank-Condon diagram for N_2 excited states. Vibrational states in the $X^1\ \Sigma_g^+$ system would not be detected by optical emission spectroscopy. (b) Schematic reaction coordinate diagram comparing activation energies (E_a) for N_2 dissociation from the ground state (blue), a vibrationally excited state (green), and an example higher excited plasma state from the $B^3\ \Pi_g$ system (orange).[367]

additional NH_3 formation in the bias with plasma (PWB) condition that is not permitted in either PNB or BNP conditions.

Plasma-assisted Electrolyzer Stability

A practical electrolyzer for industrial use should be stable for thousands of hours. Although the PEM electrolyzer used in this work maintained its *J-V* performance for up to 14 h of cumulative exposure of the MEA to the N_2/He plasma, it subsequently experienced irreversible degradation. The electrolyzer *J-V* curves of

Fig. S5 show that the current density at 3.5 V applied bias decreased 13% after 26 h of operation with plasma impinging on the cathode. The measured steady state membrane ionic conductivity did not appreciably change during this period, so we instead attribute this loss of performance to degradation of the catalyst. High-energy excited molecules and ions impacting the catalyst particles and carbon supports may induce gradual degradation via a sputtering mechanism.[365] Improving the electrolyzer stability, by catalyst protection or an altered plasma discharge with fewer high-energy states, would be necessary to harness the plasma-assisted electrochemical process in a practical device.

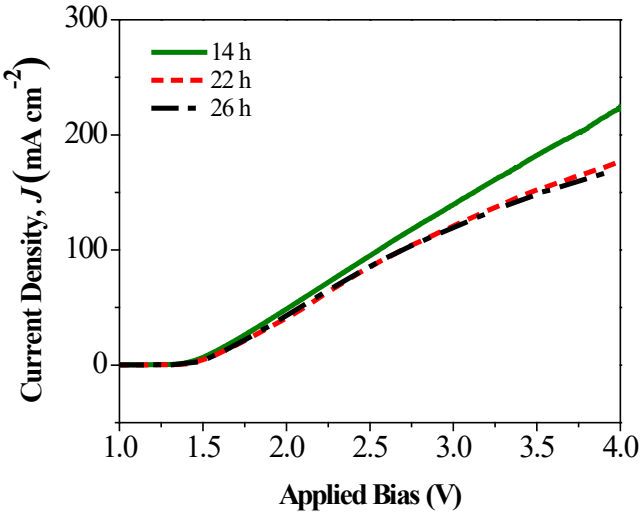

Figure S5. Current density vs. applied bias (*J-V*) behavior for the electrolyzer under plasma with bias conditions after cumulative exposure of the MEA to the N_2/He plasma for a time as shown in the legend. Up to 14 h, the performance was observed to be near its maximum but demonstrated decreasing performance thereafter.

APPENDIX II

SUPPORTING INFORMATION OF CHAPTER 3

Photoelectrochemical energy-conversion behavior

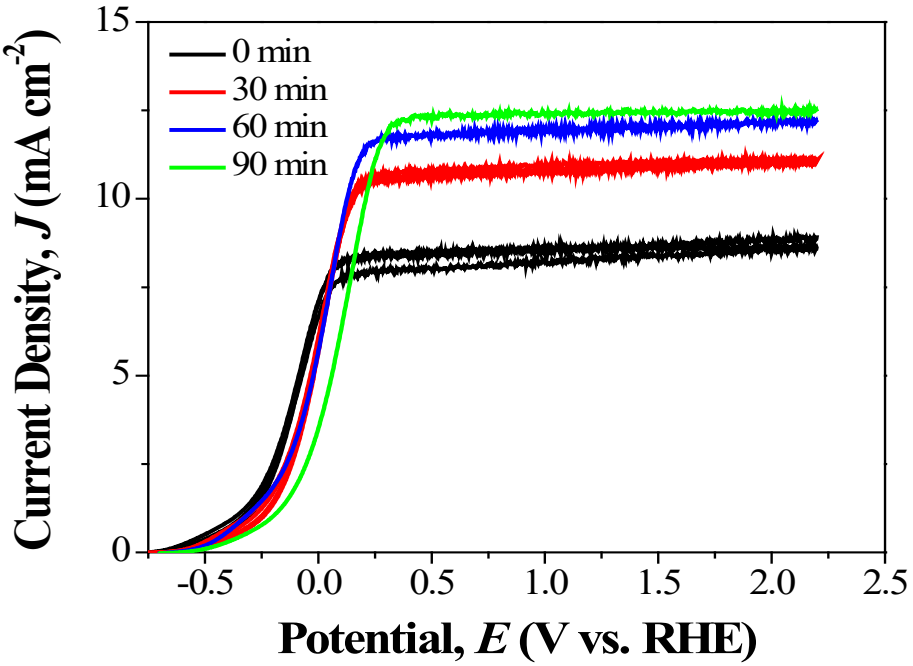

Fig. S1. Current density vs. potential (*J*-*E*) behavior for n-GaP in 1 M H_2SO_4 under 2 Suns AM1.5 illumination. The legend refers to how long the photoanode was under applied bias at 1.5 – 2.0 V vs. RHE.

In-situ UV-Vis spectroscopy

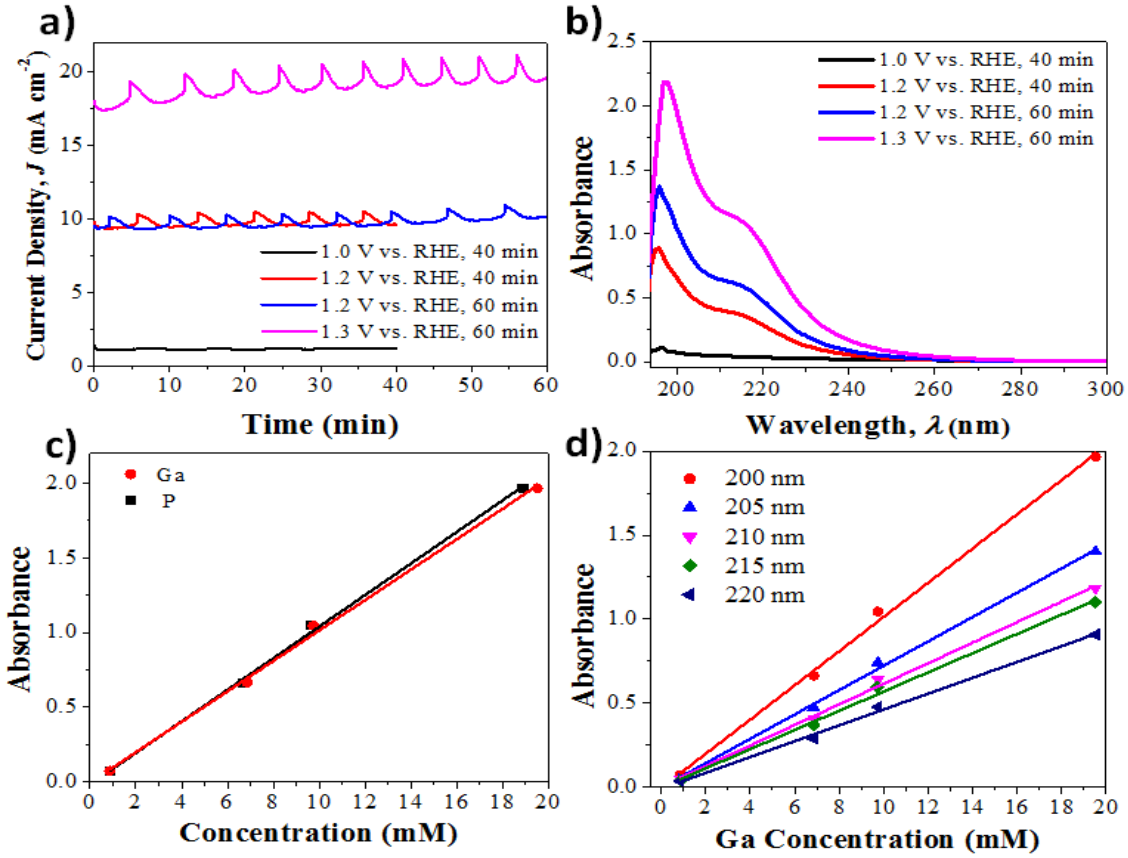

Fig. S2. Calibration for p^+-GaP in-situ UV-Vis spectroscopy. (a) Current density vs. time for p^+-GaP photoanodes at 1.2 V vs. RHE in 1 M H_2SO_4 and corresponding (b) absorbance vs. wavelength data. (c) Concentration of dissolved Ga and P in the electrolyte as measured by ICP-MS. (d) Resulting absorbance vs. Ga concentration calibration data.

The Pourbaix diagram for GaP was generated using the online platform of the Materials Project,[376-377] specifically the Pourbaix Diagram application.

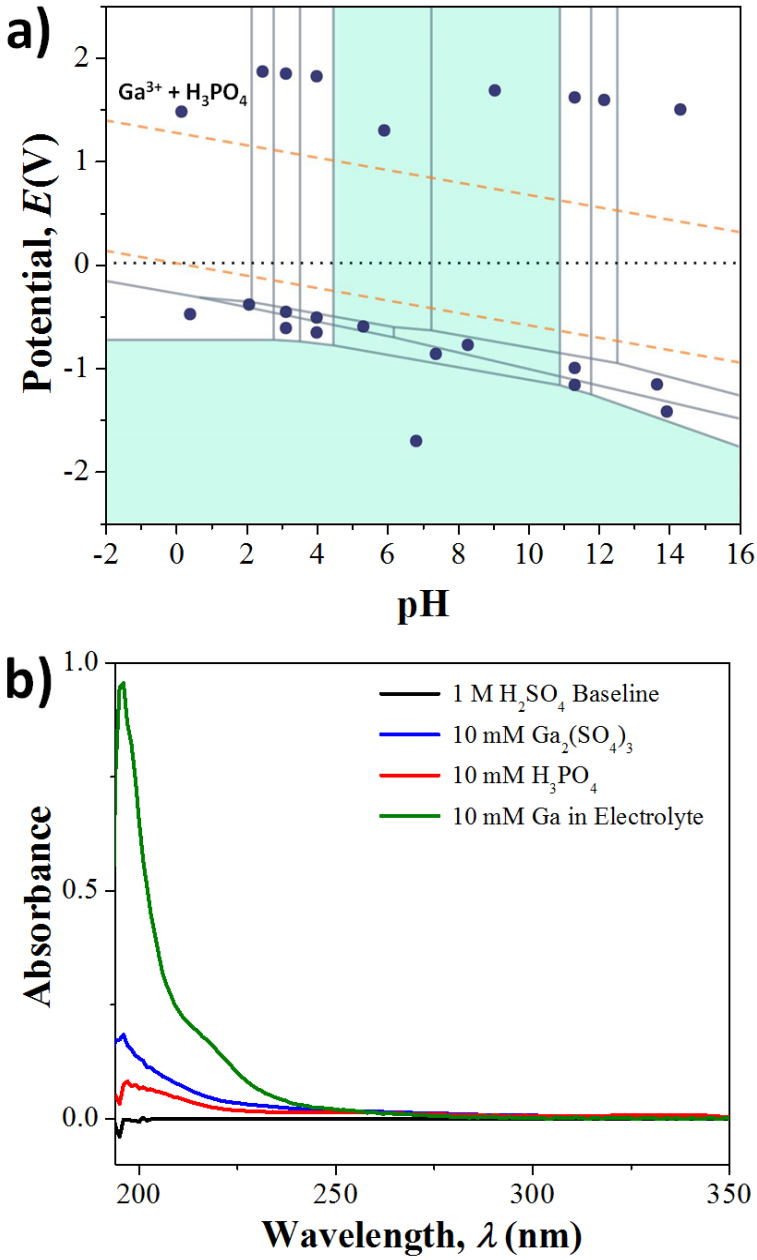

Fig. S3. (a) Calculated Pourbaix diagram for GaP predicting stable phases of Ga^{3+} and H_3PO_4 for oxidative potentials in strong acid. (b) UV-Vis absorbance spectra for electrolyte from n-GaP under illumination at 1.4 V vs. RHE corresponding to a Ga concentration of 10 mM (green), a 10 mM solution of $Ga_2(SO_4)_3$ (blue), and a 10 mM solution of H_3PO_4 (red), all in aqueous 1 M H_2SO_4.

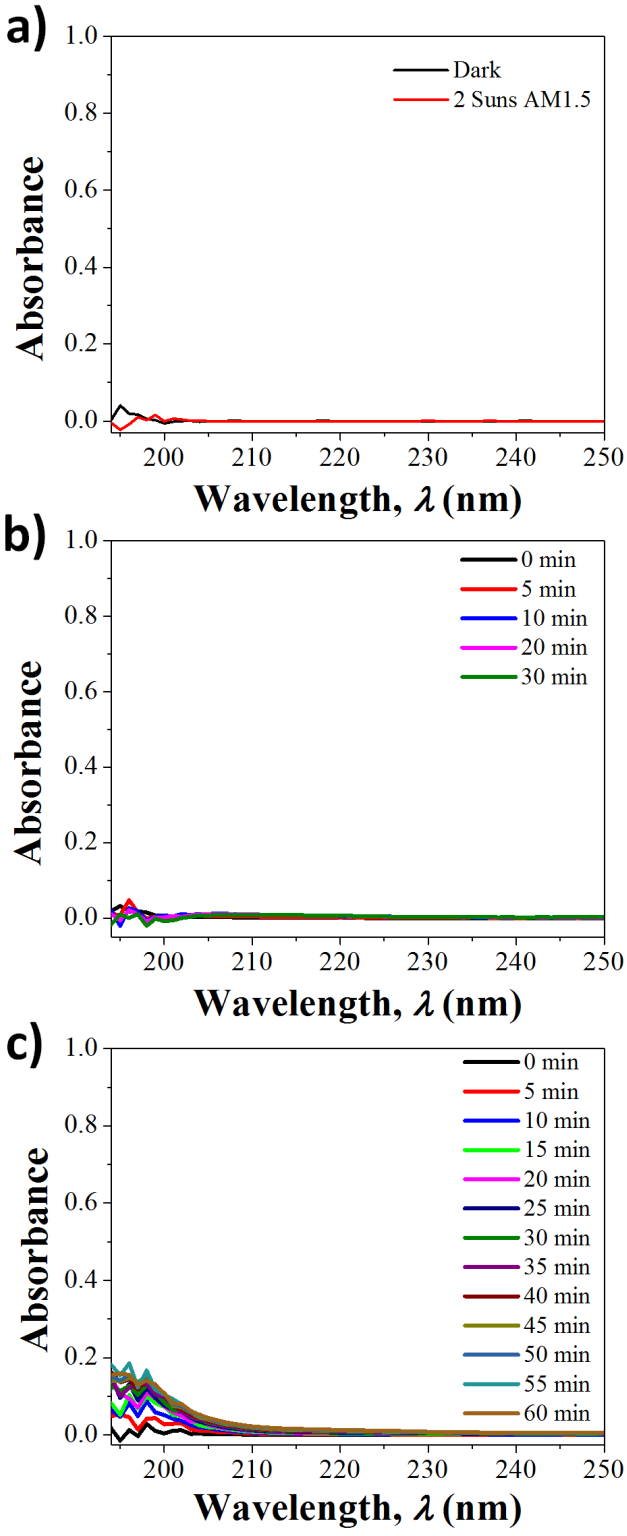

Fig. S4. Control measurements for in-situ UV-Vis spectroscopy with PEC characterization. (a) Absorbance spectra for pure 1 M H_2SO_4 electrolyte in the dark (the condition for background correction) and with 2 Suns AM1.5 illumination orthogonal to the monochromatic UV-Vis signal. (b) Absorbance spectra for n-GaP at 1.8 V vs. RHE in the dark. (c) Absorbance spectra over time for pure 1 M H_2SO_4 with 2 Suns AM1.5 illumination orthogonal to the monochromatic UV-Vis signal with no n-GaP present.

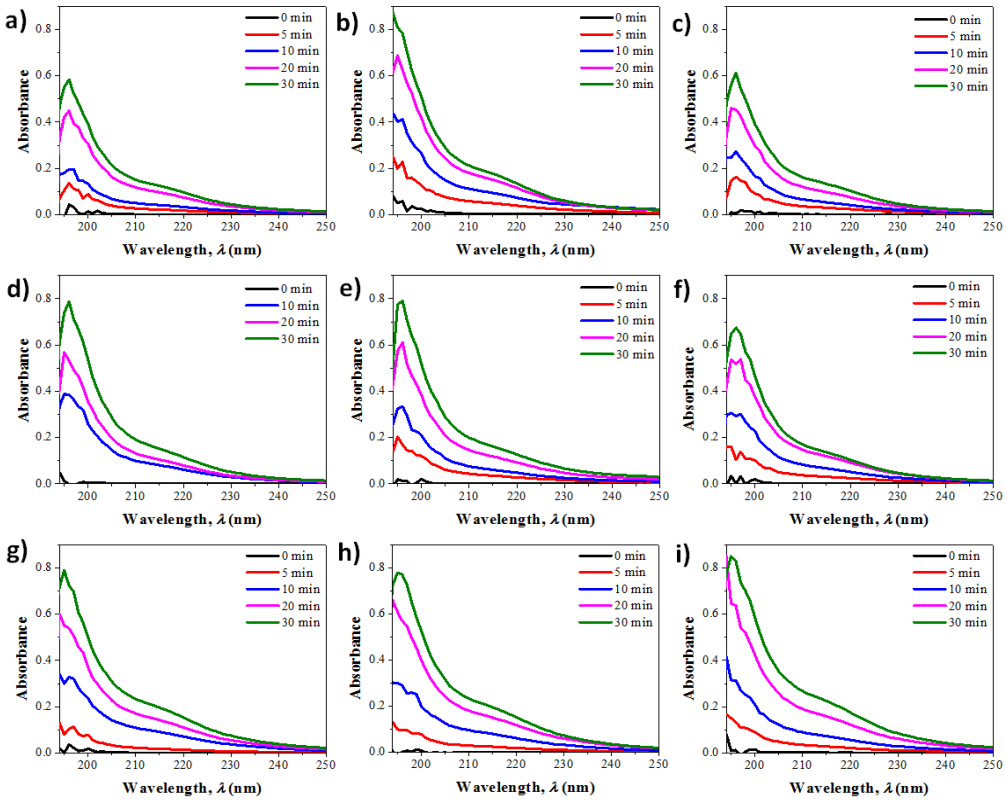

Fig. S5. Example absorbance data vs. time for n-GaP under 2 Suns AM1.5 illumination in 1 M H_2SO_4, operating potentiostatically at (a) 0.4 V, (b) 0.6 V, (c) 0.8 V, (d) 1.0 V, (e) 1.2 V, (f) 1.4 V, (g) 1.6 V, (h) 1.8 V, and (i) 2.0 V vs. RHE.

Corrosion of n-GaP photoanodes

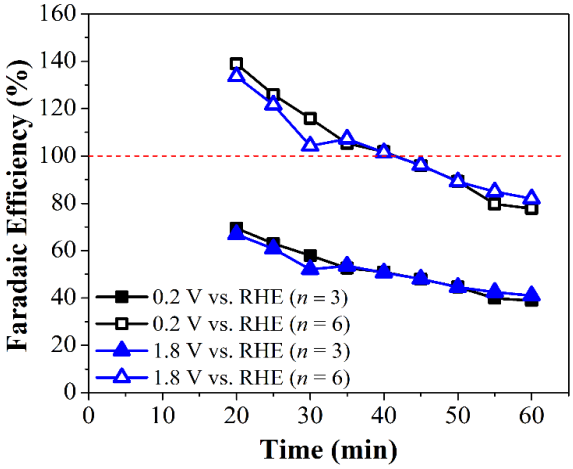

Fig. S6. Extended 1 h measurements of n-GaP under 2 Suns. Calculated faradaic efficiency for GaP oxidation using either $n = 3$ (filled markers) or $n = 6$ (open markers), from Ga concentration determined with in-situ UV-Vis spectroscopy.

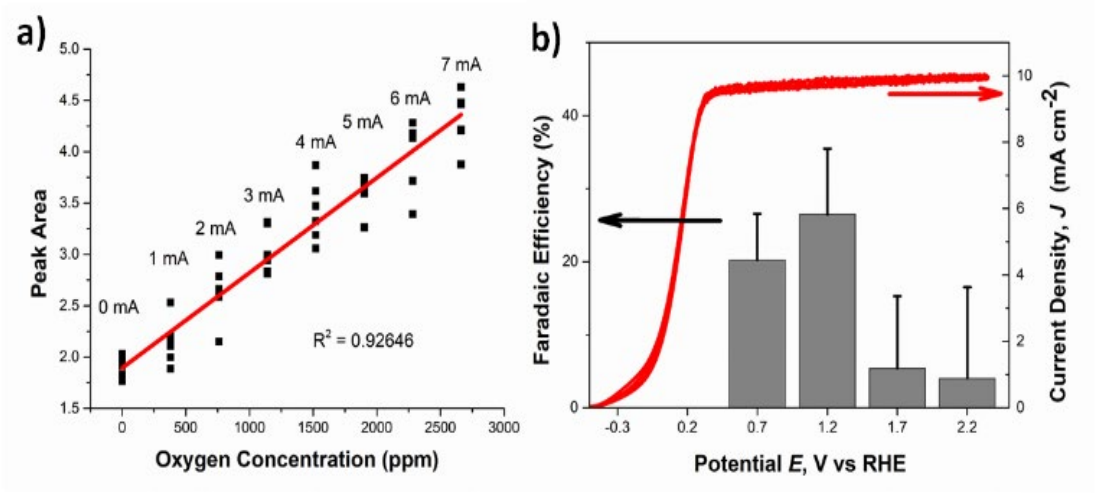

Fig. S7. Characterization of gaseous oxygen in the reactor headspace. (a) O_2 calibration curve produced a Pt anode for water-splitting. (b) Calculated faradaic efficiency for OER (grey, left scale) vs. potential based on measured O_2 concentration and the charge passed, and corresponding n-GaP current density (red, right scale) vs. potential. Bare n-GaP was measured in 1 M H_2SO_4 under 2 Suns AM1.5 illumination.

Oxygen concentration calibration was performed with a three–electrode setup using a Pt mesh working electrode, a Pt mesh counter electrode and a Ag/AgCl reference electrode in a four-neck flask containing 1 M H_2SO_4. The counter electrode was separated from the rest of the cell with a glass frit to avoid hydrogen gas from mixing into the exhaust of the dynamic sampling loop of the gas chromatograph, and to prevent oxygen reduction at the cathode. N_2 carrier gas was bubbled through the electrolyte at 10 sccm, and the gas outlet stream was sampled in a 1 mL sampling loop. The GC was an SRI 6810C Gas Mix #3 configuration. Oxygen was detected by a thermal conductivity detector (TCD). The calibration was performed using chronopotentiometry at 0, 1, 2, 3, 4, 5, 6, and 7 mA with at least 6 measurements for each current level (Fig. S7a).

OER on n-GaP was performed in a similar fashion with the n-GaP as the working electrode and the position calibrated for 2 Suns intensity. OER faradaic

efficiency was determined at a no bias (no sun) condition as well as 0.7, 1.2, 1.7, and 2.2 V vs. RHE. No oxygen beyond the baseline value was detected at the no bias condition. Each faradaic efficiency value measured consisted of an average of 6 oxygen measurements conducted sequentially over ~ 2 h.

Effect of TiO_2 protective layer

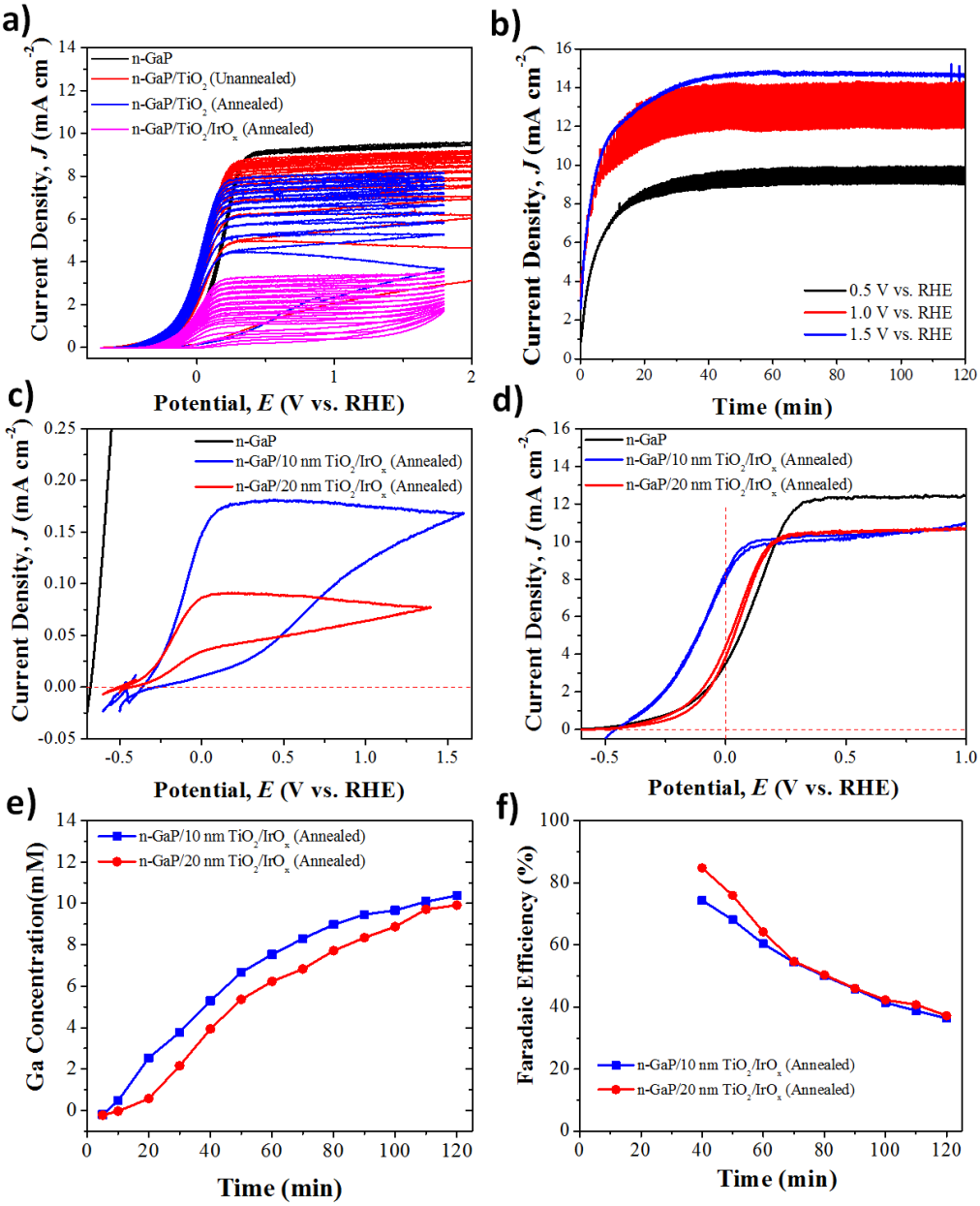

Fig. S8. n-GaP photocorrosion under 2 Suns with variable ALD TiO_2 thickness. (a) Current density vs. potential (*J*-*E*) behavior for multiple cycles for n-GaP with different protective layers. (b) Chronoamperometric behavior for n-GaP/TiO_2/IrO_x (Annealed) at different potentials. TiO_2 in (a-b) was 4 nm thick. (c-d) *J*-*E* behavior (c) before and (d) after 2 h at 2 V vs. RHE, and corresponding time dependence for (e) Ga concentration and (f) faradaic efficiency for GaP oxidation.

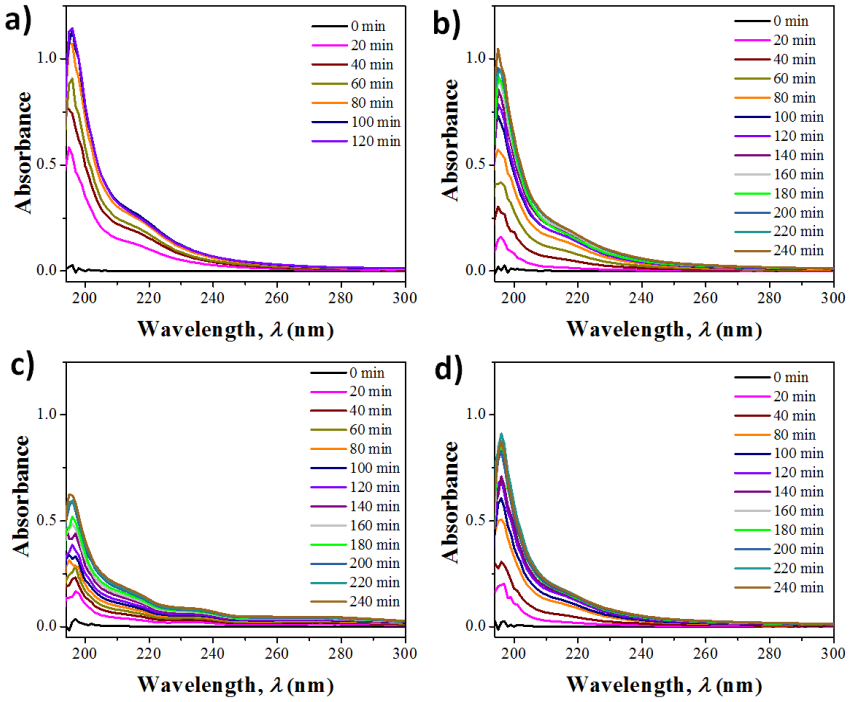

Fig. S9. In-situ UV-Vis spectroscopic measurement of absorbance over time at 0.2 V vs. RHE under 2 Suns for (a) n-GaP, (b) n-GaP/TiO_2 (Unannealed), (c) n-GaP/TiO_2 (Annealed), and (d) n-GaP/TiO_2/IrO_x (Annealed). The TiO_2 was 20 nm thick by ALD in (b-d).

GaP electrode surface characterization

Energy dispersive X-ray spectroscopy (EDS) mapping measurements were conducted using an FEI Tecnai F20 microscope with an accelerating voltage of 200 kV.

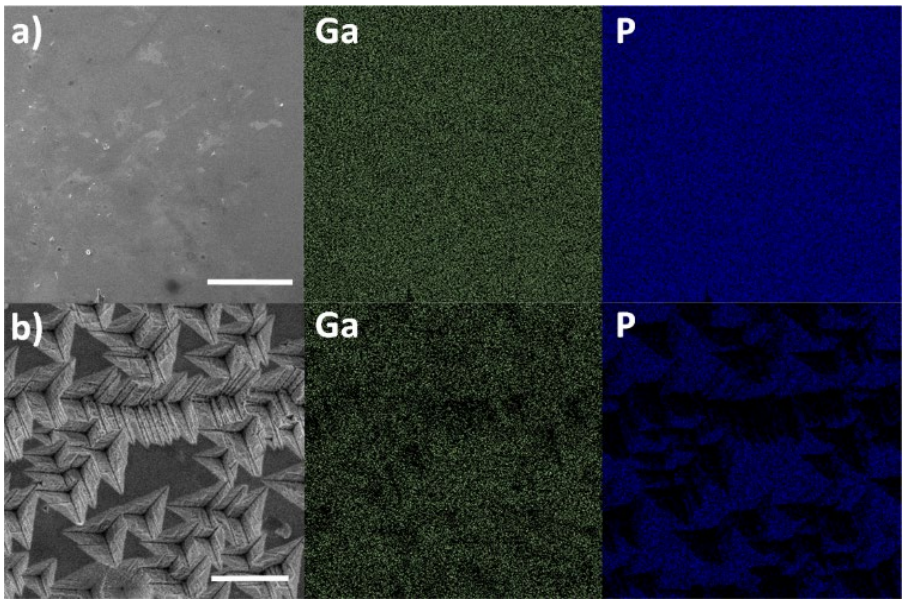

Fig. S10. SEM images (left) and EDS maps for Ga (center) and P (right) for annealed n-GaP/TiO_2 (a) before and (b) after 4 h at 0.2 V vs. RHE under 2 Suns. The scale bar is 500 μm in (a) and 100 μm in (b).

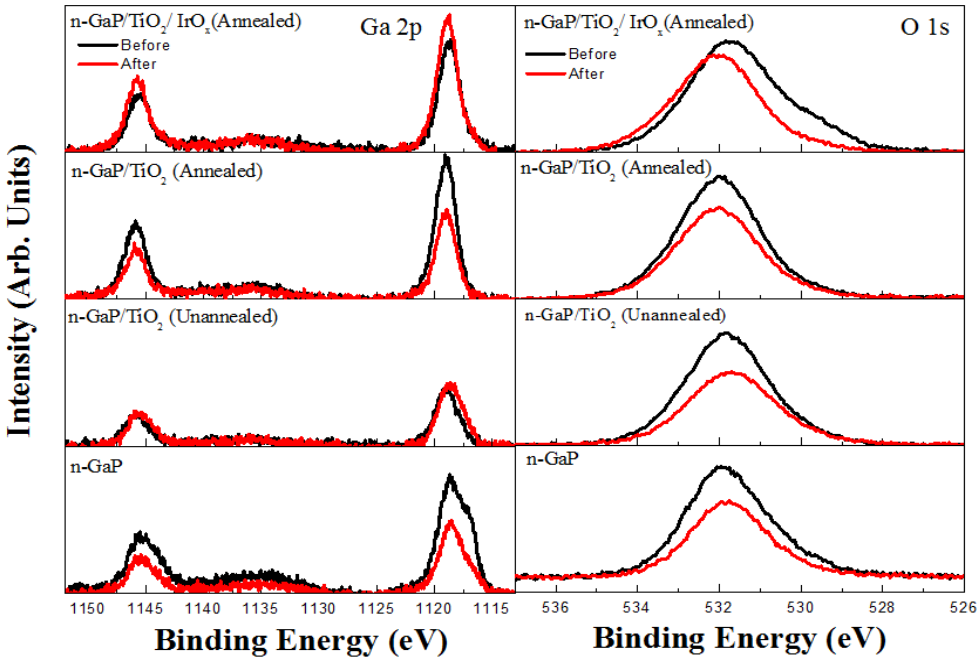

Fig. S11. XPS spectra for the n-GaP with and without protective layers before (black) and after (red) extended potentiostatic operation at 0.2 V vs RHE under 2 Suns for the Ga 2p (left) and O 1s (right) regions.

APPENDIX III

SUPPORTING INFORMATION OF CHAPTER 4

Photoelectrochemical energy-conversion behavior

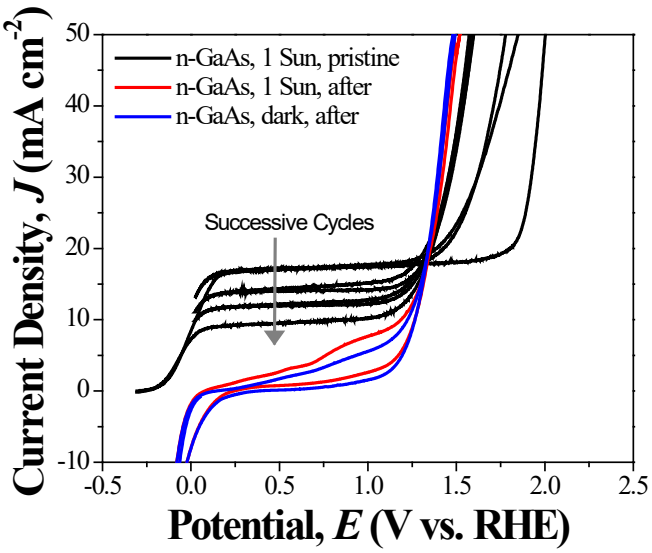

Fig. S1. Current density vs. potential (*J*-*E*) behavior for a (black curve) bare, pristine n-GaAs ($N_D \sim 10^{18}$ cm^{-3}) photoanode under 1 Sun AM1.5 illumination in 1 M H_2SO_4, and after 60 min at 1.5 V vs. RHE (red curve) under illumination and (blue curve) in the dark.

In-situ UV-Vis spectroscopy

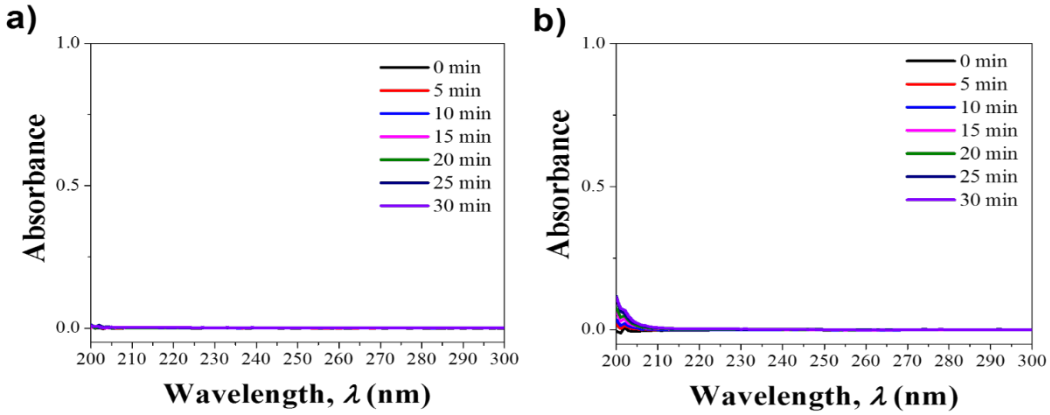

Fig. S2. In-situ UV-Vis spectroscopy control measurements. Absorbance vs. wavelength for 1 M H_2SO_4 electrolyte under 1 Sun illumination (a) in the absence of a GaAs electrode, and (b) with an n-GaAs electrode present without applied bias.

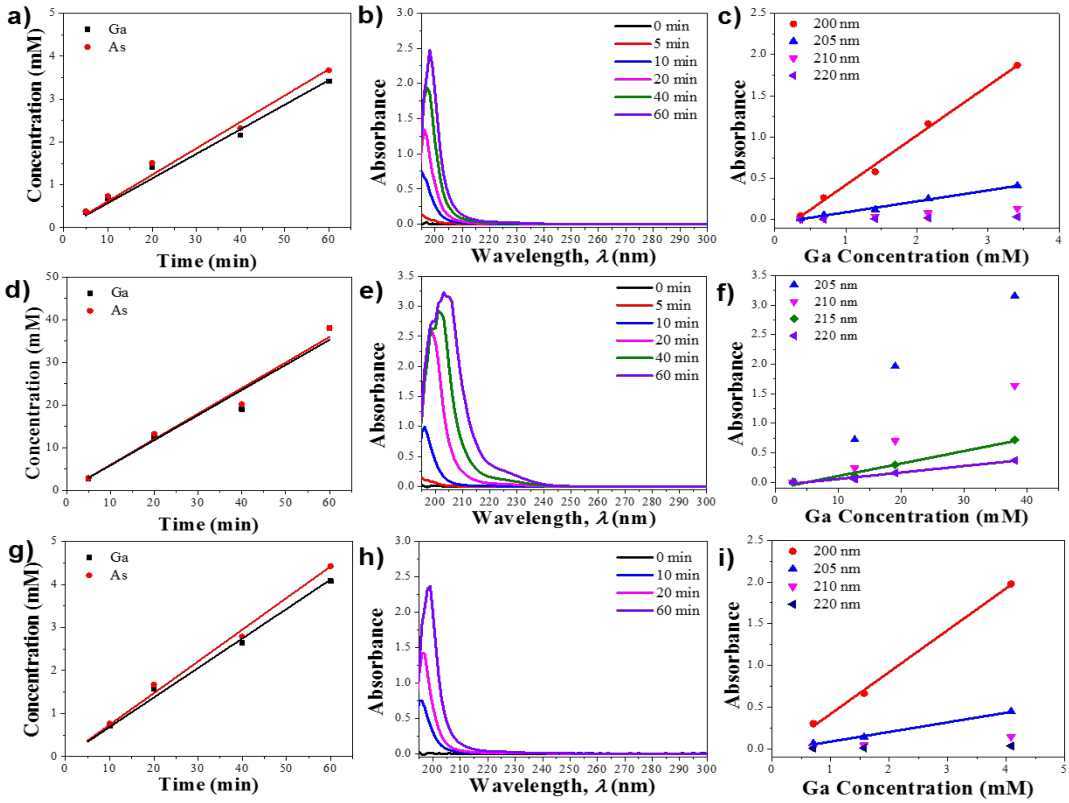

Fig. S3. In-situ UV-Vis spectroscopy calibration data. (a, d,g) Concentration of dissolved Ga and As in the electrolyte as measured by ICP-MS. (b, e, h) In-situ UV-Vis absorbance vs. wavelength data. (c, f, i) Selected wavelengths for absorbance vs. Ga concentration calibration curves. Data is for 1 M H_2SO_4 with 1 Sun, AM1.5 illumination on (a-c) bare n-GaAs at 1.0 V vs. RHE, (d-f) bare n-GaAs at 1.5 V vs. RHE, and (g-i) Ir(el)/n-GaAs at 1.0 V vs. RHE. All wafers were Micro Optics GaAs.

Bare n-GaAs photocorrosion behavior

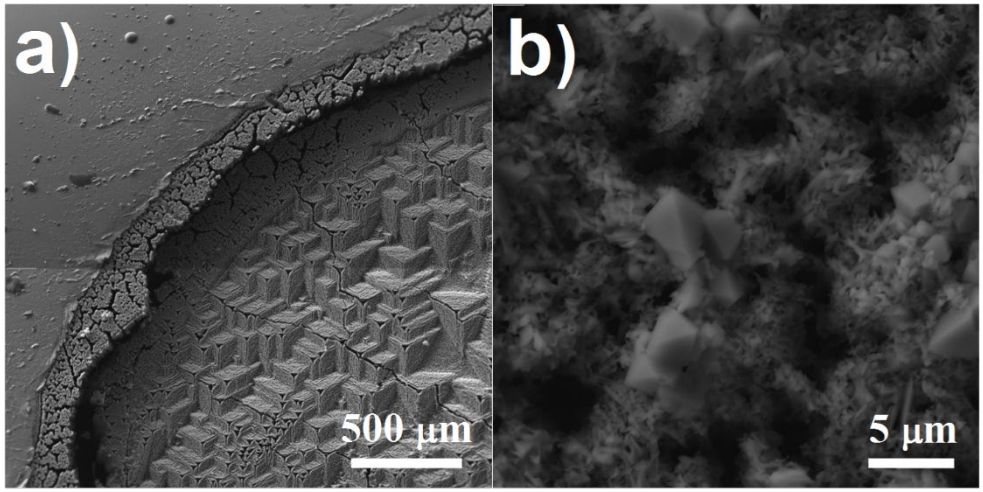

Fig. S4. SEM images for bare n-GaAs photoanodes after 2 h at 1.5 V vs. RHE at a scale of (a) 500 µm and (b) 5 µm.

Thin layer Ir-coated n-GaAs photocorrosion behavior

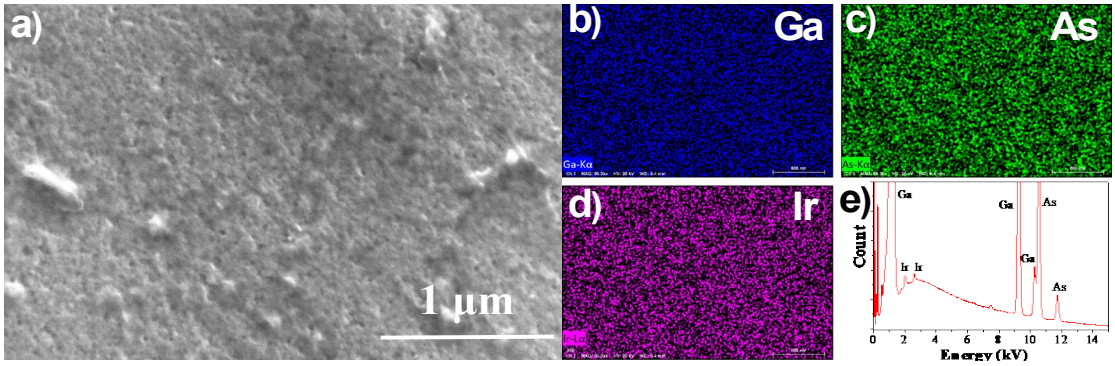

Fig. S5. Ir electrolessly deposited for 24 h on n-GaAs. (a) SEM image, EDS maps of (b) Ga, (c) As, and (d) Ir, and (e) corresponding EDS spectra.

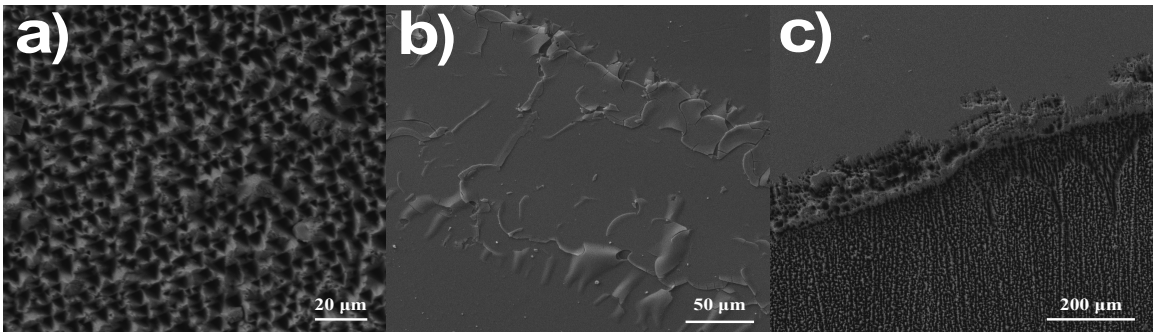

Fig. S6. SEM images for Ir/n-GaAs photoanodes at 2 h at 1.0 V vs. RHE. (a) Ir(el)/n-GaAs displaying triangular etch pits. (b) Ir(ch)/n-GaAs at edge of the active area showing flaking of the thin Ir layer, and (c) along the edge of the GaAs exposed to electrolyte showing the extent of corrosion.

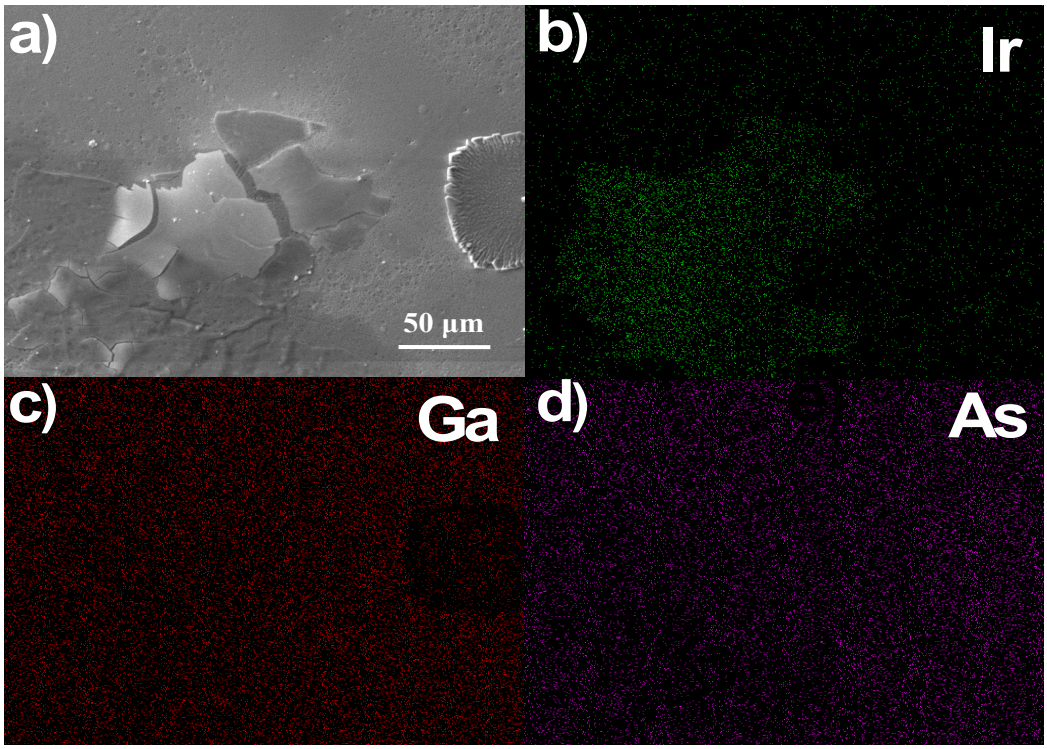

Fig. S7. Spin-coated iridium chloride (Ir(ch)) on n-GaAs after 10 min at 1.0 V vs. RHE at 1 Sun in 1 M H_2SO_4. (a) SEM image, and EDS maps of (b) Ir, (c) Ga, and (d) As.

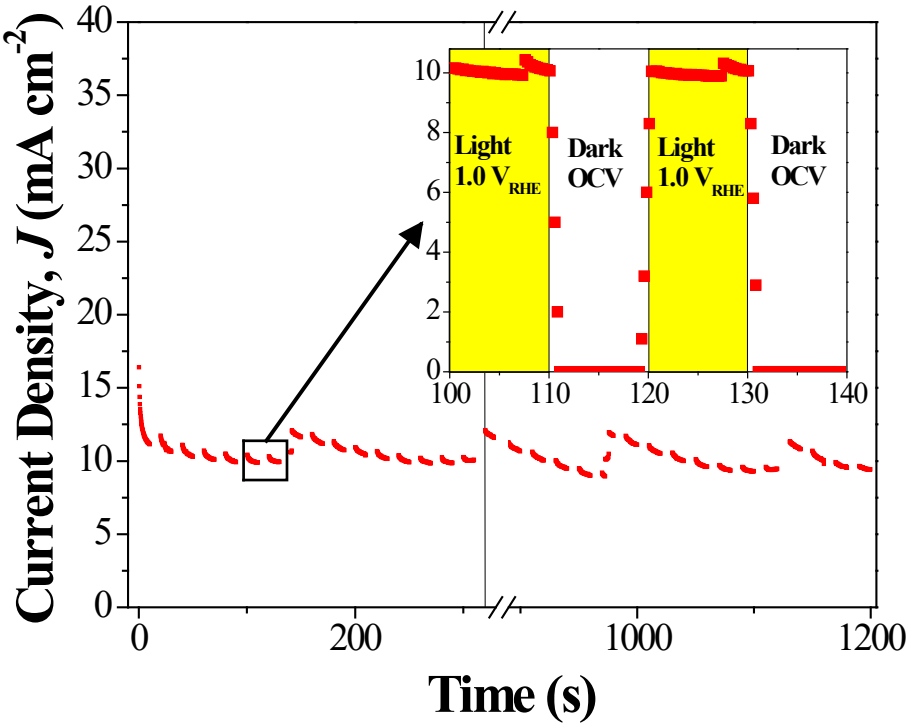

Fig. S8. Current density vs. potential behavior for Ir(el)/n-GaAs in 1 mM H_2IrCl_6, 1 M H_2SO_4 cycled for 10 min between 10 s at 1.0 V vs. RHE under 1 Sun followed by 10 s at the open-circuit voltage (OCV) in the dark. The inset plot shows a zoomed in set of data for two typical pulse cycles.

APPENDIX IV

COPYRIGHT PERMISSIONS OF FIGURES

Figure 4: Reprinted with permission from S. Y. Chen and L. W. Wang, *Chem. Mater.*, 2012, 24, 3659-3666. Copyright 2012 American Chemical Society.

Figure 6: Reprinted with permission from S. Y. Chen and L. W. Wang, *Chem. Mater.*, 2012, 24, 3659-3666. Copyright 2012 American Chemical Society.

Figure 7: (a) reprinted from *Corrosion Science*, Vol. 74, Y. Li, J. B. He, M. Zhang and X. L. He, "Corrosion inhibition effect of sodium phytate on brass in NaOH media. Potential-resolved formation of soluble corrosion products," 116-122, Copyright 2013, with permission from Elsevier. Panels (b-d) from S. Pishgar, J. M. Strain, S. Gulati, G. Sumanasekera, G. Gupta and J. M. Spurgeon, *J. Mater. Chem. A*, 2019, 7, 25377-25388 reproduced by permission of the Royal Society of Chemistry.

Figure 8: Panels (a-d) from S. Axnanda et al., *Scientific Reports*, 2015, 5, 09788, Copyright 2015. Panels (e-f) from M. F. Lichterman et al., *Energy Environ. Sci.*, 2015, 8, 2409-2416 reproduced by permission of the Royal Society of Chemistry.

Figure 9: Panels (a, d) reprinted from *J. Electroanal. Chem.*, Vol. 871, F. Tang, T. Liu, W. L. Jiang and L. Gan, "Windowless thin layer electrochemical Raman spectroscopy of Ni-Fe oxide electrocatalysts during oxygen evolution reaction", 114282, Copyright 2020, with

permission from Elsevier. Panel (b) reprinted with permission from Z. C. Zeng et al., *Anal. Chem.*, 2016, 88, 9381-9385. Copyright 2016 American Chemical Society. Panel (c) reprinted with permission from Y. L. Deng et al., *ACS Catal.*, 2016, 6, 2473-2481. Copyright 2016 American Chemical Society.

Figure 10: Panel (a) republished with permission of the Royal Society of Chemistry, from *J. Mater. Chem. A*, "Photocatalytic hydrogen production over CdS: effects of reaction atmosphere studied by in situ Raman spectroscopy", L. J. Ma et al., Vol. 3, 2015, permission conveyed through Copyright Clearance Center, Inc. Panel (b) republished with permission of IOP Publishing, Ltd., from *Semicond. Sci. Technol.*, "In situ Raman spectroscopy of the selective etching of antimonides in GaSb/AlSb/InAs heterostructures", C. Gatzke et al., Vol. 13, 1998, permission conveyed through Copyright Clearance Center, Inc.

Figure 11: Panel (a) from C. H. Choi et al., *Angew. Chem.-Int. Edit.*, 2015, 54, 12753-12757, reprinted with permission from John Wiley and Sons, Copyright 2015. Panels (b, c) reprinted from *Electrochem. Commun.*, Vol. 96, J. Knoppel et al., "Time-resolved analysis of dissolution phenomena in photoelectrochemistry - A case study of WO_3 photocorrosion", 53-56, Copyright 2018, with permission from Elsevier. Panel (d) reprinted with permission from S. Y. Zhang et al., *J. Phys. Chem. C*, 2019, 123, 23410-23418, https://pubs.acs.org/doi/full/10.1021/acs.jpcc.9b07220, Copyright 2019 American Chemical Society.

Figure 12: Panels (a, b) reprinted with permission from E. L. Clark and A. T. Bell, *J. Am. Chem. Soc.*, 2018, 140, 7012-7020. Copyright 2018 American Chemical Society. Panels (c, d) republished with permission of IOP Publishing, Ltd., from *J. Electrochem. Soc.*, "A

New Inlet System for Differential Electrochemical Mass Spectroscopy Applied to the Photocorrosion of p-InP(111) Single Crystals", P. Bogdanoff, P. Friebe and N. Alonso-Vante, Vol. 145, 1998, permission conveyed through Copyright Clearance Center, Inc.

Figure 13: Panels (a-c) reprinted with permission from N. O. Pena et al., *ACS Nano*, 2019, 13, 11372-11381. Copyright 2019 American Chemical Society. Panels (d-f) republished with permission of IOP Publishing, Ltd., from *Nanotechnology*, "In situ transmission electron microscopy of light induced photocatalytic reactions", F. Cavalca et al., Vol. 23, 2012, permission conveyed through Copyright Clearance Center, Inc.

Figure 14: Panel (a) from Y. Liang et al., *Small Methods*, 2019, 3, 1800387, reprinted with permission from John Wiley and Sons, Copyright 2019. Panel (b) adapted from C. Dette et al., *ACS Applied Materials & Interfaces*, 2019, 11, 5590-5594. Copyright 2019 American Chemical Society. Panels (c-e) reprinted from F. M. Toma et al., *Nat. Commun.*, 2016, 7, 12012.

Figure 15: Panel (a) from Y. Liang et al., *Small Methods*, 2019, 3, 1800387, reprinted with permission from John Wiley and Sons, Copyright 2019. Panel (b) reprinted from E. A. Paoli et al., *Chem. Sci.*, 2015, 6, 190-196. Published by the Royal Society of Chemistry. Panel (c) reprinted with permission from Y. G. Kim et al., *Langmuir*, 2014, 30, 15053-15056. Copyright 2014 American Chemical Society.

Figure 16: Panels (a, b) reprinted (adapted) with permission from D. Polcari, P. Dauphin-Ducharme and J. Mauzeroll, *Chem. Rev.*, 2016, 116, 13234-13278. Copyright 2016 American Chemical Society. Panel (c) from R. M. Souto et al., *Chem.-Eur. J.*, 2012, 18, 230-236, reprinted with permission from John Wiley and Sons, Copyright 2012. Panel (d) from T. Nickchi et al., *J. Mater. Sci.*, 2019, 54, 9213-9221 reprinted with permission from

Springer Nature, Copyright 2019. Panel (e) reprinted with permission from L. A. Naslund et al., *J. Phys. Chem. C*, 2013, 117, 6126-6135. Copyright 2013 American Chemical Society. Panel (f) reprinted with permission from H. S. Park et al., *J. Phys. Chem. C*, 2011, 115, 17870-17879. Copyright 2011 American Chemical Society.

CURRICULUM VITA

Sahar Pishgar

Contact Information

Department of Physics and Astronomy
Conn Center for Renewable Energy Research, Solar Fuels Lab
University of Louisville
Cell: (+1) 502-759-7519
E-mail:sahar.pishgar@louisville.edu

Education

- **University of Louisville (UofL)**, Department of Physics and Astronomy, Louisville, USA, 2017-2021, Ph.D.
- **University of Louisville**, Louisville, USA, 2015- 2017, M.Sc. in Physics
- **Sharif University of Technology (SUT)**, Tehran, Iran 2012-2015, M.Sc. in Physics
- **Sharif University of Technology**, Tehran, Iran 2007-2012, B.Sc. in Physics

Research Experience

Conn Center for Renewable Energy Research, University of Louisville, Kentucky. 2015-Present
Supervisor: Dr. Joshua Spurgeon and Dr. Gamini Sumanasekera

- **Investigation of n-GaAs photoanode corrosion in acidic media with various thin Ir co-catalyst layers**
- **Investigation of the photocorrosion of GaP and GaSbP III-V photoanodes in acid with *in-situ* UV/vis spectroscopy**
- **Characterization and implementation of a III-V $GaSb_xP_{(1-x)}$ alloy semiconductor for efficient solar-driven water-splitting**
- **Photoelectrochemical reduction of CO_2 to HCOOH on silicon photocathodes with reduced SnO_2 porous nanowire catalysts**
- **Synergistic plasma-assisted electrochemical reduction of nitrogen to ammonia**
- **Investigation of optical and vibrational features of Phosphorene**

Department of Physics, Sharif University of Technology, Nanoparticles and coating lab (NCL), Tehran, Iran 2013-2015.
Supervisor: Dr. Nima Taghavinia

- **M.Sc. Thesis: Flexible dye sensitized solar cells based on titanium mesh as the substrate",**
- **Electrophoretic deposition of Mesoporous TiO_2 Nanoparticles on stainless steel mesh"**

Honors and Awards

- **Dissertation Completion award**, University of Louisville, Graduate School, Spring 2021
- Graduate Teaching Assistantship, University of Louisville, Department of Chemistry, 2018-present
- Graduate Research Assistantship, Conn Center for Renewable Energy Research, University of Louisville, Fall 2017
- Graduate Teaching Assistantship, University of Louisville, Department of Physics and Astronomy. 2015- 2017
- **Graduate Network in Arts and Sciences, Research Fund,** Spring 2019 and Fall 2018

- **Graduate Student Council Research Grant**, University of Louisville, Spring 2017.
- Member of Graduate Teaching Assistant Academy, University of Louisville
- **Fellowship**, Sharif University of Technology, 2012-2015, M.Sc. student in physics.
- **Fellowship**, Sharif University of Technology, 2007-2012, B.Sc. student in physics.
- **Ranked 49th** among almost 13000 participants in the nationwide university entrance exam in the field of Physics for M.Sc. degree, Iran 2012.
- **Ranked in top 0.5%** among almost 320000 participants in the nationwide university entrance exam in the field of mathematics and physics for B.Sc. degree, Iran 2007.
- **Ranked 1st** in nationwide Azad University entrance exam in field of physics, Iran 2007.

Student Leadership Experiences

- Vice president of Iranian Student Organization, University of Louisville. 2017-2019
- Supervising undergrad and graduate students at solar fuels group, Conn Center, 2017-2019

Publications (Google Scholars)

- Analytical Techniques for the Investigation of Semiconductor Corrosion**. Sahar Pishgar**, Joshua Spurgeon. [To be submitted]

- Intense Pulse Light Annealing of Perovskite Photovoltaics Using Gradient Flashes. Amir H. Ghahremani, **Sahar Pishgar**, Jitendra Bahadur, and Thad Druffel. ACS Appl. Energy Materials, 2020.

- Pulsed electrochemical carbon monoxide reduction on oxide-derived copper catalyst Jacob M Strain, Saumya Gulati, **Sahar Pishgar**, Joshua M Spurgeon. ChemSusChem, 2020.

- Investigation of the photocorrosion of n-GaP photoanodes in acid with in-situ UV-Vis spectroscopy, **S Pishgar,** J Strain, S Gulati, G Sumanasekera, G Gupta, J Spurgeon. Journal of Materials Chemistry A, 7 (44), 25377-25388, 2019.

- Photocatalytic hydrogen evolution on Si photocathodes modified with bis (thiosemicarbazonato) nickel (ii)/Nafion. Saumya Gulati, Oleksandr Hietsoi, Caleb A Calvary, Jacob M Strain, **Sahar Pishgar**, Henry C Brun, Craig A Grapperhaus, Robert M Buchanan, Joshua M Spurgeon, Chemical Communications 55 (64), 9440-9443, 2019.

- A study on the material characteristics of low temperature cured SnO_2 films for perovskite solar cells under high humidity**.** Jitendra Bahadur, Amir H Ghahremani, Blake Martin, **Sahar Pishgar**, Thad Druffel, Mahendra K Sunkara, Kaushik Pa, Journal of Materials Science: Materials in Electronics, 2019.

- Synergistic plasma-assisted electrochemical reduction of nitrogen to ammonia. **S Pishgar**, S Kumari, ME Schwarting, WF Paxton, JM Spurgeon, Chemical Communications 54 (95), 13347-13350, 2018.

- Photoelectrochemical reduction of CO_2 to HCOOH on silicon photocathodes with reduced SnO_2 porous nanowire catalysts**.** KR Rao, **S Pishgar**, J Strain, B Kumar, V Atla, S Kumari, JM Spurgeon, Journal of Materials Chemistry A 6 (4), 1736-1742, 2018.

Presentations

- Materials Research Society Fall/Spring Virtual Meeting, 2020.
- Materials Research Society Spring Meeting, Phoenix, AZ, 2019.
- Graduate Students Regional Research Conference, Louisville, KY, 2019.
- Graduate Network in Arts and Sciences conference, Louisville, KY, 2019.

Workshops Attended

- **Hands-On Photovoltaic Experience (HOPE), National Renewable Energy Laboratory, Golden, CO, 2020.**

Skills

- **Microscopy: Optical, SEM, EDS**
- **Spectroscopy: XPS, UPS, Raman, Photoluminescence (PL), UV-Vis**
- **Electrical: 4-point probe, Hall effect measurement**
- **Deposition: Atomic layer deposition (ALD), Thermal evaporator, Electrodeposition**
- **Photo-electrochemistry**

Computer Skills

- Programming language: MATLAB
- Microsoft Office (Excel, Word, PowerPoint)
- Origin-pro
- SolidWorks

Highlights of Qualification

- Creative and Innovative quick learner
- Strong in meeting deadlines
- Excellent public speaking, communication skills and teamwork attitude
- Flexible and adaptive to any environment
- **Lab work experiences: 8 years of experience in Nanoparticles and Coating Lab (SUT) and Conn Center for Renewable Energy Research (UofL)**
- Ability to manage multiple projects and tasks simultaneously